Sediment Transport and Morphodynamics at an Estuary Mouth: a Study using Coupled Remote Sensing and Numerical Modelling

by

Eduardo Siegle

A thesis submitted to the University of Plymouth
in partial fulfilment for the degree of

Doctor of Philosophy

School of Earth, Ocean and Environmental Sciences
Faculty of Science

September 2003

REFERENCE ONLY

LIBRARY STORE

UNIVERSITY OF PLYMOUTH
Item No. 9005685856
Date 16 OCT 2003 S
Class No. THESIS 557.4609 SIE
Cont. No. X704637315
PLYMOUTH LIBRARY

Aos meus pais

To my parents

Abstract

Sediment Transport and Morphodynamics at an Estuary Mouth: a Study using Coupled Remote Sensing and Numerical Modelling

Eduardo Siegle

The balance of the physical processes that drive the morphodynamics of a complex inlet system is investigated in this work. For this purpose, an innovative technique using coupled video imaging and numerical modelling has been used to study the relative importance of the driving forces that control the sandbar dynamics at the Teignmouth inlet system. The sandbars that form the ebb tidal delta are highly dynamic, leading to a cyclic morphological behaviour.

Application of the numerical model (MIKE21 HD, NSW, ST) served two separate functions. The hydrodynamic model has been used for the image processing and, combined with the sediment transport module, the full model has been used to understand the relative importance of the driving forces at the region. The iterative application of the hydrodynamic model and the video images, with the modelled water levels used as input to the image processing, provides the video-based intertidal morphology that is used in further modelling experiments. This loop is repeated several times during the three-year study period that covered a complete morphological cycle. This results in a quantitative assessment of the relative influence of the key processes that control the environment and in initial steps towards the prediction of its evolution. In order to assess the relative importance of the driving forces a series of modelling experiments were designed to include a variety of forcing conditions. These include the tidal range, wave conditions and river discharge values.

The relative importance of each of the physical processes on the sediment transport and consequent morphodynamics varies across the region. The main inlet channel is dominated by tidal action that directs the sediment transport as a consequence of the varying tidal flow asymmetry, resulting in net offshore transport. Sediment transport over the shoals and secondary channels at both sides of the main channel is dominated by wave related processes, displacing sediment onshore. The interaction between waves and tide generated currents controls the transport over the submerged sandbar that defines the channel's seaward extent. High river discharge events are also proven to be important in this region as they can change sediment transport patterns across the area. Waves play a major role in the sandbar morphodynamics. Despite the relative low frequency of high wave energy events that reach the region they are responsible for large amounts of sediment displacement, catalysing some dramatic morphological changes. Therefore, the temporal distribution of storms defines the cyclic behaviour of such environments, making the system more dynamically active over the winter months. It is also during this period that river discharge values reach high peaks, increasing the capacity of the ebbing tidal flows and interacting with the opposing waves. The opposite occurs during summer periods, when less energetic conditions lead to slower morphological changes. The application of an initial sedimentation/erosion model proved to be useful in giving qualitative predictions of the morphological evolution of such a complex sandbar system, reflecting the initial morphological changes for different forcing conditions. Qualitative comparisons between the modelled sedimentation/erosion patterns and the video based observations of the changes at the dynamic offshore sandbar show that the model is able to reproduce its overall evolutionary tendency. The morphological adjustment of the system to the forcing conditions shows the progression towards the next morphological stage, allowing the initial steps towards predicting the evolution to be taken.

The technique applied, coupling the numerical model with the video images, has been shown to be of great value in providing a better understanding of the processes that control the dynamics of inlet systems. At short time-scales, quantitative information about the acting processes and how they interact has been gained by the modelling experiments, and at medium time scales, the combined application resulted in qualitative predictions of the evolution of most regions of the system.

Contents

Abstract iv
List of Figures ix
List of Tables xvi
List of Symbols xvii
Acknowledgements xx

Chapter 1

Introduction 1

1.1. General Introduction 1
1.2. Specific Objectives 3
1.3. Thesis outline 3

Chapter 2

Literature Review 5

2.1. Foreword 5
2.2. Inlet Systems 5
2.2.1. Definition and general morphology 5
2.2.2. Importance of inlet systems 9
2.2.4. Morphodynamics 10
2.3. Modelling Inlet Processes 13
2.3.1. Initial sedimentation/erosion models 15
2.4. Application of video imaging techniques 18
2.4.1. Extracting information from images 19
2.4.2. Video imaging of inlet systems 23
2.4.3. Combining video imaging and numerical modelling 23

Chapter 3

Study Area and Available Data 25

3.1. Site description 25
3.1.1. Relevant Previous Studies at the River Teign Inlet 27
3.1.2. Nomenclature and Main Morphologic Features 32

3.2. Available data 34
3.2.1. COAST3D main experiment *34*
3.2.2. Argus Video System *41*
3.2.3. Weather Station and Pressure Sensor (pier) *50*
3.3. Conclusion 51

Chapter 4

Numerical Modelling 52

4.1. Introduction 52
4.2. Model Setup 53
4.2.1. Hydrodynamic module setup (HD) *55*
4.3.2. Nearshore Spectral Wind-Wave module setup (NSW) *60*
4.3.3. Sediment Transport module setup (ST) *62*
4.4. Model Calibration and Validation 63
4.4.1. Calibration *64*
4.4.2. Validation *84*
4.4.3. Sediment Transport *88*
4.6. Conclusions 95

Chapter 5

Video Imaging and Numerical Modelling 98

5.1. Introduction 98
5.2. Technique Applied to Extract Intertidal Morphology from Images 99
5.3. Combination of Numerical Modelling and Video Imaging 101
5.3.1. Water Surface Topography *102*
5.3.2. Modelled Water Levels as Input for Video Imaging Techniques *109*
5.3.3. Extracted Intertidal Morphology as Input for Numerical Model Simulations 111
5.4. Technique Validation 116
5.5. Application 125
5.6. Discussion and Conclusions 129

Chapter 6

Physical Controls on the Sandbar Dynamics 133

6.1. Introduction 133
6.2. Numerical Simulations 133
6.3. General Hydrodynamics 135
6.3.1. Tidal circulation *135*
6.3.2. River discharge *136*
6.3.3. Wave driven circulation *138*
6.4. Sediment Transport 143
6.4.1. General Sediment Transport Patterns *143*
6.4.2. Driving forces on the sediment transport *146*
6.5. Discussion and Conclusions 162

Chapter 7

Sediment Transport Patterns and Morphodynamics 165

7.1. Introduction 165
7.2. Model Setup 166
7.2.3. Bed resistance *167*
7.2.4. Sediment data *167*
7.3. Numerical Simulations 168
7.4. Sediment Transport and Morphological Evolution 168
7.4.1. Stage 1 ..... *169*
7.4.2. Stage 2 ..... *178*
7.4.3. Stage 3 ..... *185*
7.4.4. Stage 4 ..... *192*
7.5. Conceptual Model of the Cyclic Evolution at Teignmouth 196
7.5.1. Origin of the sandbars *196*
7.5.2. Onshore migration of the sandbar *197*
7.5.3. Spreading of the attached sandbar and formation of a new offshore sandbar 198
7.6. Conclusions 200

Chapter 8

Conclusions and Future Directions 202

8.1. General Conclusions 202
8.2. Future work 209

Appendix I – Numerical Model Description **211**

AI.1. Model Description 212

AI.1.1. MIKE21 Hydrodynamic Module (HD) *212*

AI.1.2. MIKE21 Nearshore Spectral Wind-Wave Module (NSW) *221*

AI.1.3. MIKE21 Sediment Transport Module (ST) *224*

Appendix II **232**

References **244**

List of Figures

Chapter 2

2.1. General inlet morphology (modified from Davis, 1994). 6

2.2. Schematic diagrams depicting controls on ebb delta size and shape, where a) free-form ebb delta; b) constricted ebb delta; c) high-angle half delta; and d) low-angle half-delta (after Hicks and Hume, 1996). 8

2.3. Coastal morphodynamic system. 11

2.4. Inlet features (bold) and their main forcings (italic) as a function of time and space (after De Vriend, 1991). 12

2.5. Concept of the initial erosion deposition (ISE), medium term (MT) and long term (LT) models (modified from De Vriend et al., 1993). In the present application, the left-hand side of the diagram is applied (ISE model and data assimilation). 16

2.6. Behaviour of a "distorted" system (modified from De Vriend, 1994). 17

2.7. Example of snap-shot (a) and time-exposure Argus video images. 19

Chapter 3

3.1. Study area. The nearshore bathymetry (for October 1999) is plotted over a rectified Argus image. 25

3.2. The beach, protected by a seawall with The Ness headland in the background. 26

3.3. Diagrammatic representation of the main changes in bank positions (Robinson, 1975). 28

3.4. Sediment transport at the Teignmouth region (from Carter and Bray, 2003). 31

3.5. Oblique and rectified merged Argus video images of the study area with the definition of the nomenclature used in this study (Images from the 24/01/2000). 33

3.6. Locations of instruments during the main field campaign in Teignmouth (October 1999 bathymetry in relation to the ACD). Figure taken from Whitehouse and Sutherland, 2001). Each numbered circle represents a sensor location. Those used in the present work are detailed in Table 3.1. 36

3.7. Example of the COAST3D surveys coverage area and resolution. Black points indicate the vessel bathymetric survey and red points indicate the beach quad bike survey (6 – 8 November 1999, Survey 1, OSGB). 40

3.8. Sediment samples distribution and median grain size values for the COAST3D experiments. Co-ordinates are in OSGB, depths in ODN and grain size in millimetres. 41

3.9. The Ness, with the arrow indicating the position of the Argus video cameras, detailed in the right hand side. 42

3.10. Images from the five cameras in Teignmouth and a merged image showing a panoramic view of the cameras field of view (05 March 2000, 12:00h). 42

3.11. Geometric conventions for Argus photogrammetry (Lippmann and Holman, 1989). 45

3.12. Argus video images pixel resolution for the Teignmouth cameras system (26 October 1999). 50

Chapter 4

4.1. Interaction of MIKE21 ST with other modules of the MIKE21 system 54

4.2. Model grid and bathymetry for the "initial" (a) and "final" (b) grid. 58

4.3. Water level and wave height during each calibration period. a) 25/10/1999 18:50 – 27/10/1999 18:50; b) 10/11/1999 19:40 – 12/11/1999 19:40. 68

4.4. Sensitivity of the RMAE values according to the Chézy numbers. 69

4.5. Time series of measured (dotted line) and predicted water level (solid line) with respective residual values for the calibration period 1 (25/10/1999 18:50 – 27/10/1999 18:50). 71

4.6. Time series of measured (dotted line) and predicted water level (solid line) with respective residual values for the calibration period 2 (10/11/1999 19:40 – 12/11/1999 19:40). RMAE pier: 0.0133; RMAE harbour: 0.099. 72

4.7. Station 14, CP1. Upper panel: Time series of flow velocities; measured (lines) and predicted (dots). Middle panel: scatter plots of measured and predicted velocity components. Lower panel: Linear regression between predicted and observed velocities. 76

4.8. Station 14, CP2. Upper panel: Time series of flow velocities; measured (lines) and predicted (dots). Middle panel: scatter plots of measured and predicted velocity components. Lower panel: Linear regression between predicted and observed velocities. 77

4.9. Station 24, CP1. Upper panel: Time series of flow velocities; measured (lines) and predicted (dots). Middle panel: scatter plots of measured and predicted velocity components. Lower panel: Linear regression between predicted and observed velocities. 78

4.10. Station 24, CP2. Upper panel: Time series of flow velocities; measured (lines) and predicted (dots). Middle panel: scatter plots of measured and predicted velocity components. Lower panel: Linear regression between predicted and observed velocities. 79

4.11. Station 28, CP1. Upper panel: Time series of flow velocities; measured (lines) and predicted (dots). Middle panel: scatter plots of measured and predicted velocity components. Lower panel: Linear regression between predicted and observed velocities. 80

4.12. Station 25, CP2. Upper panel: Time series of flow velocities; measured (lines) and predicted (dots). Middle panel: scatter plots of measured and predicted velocity components. Lower panel: Linear regression between predicted and observed

velocities. 81

4.13. Comparison of measured (dots) and modelled (lines) wave parameters for a) station 7, significant wave heights (upper panel), significant wave period (middle panel), wave direction from true North (lower panel); b) station 4, significant wave heights (upper panel), significant wave period (lower panel); and c) station 25, significant wave heights (upper panel), significant wave period (lower panel). 83

4.14. Water level and significant wave heights (a) and river discharge (b) during the validation experiment period. 85

4.15. Time series of measured (lines) and predicted (dots) flow velocity components for a) station14; b) station 24; c) station 25 and d) station 26. 87

4.16. Measured (a) and modelled using the deterministic STP transport formulation (b) morphological changes over a 14 days period, between surveys 2 and 4 of the COAST3D main experiment. 92

4.17. Measured (a) and modelled using Bijker's transport formulation (b) morphological changes over a 14 days period, between surveys 2 and 4 of the COAST3D main experiment. 93

Chapter 5

5.1. Diagram of the procedure applied for the extraction of the intertidal morphology from video images. 101

5.2. a) Measured tide levels at the pier (black line) and harbour (blue line), and b) measured difference in tide level between the pier and the harbour. (October – November 1999). 103

5.3. Contour plot of the water surface topography in relation to the pier water level (a) and velocity vector plot (b) at maximum ebb flow. 105

5.4. Time series of water level residuals (thick line) and water level (a – thin line) and current velocity (b – thin line) in the middle of the channel. 106

5.5. Along channel profile of water level differential (a), x-velocity (b) and y-velocity (c). The situation represented is at approximately LW – 1 hour during spring tide (27/10/1999 00:40:00). 107

5.6. Wave effect on the water levels around the sandbars. The represented profile starts offshore (0 m) and ends onshore (700 m) and its exact position is given in Figure 1 in Appendix II (P3). The figure legend shows the modelled wave heights. 108

5.7. Mid channel water slope for real measured discharge and for high river discharge conditions. The arrow indicates the flattening in the curve at around 400 m distance. 108

5.8. Example of coastline segmentation for the image processing using modelled water levels for: camera 1 (a) and camera 2 (b) at 13:00h on the 27/10/1999. Black crosses indicate positions (U, V) of water levels extracted from the model with elevation values indicated by black labels. Yellow lines show the stretches of coastline processed from average water level (yellow numbers). At the given time, the measured water level at the pier is –1.98 m. 112

5.9. Diagram representing the framework of the applied method. Red arrows represent the links between the numerical modelling and video imaging techniques. 113

5.10. Example of modelled hydrodynamics overlaid on video images at different tidal levels in order to test the intertidal morphology applied in the simulations through the wetting and drying areas. Example for 31/08/2000. 115

5.11. Validation profiles of the morphology extraction technique from the video images. Yellow contour lines are the shorelines extracted from the images; red dots are the surveyed points; and black lines are the compared profiles indicated by the numbers. Survey carried out on 25 – 27/10/99 and image from the 26/10/1999. Contour lines were extracted from images covering a two day interval (26 – 27/10/1999). 118

5.12. Comparison of measured morphology profiles (circles) and extracted from images using the modelled water level (stars) and constant water level (diamonds) at the Sprat sandbar for the 26-27/10/1999. Profile locations are shown in Figure 5.11. 119

5.13. Comparison of measured morphology profiles (circles) and extracted from images (stars). Profile locations are shown in Figure 5.11. 120

5.14. Comparison of measured morphology profiles (circles) and extracted from images using the modelled water level (stars) and constant water level (diamonds) at the offshore sandbar for the 26-27/10/1999. Profile locations are shown in Figure 5.11. 121

5.15. Validation profiles of the morphology extraction technique from the video images. Yellow contour lines are the shorelines extracted from the images; red dots are the surveyed points; and black lines are the compared profiles indicated by the numbers. Survey and image from the 05/07/2000. Contour lines were extracted from images covering a three day interval (04 – 06/07/2000). 122

5.16. Comparison of measured morphology profiles (circles) and extracted from images (stars) at the attached sandbar for the 05/07/2000. Profile locations are shown in Figure 5.15. 123

5.17. Comparison of measured morphology profiles (circles) and extracted from images (stars) using the modelled water levels with the previous morphology. These profiles were extracted from 30/08/2000 images using modelled water levels from the previous model runs (May 2000 morphology). 124

5.18. Rectified images and nearshore morphology for each of the modelled periods using the extracted intertidal morphology with constant subtidal morphology. These morphologies are applied in the modelling experiments (Chapter 7). 127

Chapter 6

6.1. Example vector plots indicating the modelled velocity field at the inlet region for maximum ebb (a) and maximum flood (b) conditions. Red numbers in (a) represent the position of the extracted time series shown in Figure 6.2. 136

6.2. Channel x-component of modelled current velocities from the mouth to the outer part ranging from spring (26/10/1999) to neap tide (04/11/1999) conditions. Positive values indicate ebb flow and negative represent flood flow. Station

positions are indicated in Figure 6.1a. 138

6.3. Incident wave direction scatter plot. 139

6.4. Example vector plots indicating the modelled velocity field without (a) and with (b) the presence of waves (12/11/1999 13:00h). Vectors are plotted over rectified video images of the inlet region. 140

6.5. Vector plots showing the ebb flow deflection due to the wave action 12/11/1999 00:40h). Yellow shading represents the region where current velocities are higher than 0.2 m s^{-1}. The profile p-p' (a) indicates the position of the profile in Figure 6.6. 142

6.6. Significant wave height for simulations without considering the wave-current interaction (a - black line) and considering the wave-current interaction (a - blue line) and the *x*-velocity component along the profile (b) along the profile p-p' indicated in Figure 6.5 (12/11/1999 11:00h). The profile starts offshore. 142

6.7. Schematic diagrams of calculated sediment transport patterns averaged over two tidal cycles for a) spring tide and b) neap tide. Arrow lengths are schematically related to strength of transport. 145

6.8. Locations of extracted time series of modelled sediment transport. The nearshore bathymetry is plotted over a rectified Argus image. 145

6.9. Time series of boundary conditions (a), sediment transport (ST) at station A (b), station B (c), station C (d), station D (e) and station E (f). x-components (dots), y-components (line). 148

6.10. Time series of boundary conditions, current velocity and sediment transport over the offshore sandbar (station F). x-components (dots), y-components (line). 149

6.11. Diagrams showing different stages of wave – current interaction driving the sediment transport over the intertidal sandbar (centre) and the modelled hydrodynamic over the sandbar (right hand side). Tidal currents (light arrows), wave driven currents (dark arrows). 151

6.12. Modelled sediment transport patterns over the intertidal offshore sandbar. The correspondent tidal phase of each plot is indicated in the lower plot. 154

6.13. Time series of boundary conditions, current velocity and sediment transport over the Ness sandbar (station G). x-components (dots), y-components (line). 155

6.14. Sediment transport patterns for different angles of incident waves (H_{sig} = 1.8 m). Yellow vectors (80°); black vectors (115°); and red vectors (130°). 155

6.15. Vectors of sediment transport along profiles over the Ness sandbar, the submerged sandbar at the outer part of the channel and the offshore sandbar during high energy wave event at neap tide conditions (a) and spring tide conditions (b). Black vectors represent sediment transport during low river discharge (8 m^3 s^{-1}) and red vectors represent results for high river discharge events (150 m^3 s^{-1}). 158

6.16. Modelled sediment transport rates across the sandbar system for the thirteen-day simulation. 161

6.17. Morphological changes of the offshore sandbar over a one-month period represent the pre- and post-storm situation. The block diagrams represent the morphology of the sandbar (extracted from video images) detailed by the box in the

rectified image. The October (a) digitised sandbars shoreline is overlaid on the November (b) image. 162

6.18. Summarised areas of relative dominance of tides, waves and river discharge over the sediment transport. 164

Chapter 7

7.1. Rectified video images showing the evolution of the sandbar system from March 1999 to April 2002. Images were gathered at similar tide levels of about –1.90 m. 170

7.2. Schematic diagrams with the diagnostic morphologic features of each evolutionary stage. Arrows indicate the direction of the sandbars migration. 171

7.3. Rectified images for April and September 1999. Continuous black lines in b represent the digitised shoreline in a, and the doted line represents the estimated location of the submerged sandbar through the breaking waves. 173

7.4. Detail of the modelled sediment transport for a high-energy event (H_{sig} = 1.8 m) over the offshore sandbar in March 1999. Sediment transport patterns (a) and initial sedimentation/erosion rates (b), where deposition is represented by blue lines and erosion by yellow lines. 173

7.5. Pre- and post-storm images at the same tidal level showing the increase in area. Shoreline of the sandbar before the storm (a) is overlaid on the image gathered after the storm (b). 174

7.6. Morphological changes of the offshore sandbar over a one-month period represent the pre- and post-storm situation. The October (a) digitised sandbars shoreline is overlaid on the November (b) image. 176

7.7. Detail of the modelled sediment transport over a thirteen-day simulation covering the storm that reshaped the offshore sandbar in October 1999. Sediment transport patterns (a) and initial sedimentation/erosion rates (b), where deposition is represented by blue lines and erosion by yellow lines (interval between lines is 0.20 m). 177

7.8. Time series of water level, cross-shore velocity and magnitudes of sediment transport over the offshore sandbar for neap (left) and spring (right) tide during high wave energy conditions (H_{sig} = 1.8 m) for the October/November 1999 situation. 178

7.9. Morphological evolution from January to December 2000. Continuous black lines represent the sandbar shoreline from the previous image and dotted line represents the approximate position and of the submerged sandbar. Tidal levels vary between images. 180

7.10. Detail of the modelled sediment transport for a high-energy event (H_{sig} = 1.8 m) over the offshore sandbar in January 2000. Sediment transport patterns (a) and initial sedimentation/erosion rates (b), where deposition is represented by blue lines and erosion by yellow lines (interval between lines is 0.05 m). 181

7.11. Detail of the modelled sediment transport for a high-energy event (H_{sig} = 1.8 m) over the offshore sandbar in August 2000. Sediment transport patterns (a) and initial sedimentation/erosion rates (b), where deposition is represented by blue

lines and erosion by yellow lines (interval between lines is 0.05 m). 183

7.12. Top: predicted patterns of sediment transport along the indicated profile for low river discharge (black vectors) and high river discharge ($100m^3\ s^{-1}$) (red vectors). Bottom: initial sedimentation/erosion rates along the indicated profile (p-p') for low river discharge (black line) and high river discharge (red line). 184

7.13. Morphological evolution from February to December 2001. Continuous black lines represent the sandbar shoreline from the previous image and dotted line represents the approximate position and of the submerged sandbar. Tidal levels vary between images. 186

7.14. Predicted water level (a), measured waves at the pier (b), and river discharge (c) for January/February 2001. 187

7.15. Detail of the modelled sediment transport for a high-energy event (H_{sig} = 1.8 m) over the offshore sandbar in February 2001. Sediment transport patterns (a) and initial sedimentation/erosion rates (b), where deposition is represented by blue lines and erosion by yellow lines (interval between lines is 0.05 m). 190

7.16. Predicted sediment transport (a) and initial sedimentation/erosion patterns for February 2001 overlaid on the April 2001 image. In (a) the red circle highlights the new offshore sandbar and the yellow dots indicate the channel and shoal velocity time series location. In (b) the red circle indicates the location of the modelled sedimentation region. 191

7.17. Top: residual flow vectors for only tide simulation (black) and under the influence of waves (H_{sig} = 1.8 m – yellow) over two spring tidal cycles in February 2001. Bottom: time series of modelled cross-shore component of the velocities over the two-tidal cycles at the channel (line) and shoal (dots) locations indicated in Figure 7.16 for both wave energy situations. Negative values = onshore; positive = offshore. 192

7.18. Morphological evolution from January to April 2002. 193

7.19. Detail of the modelled sediment transport for a high-energy event (H_{sig} = 1.8 m) over the offshore sandbar in April 2002. Sediment transport patterns (a) and initial sedimentation/erosion rates (b), where deposition is represented by blue lines and erosion by yellow lines (interval between lines is 0.05 m). 195

7.20. Conceptual model for the evolutionary cycle of the ebb tidal delta sandbars at Teignmouth. 199

Chapter 8

8.1. Degree of sandbar morphological changes as function of tidal range and wave height. 208

List of Tables

Chapter 3

3.1. COAST3D main experiment instruments used for the model validation. 35

3.2. Bathymetric surveys carried out during the main experiment. 39

Chapter 4

4.1. Summary of the boundary conditions for the "final" HD simulation. 58

4.2. Qualification of RMAE ranges for velocity and wave heights comparison according to Van Rijn et al. (2003). 66

4.3. Depth varying Chézy numbers. 69

4.4. Statistical parameters for the water level at the pier and harbour for both calibration periods. 82

4.5. Statistical parameters for the current velocity time series at the indicated stations for both calibration periods. 82

4.6. Statistical parameters for the significant wave heights time series at the indicated stations. 84

4.7. Statistical parameters for the water level at the pier and harbour for the validation period. 86

4.8. Statistical parameters for the current velocity time series at the indicated stations for the validation period. 86

4.9. BSS sensitivity to grain size and formulation. 91

4.10. Decomposition of BSS (offshore sandbar) 94

Chapter 5

5.1. RMSE (m) values of the compared profiles. 125

5.2. Stages chosen for the numerical modelling and image processing. 126

List of Symbols

(variations in symbolism or other symbols are stated in the text next to derivation)

α	parameter governing wave breaking – adjustable constant
θ	direction of wave propagation (degrees)
ϕ	camera's angle of rotation
κ	van Karman's constant
δ	camera field of view
ξ	dimensionless factor in Bijker's sediment formulation
μ	ripple-factor
τ	camera tilt
ω	absolute wave frequency
$\Omega(x,y)$	Coriolis parameter, latitude dependent (s^{-1})
$\zeta(x,y,t)$	surface elevation (m)
θ'	skin friction
γ_1	parameter governing wave breaking – maximum steepness parameter
γ_2	parameter governing wave breaking – maximum *H/d* parameter
ρ_s	density of the sediment
ε_s	diffusion coefficient
ρ_w	density of water ($kg/m/s^2$)
τ_{xx}, τ_{xy}, τ_{yy}	components of effective shear stress
$A...L$	eleven parameters which describe the geometry (Walton vector)
a_b	amplitude of the wave-induced motion at the bottom
B	dimensionless coefficient for bed load transport (Bijker)
c	celerity (m/s)
C(x,y)	Chézy resistance ($m^{1/2}/s$)
c_b	bed concentration
c_{gx}, c_{gy}, c_θ	wave propagation speeds (m/s)
C_R	Courant number
C_s	Smagorinsky factor
c_s	volume concentration of suspended sediment

d	water depth (m)
d_{50}	median grain size (mm)
d_{90}	sediment size for which 90 % of the bed material is finer
E	eddy viscosity coefficient (m^2/s)
f(V)	wind friction factor
f_c	focal length
f_w	wave friction factor
g	acceleration due to gravity (m/s^2)
H	wave height (m)
h(x,y,t)	water depth (m)
H_m	maximum allowable wave height (m)
H_{rms}	root mean square value of the wave height (m)
H_{sig}	significant wave height (m)
I_1, I_2	Einstein's integrals
k	wave number
k_N	Nikuradse roughness parameter
m_n	moments of the wave-action spectrum
N	camera Nadir
O	optic centre of the camera
p, q(x,y,t)	flux densities in x- and y-directions ($m^3/s/m$)=(uh,vh);(u,v)=depth averaged velocities in x- and y-directions
P_a(x,y,t)	atmospheric pressure ($kg/m/s^2$)
Q_b	rate of wave dissipation
q_b	bed load sediment transport ($m^3/s/m$)
q_s	suspended load sediment transport ($m^3/s/m$)
q_t	total sediment transport ($m^3/s/m$)
R	straight distance from ground location to the camera
r	bed roughness
s	relative density of the sediment
S_{xx}, S_{xy}, S_{yy}	radiation stresses
t	time (s)
T	wave period (s)
T_{diss}	wave dissipation period
U, V	depth averaged velocity components in the x- and y-direction

u, v	velocities in the x- and y-directions (m/s)
U'_f	instantaneous shear velocity related to skin friction
$U_{f,wc}$	shear velocity for combined wave-current
U_i, V_i	image coordinates
$V, V_x, V_y(x,y,t)$	wind speed and components in x- and y-directions (m/s)
w_s	settling velocity
x, y	space coordinates (m)
z	vertical elevation (m)
Z_c	distance from the ground plan to the camera

Acknowledgements

I would like to express my extreme gratitude for the excellent guidance and supervision of Professor David Huntley, my principle supervisor. His continuous support, patience and passion for research were fundamental throughout the project. Thanks David!

A big thank you also goes to Dr Mark Davidson, my second supervisor. Being "next door" and always available for any discussion was really helpful.

I'm indebted to several people who helped throughout the development of the thesis, including Dr Pierre Regnier and Dr Hans J. Vested (DHI Water & Environment) for the collaboration and assistance in using the MIKE21 modelling system; Dr James Sutherland (HR Wallingford) and Dr Dirk-Jan Walstra (Delft Hydraulics) for the assistance with the COAST3D field data; Dr Cyril Mallet, Dr Mark Davidson, Dr Ken Kingston, Dr Stefan Aarninkhof and Prof. Rob Holman for introducing me and guiding me through the "Argus world".

Thanks to the Brazilian National Research Council (*Conselho Nacional de Desenvolvimento Científico e Tecnológico* – CNPq) for sponsoring this research at the University of Plymouth.

I would like to thank my Brazilian colleagues and friends for "showing me the way" to the PhD: Dr Lauro Calliari, Dr Elírio Toldo Jr., Dr Antonio Klein and Dr Carlos Schettini.

Thank you to all my friends! The good moments we had together will be always remembered. I would like to mention Marcos and Caína (Marcos, thanks for reading the chapters' drafts; and of course, for your willingness for a pint...), Covi and Pablo, Elisa and Gilberto, Ismael and Cecilia, Alex, Gise, James, Kevin, Linda, Giovanni and Sandrine, Kate and Paulo... and the "Coffe Club" members over the past few years: Peter, Dave, Tim, Jon, Mark D., Sarah, Alex, Keith, Rose, Christophe, Ken, Nigel, Cyril, Mark P...

And Claudia... Thank you so much for your help, support, patience and love. Being together has been always special... *Te amo!*

Lastly, and most importantly, I wish to thank my parents, Hariet and Manfredo. I will be always grateful for their constant support and encouragement. *Obrigado!*

Author's Declaration

At no time during the registration for the Degree of Doctor of Philosophy has the author been registered for any other University award.

This study was financed with the aid of a studentship from the Brazilian National Research Council (CNPq).

Relevant scientific seminars and conferences were regularly attended at which work was often presented; external institutions were visited for consultation purposes.

Publications:

Siegle, E.; Huntley, D.A. and Davidson, M.A. 2002. Modelling water surface topography at a complex inlet system – Teignmouth, UK. *Journal of Coastal Research*, SI 36, 675-685.

Siegle, E.; Huntley, D.A. and Davidson, M.A. (accepted). Physical controls on the dynamics of inlet sandbar systems. *Ocean Dynamics*.

Siegle, E.; Huntley, D.A. and Davidson, M.A. 2003. Sediment transport patterns and morphodynamics at a complex inlet system. *Coastal Sediments'03*, Clearwater Beach, Florida, USA.

Presentations and Conferences Attended:

UK Marine Science, 11-15 September 2000. Norwich, UK.
Oral presentation: Video imaging for the study of estuarine sandbar dynamics (Siegle, E.; Mallet, C.; Huntley, D.A. and Davidson, M.A.)

Coastal Dynamics, 11- 15 June 2001. Lund, Sweden.

International Coastal Symposium, 25-29 March 2002. Templepatrick, Northern Ireland.
Oral presentation: Modelling water surface topography at a complex inlet system – Teignmouth, UK (Siegle, E.; Huntley, D.A. and Davidson, M.A).

Physics of Estuaries and Coastal Seas, 17-20 September 2002. Hamburg, Germany.
Oral presentation: Physical controls on the dynamics of inlet sandbar systems (Siegle, E.; Huntley, D.A. and Davidson, M.A).

Coastal Sediments, 17-23 May 2003. Clearwater Beach, USA.
Oral presentation: Sediment transport patterns and morphodynamics at a complex inlet system (Siegle, E.; Huntley, D.A. and Davidson, M.A).

Four oral presentations in the Institute of Marine Studies, University of Plymouth, Research Seminar Series 2000-2003.

External Contacts:

DHI Water & Environment (Copenhagen, Denmark)
HR Wallingford (Wallingford, UK)

Signed Eduardo Siegle

Date 13/10/2003

Chapter 1

Introduction

1.1. General Introduction

Inlet systems are common features around the world's coastline, being highly important for the exchange of materials between land and sea. The influence of these systems over the adjacent environments and their ecological and economical importance has afforded them special considerations within coastal sciences. Geographically, coastal regions are amongst the most densely populated by humans due to favourable conditions, being home for 70 % of all human beings (Charfas, 1990). Anthropogenic pressures on these region results in serious environmental stress, with some of the most dramatic consequences being related to the river mouths. Construction, dredging, changes in freshwater flow, and pollution are some of the activities that affect these systems. Additionally, natural pressures are also expected to increase due to global changes, making understanding and managing coastal zones one of the most important challenges facing us (Huntley et al., 2001).

Since the nineteenth century, with the expansion of sea routes and ports, studies trying to understand the interactions between the flow, sediment and structures became increasingly common (Stevenson, 1886). This resulted in several studies using empirical relationships to understand the hydraulic and sedimentary behaviours of inlets (e.g. LeConte, 1905; O'Brien, 1931) and observational studies aiming at the management of inlet systems. More recently, as a result of the better understanding of some of the physical processes and available computer technology, tidal inlets have come within the reach of mathematical modellers. The possibility of modelling many of the complex physical processes which take place within inlets enables researchers to test hypotheses on how these systems work and to identify the most important knowledge gaps (as reviewed by De Vriend, 1996 and De Vriend and Ribberink, 1996). Additionally, during the last decade the development of alternative monitoring techniques such as the use of video imaging of the nearshore

regions (Lippmann and Holman, 1991; Holman, 1994) resulted in a valuable database documenting their evolution.

The overall aim of this thesis is to better understand the processes that drive the morphological evolution of inlet sandbar systems. Through the combined application of *in situ* measurements, numerical modelling and video imaging, tests have been carried out in order to assess the importance of the processes controlling morphological evolution, and the relative importance of these processes in different regions of the system. By applying these techniques to different stages of the evolutionary cycle, the initial steps towards improving the predictability of the behaviour of the sandbar system have also been taken. In this study the nomenclature proposed by Hayes (1975) is used, with the estuary mouth being considered an inlet due to the dominance of tidal flows.

The Teign inlet, Teignmouth, Devon, UK was chosen for this study due to its complex and active morphodynamic behaviour. Due to its challenging nature, this site has been the subject of a series of studies and field campaigns (e.g. EU projects such as COAST3D[1] and COASTVIEW[2]) and is also one of the selected sites in the Argus programme (Holman, 1994). Since February 1999 an Argus video system gathers hourly video images from the area, providing invaluable information on the morphological evolution of the sandbar system. Thus Teignmouth displays large morphological changes over short periods of time, and there is a large quantity of high quality data available to document these changes and to drive and calibrate numerical models. The numerical model applied in this study is the MIKE21 modelling system developed by the DHI Water & Environment. This model was applied in this study as part of a collaboration between the University of Plymouth and the DHI Water & Environment within the EU SWAMIEE project (Contract No. ERBFMRXCT97-0111).

[1] for details see the project web site at http://www.hrwallingford.co.uk/projects/COAST3D/
[2] for details see the project web site at http://www.thecoastviewproject.org

1.2. Specific Objectives

Within the overall aim of better understanding the balance of driving forces at the vicinity of an inlet system and assessing the value of the innovative technique applied in this study, some specific objectives were defined:

- Apply, calibrate and validate a numerical area model (MIKE21) at the Teignmouth area;
- Apply and validate techniques to extract morphological information from video images;
- Integrate video imaging information with numerical modelling experiments, to better understand the behaviour of the sandbar dynamics from short to medium temporal scales;
- Identify and assess the relative importance of the key processes across the complex sandbar system at the Teign inlet, through the combined application of a numerical model, field data and Argus video images;
- Take initial steps towards assessing the predictability of such complex environments.

1.3. Thesis outline

Following this introductory chapter (Chapter 1) is the theoretical background to the study in the Literature Review (Chapter 2). A synthesis of the research conducted on the subject of inlet sandbar dynamics is presented in this chapter focusing on applied techniques such as numerical modelling and video imaging in the study of coastal processes.

The area of the present study is the Teign inlet system (Teignmouth, UK). A detailed description of the study area is presented in the first section of Chapter 3. The second section of Chapter 3 describes the field data available to this study with a brief description of the instrumentation and analysis used.

In Chapter 4 the setup of the numerical model is described followed by the presentation of its calibration and validation through comparisons with the measured data via time-series

comparisons and statistical parameters that help in assessing the quality of the modelled results. This chapter shows the quality of the calibrated model that is applied in the experiments carried out in Chapters 5 and 7. The description of each module is given in Appendix I.

A description of the video imaging techniques applied to obtain and extract information from the images is presented in Chapter 5. This chapter also includes the integration of numerical modelling and video imaging through the application of the modelled water levels to the image analysis. The use in the model of the intertidal morphology extracted from the video images allows modelling to be carried out for different evolution stages of the ebb-tidal delta system in Teignmouth. The results are then compared with measurements made through the use of traditional surveying techniques.

Chapter 6 looks at the physical controls of the sandbar system based on experiments carried out with the validated model. These experiments include a range of forcing conditions whose relative importance on the sediment transport is assessed during one morphological stage (October/November 1999).

The numerical model (Chapter 4) and the imaging techniques (Chapter 5) are applied in Chapter 7 in order to extend the modelling experiments at different stages of the evolutionary cycle, providing quantitative information on the processes that govern the morphological evolution. The comparison of the modelled sedimentation/erosion patterns with video images allows a qualitative prediction of the system's evolution. Finally, a conceptual model of the functioning of the Teignmouth sandbar system is given.

General conclusions of this study and suggestions for future work are presented in the concluding Chapter 8.

Chapter 2

Literature Review

2.1. Foreword

The present study is focused on improving understanding of the processes that drive the dynamics of the sandbars that form an ebb-tidal delta system. As these processes involve different temporal scales, the coupled application of a numerical model and video imaging is applied in order to carry out several "small scale" modelling experiments at a "medium scale" of morphological process. Hence, the literature review in this chapter is divided into three main sections: 1) a general overview of inlet systems and their morphodynamic behaviour; 2) the modelling of inlet processes and limitations that arise from the application of numerical models at such complex systems; and finally 3) an overview of the video imaging technique applied in order to link the different time scales.

2.2. Inlet Systems

2.2.1. Definition and general morphology

Inlet systems are defined as being the passage between the ocean and the adjacent estuary or lagoon, encompassing the channel and associated sediment bodies (Hayes, 1969, 1980). Inlets have a large variety of forms, associated with barrier islands or being in essence the mouth of a river where the discharge of freshwater may be significant (Komar, 1996). According to Bruun (1978) three main features form a tidal inlet: the ocean section, which includes the external sediment bodies (ebb-tidal delta) and one or several channels; the gorge channel, meaning the section with minimum cross-sectional area and the bay section

with its shoals (flood tidal delta) and channels. The nomenclature commonly used in the studies of tidal inlets is the one proposed by Hayes (1975) and is represented in Figure 2.1.

Ebb-tidal delta

The ebb-tidal delta represents the sediment body resulting from the interaction of tidal currents, waves and wave generated longshore currents acting at the ocean section of the inlet. The typical morphology of ebb-tidal deltas is shown in Figure 2.1. The main components of the ebb-tidal delta are the main ebb channel; channel margin linear bars; the terminal lobe, at the end of the main ebb channel; the swash platforms, formed by the wave action over the shoals; and marginal flood channels which may occur at both updrift and downdrift sides of the inlet running parallel to the shore. The detailed morphology and sedimentary structures of such deposits can be found in Hayes (1975, 1980); FitzGerald and Nummedal (1977) and Boothroyd (1985).

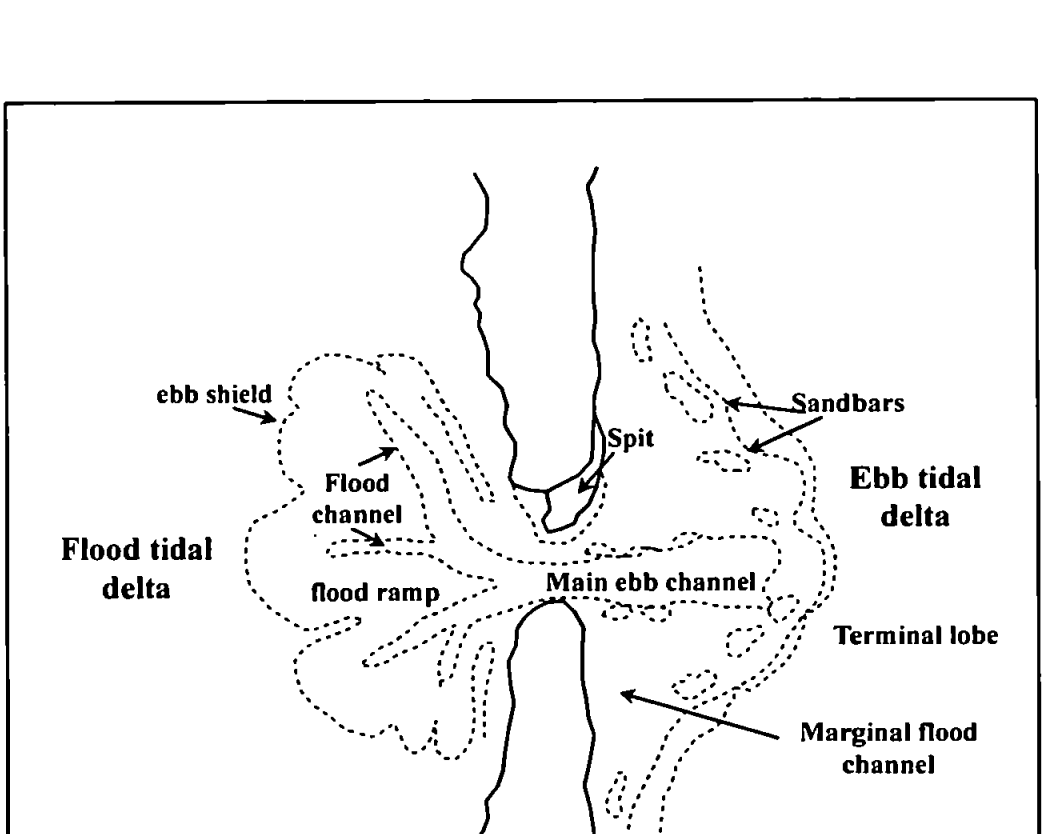

Figure 2.1. General inlet morphology (modified from Davis, 1994).

Flood-tidal delta

Sediment transported into the estuarine portion of the inlet and deposited by the decelerating flood tidal currents form the flood-tidal delta (Figure 2.1). The major components are the flood ramps, flood channels and the higher landward margin that protects the delta from ebb currents (ebb shield). Details of the flood-tidal delta morphology are described in Hayes (1975, 1980), Boothroyd (1985) and Moslow and Heron (1994).

Channel

The narrowest and deepest part of the inlet connecting the ocean to the embayment or estuary is the inlet channel. The channel is responsible for the exchange of flows and sediments in both directions, landwards and seawards. The channel variability is also a result of the relative influence of waves and tidal processes. Under the dominance of tidal processes, the channel is deeper and relatively stable, with strong tidal currents removing deposited sediment (Boothroyd, 1985). With the increasing influence of wave related processes, such as longshore currents, the channel becomes less stable and tends to migrate. The channel migration is usually downdrift (FitzGerald, 1988; Davis, 1994), however the updrift migration was also registered in some cases (Davis, 1983; Aubrey and Speer, 1983; Reddering, 1983). In situations of channel migration the channel presents an asymmetric profile, reflecting the accumulation of sediments at one of its margins (Hayes, 1980).

Based on the inlet morphology as a result of the controlling processes, several classifications of inlets were proposed (e.g. Hayes, 1979; Oertel, 1975; Davis, 1994; Hicks and Hume, 1996). Most of these studies refer to typical barrier-island inlets with no structural control. As the present study focuses on an inlet influenced by the presence of a headland, some attention will be given to this kind of environment. The influence of a structural control on the ebb tidal delta morphology was shown for example in studies of a rock-bound tide-dominated estuary (Kennebec River, USA – FitzGerald et al., 2000a) and at inlets of the New Zealand coast (Hume and Herdendorf, 1992, Hicks and Hume, 1996).

Hicks and Hume (1996) classified seventeen inlets of the New Zealand coast according to the morphology and size of their ebb tidal deltas. The authors identified four basic shapes of ebb deltas (Figure 2.2). These shapes appear to be related mainly to delta size and the shoreline configuration through its control on wave exposure, shape of the space available for the delta to occupy, and alignment of the ebb tidal jet.

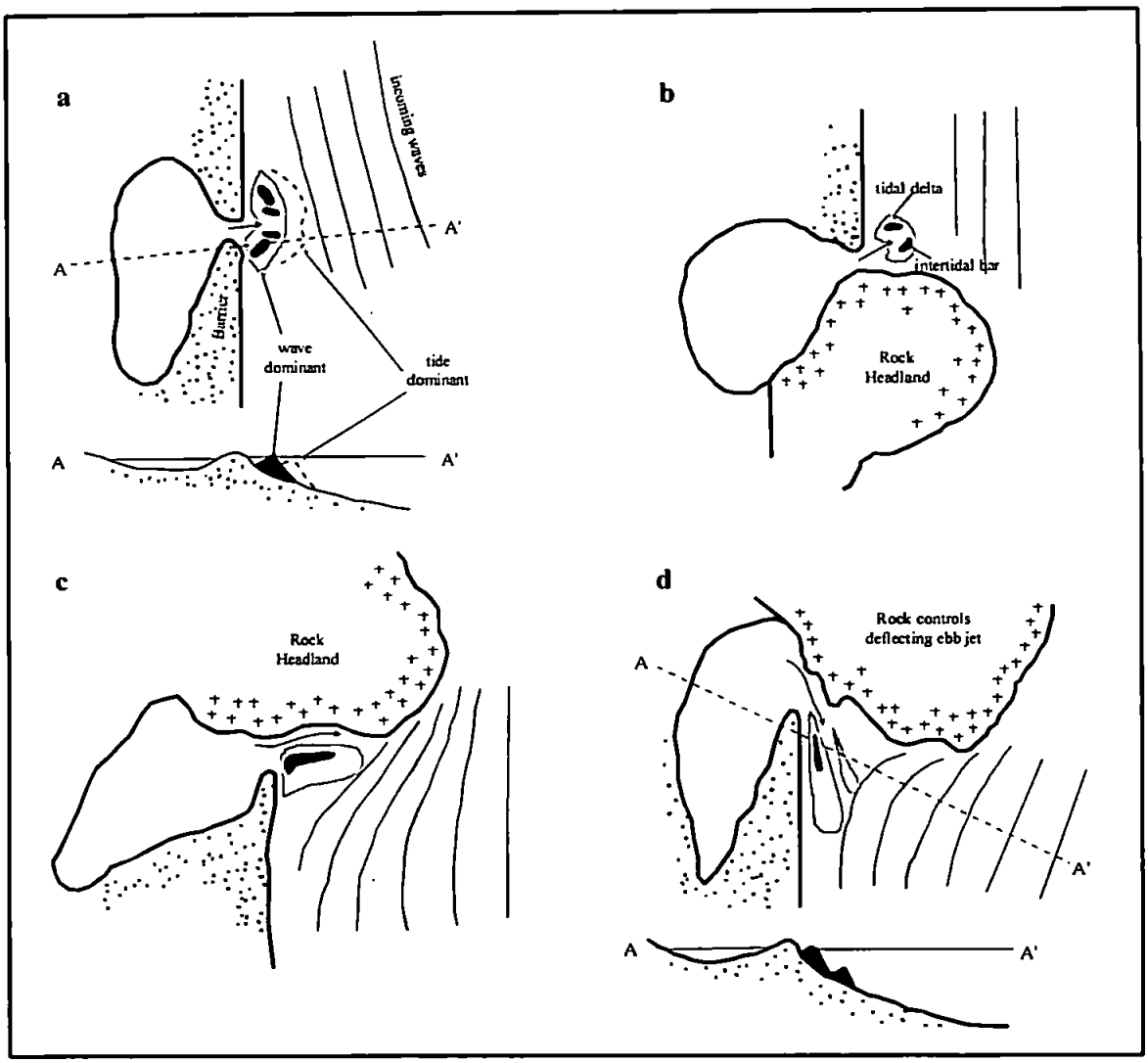

Figure 2.2. Schematic diagrams depicting controls on ebb delta size and shape, where a) free-form ebb delta; b) constricted ebb delta; c) high-angle half delta; and d) low-angle half-delta (after Hicks and Hume, 1996).

The free-form ebb delta (Figure 2.2a) is a longshore elongated and reasonably symmetrical delta occurring off inlets on relatively straight, exposed shorelines experiencing significant littoral drift. The constricted ebb delta (Figure 2.2b) presents a similar basic shape but is less elongated alongshore and occurs where the inlet occupies a broad shoreline angle. The lateral spread of the delta is restricted by the offset between the headland and the barrier. Figure 2.2c shows the shape of the high-angle half-delta, which presents a near shore-normal bar. This type of delta occurs when the ebb jet runs hard against the headland, resulting in a significant shoal forming on the barrier side of the inlet. The low-angle half-delta (Figure 2.2d) occurs in the form of a longshore-elongated wedge-shaped deposit. The delta is pinched between the beach and an ebb tidal jet forced to flow at a low angle to the shoreline.

The presence of a structural control typically results in asymmetric ebb shoals, usually with triangular or elongate wave-dominated swash platforms of shore-normal orientation built in the lee of the headland (Hume and Herdendorf, 1992; Hicks and Hume, 1996). This delta morphology is akin to that described by Oertel (1977) and suggests that inlet currents rather than longshore currents are the dominant factor influencing the accumulation of sediments at the inlet. Typically a marginal flood tidal channel separates the ebb tidal delta from the beach. The size of the ebb tidal delta varies as a factor of the headland shelter (Hume and Herdendorf, 1992).

2.2.2. Importance of inlet systems

Due to their high ecological and commercial importance and the influence they have over neighbouring areas, inlets have been the subjects of many studies within the field of coastal science and engineering. Historically, the need for navigation has been the most important application driving research for understanding physical processes at inlet systems (Mehta, 1996). With many harbours and marinas associated with inlet entrances, they are important for economical and recreational activities that rely on the channel stability. With the objective of maintaining the navigable channel, several studies focused on the channel stability controls considering empirical relationships between morphological and hydrological processes (e.g. LeConte, 1905; O'Brien, 1931, 1969; Escoffier, 1940; Bruun

and Gerritsen, 1960; Jarret, 1976; Walton and Adams, 1976; Hume and Herdendorf, 1988; Van de Kreeke, 1992). The importance of the channel stability is also related to ecological aspects, due to the exchange of dissolved and particulate substances controlling the water quality and ecology of the associated embayment or estuary (Goodwin, 1996).

Inlets have also a strong influence over the sediment budget of the coastal regions, affecting the stability of adjacent beaches and/or barrier islands (e.g. Oertel, 1977; FitzGerald et al., 1984; FitzGerald, 1988; Fenster and Dolan, 1996; Williams et al., 2003). The sand bodies associated with inlets, such as the flood and ebb-tidal deltas are important temporary and permanent sand reservoirs. Additionally, ebb-tidal deltas strongly influence the wave energy distribution along the adjacent shoreline. This protects the shoreline from the incoming waves and defines the sediment transport patterns dictating the inlet sand bypass processes. (e.g. Goldsmith et al., 1975; Hayes, 1979; FitzGerald et al., 1984; Oertel, 1988; FitzGerald, 1996).

2.2.4. Morphodynamics

Inlets can be considered morphodynamic systems, functioning through the interaction of three main components: fluid dynamics, sediment transport and morphological changes (Figure 2.3). The fluid dynamics is induced by the energy input in the system through waves and currents and is influenced by the bottom topography. This mutual adjustment of topography and fluid dynamics is linked by the sediment transport over time. Gradients in sediment transport result in local erosion and deposition changing the morphology. The changed morphology will lead to changes in the hydrodynamics that may then re-inforce or suppress the morphological changes imposed by the forcing conditions.

Morphodynamic processes are time-dependent and occur at different time-scales. Based on the idea of "primary-scale relationship" proposed by De Vriend (1991), for each scale level it is possible to identify a specific morphodynamic system (Figure 2.4). Small scale processes (e.g. ripples formation) are forced by single events, such as waves or tides. In this case the morphodynamic adjustment can be followed in detail as a real time-process. The evolution of channel and sandbars is a response to single events (such as a storm)

through to seasonal variations in the forcing conditions. In general, at lower time and temporal scales individual fluctuations in the forcing conditions are important, whilst at large scales the evolution is a response to mean trends in environmental conditions. The time scales involved in this study range from small, by applying the model in order to understand the physical processes acting on the system (Chapter 6), to medium, when combining the model application with the video imaging techniques in order to extend the small scale model applications over a larger period of time (Chapters 5 and 7).

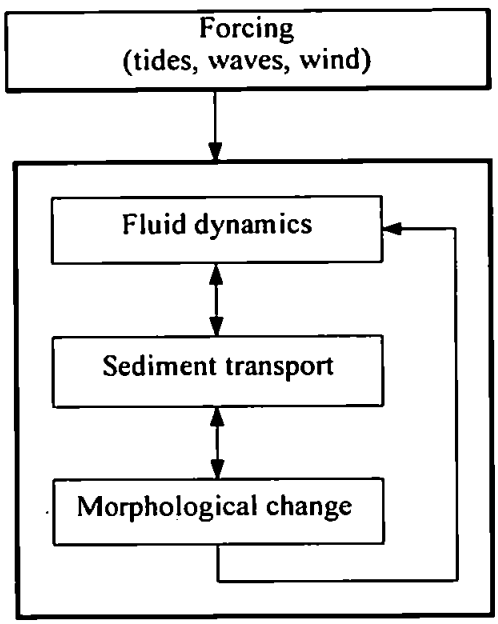

Figure 2.3. Coastal morphodynamic system.

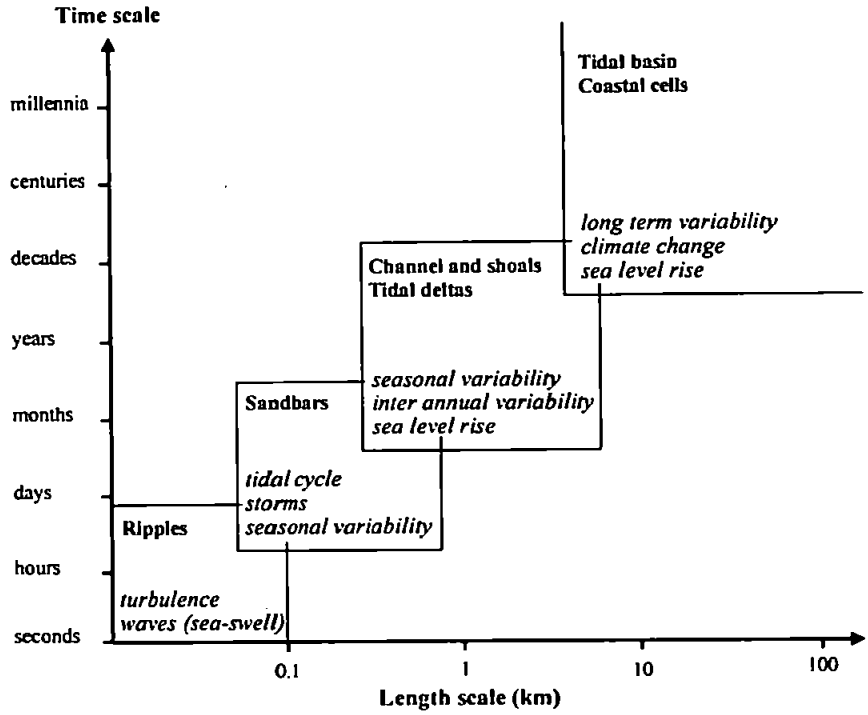

Figure 2.4. Inlet features (bold) and their main forcings (italic) as a function of time and space (after De Vriend, 1991).

At inlet systems, probably the most dynamic region is the ebb-tidal delta, which is under the influence of several forcing conditions (e.g. tides, waves, winds) causing changes at different temporal scales, ranging from short- to long-term related changes. Assuming that the forcing conditions remain constant throughout time, it is expected that the morphology will reach an equilibrium state, characterised by relationships between morphology and hydrodynamics. Examples are the relationships between the inlet tidal prism and the ebb-tidal delta volume (Walton and Adams, 1976) and between the tidal prism and the cross-sectional area of the inlet channel (LeConte, 1905; O'Brien, 1931, 1969; Jarrett, 1976, Hume and Herdendorf, 1988). However, even when comparing inlets under similar energy conditions, there is still scatter in the data of such relationships. Additionally, the variability in the ebb-tidal delta volume at individual inlets is also not taken into account (FitzGerald, 1996). As shown by several authors, ebb-tidal delta volumes may change considerably over time, mainly at mixed energy (tide-dominated) shorelines, with cyclic behaviour of volume growth and decay (e.g. Oertel, 1977; FitzGerald, 1982, 1984; Slingerland, 1983; Sha, 1989; Smith and FitzGerald, 1994; Van de Kreeke, 1996; Kana et

al., 1999; FitzGerald et al., 2000a; Williams et al., 2003). A series of conceptual models with regard to processes on outer deltas were derived from these studies and reviews were given by FitzGerald (1996) and FitzGerald et al. (2000b).

These investigations documented the variables that control the morphodynamic processes, highlighting the importance of the wave and tidal energy, tidal prism, inlet geometry, sediment supply, regional stratigraphy, slope of the nearshore and engineering modifications. The interactions of these processes combined with the spatial extension of the inlet system define the temporal scale of the cyclic behaviour of the ebb-tidal deltas. Sediment transport in the inlet channels is controlled by the ebb/flood dominance, with most inlets presenting landward transport during storms, when large waves result in more sediment being transported to the channel and the storm surge increasing the flood currents, driving sediment towards the flood-tidal delta. Under less energetic situations, sand is transported in a net seaward direction being deposited on the ebb-tidal delta. Wave action over the delta generates onshore currents that will interact with the ebb flows. During higher wave energy conditions, when the wave generated currents dominate the ebb flows, sediment over the shoals is transported onshore, usually in the form of sandbars. These sediment transport processes are usually associated with large amounts of sediment being bypassed to the downdrift shoreline, and at stable inlets this process occurs through the formation, landward migration and attachment of large sandbar complexes (FitzGerald et al., 2000b). This study focuses on a stable inlet, but influenced by the presence of a structural control (headland), resulting in less sediment bypass and in a consequent retention of sediment, which is a function of the amount of headland shelter (Hume and Herdendorf, 1992; Hicks and Hume, 1996). Few studies focused on the dynamics of these structurally controlled inlets and there is relatively little known about the net sediment transport patterns at the entrance of such inlets (Stumpf and Goldschmidt, 1992; Fenster and FitzGerald, 1996; Fitzgerald et al., 2000a).

2.3. Modelling Inlet Processes

Inlet processes are very sensitive to the external forcing conditions. Thus, changes to these conditions due to natural causes (e.g. sea level rise) or induced by human activities (e.g.

structures, dredging) can have considerable impacts on the system. The need to better understand and predict these highly complex and dynamic systems led, in recent years, to the development of mathematical models of their behaviour. It has become possible to model many of the complex processes (waves, currents, sediment transport, morphological changes) which take place in the vicinity of an inlet (De Vriend, 1996). However, due to the range in time and space scales involved in inlet processes, limitations arise in the application of process-based models over larger time scales (De Vriend, 1996; Van de Kreeke, 1996). Since models that predict the small-scale processes well are not necessarily appropriate for long-term predictions, De Vriend (1996) classified different types of models according to the scales of the modelled morphodynamic process:

- Data-based models: use only measured data aiming directly at the phenomena to be described (e.g. geostatistical models such as the extrapolation in time of a certain parameter of the system's state via a linear regression analysis of observed values);
- Empirical relationships: also based on observations, but establishing relationships between measured parameters (e.g. linear relationships between tidal prism and channel cross-sectional area or ebb-tidal delta volume);
- Process-based models: based on first physical principles (conservation of mass, momentum, energy, etc) and use mathematical equations to describe waves, currents, sediment transport and bottom change;
- Formally integrated, long-term models: derived from a process-based model by formal integration over time and space, with empirical or parametric closure relationships to prevent the model becoming unstable;
- Semi-empirical, long term models: describe the dynamic interaction between large elements of the system, using empirical relationships to represent the effects of smaller-scale processes.

As the model applied in this study is a process-based model, more details are given about the concepts of such models. The basic concepts of process-based models is the coupling of standard models of the constituent physical processes (waves, currents, sediment transport) via a bottom evolution module based on sediment conservation (De Vriend et al., 1993). Figure 2.5 shows the basic model concepts summarised here and indicating the type of application carried out in this study:

- "initial sedimentation/erosion" (ISE) models go only once through the sequence of constituent models. Calculations are based on the assumption of an constant bed topography and only the rate of sedimentation or erosion is computed at every location;
- "medium-term morphodynamics" (MTM) models include the feedback of the new bottom topography into the hydrodynamic and sediment transport computations through a looped system which describes the dynamic time-evolution of the bed;
- "long-term morphological" (LTM) models, in which the constituent equations are not describing the individual physical processes, but integrated processes at higher level of aggregation.

As the present study makes use of an "initial sedimentation/erosion" (ISE) model, more details about this type of models are given in the next section. In the present study, in order to extend the application of an ISE model at different morphological conditions, a data assimilation process (from video derived intertidal morphology – section 2.4) is combined with the model application (Figure 2.5).

Details of the morphodynamic models (MTM) with their potentials and limitations can be found in several applications carried out over recent years (e.g. Latteux, 1980; O'Connor et al., 1981; De Vriend, 1987; Andersen et al., 1988, 1991; O'Connor and Nicholson, 1992; De Vriend et al., 1993; Roelvink and Van Banning, 1994; Wang et al., 1995; Cayocca, 2001; Van Leeuwen and De Swart, 2002).

2.3.1. Initial sedimentation/erosion models

The initial sedimentation/erosion models are the widest used in practice, mainly when studying 3D environments such as inlets. Advantages of this type of models over the MTM models include the smaller computational effort, relatively easy implementation and, the latest process descriptions can usually be included without too many unexpected complications (De Vriend et al. 1993). However, models of this type are difficult to interpret in terms of longer-term morphological evolution, and they can only provide information on phenomena at a time scale much smaller than the morphological one. Without the feedback mechanism between the morphological evolution and the hydrodynamics and sediment transport, the ISE models cannot predict near equilibrium

situations. They only describe the first morphological adjustment after a strong distortion of the system (e.g. due to human interference, or in this study, the presence of a sandbar). According to De Vriend (1994), in such distorted systems, a few "primary" transport phenomena appear to be predominant, and the morphological adjustment process tends to be monotonous in time. Therefore an ISE model can be expected to yield a reliable indication of this process (Figure 2.6). The cyclic behaviour of the sandbar system subject of this study means that it would never reach the dynamic equilibrium situation represented by the solid line in Figure 2.6. Due to its cyclic bar migration, the system is always "strongly distorted" and thus evolving to a new state (as represented by the dashed line in Figure 2.6). Therefore, the ISE model is applied at different "strongly distorted" situations during the evolutionary cycle of the system, reproducing the "primary" transport phenomena for each situation, resulting in a qualitative prediction of its morphological evolution.

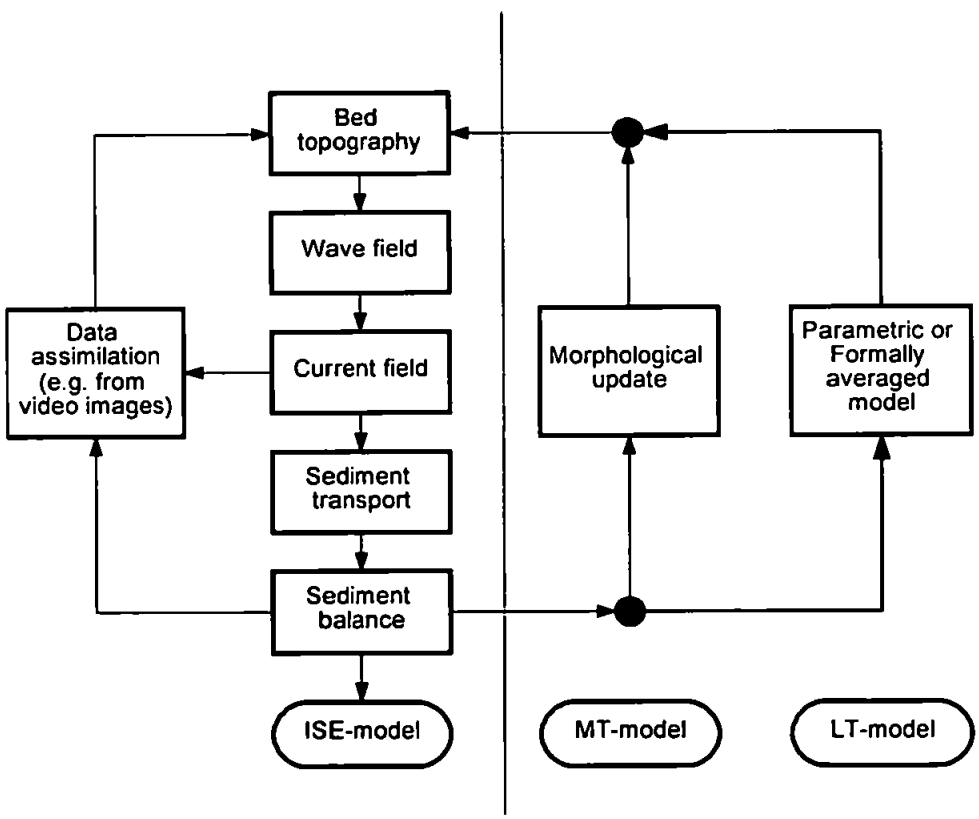

Figure 2.5. Concept of the initial erosion deposition (ISE), medium term (MT) and long term (LT) models (modified from De Vriend et al., 1993). In the present application, the left-hand side of the diagram is applied (ISE model and data assimilation).

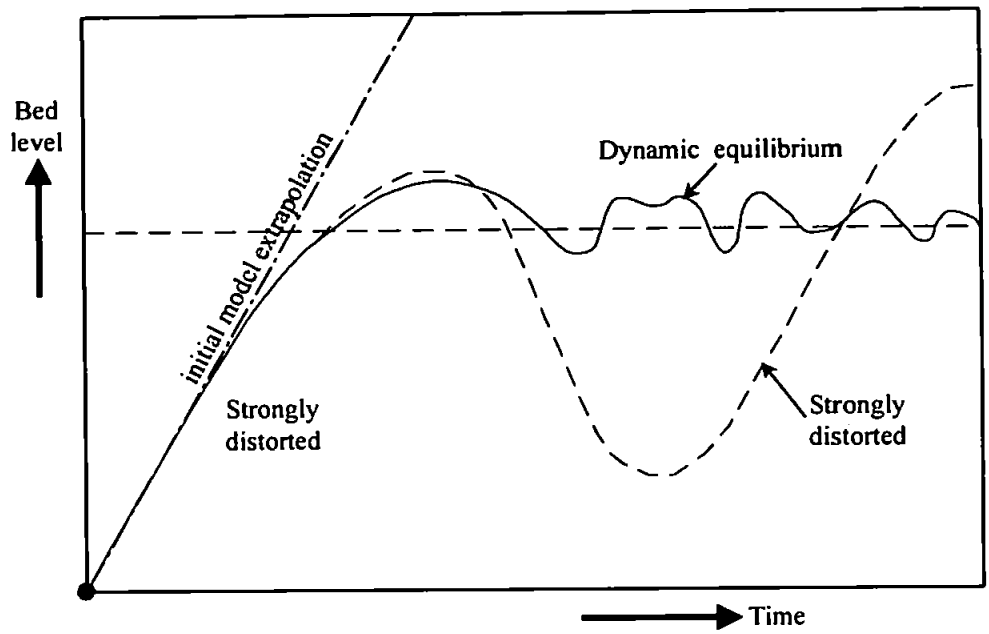

Figure 2.6. Behaviour of a "distorted" system (modified from De Vriend, 1994).

The main results of the ISE models are the transport patterns and the consequent sedimentation/erosion rates. The sedimentation/erosion rates are not always very representative of the actual evolution after some time, whereas the transport pattern is usually more so (De Vriend et al., 1993). This makes the interpretation of longer-term ISE models simulation easier on the basis of the estimated yearly residual transport rates. Studies using ISE models are usually comparative, in order to predict the hydrodynamic and morphological changes due to alterations to the environment or to test the effects of different forcing conditions on the sediment transport patterns and initial sedimentation/erosion rates.

As mentioned above, limitations of the application of such models are not only associated with the assumption of constant bed morphology, and some others are listed here:

- lack of knowledge of relevant physical processes. Inlets are extremely complex dynamic systems with a variety of processes and mechanisms. At this moment they are insufficiently understood to be sure that the elementary physics incorporated in a simulation model is sufficient to reproduce the phenomena of interest;

- inability to incorporate all the relevant processes in models. Any simulation model depends on empirical or parametric submodels, implying simplifications and approximations which may affect the results;
- the wide range of different length and time-scales involved;
- lack of relevant data;
- errors in input data;
- accumulation of result errors through time.

2.4. Application of video imaging techniques

Until a few years ago, information on coastal morphodynamics has been obtained from field experiments. Although much of our present understanding of nearshore processes originated from these field measurements, they are limited to an observation time scale (instantaneous and event scales – Figure 2.4), are conditioned by weather and wave conditions and are relatively expensive. Recent monitoring techniques, based on video observations of the nearshore zone are a good alternative to cope with these limitations of traditional measurement campaigns. By applying video imaging techniques, knowledge of coastal dynamics can be enlarged through the provision of useful information about hydrodynamics and morphodynamics of the coastal zone. Furthermore, the application of such techniques provides data over a wide range of space and time scales, varying from a storm-event (hours-days) to longer-term beach development (years-decades).

In 1992 the Coastal Imaging Lab (Oregon State University - USA) started the Argus program (Holman, 1994), based on the work of Lippmann and Holman (1989) which showed the usefulness of video imaging for coastal monitoring. An Argus station is equipped with one or more video cameras connected to a personal computer with an image processing system. These cameras are pointed obliquely along the nearshore region of interest. Every daylight hour data are gathered, comprising one snap shot image and a ten-minute time-exposure image (Figure 2.7). A time exposure image is an averaged image of 600 snap shots, recorded every second during a period of ten minutes (Figure 2.7b), such that it averages image intensity removing short-term variability revealing features of

interest. This data set provides information with a large temporal and spatial extent, as well as a high temporal and spatial resolution.

Nowadays, around twenty Argus stations are present at selected locations around the world. In the United Kingdom, the Institute of Marine Studies of the University of Plymouth collaborate closely with the Coastal Imaging Lab of the Oregon State University (USA) within the context of the Argus Program.

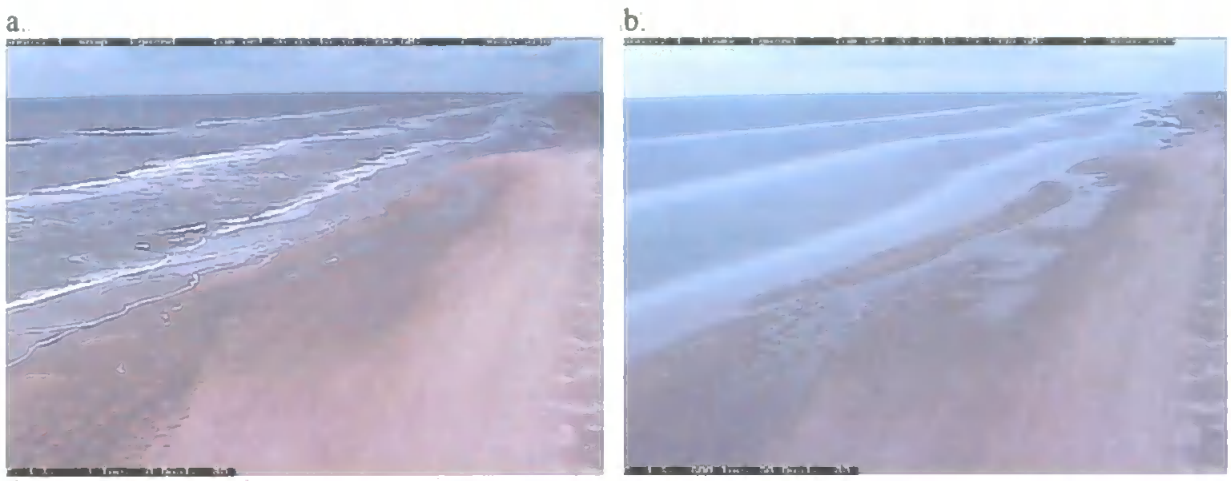

Figure 2.7. Example of snap-shot (a) and time-exposure (b) Argus video images.

2.4.1. Extracting information from images

The quantification of intensity variability of an image into a two-dimensional array of picture elements is the basis of video image processing. Variations in the intensity of each pixel are determined by the amount of light reflected by the pixel area. Pixel intensities may change on very short time-scales, and the amount, and rate, at which they change may be attributable to nearshore hydrodynamic processes, and subsequently quantified (Down, 1999). Using time-exposure images, rectified to produce a map view with known scaling, cross-shore intensity profiles at prescribed longshore distances can be easily found (Lippmann and Holman, 1989). The time series data from video images are usually in the form of non-dimensional image units, with 256 grey shades ranging linearly in value from 0 (black) to 255 (white) or in the case of colour images pixel values are given in terms of

red, green and blue (RGB). To improve contrast, images can be adjusted to the full dynamic range using the limit values in the image prior to sampling (Lippmann and Holman, 1989).

The analysis of intensity time series from Argus images pixels allows observation of different geophysical signals, such as flow velocities (Down, 1999); wave parameters (Lippmann and Holman, 1991; Holman et al., 1993; Stockdon and Holman, 2000; of rip currents (Van Noort, 1997; Symonds et al., 1997; Ranasinghe et al., 1999, Reniers et al., 2001); beach cusps (Holland, 1998); bar morphology (Van Enckevort and Ruessink, 2003a, b) nearshore bathymetric information (Aarninkhof et al., 2003) and intertidal morphology. The latter is of interest of the present study and is described in more detail below.

One promising application of video images developed over the recent years is the extraction of the intertidal morphology for the study of coastal morphodynamics. All techniques aimed at the extraction of the morphology from the video images are based on the detection of the shoreline location at different times during a tidal cycle, with the shoreline being considered the contour line of the local water level. In order to define the morphology, the horizontal and vertical location of the shoreline needs to be defined.

The first approach for the estimation of subaerial profiles using video images was made by Holman et al. (1991). They developed a technique to estimate beach profile by video imagery using either a shadow from a pole or the light from a narrow slit, drawing a line across the beach at a known location and orientation. Viewed from the longshore direction, the line will appear as a visible beach profile that can be digitised from the image and the ground coordinates of the profile uniquely determined. The authors conclude that the success of this technique suggests that profile data may be routinely collected using an automated system without the need for a survey team, thus allowing the ready collection of long time series for climatological studies.

Plant and Holman (1997) developed a technique to map the Shoreline Intensity Maximum (SLIM) from time-averaged video images. The SLIM is a peak in the cross-shore intensity profile, related to the ultimate dissipation of wave energy or shoreline break. The main limitation of this technique is the need for a well defined SLIM which is a function of the

wave conditions and shoreface gradient. The measurement error for individual shoreline estimates on the steeply sloping beach used in field comparison was of about 0.10 m (in the vertical). Estimates of the cross-shore component of the beach slope were made accurately to within 10 % of the mean slope and the cross-shore position of the mean slope and the cross-shore position of the mean water level could be estimated to within 1 m, on average.

At some sites, the method developed by Plant and Holman (1997) is not applicable since often no shoreline break is present. An example is Noordwijk, Netherlands, where the existence of an almost emerging inner breaker bar results in hardly any dissipation at the waterline (Janssen, 1997). Focusing on this problem, Janssen (1997) developed a method to estimate intertidal beach levels from the images also if no shoreline break is present, using the standard deviation images. These images highlight regions of high and low variance in images taken over the same time as the time averaged images. He showed the presence of a spatial shift between the location of the standard deviation maximum and the time average maximums in the cross-shore transect, with the detected shoreline being situated seaward of the surveyed shorelines. This, combined with the detection of some spatial jumps of the cross-shore location led to certain uncertainties in the correct shoreline position.

Davidson et al. (1997) analysed video images from a strongly macrotidal beach (maximum tidal range $\approx$ 7.5 m) at Perranporth, United Kingdom where the shoreline features identified by Plant and Holman (1997) and Janssen (1997) were not always recognisable. One of the most consistently observed shoreline features in both the standard deviation and time-exposure images was the sharp increase in intensity with offshore distance which is theoretically located close to the point of maximum run-up. The technique developed by Davidson et al. (1997) is based on mapping the maximum extent of shoreward swash as indicated by the rapid spatial intensity change. Comparisons between the video data and a total station survey show an excellent agreement in the estimated 3-dimensional intertidal morphology with standard errors of less than 0.1 m.

Considering the limitations of the above described methods, Aarninkhof and Roelvink (1999) developed a new method, which has a more generic applicability. The method

presented by Aarninkhof and Roelvink (1999) makes use of the colour information from the Argus images. Generally, image intensities are defined in the red, green and blue (RGB) colour space, where the colour of each pixel is defined as a mixture of these colours. The application presented uses the pixel intensities within a region of interest converted to the Hue Saturation Value (HSV) colour space. The reason to do so is that the HSV colour space separately treats the colour information (by means of H and S) and the greyscale information (by means of V). Investigation of HSV intensities of multiple images from different Argus stations has indicated that both dry and wet pixels are clustered in the HS space, but at rather different locations. Using techniques to separate wet and dry pixels they obtain the definition of the horizontal co-ordinates of the time averaged location of the waterline.

With the objective of producing a non-site specific technique for the detection of the shoreline for a range of different wave conditions and beach characteristics, Kingston et al (in prep.) applied an Artificial Neural Network model to differentiate between sand and water regions in a video image. In order to identify the horizontal spatial location of the shoreline, the authors trained the Artificial Neural Network with RGB values obtained from sample inputs and a manual binary classification of sand or water as the output. The shoreline pixel intensities are estimated from histograms of pixel intensities, resulting in the threshold value of the shoreline intensity. By testing their technique at different sites, typical root mean square errors in the range of 0.2 to 0.5 m were found when comparing the extracted morphology to intertidal maps produced by traditional survey techniques.

One source of inaccuracy in these above mentioned methods comes from the assumption of a spatially horizontal water surface, an assumption that is often invalid in coastal regions where pressure gradients associated to inlets are important (Siegle et al., 2002 – Appendix II). As the image processing depends heavily on accurate water level information, care needs to be taken when applying these techniques to inlet regions. This problem is later addressed in Chapter 5, were more details on the image processing can be found.

2.4.2. Video imaging of inlet systems

The first application of video imaging to the study of the dynamics of an inlet system was within the EU funded INDIA (*I*Met *D*ynamic *I*nitiative – *A*lgarve) project (for more details about the project see O'Connor et al., 1998; Williams et al., 1999; Williams et al., 2003). This video system was deployed over a fourteen-month period overlooking the Barra Nova Inlet, Algarve, Portugal.

Using the video images gathered at this location, Morris et al. (2001), Morris et al. (in press) and Balouin and Howa (2002) undertook a qualitative and quantitative analysis of the morphological evolution of the inlet system. Results of quantitative time-stack analysis of the images (Morris et al., 2001; Morris et al., in press) enabled the analysis of the rapid morphological changes in the channel morphology; whilst a more qualitative analyses of the rectified video images combined with some digitisation techniques (Balouin et al., submitted) resulted in a conceptual model of the inlet functioning.

These studies provided a good description of the morphological variability of this inlet system by quantifying its temporal evolution. The comparison with *in situ* measurements allowed the correlation of the video-derived morphological changes with the forcing conditions. Through the analysis of this fourteen-month period, these authors found that the inlet morphology has a seasonal cyclic behaviour. The seasonal variation in the wave climate defines the main perturbations to the inlet morphology (Morris et al., 2001).

A similar approach to study the morphological evolution of an ebb-tidal delta from the analysis of video images is taken in this study, with the observation and digitisation of morphological features providing valuable information for the understanding of the functioning of such systems.

2.4.3. Combining video imaging and numerical modelling

Only a few studies have to date focused on the coupling of video imaging techniques and numerical modelling tools. In the application of techniques for the intertidal morphology extraction from images (as described in section 2.4.1) some techniques are combined with

the modelling of waves in order to establish their setup on the shoreface, reducing errors in the vertical estimation of the shoreline location (e.g. Janssen, 1997; Aarninkhof and Roelvink, 1999). For the quantification of the surf-zone bathymetry from video images, Aarninkhof et al. (2003) combined a Breaker Intensity Model with images in order to correlate the video-observed wave parameters with the nearshore morphology.

Reniers et al. (2001) used the time averaged video images of the surf zone to calibrate the modelled wave dissipation coefficients by comparing the measured intensity and the computed roller energy. The wave roller energy estimated from the images was compared with that computed by the numerical model. Further visual comparisons of modelled roller energy and image intensity distribution were carried out in order to optimise the wave dissipation coefficients. Their objective was to verify the physical processes implemented in the numerical model with video and *in situ* measurements of rip currents. This application however, is a comparison of results from both techniques separately without iteratively combining them.

These studies are akin to the technique applied in Chapter 5, when using the modelled water levels for the video image processing in order to obtain the intertidal morphology. However, no attempt of iteratively coupling these techniques has been made in order to better understand the morphodynamics of such environments. Hopefully, the coupling of both numerical modelling and video imaging here applied at a relatively small but very challenging inlet system will help in the understanding of the functioning and predictive evolution of such environments.

Chapter 3

Study Area and Available Data

3.1. Site description

The current study is focused on the estuarine inlet of the river Teign at Teignmouth, Devon, UK (Figure 3.1). The inlet is located in the southern portion of Teignmouth's 2-km long beach, which is protected by a seawall (Figure 3.2). A sandy spit (The Point) extending from the north and a rocky headland (The Ness) on the south constrict the narrow inlet channel connecting the estuary to the Lyme Bay (English Channel). In the adjacent nearshore region, a complex system of intertidal sandbars composes the ebb shoals.

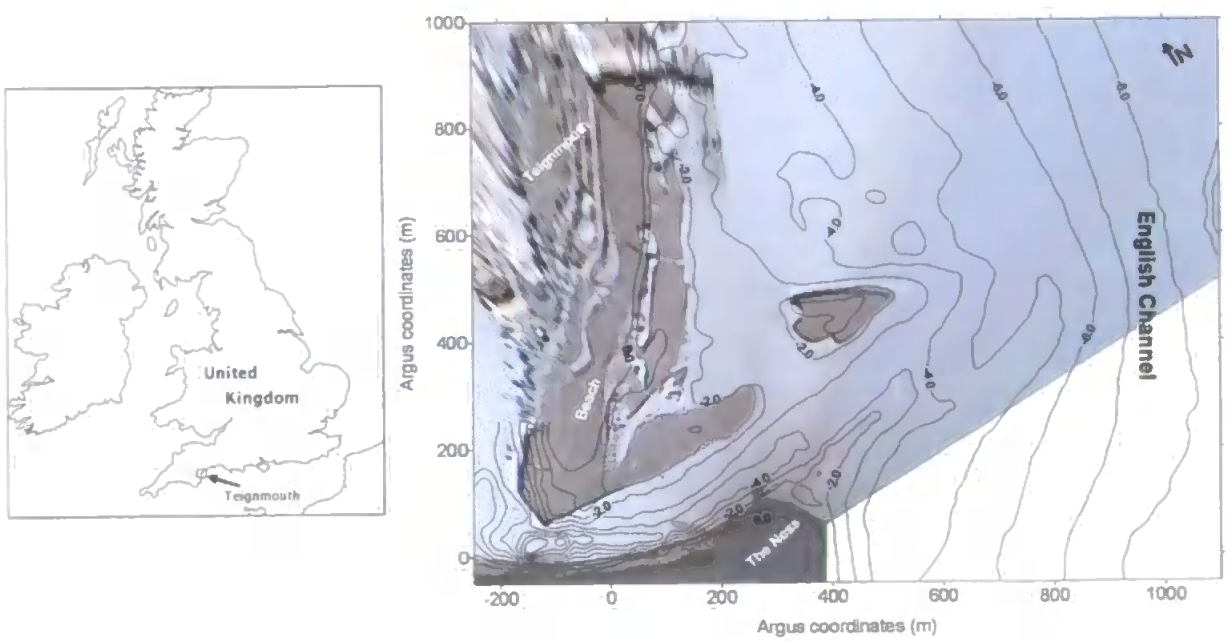

Figure 3.1. Study area. The nearshore bathymetry (for October 1999) is plotted over a rectified Argus image.

Figure 3.2. The beach, protected by a seawall with The Ness headland in the background.

The location of a harbour in the estuary makes the channel a busy waterway that is navigationally very problematic. As a result of the cyclic behaviour of the sandbar system that forms the ebb shoals described below, the channel is in need of constant drag-dredging to maintain a navigable shipping lane.

Comparable to others in East Devon the Teign estuary is a drowned river valley filled with sediments (Robinson, 1975). The estuary is approximately 6 km long and up to 800 m wide, with a total area of approximately 37 km^2, of which 21 km^2 forms its large intertidal area. The catchment area of the Teign basin is approximately 380 km^2 with additional inputs from the Rivers Lemon and Bovey. River discharge varies between less than 10 $m^3 s^{-1}$ in summer to peaks of over 150 $m^3 s^{-1}$ in winter months.

Teignmouth is a macrotidal region. Tides in the region are semi-diurnal with tidal range varying between 1.2 to 4.5 m, from neap to spring tides respectively. The site is relatively protected from Atlantic swell with significant wave heights greater than 0.5 m for less than 10 % of the year (Miles, 1997).

Sediment characteristics vary considerably around the inlet region and adjacent sandbars. Based on grab samples taken during the COAST3D project (see item 3.2.1.4) and summarised in Sutherland and Soulsby (2003), the offshore of the ebb-tidal shoal the median grain size (d_{50}) varied between 0.15 and 0.2 mm. On the beach the grain size varied from 0.2 to over 2 mm. In the main channel and to the south of the channel, near the Ness, the grain size was greater than 2 mm with the greatest measured value being 14 mm.

3.1.1. Relevant Previous Studies at the River Teign Inlet

Teignmouth's ebb-tidal delta sandbar system has been studied since the 19th century when Spratt (1856) first documented the cyclic movement of the sandbars. In his report proposing the construction of a jetty at the inlet entrance in order to maintain the navigability of the channel he suggests that the sandbar dynamics at the channel entrance follows a cyclic pattern. However, his study is based only on some sporadic observations and surveys of the area. Despite not suggesting the causes of the cyclic behaviour, he concludes that: *"the movement of the Bar sands were governed by a law, instead of being wholly fortuitous"*.

Robinson (1975) made a more detailed observation of the cyclic evolution of the sandbar dynamics at the region, presenting an illustrated and, to some extend documented history of the morphological evolution of the ebb-tidal delta. The author based his study on the observations of morphological maps of the area over a period of 10 years, from 1964 to 1974 and two tracer experiments accompanied by some hydrodynamic information. Figure 3.3 summarises the cycle described by Robinson (1975) with three main morphological stages that complete a cycle in approximately three years. Stage 1 is characterised by the growing Ness pole, which is projected across the main channel. He suggests that the instability of the Ness pole caused mainly by wave attack leads to its fragmentation. The second stage is characterised by the development of the offshore sandbars (Outer and Inner poles). Finally, stage 3 occurs when the onshore migrating sandbars attach to the beach causing the accumulation of sediments in the form of the Attached bank.

Qualitatively Robinson (1975) suggests that it is the interaction between waves and tidal currents that drives the cycle with distinct wave- and current- dominated environments. As for the sediment balance, he suggests that the system is a self-contained unit of sediment, with a closed cell of sediment isolated from the changes taking place in the coastal and offshore areas.

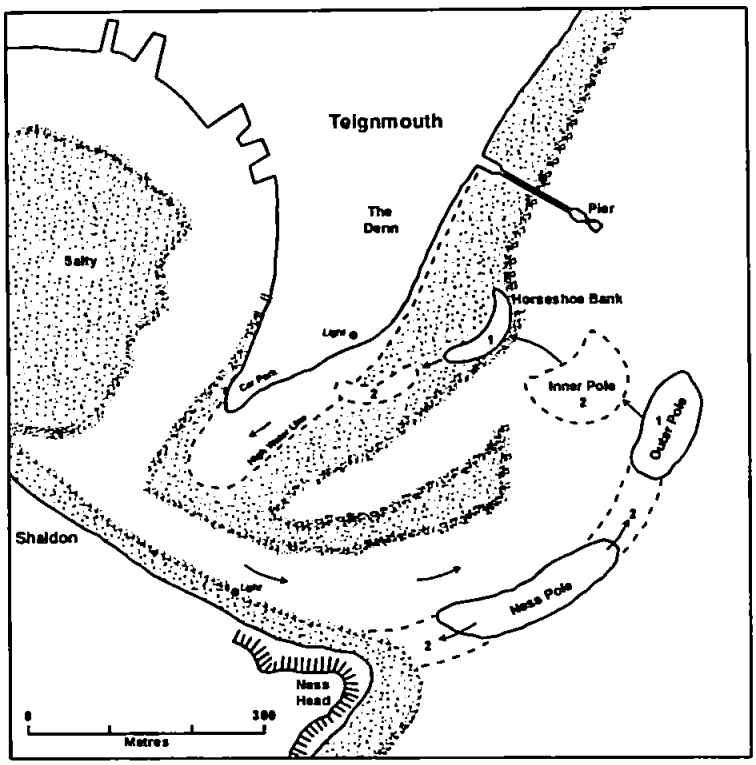

Figure 3.3. Diagrammatic representation of the main changes in bank positions (Robinson, 1975).

Nunney (1980) attempts to provide a descriptive model of the sediment dynamics in the Teign estuary. Despite focusing more at the upper part of the estuary, the author also includes the middle and lower portions of the estuary in his study. Through the analysis of the sediment characteristics and their relations to the local hydrodynamics, he found that the net transport of medium sands is always down the estuary, with more sediment being carried during ebb than flood tides. However, most important in the sediment dynamics of the lower estuary seems to be the ebb/flood dominance controlling the transport over the flood tidal delta (Salty flat). Nunney (1980) suggests a clockwise movement of sediment at

this region, with flood tides dominant at the west portion and ebb dominant at the east side of the flood delta. Studying the mineralogy of the medium sands of the flood tidal delta, he found that they are principally derived from the New Red Sandstones, with the main local source being the eroding cliffs at the southern side of the inlet. This study by Nunny (1980) also suggests a two-way exchange of material through the estuary entrance, supplying the sand circulation system within the lower part of the estuary.

Pritchard (2000) and Pritchard and Huntley (2002) carried out detailed observations of the Teign river plume front. When runoff is sufficient, a radially shaped brackish water plume, roughly symmetrical about the mouth, develops at the ebb tide (Pritchard and Huntley, 2002). According to these authors, the water is flushed from the estuary through the narrow inlet channel, and when entering Lyme Bay the discharge current immediately decelerates. Based on X-Band radar images used to map the plume development and spreading, Pritchard (2000) shows that a clear frontal development occurs only when the decelerating flow leaves the main channel. The relevance of their findings to this study is the indication that the vertical circulation is small compared to the horizontal circulation at the inlet channel region, where the application of a depth-averaged model can reproduce well the main hydrodynamic processes.

Based on geomorphological observations and previous studies, Carter and Bray (2003) made a qualitative assessment of the regional sediment transport paths. They conclude that the main sediment inputs are the cliff erosion and some fluvial input (mainly fine sediments). A summary of their findings is shown in Figure 3.4. As for the sediment transport paths, the authors divided the region in two main areas: south and north of the Teign estuary entrance. At the south of the estuary entrance, sediment supplied from the cliff erosion result in some substantial beaches, with well developed backshore berms. According to the authors, these are linked by a weak, discontinuous net northwards sediment transport pathway (Figure 3.4). Due to the configuration of the coast, with headlands confining pocket beaches, only small quantities of sediments are able to bypass the headlands. However, the authors believe that despite small, some contribution to the sediment budget of the sandbar system at the estuary mouth might come from the south. At the north of the estuary entrance, the evidence gathered by the authors shows net south/south-westwards longshore transport along Teignmouth's beach (Figure 3.4). Based on several previous studies, the authors conclude that this southwards transport takes place

whenever winds and waves from the east, south-east or east-south-east are operating. Some slight drift reversal (i.e. north-eastwards) may occur when the wave approach is from the west-south-west. However, offshore and inshore diffraction and refraction of waves from this direction is such that they have negligible capacity for littoral transport. This very qualitative information helps by providing a general overview of the main transport paths at the region, however, no quantitative information of the regional sediment budgets is available.

Within the COAST3D project (see section 3.2), the extensive field measurements resulted in further insight into sedimentary processes at the region. From sedimentological and morphological evidence based on sediment samples and side scan sonar data, Van Lancker et al. (2001) evidenced the highly dynamic changes in bedforms and sediment mobility. From the sediment trend analysis they verify the need of fair-weather and storm-dominated processes to explain the textural and morphological differentiation at this site. Hoekstra et al. (2001) studied the sediment transport at the mouth of the estuary, at the intertidal region of the Sprat Sand. Results of high resolution ripple profile measurements and sedimentology were used to estimate the bedload transport rates. The authors conclude that the bedload transport is mainly a result of migrating bedforms that develop on top of the shoal and within a thin layer of sediment. The combination of waves and currents results in a substantially increased migration rate. Both studies highlight the importance of the interaction between tidal currents and waves controlling the observed local sediment transport, with high energy wave events being responsible for large amounts of sediment displacement. These observations are however limited in terms of assessing the relative impact of each process on the sediment transport and local morphodynamics.

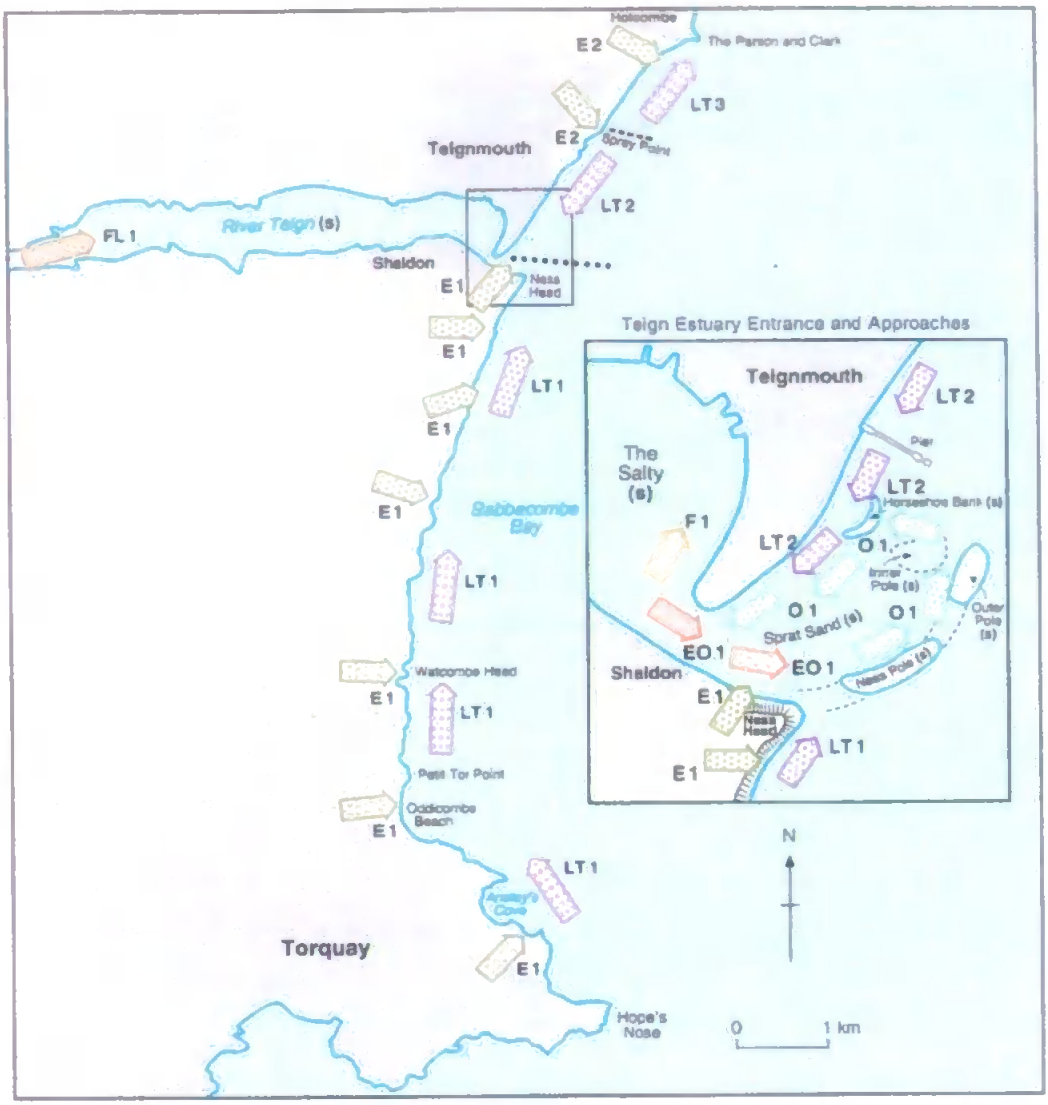

Holcombe to Hope's Nose, Torquay: Sediment Transport

Sediment Transport Mechanism

- LT Littoral drift
- O Offshore sediment transport
- E Cliff or coastal slope erosion input
- EO Estuarine sediment transport
- F Wave driven nearshore and offshore zone transport
- FL Fluvial input

Reliability of Information

Medium ⟵ High

Volume of Sediment Flow

No quantitative data

Sediment Types Involved in Transport

- Sand
- Sand and Clay
- Shingle and Sand
- Gravel and Sand
- Gravel, Sand and Clay

- Littoral drift divergence boundary
- Littoral drift convergence boundary
- (s) Sediment sink

Figure 3.4. Sediment transport at the Teignmouth region (from Carter and Bray, 2003).

3.1.2. Nomenclature and Main Morphologic Features

Despite the dynamics of the sandbars that form the ebb tidal delta at Teignmouth, some morphological features are easily identified and are characteristic to the whole evolutionary cycle. The nomenclature used in this study is based on the distinct characteristics of the morphological features visible in the region and is presented in Figure 3.5.

Inlet channels: at the region of interest there are three channels directing the tidal flows. Two of them are permanent features (the main channel and the flood channel) and one occasional (the secondary channel). The importance of the secondary channel is variable, depending on the morphological stage of the system.

Sandbars: a number of sandbar like features are visible in the study area, being divided in ebb- and flood-tidal delta features. The ebb-tidal delta sandbars are the most dynamic and complex of the system, with intertidal and subtidal features. At the southern side of the channel the elongated sandbar (Ness sandbar) is linked to the offshore sandbar, north of the channel, by the submerged sandbar, forming an overall "U" shaped depositional environment (terminal lobe) at the outer portion of the main inlet channel. Also to the north of the channel is the triangular shaped sandbar (Sprat Sand), which is separated from the beach by the flood channel. At the estuary side of the inlet, an evident flood tidal delta (The Salty) is visible at low water. This sandbar remained relatively stable over the years (Robinson, 1975; Nunney, 1980) and is mainly composed of marine sands (Nunney, 1980).

Beach: the beach adjacent to the inlet is classified as being dominantly reflective (Mariño-Tapia, 2003, according to classification proposed by Masselink and Short, 1993). The morphology is characterised by a steep reflective high tide beach and a flat terrace around low tide. On these types of beaches, surf zone processes at high tide are similar to those on reflective beaches, whereas during low tide the surf zone will be dissipative with several lines of spilling breakers (Mariño-Tapia, 2003).

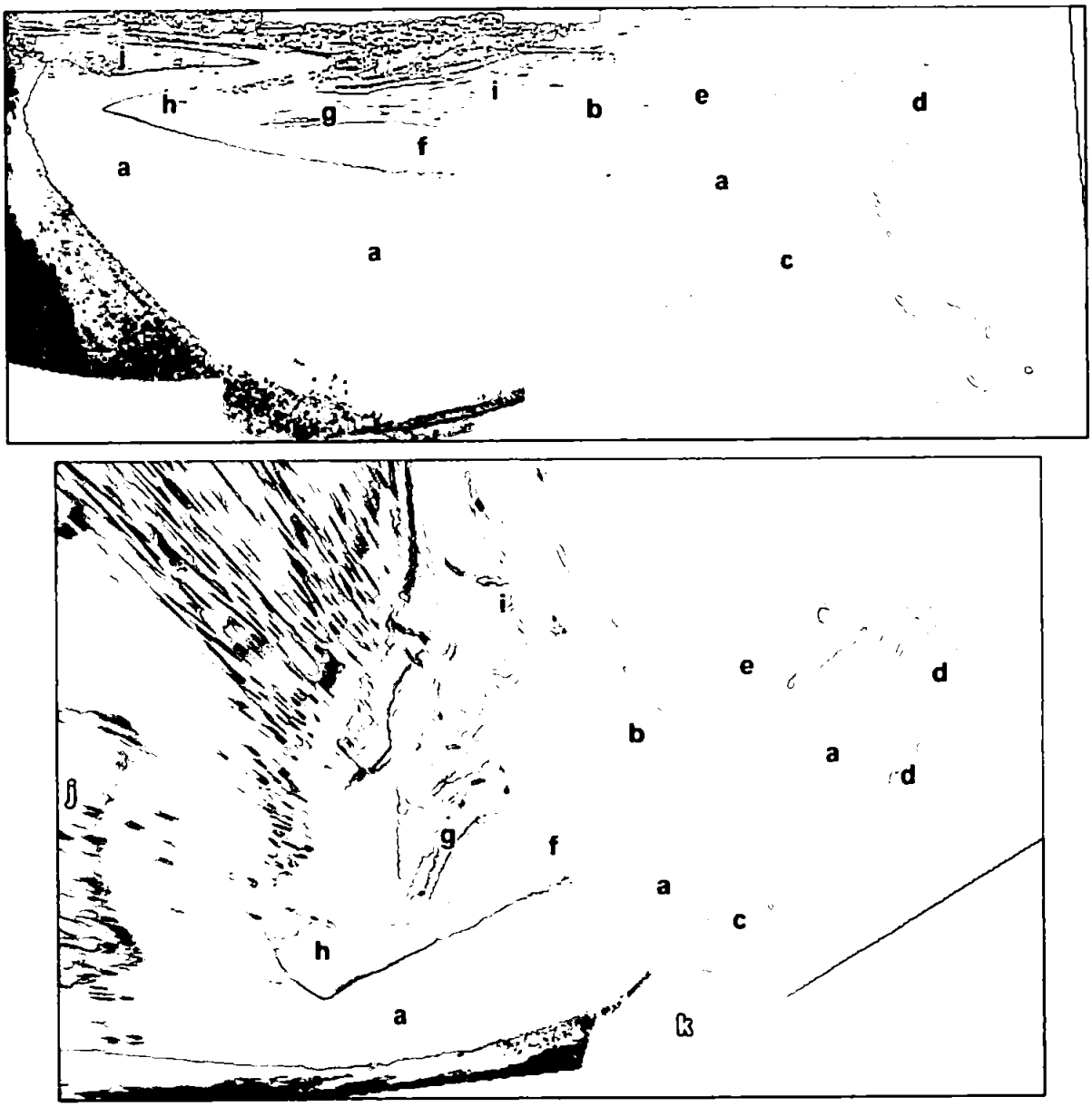

a. main inlet channel | b. secondary channel | c. Ness sandbar | d. submerged sandbar
e. offshore sandbar | f. Sprat sand | g. flood channel | h. sandy spit
i. beach | j. flood tidal delta | k. The Ness

Figure 3.5. Oblique and rectified merged Argus video images of the study area with the definition of the nomenclature used in this study (Images from the 24/01/2000).

3.2. Available data

This study covers approximately three years of the evolution of the sandbars that form Teignmouth's ebb-tidal delta (1999 – 2002). In order to accomplish this, data from several sources collected over this period is used. The main source of *in situ* measurements during this period was the COAST3D project, which provided an excellent database for the model validation. Additionally, Argus video images were collected continuously over the studied period. This data set is complemented by separate field campaigns and by the installation of a weather station by the University of Plymouth.

3.2.1. COAST3D main experiment

The international COAST3D* (COAstal STudy of three-dimensional sand transport processes and morphodynamics) project ran from October 1997 to March 2001 and was funded under the European Commission's Marine Science and Technology Research Programme (MAST-III project No. MAS3-CT97-0086). A consortium of 11 partners including hydraulic laboratories, universities and national regulatory authorities from five EU states (UK, Netherlands, France, Spain and Belgium) undertook the project. The purpose of the COAST3D project was (Soulsby, 2001):

- to improve understanding of the physics of coastal sand transport and morphodynamics.
- to remedy the present lack of validation data of sand transport and morphology suitable for testing numerical models of coastal processes.
- to deliver validated modelling tools, and methodologies for their use, in a form suitable for coastal zone management.

This was achieved by making field measurements purpose-designed for numerical model evaluation, with adequate boundary conditions and a dense horizontal array of measurement points, in conditions typical of the European coastline. Previous coastal experiments in Europe and elsewhere had placed their main emphasis on hydrodynamics; an innovative feature of the present project was that the emphasis throughout was on sand

* For more details see http://www.hrwallingford.co.uk/projects/COAST3D

transport and morphodynamics. The project focused on the dynamics of non-uniform (3D) coasts, rather than on the relatively well understood uniform (2D) cases. Experiments were performed at two sites: a quasi-uniform (2.5D) stretch of the Dutch coastline and a fully 3D site on the UK coast (Teignmouth).

Within the COAST3D project a series of numerical area models were validated using this database, including the University of Liverpool 2DH hydrodynamic and morphodynamic model (Pan et al., 2001), the DELFT3D-MOR model (Walstra et al., 2001), the TELEMAC version of PISCES model (Sutherland et al., 2001, Walstra et al., 2001) and the CIIRC model with the LIMOS wave model (Sierra et al., 2001).

The data used in this study includes only part of the data collected during the experiments at Teignmouth, UK, and is given in Table 3.1. Figure 3.6 shows the location of all the instruments deployed during the main experiment (October – November 1999) and a brief description of the data used in this study is given below. Full details can be found in Whitehouse and Sutherland (2001).

Table 3.1. COAST3D main experiment instruments used for the model validation.

Station*	Instrument**	Date deployed (GMT)	Date recovered (GMT)	Easting (OSGB)	Northing (OSGB)	Elevation (m)***
3	frame	25/10/99 16:37	23/11/99 07:45	294695	71907	1.09
5a	S4	25/10/99 15:30	16/11/99 09:43	294955	72515	0.65
5b	S4	16/11/99 09:46	22/11/99 08:55	294962	72491	0.65
7	waverider	25/10/99 08:16	23/11/99 08:10	295224	72378	--
8	tide gauge	25/10/99	26/10/99	294347	72656	--
9	frame	26/10/99 08:06	22/11/99 17:54	294593	72481	1.09
11	tide gauge	21/10/99	26/11/99	293885	72696	--
14	S4	25/10/99 15:41	22/11/99 13:23	294304	72447	0.65
24	S4	25/10/99 17:19	22/11/99 13:33	294234	72319	0.65
25	frame	26/10/99 07:14	22/11/99 17:30	293952	72218	1.12
26	ADP	25/10/99 09:16	22/11/99 09:32	294840	71810	--
28	frame	26/10/99 06:43	22/11/99 15:12	294289	72016	1.09
33	frame	25/10/99 14:20	22/11/99 07:56	294519	71312	1.00
38	met. station	20/10/99	26/11/99	294371	72642	--

*Station numbers followed by "a" or "b" indicate changes in the location. **frame: when more than one instrument was deployed (e.g. eletromagnetic velocity meter and pressure sensor). *** Elevation above the bed (if appropriate).

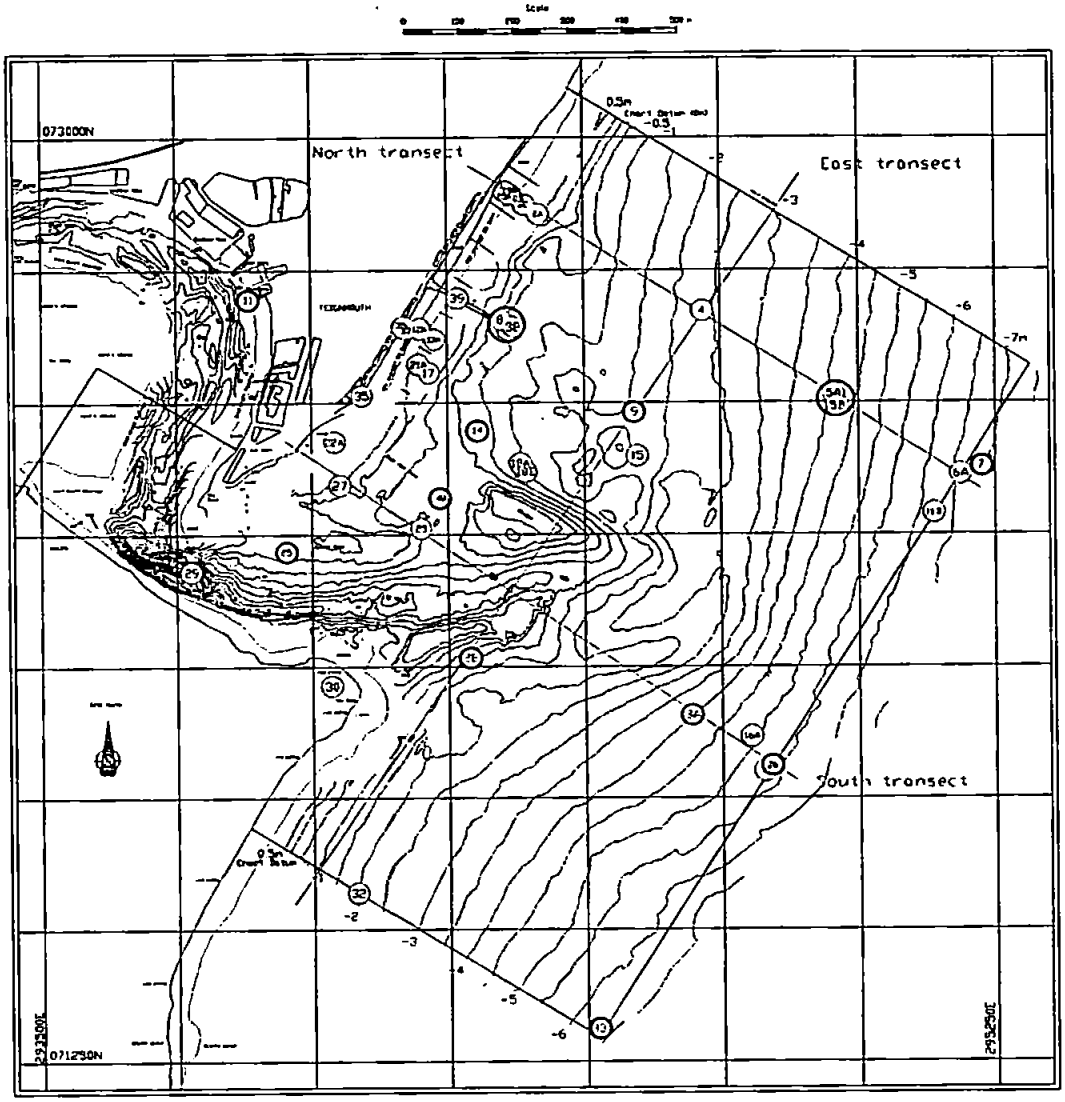

Figure 3.6. Locations of instruments during the main field campaign in Teignmouth (October 1999 bathymetry in relation to the ACD). Figure taken from Whitehouse and Sutherland, 2001). Each numbered circle represents a sensor location. Those used in the present work are highlighted (black circles) and are detailed in Table 3.1.

3.2.1.1. Hydrodynamics

Water levels: Instrument locations 8 and 11 (Figure 3.6) indicate the locations of the pressure sensors installed for the water level measurements. At location 11 (harbour) the unit averaged over 20 seconds. The unit at location 8 (Pier) averaged over 180 seconds in order to remove swell and waves, and all averages were corrected and time stamped at the

centre time of the average. Both systems were levelled by land survey closed looped traverse to the same two nearby Ordnance Survey Bench Marks. The typical resolution was 1 or 2 mm providing accuracies of around 5 mm or better (Whitehouse and Sutherland, 2001).

Wave measurements: The wave data come from stations 7, 3, 4 and 25 (Figure 3.6). At stations 7 and 3 directional data is available, while at stations 4 and 25 the data is non-directional. At station 7 a Datawell Directional Waverider buoy was deployed providing the wave boundary condition for the numerical model validation (Chapter 4). Significant wave heights and periods were determined for stations 3, 4 and 25 from pressure sensor records. The time-step of wave data collection was of one hour and the direction is given in degrees relative to the true North.

Van Rijn et al. (2000) estimated the accuracy of the wave measurements during the COAST3D experiments obtained through pressure sensors. This was done considering inaccuracies related to the water depth caused by the unknown height of the sensor above the bed, related to sedimentation/erosion near the instrument, and through comparisons with other instruments. The authors conclude that the significant wave height in non-breaking conditions derived from pressure sensors may have an uncertainty of maximum 10 %. In breaking conditions this uncertainty may increase to a maximum of 15 %.

Flow velocity measurements: The flow velocity data was collected by eletromagnetic velocity meters (stations 5, 9, 14, 24, 25, 28 and 33) and by an Acoustic Doppler Velocity meter (ADV – station 26). The eletromagnetic velocity meters used were the EMF sensors (manufactured by Delft Hydraulics) at stations 9, 25 and 28 and the S4 sensors (manufactured by InterOceans Systems Inc.) at stations 5, 14, 24 and 33. The flow velocity measurements were made every 10 minutes, being averaged over 10 minutes for the eletromagnetic velocity meters and over 40 seconds for the ADV measurements. The height above the bed where the measurements were made are indicated in Table 3.1.

Van Rijn et al. (2000) assessing the accuracy of these measurements concluded that time-averaged velocities smaller than 0.05 m s^{-1} may have an inaccuracy of maximum 100 %; time-averaged velocities in the range of 0.15 to 0.3 m s^{-1} may have an inaccuracy of

maximum 30 %; and time averaged velocities larger than 0.5 m s^{-1} are assumed to have and inaccuracy of maximum 15 %.

River discharge: The river discharge time series used in this study was obtained from the UK Environmental Agency (South West Branch) and covers more than three years (January 1999 – August 2002). The gauging station gives four measurements per hour of the fluvial inflow at the upper limit of the estuary.

3.2.1.2. Meteorological conditions

During the COAST3D main experiment, the meteorological station provided only a few days of data at the beginning and at the end of the experiment due to technical problems. The gap in data collection was completed with data provided by the UK Meteorological Office, from its station at the Isle of Portland, some 75 km east of Teignmouth (UTM 456293.12 mE, 5601008 mN), at an exposed site 52 m above the sea level. Over the short period that the measurement coincided, there was good agreement of barometric pressure and wind direction and air temperature between the two sites. However, wind speeds were generally higher at Isle of Portland. During the period of three days of coinciding measurements the wind speeds were about 3 m s^{-1} higher in average, at the Isle of Portland.

3.2.1.3. Bathymetric and topographic surveys

During the main experiment four subtidal surveys were made (Table 3.2) and the overall coverage is indicated in Figure 3.7. These surveys were made by m.v. Sir Claude Inglis (HR Wallingford) using differential GPS positioning. The intertidal region was surveyed with the use of a DGPS system and the surveyed points are also indicated in Figure 3.6. The co-ordinates system applied for the surveys was the Ordnance Survey National Grid of Great Britain (OSGB), which is a Transverse Mercator Projection with spheroid OSGB 36. Depths were measured in meters and originally reduced to the Admiralty Chart Datum (ACD), which is 2.65 m below the Ordnance Datum Newlyn (ODN). In order to work with the same datum as the one used in the Argus video imaging system (see section 3.2.2), in this study the depths were reduced to ODN.

Van Rijn et al. (2000) assessed the measurement errors for the bathymetric and topographic surveys. The beach survey performed using a DGPS receiver mounted on a small vehicle moving over the beach, presents horizontal and vertical inaccuracy of about 0.05 m on relatively flat areas and about 0.1 m on steep sloping face of bars. The inaccuracy of the ship survey used in the offshore sandbar comparison may be as large as 0.25 m in shallow depths (such as over the off shore sandbar) due to relatively large ship-induced motions.

Table 3.2. Bathymetric surveys carried out during the main experiment.

Survey	Dates	wave condition
S1	27 – 28 October 1999	0.2 to 0.3 m; 3 to 6 s
S2	6 – 8 November 1999	0.1 to 0.4 m, 3 to 10 s
S3	16 – 17, 19 November 1999	0.1 to 0.3 m, 3 to 7 s
S4	24 – 25 November 1999	0.3 to 0.75 m, 5 to 7 s

In order to obtain the bathymetry of a larger region to be included in the model domain the surveyed data was complemented with data from digitised charts. The estuary region is included by the use of a 1979 survey (Nunney, 1980) and the offshore region is represented by data derived from the Admiralty Chart 3155.

Additionally to the COAST3D surveys, some topographic surveys of the intertidal region were carried out during July and August 2000 in order to validate the application of techniques to extract quantitative information from the video images (as described in Chapter 5). These surveys were conducted using a total station referenced to the OSGB co-ordinate system and their positions are shown in Chapter 5 (Figure 5.15). These surveys were referenced to the ODN datum.

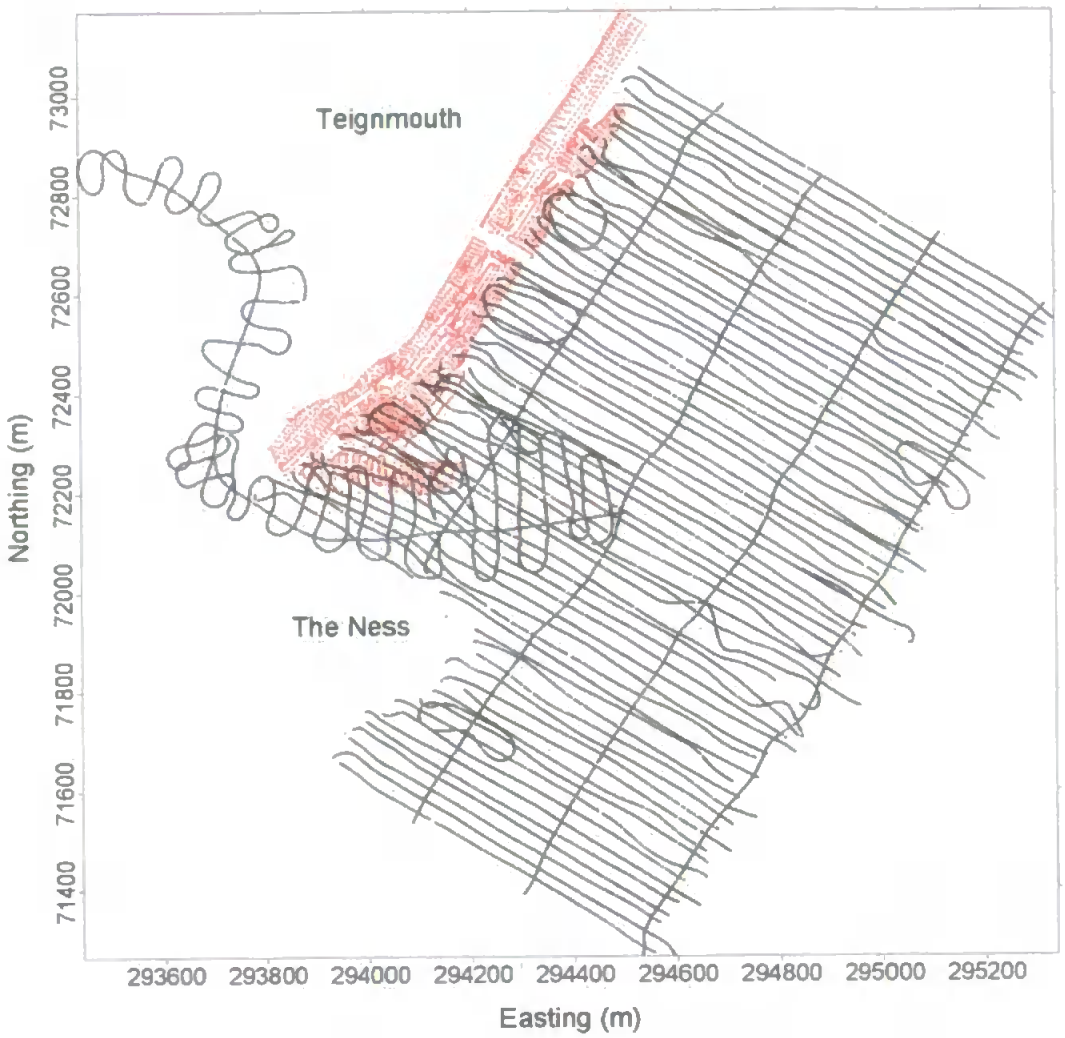

Figure 3.7. Example of the COAST3D surveys coverage area and resolution. Black points indicate the vessel bathymetric survey and red points indicate the beach quad bike survey (6 – 8 November 1999, Survey 1, OSGB).

3.2.1.4. Sediment samples

During the COAST3D pilot experiment 10 grab samples of the region of interest were analysed (sieved) whilst during the main experiment a total of 92 grab samples were analysed in order to establish their median grain size (d_{50}) and sorting (σ). Figure 3.8 shows the position and d_{50} of the grab samples for both experiments.

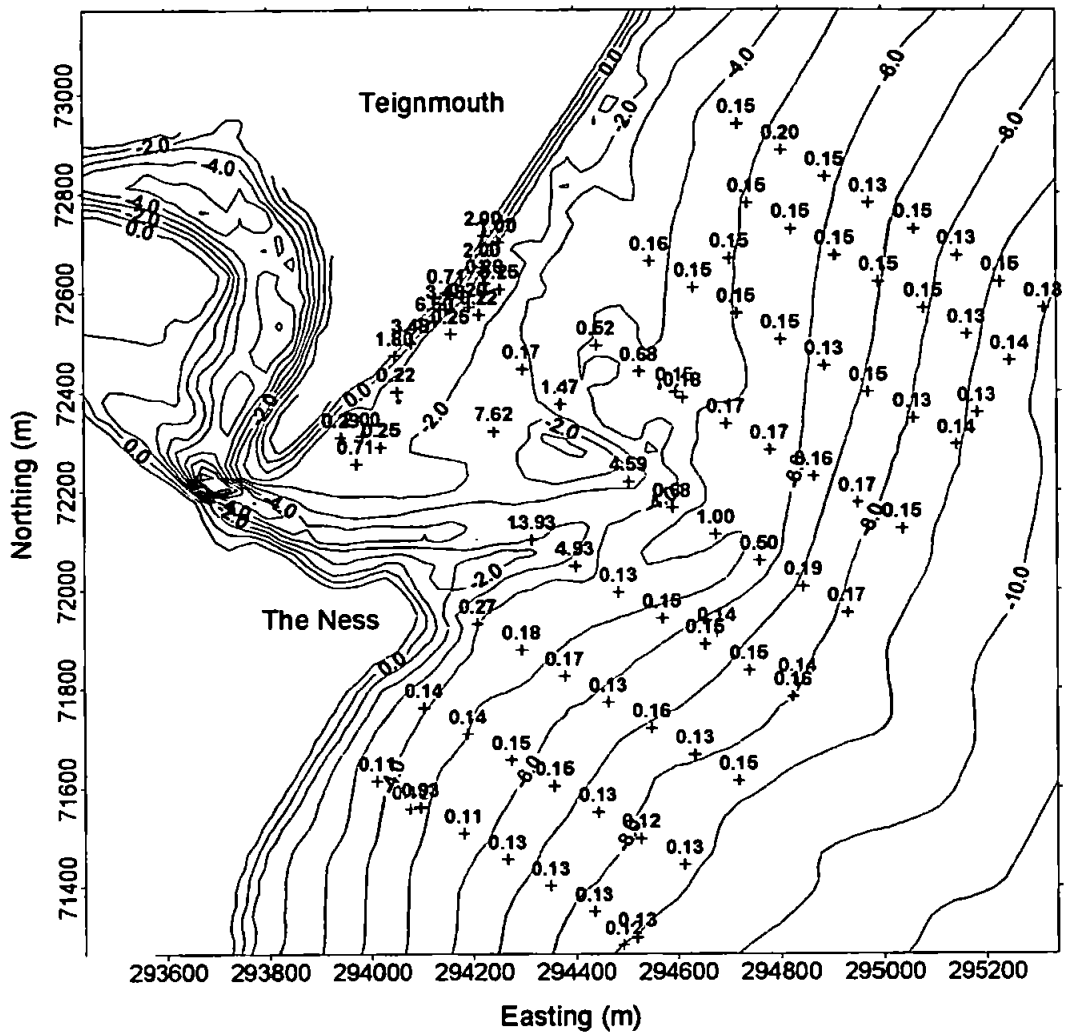

Figure 3.8. Sediment samples distribution and median grain size values for the COAST3D pilot (red) and main (black) experiments. Co-ordinates are in OSGB, depths in ODN and grain size in millimetres.

3.2.2. Argus Video System

Additionally to the *in situ* measurements, Argus video images of the study area were collected every daylight hour continuously since February 1999. The five-camera Argus system is located on the top of Ness Head close to the estuarine inlet (Figure 3.9). These five cameras are directed to cover the inlet and Teignmouth beach (Figure 3.10).

Figure 3.9. The Ness, with the arrow indicating the position of the Argus video cameras, detailed in the right hand side.

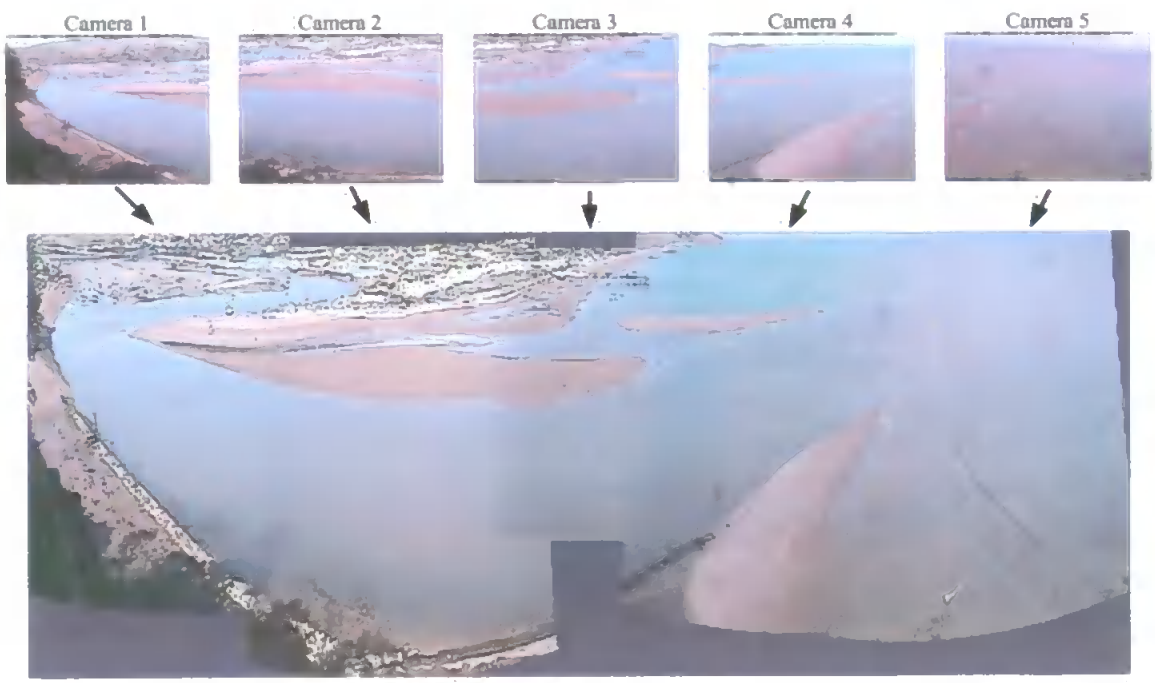

Figure 3.10. Images from the five cameras in Teignmouth and a merged image showing a panoramic view of the cameras field of view (05 March 2000, 12:00h).

The Argus system co-ordinate system is given in metres, with the origin of the grid being the shoreline (x) and the cameras position (y). As a convention, the orientation of the x-axis is shore normal, with the positive x-axis pointing in seaward direction. The y-axis is directed perpendicular to the x-axis, such that the co-ordinate system obtained is positive in mathematical sense (Aarninkhof and Kingston, 2002). The vertical reference level for the Argus system at Teignmouth is the ODN datum. Some details of the basic image processing and accuracy are given below and serve as a basis for the technique applied in Chapter 5.

The Teignmouth Argus video system was running before the start of this project, however, the author was directly involved in the maintenance of the system and determination of the cameras geometries for the image processing. Additionally, the author was involved in the planning and relocation of the cameras to a new frame in December 2001 (shown in Figure 3.9). This was necessary due to the erosion of the Ness cliff, compromising the old camera's frame.

3.2.2.1. Basic Elements of Image Processing

The basis of video images processing is the quantification of intensity variability of an image into a two-dimensional array of picture elements or pixels (Holman et al., 1993). According to these authors, the successful use of video image processing for any study requires an understanding of three component problems in increasing order of difficulty: 1) temporal aspects of video sampling, 2) spatial aspects and the transformation between image and ground coordinates, and 3) the relationship between image data and geophysical signals of interest. Some aspects related to these problems are described below and more details about the Argus imaging photogrammetry and calibration can be found in Lipmann and Holman (1989) and Holland et al. (1997).

Coordinates Transformation

In order to use oblique images to quantify offshore and longshore length scales it is necessary to transform the image using some photogrammetric equations (Lippmann and Holman, 1989). A geometric analysis is conducted by utilising objects of a known location

that are visible within the image to calculate the camera orientation relative to a given coordinate system. When transforming from ground to image coordinates the equations are fully defined. However, since the image is two-dimensional while the ground is three-dimensional, the opposite process, rectification, is not fully defined, as ground coordinates are three-dimensional, while image coordinates are two-dimensional (Lippmann and Holman, 1989). To solve this problem, one dimension is assumed known. For the Argus images the vertical coordinate (z) is assumed to be the local water level.

To make a physical analysis of the images, each oblique image produced by the cameras has to be rectified, deriving field coordinates from image coordinates. The geometry and labelling conventions used in the rectification process are shown in Figure 3.11 (after Lippmann and Holman, 1989). Small letters (x, y) represent image coordinates, and capital letters (X, Y) denote the ground coordinates. The optic centre of the camera is located at point O, a distance Z_c above the x-y (ground) plane. The camera nadir line intersects the ground at the nadir (N). The image points lie in the focal plane, which is considered the 1:1 positive, consistent with traditional photogrammetry conventions. The focal plane is separated from O by the focal length f_c, determined by the camera lens. The optic axis centre of the focal plane at point p, called the principal point, and forms an angle τ (camera tilt) with the vertical nadir line. The principal line passes through the principal point and bisects the focal plane. The principal point is also the origin for the image coordinates system with the principal line as the y axis. The nadir point acts as the origin for the camera coordinates system with the principal line in the ground plane defining the positive y axis (Lippmann and Holman, 1989).

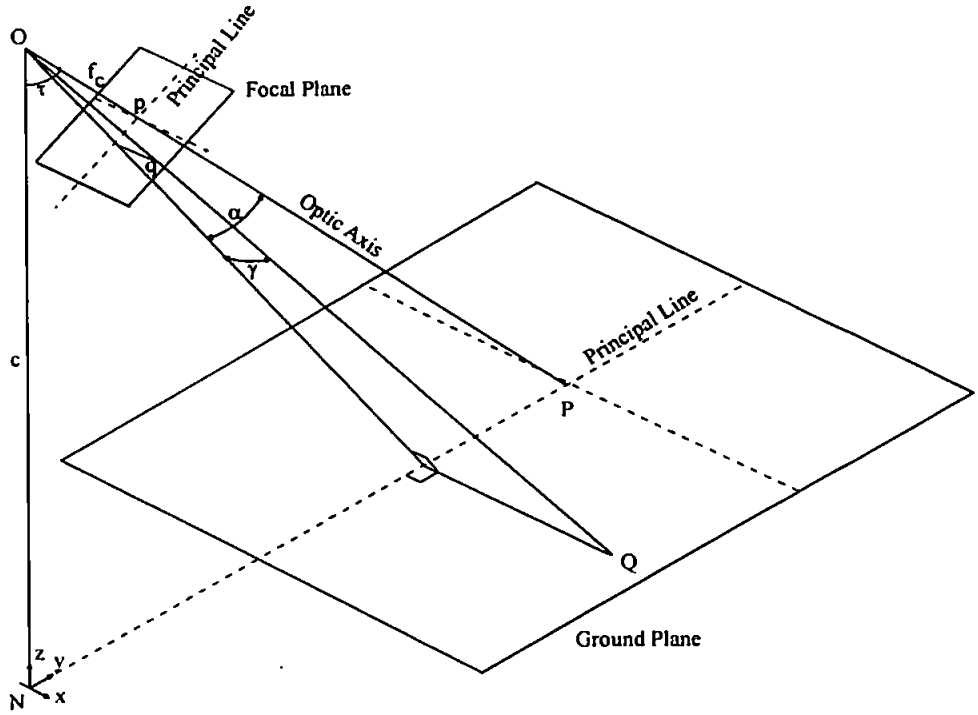

Figure 3.11. Geometric conventions for Argus photogrammetry (Lippmann and Holman, 1989).

The ground location of any point Q is determined from its image coordinates (x_q, y_q) by

$$X_Q = Z_c \sec(\tau + \alpha) \tan\gamma$$

$$Y_Q = Z_c \tan(\tau + \alpha) \tag{3.1}$$

Where the angles α and γ are defined as

$$\alpha = \tan^{-1}\left(\frac{y_q}{f_c}\right)$$

and (3.2)

$$\gamma = \tan^{-1}\left(\frac{x_q}{\sqrt{y_q^2 + f_c^2}}\right)$$

Transformation in the opposite direction, from ground to image points, is done by simply inverting and combining 3.1 and 3.2 to yield

$$y_q = f_c \tan\left(\tan^{-1}\left(\frac{Y_Q}{Z_c}\right) - \tau\right)$$

and (3.3)

$$x_q = \left(\frac{y_q^2 + f_c^2}{Z_c^2 + Y_Q^2}\right)^{1/2} - \tau$$

As these equations are function of the camera tilt (τ) and focal length (f_c), the application of these relationships in the field involves several complications (Lippmann and Holman, 1989). Field measurements of tilt are difficult and inaccurate, and the focal length of a zoom lens is also hard to estimate. The second complication arises from the use of amplified images. This will cause the apparent focal length of the image to be altered by an unknown amount. The "magnified" focal length can be solved analytically using

$$f_c' = \frac{x_e}{\tan\left(\frac{\delta}{2}\right)} \tag{3.4}$$

Where x_e is the measured distance from the principal point to the right-hand edge of the enlarged image and δ is the horizontal field of view of the lens. However, for most cases, δ itself is not accurately known, and the direction of aim of a camera in the field is generally chosen to give the best view. Therefore the ground coordinates system defined by the principal line does not match the "natural" beach related coordinates system. In particular the angle of rotation ϕ between these two coordinates systems, as well as the camera roll θ relative to the horizon, are hard to estimate in the field, complicating the use of the equations 3.1 to 3.3. In summary, the application of photogrammetry in the field requires the accurate knowledge of four camera related parameters δ, τ, ϕ and θ which cannot be measured with sufficient accuracy in the field (Lippmann and Holman, 1989).

Relatively accurate estimates of these additional unknowns (δ, τ, ϕ and θ) can be determined by making use of clearly visible and defined objects within the field of view of

the camera, with known locations in the oblique image as well as on the ground. These known points are called Ground Control Points (GCP). By knowing both the ground and image coordinates of the GCP's, equations 3.1, 3.2 and 3.3 can be solved iteratively to calculate the unknowns. To solve the four parameters (δ, τ, ϕ and θ) two GCP's are needed, thereby yielding a unique solution. If three or more GCP's are used, the problem is overdetermined and the solution can be optimised by applying a least squares solution. The use of this technique results into typical errors in the estimates of τ, ϕ and f_c less than 0.25°, 0.5° and 0.5%, values which satisfactorily compare to the errors of the order of 1° when measuring these properties directly in the field (Lippman and Holman, 1989).

Oblique Image Rectification

After the determination of the geometry through the use of GCP's, ground coordinates (x, y) can be computed for every image location (U_i, V_i). This creates a rectified image, that is the projection of the original oblique image onto a horizontal plane at a certain vertical level. Starting from a known geometry the computations are executed for every single pixel, based on the Walton approach, that works with similar triangles (Aarninkhof, 1996). Geometrically, a linear relationship between image and ground coordinates yield

$$U_i = \frac{Ax + By + Cz + D}{Ex + Fy + Gz + 1}$$

and (3.5)

$$V_i = \frac{Hx + Jy + Kz + L}{Ex + Fy + Gz + 1}$$

These expressions contain eleven parameters ($A...L$) which describe the geometry. To solve this system of eleven equations in eleven unknowns ($A...L$) six GCP's are needed, with each serving two relations between image and ground coordinates. If it is not possible to find six suitable GCP's in the cameras field of view, the parameters δ, τ, ϕ and θ and the camera position (x, y, z) can be used. The additional relations obtained through their use makes the use of two GCP's enough to obtain the eleven equations that solve the eleven unknowns. If more GCP's are used, a least squares approach is possible to solve this linear system of equations.

Knowing the eleven parameters of the Walton vector $m = (A...L)$ the ground coordinates (x, y, z) can be deduced from the inverted equations:

$$(EU_i - A)x + (FU_i - B)y + (GU_i - C)z = D - U_i$$

$$(EV_i - H)x + (FV_i - J)y + (GV_i - K)z = L - V_i \qquad (3.6)$$

$$z = z_{tide}$$

The third equation has been added to create a system of three equations and three unknowns. In nearshore applications the vertical level is assumed to be the tidal level (z_{tide}). This rectification process generates a plan view image, used for the physical analysis.

At Teignmouth, the geometry for each of the five cameras is created by calculation of the parameters δ, τ, ϕ and θ using the information of at least two GCP's. However, usually a larger number of GCP's are visible and used for the Teignmouth images. Geometries are created using MATLAB® routines (developed under the Argus Programme coordinated by the Coastal Imaging Lab - Oregon State University) containing the relations described above. For the application of these routines the MATLAB's Image Processing Toolbox is required. The input consists of a selected image that permits the clear visualisation of the GCP's, a camera file containing the (x, y, z) coordinates of the camera location and two distortion parameters and a file containing the ground plane coordinates of a number of GCP's.

GCP's for Teignmouth cameras were chosen after detailed investigation of selected images allowing the identification of each GCP which were then surveyed *in situ*. Field determination of GCP's coordinates was made through topographic surveys using a Differential Global Positioning System (DGPS). Geometries for each camera are created on a regular basis of 1 or 2 geometries per month, or according to any detected change in a camera's orientation.

Image Quantification and Pixel Resolution

Using the image processing system the oblique image is converted into a 640 x 480 array of pixels. Pixels are ordered according to a (U_i, V_i) pixel coordinates system, with origin in the upper left corner of the image. Normal image resolution is the single pixel, where the location of a circular target is defined according to the nearest pixel. This resolution can be improved by using sub-pixel techniques, which means that the location of a target is determined from centre of mass considerations: U_i- and V_i-coordinates of the target are defined as the mean values of the U_i- and V_i-coordinates of the pixels inside the target (Aarninkhof, 1996). Comparing these improved coordinates to those obtained with normal image resolution yields an indication of the error within the digitised image. The observed differences are a function of the distance of a pixel to the centre of the screen. As such the image is said to be radially distorted (lens distortion). In order to correct this, image coordinates are undistorted first before being transformed into ground coordinates (see Holland et al., 1997). For this process another MATLAB® routine developed under the Argus Programme is applied (Holland et al., 1997).

With every pixel representing a part ($\Delta\delta$) of the camera field of view (δ) of approximately 30°, the method of breaking up the images into the array of pixels implies in a fundamental limit on resolution. For the Teignmouth cameras, the angular field of view of every pixel ($\Delta\delta$) is approximately 30°/640 (= 0.047°), allowing estimation of the pixel resolution in x and y dimensions. As it is based on the straight distance (R) from ground location to the camera, the pixel resolution depends on the position in the field of view:

$$\Delta x \approx R \cdot \Delta\delta$$

and (3.7)

$$\Delta y \approx \frac{R \cdot \Delta\delta}{\cos(\tau + \alpha)}$$

Numerically, the pixel resolution can be obtained through the known geometries for a given image. With the definition of image and ground coordinates as described in section 5.2., one can start from a location within the ground plane, compute its screen coordinates, move half a pixel in both positive and negative x- and y- direction and recompute the ground plane coordinates of the new "moved" points. The latter two represent the corners

of the "footprint" of the original pixel on the ground plane. After a correction for the camera orientation the dimensions of this footprint in x- and y- direction can be calculated (Aarninkhof, 1996). An example of calculated longshore and cross-shore pixel resolution for Teignmouth Argus images is shown in Figure 3.12.

3.2.3. Weather Station and Pressure Sensor (pier)

In order to support the video image data, the University of Plymouth installed a weather station and a pressure sensor at the Teignmouth pier that started collecting data from August 2000. Since then it is recording the meteorological conditions, water levels and non-directional wave data. The water levels measured at this station are used in the image processing, being referenced to the ODN datum. When technical problems result in gaps in the recorded time series the predicted water levels are applied.

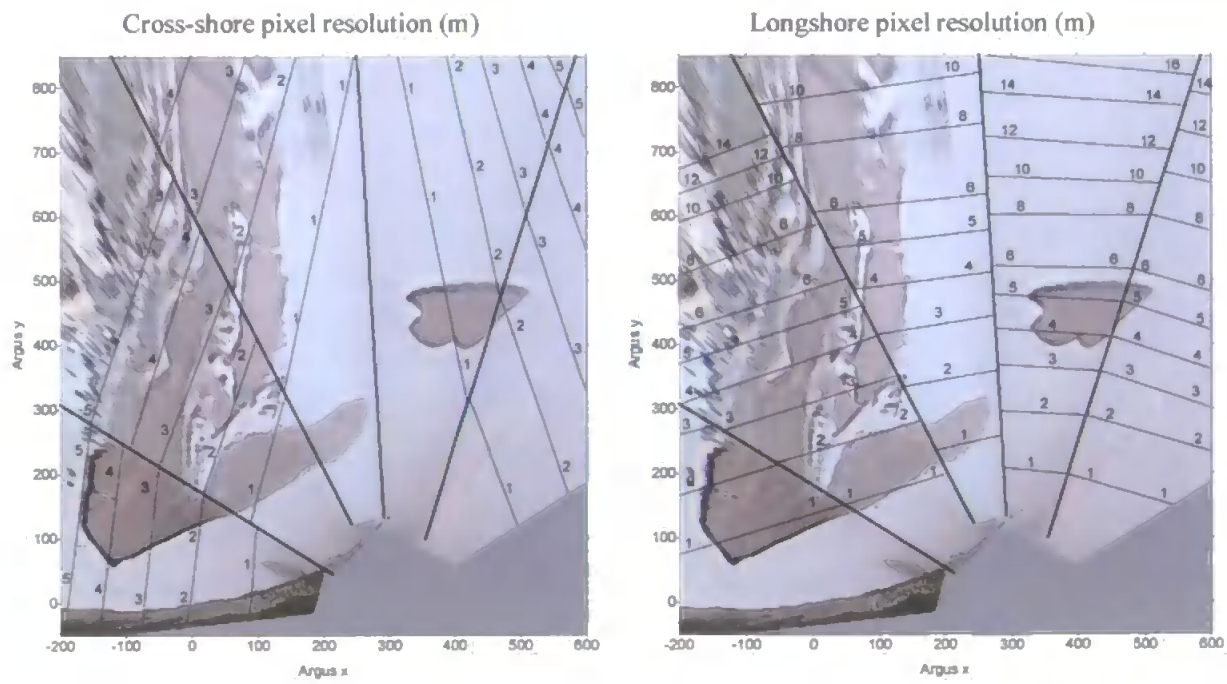

Figure 3.12. Argus video images pixel resolution for the Teignmouth cameras system (26 October 1999).

3.3. Conclusion

This chapter provided the information about the study area, the nomenclature used to describe its morphological features, and the data available for the study. The high quality data set available for this region allows the numerical calibration and validation (Chapter 4) and to describe the morphological evolution of the dynamic sandbars (Chapters 5 to 7).

The photogrammetric relations used in the image processing are applied in Chapter 5 when combining the numerical model and video images, and also for the description of the morphological evolution through the use of rectified video images (Chapters 6 and 7). Throughout the thesis, several references are made to the description here provided.

Chapter 4

Numerical Modelling

4.1. Introduction

The high level of complexity of regions such as estuarine inlets involves the interaction of several forcing parameters. Tidal currents interacting with the discharge through the inlet and with incoming waves result in complex flow patterns that are also shaping and co-interacting with the local morphology. The application of numerical area models at the coastal environment is a powerful tool that combined with field measurements can add to the understanding of such regions. Modelled results can help in filling spatial and temporal gaps of field measurements.

Recently, much effort has been devoted in the development and application of numerical area models (for hydrodynamics, waves, sediment transport and morphodynamics) in order to simulate the physical processes at such sites. A review of the development and application of two-dimensional, depth-averaged models is given by De Vriend (1994). The advances in such applications lead to more recent intercomparisons of several area models, such as De Vriend et al. (1993); Nicholson et al. (1997); Péchon et al. (1997); Davies et al. (1997); Walstra et al. (2001); Davies et al. (2002); Davies and Villaret (2002) among others.

A difficulty for the evaluation of such numerical area models arises from the usually limited measured data sets available for coastal regions. A unique database for the calibration and validation of such numerical models is one of the achievements of the COAST3D project (Soulsby, 1998, 2001). Measurements at Teignmouth, one of the studied field sites within the COAST3D project, included a dense spatial coverage of instruments, allowing the assessment of model performance over the entire study area (Sutherland et al., 2001). Using this database, several numerical models were applied and

validated for the Teignmouth region by the COAST3D project partners (e.g. Hall et al. 2001; Sutherland et al., 2001; Pan et al, 2001; Sierra et al., 2001; Walstra et al. 2001a, b).

In this study, the well-known MIKE21 modelling system developed by the DHI Water & Environment is applied at Teignmouth and validated using the COAST3D database. Three modules of the MIKE21 system were applied, including the two-dimensional hydrodynamic module (HD), the nearshore spectral wind-wave module (NSW) and the non-cohesive sediment transport module (ST). The development of MIKE21 started at DHI in 1970 and has since been extended for different applications (e.g. Abbott et al., 1981; Abbott and Larsen, 1985). A description of each of the applied modules and their formulations is given in Appendix I and is based on the scientific documentation of the MIKE21 system and on relevant literature.

During this study no changes were made to the model formulation and algorithms, the author was involved in the pre- and post-processing of data and modelled results of the experiments, in the model setup, and in the adjustment of parameters relevant to the calibration and calibration of the numerical model.

The chapter structure includes the description of the model setup used in this application followed by the calibration and validation of each module, which compares the modelled results to the measured data from the COAST3D main experiment. This allows a qualitative and quantitative (through the use of statistical parameters) judgement of the quality of the applied numerical model. Combined with the remote sensing techniques (Chapter 5) the validated numerical model is applied for the study of the physical processes driving this complex region in Chapters 5, 6 and 7.

4.2. Model Setup

Since the MIKE21 modules (HD, NSW and ST – Appendix I) work separately, it is necessary to run them sequentially and apply the results from one module as input for the next module. The first module to be run is the NSW module, since its results (wave radiation stresses) serve as input for the HD module. The ST module uses results of both

previous modules as input, being the last module to be run. Without running the modules in order to get an equilibrium condition at each tidal level, the model is assumed to be operating at a "frozen tidal state", which is a limitation of every standard numerical model. Figure 4.1 shows the interrelation of the different MIKE21 modules with the ST module. The setup of each module applied in this study is described separately below.

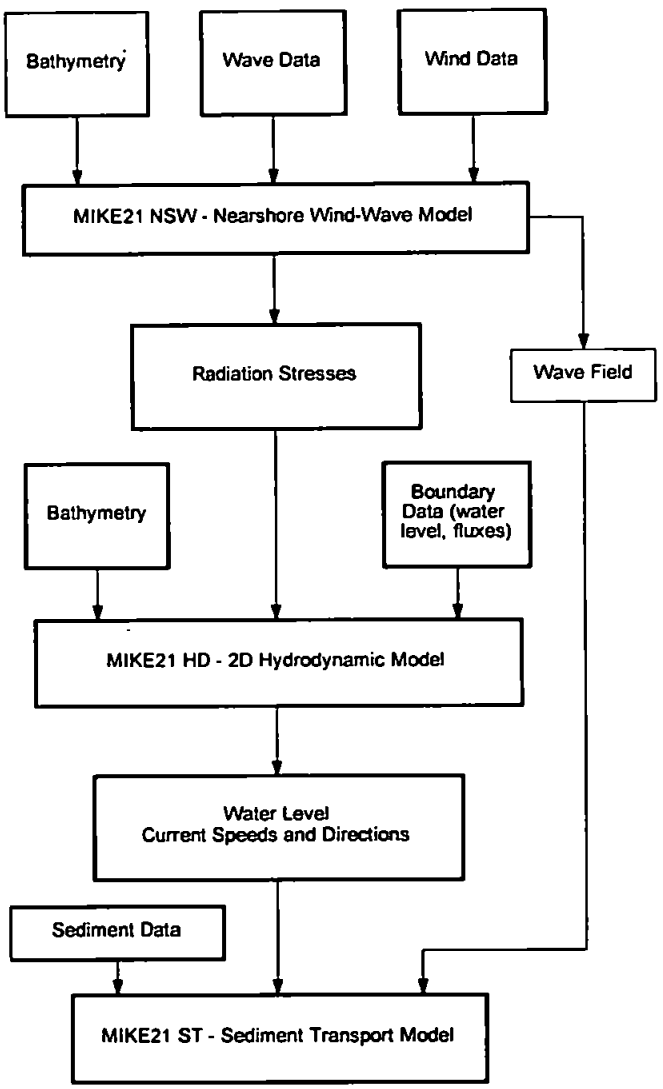

Figure 4.1. Interaction of MIKE21 ST with other modules of the MIKE21 system

4.2.1. Hydrodynamic module setup (HD)

4.2.1.1. Bottom schematisation

The definition of the model area bathymetry is one of the most important steps in the modelling process. The quality of the results will be directly related to the quality and resolution of the bathymetry applied to the model. Several sources of bathymetric data were used in the present set up:

a. HR Wallingford surveys made by m.v. Sir Claude Inglis during the COAST3D main experiment;
b. DGPS beach surveys of the intertidal zone;
c. data digitised from a survey chart of the estuary from 1979;
d. data digitised from Admiralty Chart 3155.

The coverage area of "a" and "b" is given in Chapter 3 (item 3.2.1.3) with details about their resolution. The digitised chart of the estuary (c) covers the whole estuary and is overlapped by the survey (a) at the lower estuary in the channel region. At regions where data is overlapped the most recent surveys are used ("a" and "b"). Data from "d" was used in order to cover the offshore region. The data from all sources was combined into a single database with bed level specified relative to Ordnance Datum Newlyn (ODN). In the MIKE21 bathymetry editor the bathymetric data was interpolated and converted into the model grid.

4.2.1.2. Grid resolution

With the available bathymetric data, two grids were designed for the Teignmouth region in order to nest the local model according to the available boundary conditions (as described in section 4.2.1.3):

a. The initial grid includes the whole area covered by the available bathymetric data, covering the entire estuary spanning 4 km in the offshore direction and 5.5 km in the alongshore direction (Figure 4.2a). The grid resolution is 25 m in the x and y directions

and is rotated 32 degrees anticlockwise, in relation to the true North, in order to accommodate the initial boundary conditions to the rectangular grid.

b. The final grid that is used in the modelling experiments represents the non-rotated bathymetry, and covers the entire estuary and an area of approximately 3.5 km seaward and 4 km alongshore, resulting in a total grid area of approximately 10 x 4 km (Figure 4.2b). The grid resolution is 10 m in the x and y directions, resulting in approximately 180,000 water points. This resolution was chosen according to the resolution of the bathymetric survey carried out at the nearshore region and also in order to get a balance between the bathymetry resolution and computer time, taking into account the Courant number (section 4.2.1.4).

c. An extended version of the final grid was also created in order to apply the water level only boundary conditions. In this case the north and south boundaries are closed and only water levels are applied at the offshore boundary. This version of the grid is used for the simulations were no flow boundaries are available. The extension is based on Admiralty Chart digitised data, adding approximately 1 km in the alongshore extension of the grid.

Model simulations with the "initial" grid are used to obtain the boundary conditions for the "final" grid, as described in the next sections.

4.2.1.3. Boundary conditions

For the calibration and validation period (COAST3D main experiment), boundary conditions are provided by a larger regional model, as applied by the numerical modelling teams in the COAST3D project[3]. These boundary conditions are derived from the DELFT3D Continental Shelf Model (CSM) and Lyme Bay Model (LBM) and were generated by nesting the LBM in the CSM.

The CSM is a hydrodynamic model for the entire North European continental shelf consisting of 18,050 grid cells with grid resolution of about 9 km. Due to its coarse grid resolution, it is not possible to obtain the boundary conditions for the local model directly. Therefore, a regional model covering the Lyme Bay was constructed. Using the water level

[3] The applied boundary conditions were provided by Dr Dirk-Jan Walstra (DELFT Hydraulics).

boundaries provided by the CSM, the LBM has a grid size of approximately 200 x 300 m in the Teignmouth area, including also the wind forcing in the simulations. Flow and water level conditions that fit the local model boundaries were extracted from this model and interpolated in order to adjust them to the 25 m grid resolution of the local model ("initial" grid).

The MIKE21 model with the "initial" grid was run for the whole period corresponding to the available boundary conditions (October – November 1999), and through the use of the MIKE21 toolbox ("Transfer Boundary") the boundaries for the "final" grid were extracted from this simulation. These boundary conditions (flow and water level) were interpolated and applied in the "final" grid simulations with the 10 x 10 m resolution. Table 4.1 summarises the boundary conditions used in the "final" model grid.

The transitions between land and water in MIKE21 HD are represented by closed boundaries (flow equal zero). At the open boundaries, regions that become dry at lower water levels are also considered "closed", since the model can not cope with "dry" open boundaries.

An additional set of experiments was conducted in order to assess the modelling quality using "closed" north and south boundaries. In these experiments, the water flux boundaries were defined through the use of the MIKE21 *wavcur* tool. This tool generates boundary conditions for the hydrodynamic model from the result of the wave module simulations. Wave-driven currents are incorporated in the boundary conditions by converting the radiation stresses calculated by the wave module into water levels and fluxes along the northern and southern limits of the model domain. In applying these extracted flow boundaries, longshore uniformity of the bathymetry and the wave conditions outside the model area is assumed.

In these "closed" hydrodynamic simulations, the boundary conditions are the offshore water level, fluxes and levels obtained from the wave simulation and the river discharge. The objective of these experiments is to assess the quality of the modelling results without the use of boundaries extracted from a regional model, allowing it to be applied at different periods with different morphological conditions.

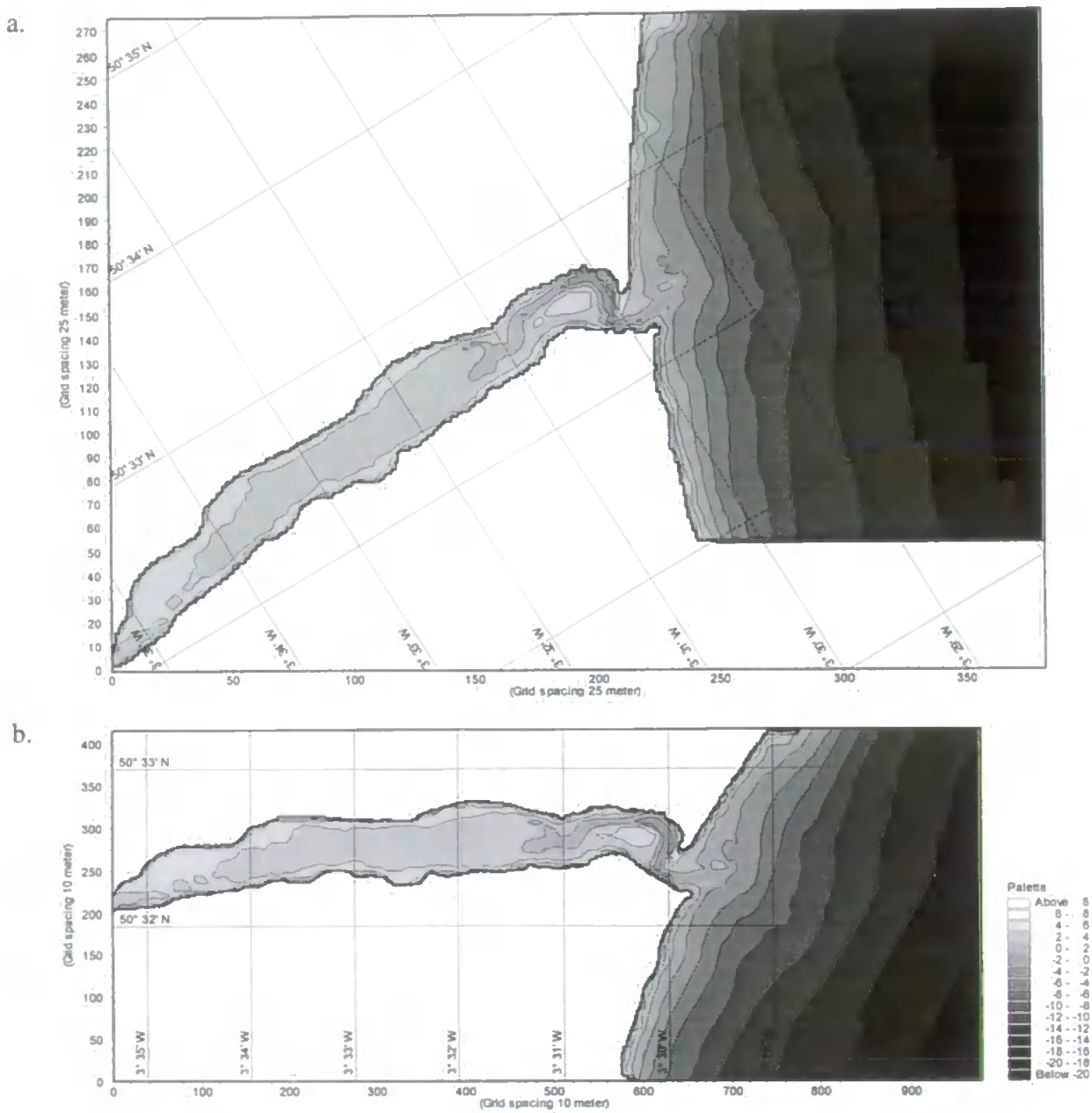

Figure 4.2. Model grid and bathymetry for the "initial" (a) and "final" (b) grid.

Table 4.1. Summary of the boundary conditions for the "final" HD simulation.

Boundary	Type	Start – End	Interval	Origin
North	flux ($m^3/s/m$)	25/10/99 - 25/11/99	10 min.	extracted from the "initial" simulation
South	flux ($m^3/s/m$)	25/10/99 - 25/11/99	10 min.	
East	water level (m ODN)	25/10/99 - 25/11/99	10 min.	
West	flux (river discharge – m^3/s)	16/10/99 - 25/11/99	15 min.	measured

4.2.1.4. Numerical and physical parameters

Time step: The size of the time step defines the computation time of the model run and its ideal size should be defined in order to balance the computer time and accuracy and stability of the model. An indication of the required time step is given by the Courant number, which is a relation between the celerity, time step and grid size:

$$C_R = c\frac{\Delta t}{\Delta x} \tag{4.1}$$

where c is the celerity, Δt the time step and Δx the grid spacing. For a tidal wave the celerity is:

$$c = \sqrt{gh} \tag{4.2}$$

where g is gravity and h is the water depth. As the information (about water level and fluxes) in the computational grid travels at a speed corresponding to the celerity, the Courant number actually expresses how many grid points the information moves in one time step. The MIKE21 HD module is designed for Courant numbers up to about 20, but high values should only be allowed in areas where the bathymetry is smooth (DHI, 2000a). Recommended Courant number values for the MIKE21 HD should not exceed 8 to 10. In this application the time step was defined as 10 s for most applications, resulting in a Courant number of about 5.

Warm-up period: In order to avoid initial disturbances derived from the unknown initial conditions, a warm-up period was defined for the simulations. The warm-up period is a defined number of time steps over which the forcing functions are gradually increased from zero to 100 % of their value. Additional disturbances of flooded dry points are also avoided by starting the simulations at high water, when flow velocities are low and the number of dry points in the model domain is at its minimum.

Coriolis effect: The Coriolis term is included in the HD simulations and is a function of the latitude of the model domain, which is defined when creating the model grid.

Bed resistance: For the HD module, the bed resistance was defined in Chézy numbers and varying across the model grid. The used Chézy numbers were defined as a function of water depth and are one of the main calibration factors of the model. The values used are discussed in section 4.4 (Calibration and Validation).

Eddy viscosity: The used eddy viscosity formulation in this application is the velocity based formulation (see Appendix I for details). Values of the eddy viscosity were also defined as varying across the grid, and the used values are given in section 4.4.

Wave radiation stresses: The wave radiation stresses can be included in the hydrodynamic simulations. In this case, the radiation stresses field for each time-step given by the NSW module (section 4.2.2) is used as input in the HD module.

The outputs of the MIKE21 HD module are fluxes and levels inside a model sub-area and at a frequency selected as appropriate to the varying studies being addressed.

4.3.2. Nearshore Spectral Wind-Wave module setup (NSW)

The NSW module operates over the same bathymetry and grid spacing than the one used in the HD module. As described in the NSW module description (Appendix I), the nonlinear algebraic equations in NSW are solved using a once-through marching procedure in the x-direction. Therefore, the boundary conditions in terms of wave parameters need to be defined at the offshore boundary (x=0). To adjust the Teignmouth grid to these requirements, it is rotated 180 degrees from North. The basic data necessary to fulfil the offshore requirements are the significant wave height (H_{m0}), mean wave period (T_m), mean wave direction (*MWD*), and the directional standard deviation (*DSD*). This boundary is defined with the measured wave data covering the whole simulation period with a temporal resolution of one hour. In this case the wave data used as the offshore boundary is originated from the measurements at depth of about 10 m (measurement point 07 Chapter 3).

The lateral boundary conditions (model north and south boundaries) can be chosen as symmetrical or absorbing. In the case of symmetrical boundary the derivatives normal to the boundary of the dependent variables, the zeroth and first moment of the action, are set equal to zero. Basically, this means that the contours are locally straight and parallel near the boundary. In the absorbing boundary, the incident waves at the boundary are fully absorbed. At the downwave lateral boundary, incident waves propagate out of the model without any reflection, while at inflow lateral boundary no waves can propagate into the model area. Different tests were carried out to define which option of lateral boundaries would be the most appropriate in this study. As the interest area lies well inside the model grid, these tests showed that there was no difference between using symmetrical or absorbing boundary conditions.

The numerical scheme applied in the modelling exercises was the "upwind differencing" (UD). This is a first order scheme with inherent numerical diffusion in the discretization of the convective terms in the y- and θ-direction. This numerical scheme is recommended if the purpose of the wave modelling is to obtain radiation stresses for the application in the HD module (DHI, 2000b).

Bottom dissipation in the NSW module is given by the Nikuradse roughness parameter (k_N) and in this application it was defined as variable over the model area. The bottom friction in areas dominated by sand depends on the grain size of the sediment and the presence of bed forms (Nielsen, 1979 and Roudkivi, 1988). For the case where there is no bed form, the Nikuradse roughness parameter can be estimated by (Nielsen, 1979):

$$k_N = 2.5 \cdot d_{50} \tag{4.3}$$

where d_{50} is the median grain size. In the presence of ripples k_N can be much larger and should be estimated including the ripple characteristics. Based on the sedimentary characteristics of the studied region the preliminary k_N parameter was calculated according to Equation 4.3. Afterwards, according to the presence of bedforms, the parameter was adjusted and also used as a calibration factor. This adjustment to the presence of bedforms is based on side scan sonar surveys of the area of interest during the COAST3D main experiment (Van Lancker et al., 2001). It is close to the main channel region that the

surveys show the presence of ripples and megaripples (with typical wave length of 1 m), while the remaining of the region is generally devoid of bedforms. Values of the Nikuradse roughness parameter (k_N) can be much higher for sheet flow conditions, however these situations were not included in the modelling experiments.

As the modelled area is in a macro-tidal region, correct surface elevations will ensure that the changes in wave conditions due to varying water depths are properly modelled. Tests were carried out using a constant surface elevation variation across the model grid using a water level time series as input and also using the result of the hydrodynamic simulations as input for the water level in the wave simulations (two-dimensional map). In the second case the variable water level across the region is also considered. Water levels used for the wave simulations were the same as the boundary conditions for the hydrodynamic simulations.

Values for the three wave breaking constants were used as suggested in MIKE21 NSW scientific documentation. The default value for γ_1 is 1.0, as suggested by Holthuijsen et al. (1989), while for α and γ_2 the default values are those used by Battjes and Janssen (1978).

The basic type of data outputs from a NSW simulation are the four integral wave parameters (H_{sig}, T, dir, DSD), the x- and y-components of the vector showing the mean wave direction, the three radiation stresses (S_{xx}, S_{xy}, S_{yy}) or a combination of these three types of output over a selected output area.

4.3.3. Sediment Transport module setup (ST)

As described in item 4.2.3 and shown schematised in Figure 4.2 the sediment transport (ST) module uses as input the result of hydrodynamic (HD) simulations or a combination of HD and wave (NSW) simulations. This is defined in the simulation type, when it is specified whether the simulations of non-cohesive sediment transport will be due to pure current or waves and currents in combination.

The HD input data file needs to contain three items (water levels and fluxes in the x and y directions), and the grid spacing in the transport simulations is identical to that grid spacing used in the HD simulation. The sub-area and simulation period for the ST simulation are specified relative to the model grid used in the HD simulation. The wave input data must contain the wave height, period and direction, required for the calculation of transport rates.

The bed resistance used in the ST module is the same then in the HD module, with Chézy numbers varying across the model grid according to the water depth. The sediment data to be used in the sediment transport computations was also specified as spatially varying, according to the data from sediment samples (Chapter 3). The bed material is characterised through a map of the median grain size (d_{50}), and the geometric standard deviation (σ_g) distribution. As described in section 4.2.3 both transport formulations for combined waves and currents available in MIKE21 ST are applied. The output data obtained from a MIKE21 ST simulation are averaged sediment transport rates and initial rates of bed level change (over the simulation period), and time series of transport rates over chosen time intervals. These results are saved within the previously selected sub-areas.

4.4. Model Calibration and Validation

In order to apply a numerical model as a valid research tool, it needs to be calibrated and validated against measured data. This section contains the description and discussion of the calibration and validation process carried out to evaluate the application of the MIKE21 model to the Teignmouth estuarine inlet.

There is no standard procedure for model calibration and validation in the modelling literature (Cheng et al., 1991). Typically, calibration and validation is accomplished by qualitative comparison of short time-series of water level or velocity produced by the numerical model with field data for the same location and for the same period of time (Cheng et al., 1993). According to Dyke (1996, 2001) the validation of a model is the comparison of model output with what can be termed current knowledge. This knowledge comes from *in situ* measurements of the compared parameters. However, a series of factors

needs to be taken into account when comparing model outputs to those obtained from measurements. These include the accuracy of the measurements (instrument calibration and reliability), the measurement location, which may not be precisely the same as the model grid points, and the fact that the model provides vertically averaged values while measurements are taken at one or more depths of the water column. At the present application, calibration is considered the process of adjusting the model in order to obtain calculated results that best reproduce the measurements and validation is the application of these "tuned" model over different periods of time in order to verify its validity. Validation is a continuous process throughout the entire model application, by comparing the output with measurements and with the system's observed behaviour.

In the calibration and validation description, the hydrodynamic simulations include the computed wave radiation stresses, so that these simulations reproduce more realistically the observed data.

4.4.1. Calibration

In this study, comparison of water levels and time-averaged current velocities (averaged over 10 minutes) measured at a number of stations deployed during the COAST3D main experiment with the model predictions form the basis for the calibration and validation. Qualitative analysis of time series provides a general assessment of the model performance, and was carried out for different pre-defined simulation periods. A more quantitative verification method was also applied through the use of the relative mean absolute error (RMAE) (Sutherland et al., 2001; Van Rijn et al., 2003), described in the next paragraph.

Statistics representing averages of appropriate quantities, such as RMAE are based on the mean absolute values of measured and predicted current vectors and by the mean absolute error. The mean absolute value of the measured (X) and predicted (Y) values are given by:

$$MAX = \langle |X| \rangle \tag{4.4}$$

and

$$MAY = \langle |Y| \rangle \tag{4.5}$$

where the angled brackets denotes an average and $|X|$ and $|Y|$ is the modulus of X and Y respectively. The mean absolute error is:

$$MAE = \langle |Y - X| \rangle \tag{4.6}$$

As discussed in Sutherland et al. (2001), the use of the modulus makes the statistic non-analytic and thus more difficult to work with than using a root-mean-square error (RMSE). However the MAE is not as heavily influenced by outliers as RMSE and it is equally applicable to vector and scalar quantities. The MAE includes errors in mean, phase, amplitude and directions.

The quality of the modelled results is then given by the relative mean absolute error (RMAE):

$$RMAE = \frac{\langle |Y - X| - ME \rangle}{\langle |X| \rangle} \tag{4.7}$$

where ME is the measurement error.

A perfect match between measurements and model results would be obtained with a RMAE value of zero. However, this will never be achieved as the RMAE includes contributions from the measurement error. As the RMAE is derived from the ratio of two quantities it is highly sensitive to small changes in the numerator when the denominator is small.

As described in Chapter 3, the average current velocity and wave height measurement errors are 0.05 m s^{-1} and 0.1 m respectively (Van Rijn et al., 2000). The absolute difference of the computed and measured values minus the measurement error cannot be smaller than zero (e.g. $|Y - X| - ME$ is set to zero, if <0). It means that the computed value is within the error band range of the measured value (Van Rijn et al., 2003). Table 4.2

gives the qualification of model performance proposed by Van Rijn et al. (2003) as being a tough set of standards for models to achieve.

As with any statistics the inherent variability of the statistics reduces as the number of samples increases. Sutherland et al. (2001) recommended that 100 samples or more are used whenever possible. Therefore, in this study, for each two-day calibration period, RMAE calculations were made with a minimum of 100 samples.

Table 4.2. Qualification of RMAE ranges for velocity and wave heights comparison according to Van Rijn et al. (2003).

Qualification	Velocity	Wave height
Excellent	< 0.1	< 0.05
Good	0.1 – 0.3	0.05 – 0.1
Reasonable/fair	0.3 – 0.5	0.1 – 0.2
Poor	0.5 – 0.7	0.2 – 0.3
Bad	> 0.7	> 0.3

The main calibration factors are the bed resistance (Chézy numbers – $m^{½}s^{-1}$) and the eddy viscosity (m^2s^{-1}), whose importance was assessed through a series of sensitivity tests which were initially carried out.

Two calibration periods (CP1 and CP2) were defined within the COAST3D main experiment period: from 25/10/99 to 27/10/99 (CP1) and from 10/11/99 to 12/11/99 (CP2). Both periods are during spring tide conditions, the first one being during low wave conditions and the second one during storm conditions (Figure 4.3).

During the calibration process, combinations of different values of bed resistance and eddy viscosity were applied and their results assessed through time series comparisons and RMAE values. Each parameter was adjusted separately, with the eddy viscosity kept constant while the bed resistance was adjusted and vice-versa. The calibration was started using realistic Chézy numbers derived from the Nikuradse roughness parameter, with small adjustments being made during the calibration procedure. An example of the sensitivity of

the modelled flow velocities to different values of Chézy numbers in terms of the quality of the modelled results (RMAE values) is shown in Figure 4.4. The sensitivity test showed that the optimal model output in relation to the Chézy numbers is depth dependent. Although sensitivity varies from station to station, the best results in terms of RMAE are represented by values around 38 $m^{1/2}s^{-1}$ at stations located in deeper regions (e.g. stations 14, 24, 26 and 9 in Figure 3.6) and values of around 34 $m^{1/2}s^{-1}$ in shallow areas (e.g. stations 28 and 25 in Figure 3.6). Based on this sensitivity analysis the Chézy numbers were defined as varying across the model domain, with lower resistance values at deeper regions and higher at shallow regions. Only the best combination of calibration factors, resulting in the most accurate reproduction of the *in situ* measured conditions, is described and discussed in this section.

The best combination of depth varying resistance coefficients (Chézy numbers) during the calibration process is given in Table 4.3. A coefficient value was assigned to each of several depth ranges with the most friction in the shallows and the least friction in the deepest areas. The set of coefficients was adjusted as a group until time series plots of measurements and predictions agreed satisfactorily and RMAE reached the lowest possible values. This final set of Chézy numbers is overall realistically correlated with the Nikuradse roughness parameter calculated for the area by Eq. 4.3 (page 60). Despite the fact that eddy viscosity values do not have the same influence in the calibration as the bed resistance, they are important throughout the calibration process. Values of eddy viscosity were also defined as varying across the modelled area, with values of 0.16 m^2s^{-1} inside the estuary and values of 0.5 m^2s^{-1} in the offshore region.

a

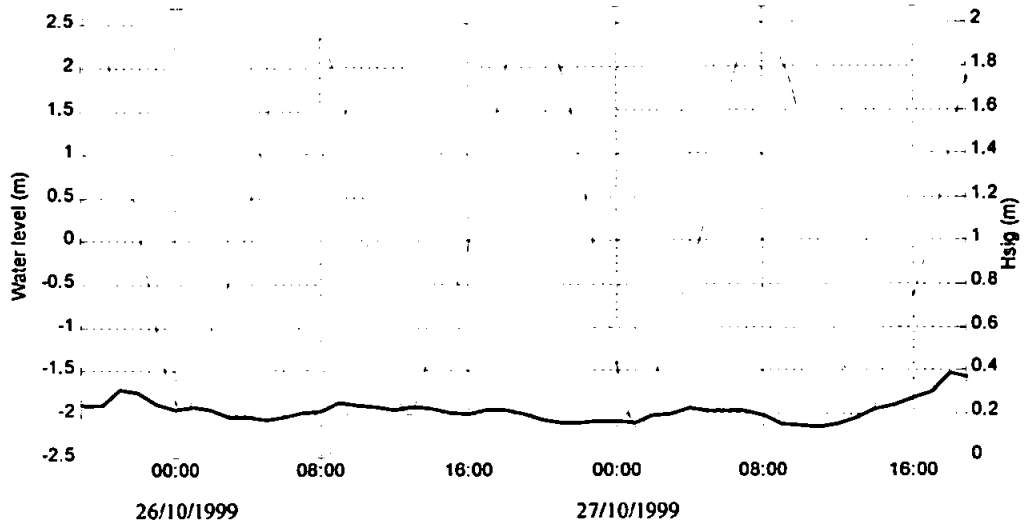

b

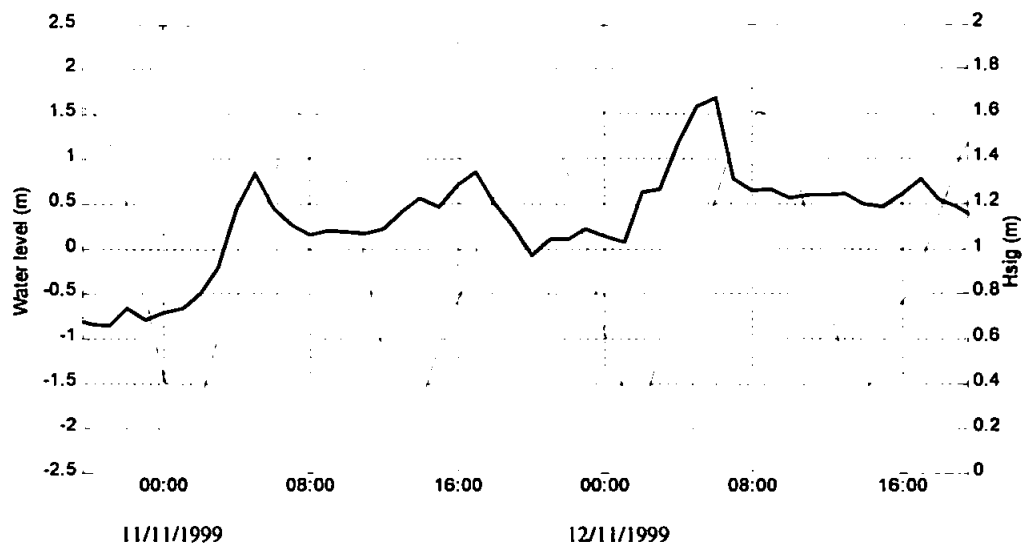

Figure 4.3. Water level and wave height during each calibration period. a) 25/10/1999 18:50 – 27/10/1999 18:50; b) 10/11/1999 19:40 – 12/11/1999 19:40.

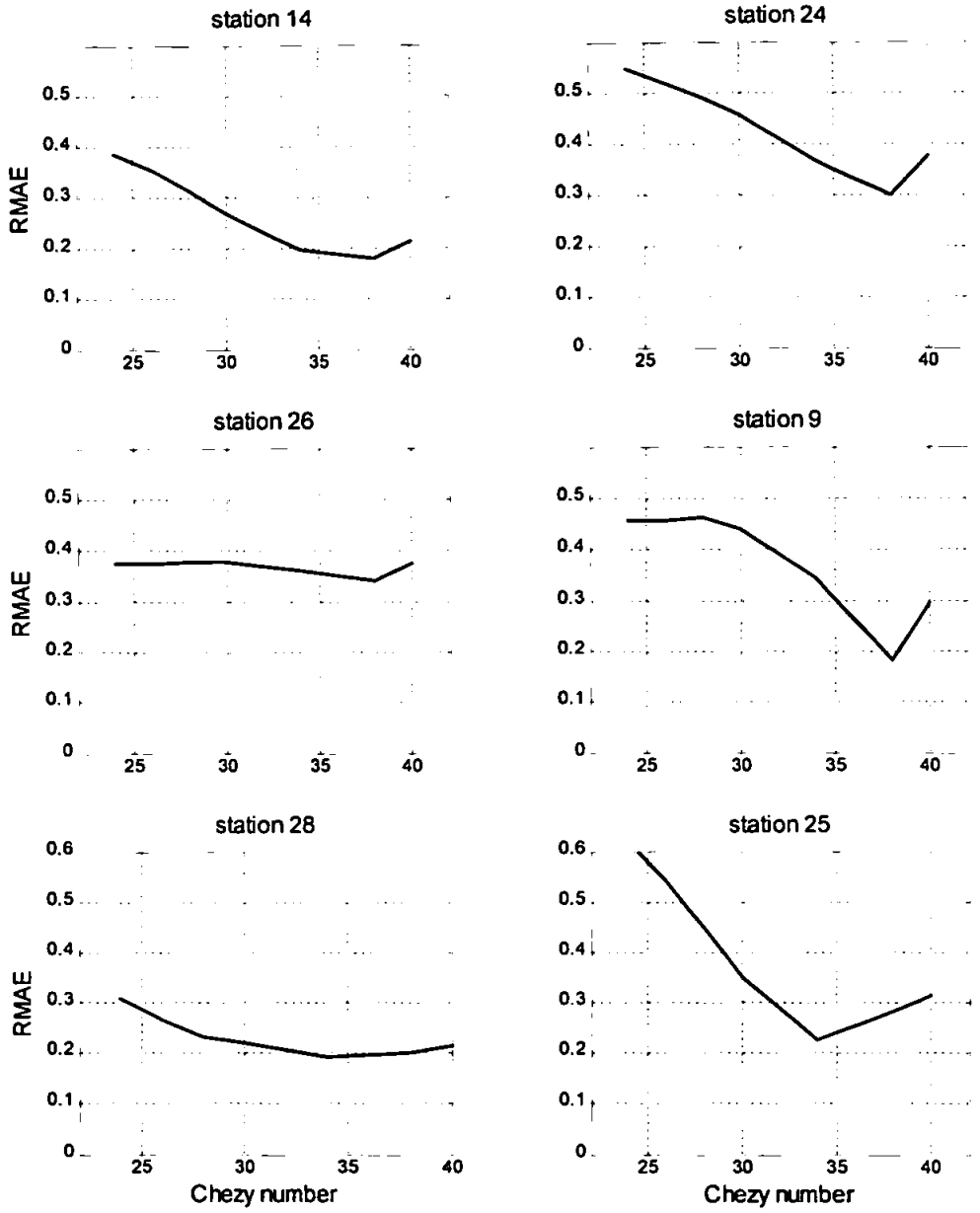

Figure 4.4. Sensitivity of the RMAE values for the flow velocity components according to the Chézy numbers ($m^{1/2}s^{-1}$).

Table 4.3. Depth varying Chézy numbers.

Depth (m ODN)			Chézy numbers ($m^{1/2}$ s^{-1})
	H	< -3	38
-3 <	H	< -1	34
-1 <	H	< 1	32
1 <	H		30

The model calibration and validation is assessed with the use of time series and statistic parameters. Figures 4.5 to 4.12 show the plots of measured and modelled data for some of the most relevant stations (within the area of interest) with available measured data. These figures show plots of time series of measured and modelled water levels or currents for northerly and easterly components. Scatter plots of observed and predicted currents showing the northerly component of current plotted against the easterly component are also shown, indicating whether the modelled and measured currents present a similar distribution. Linear regression analyses of predicted (y-axis) against observed (x-axis) current components are also plotted for each station. Statistical parameters for water level and currents for each calibration period are shown in Table 4.4 and 4.5 (page 80) when more than 100 samples of measured data are available and are shown for all the compared stations. Both calibration periods are described and discussed together in this section, being compared whenever possible. Calibration parameters were the same for both periods.

The model reproduces well the water level and the overall circulation patterns at the compared positions in the area of interest, with low RMAE values for the compared time series. Water level time series corresponding to the pier (offshore) and harbour (in the estuary) are compared and shown with the respective residuals in Figures 4.5 and 4.6 for each period. The model reproduces the phase and amplitude of the tidal wave excellently. Agreement of the offshore water level is virtually perfect, with maximum residuals of about 0.05 m offshore with MAE of 0.013 m and 0.015 m for CP1 and CP2 respectively. Water level in the estuary (harbour) presents maximum residuals of 0.1 m during calm conditions (CP1) and 0.2 m during storm conditions (CP2). Harbour MAE values of 0.048 m and 0.091 m were obtained for CP1 and CP2 respectively. RMAE values obtained during both calibration periods were very low (Table 4.4) showing an overall excellent agreement between measured and modelled water levels. Linear regression analysis between measured and modelled water levels result in r^2 larger than 0.99 for all cases.

For several reasons the same degree of agreement cannot be achieved between measured and modelled currents as for the case of water levels. In the present study these reasons include mainly the model grid resolution (10 x 10 m) that at some points may not cover smaller-scale bathymetric features or hydrodynamic patterns of the complex environment, and errors originated from measurements (as discussed in Chapter 3).

The overall agreement in the comparison of current velocity components indicates that the model predicts the general measured phenomena, with some differences in magnitudes. A subjective analysis of the time series comparing measured and predicted northerly (y-velocity) and easterly (x-velocity) current components represented in Figures 4.7 to 4.12 shows that the model reproduces the main features measured *in situ*. However, some of the precise details and magnitudes of the currents are not always modelled correctly, as discussed below for each of the compared stations. The statistical parameters that provide an objective judgement of the model are shown in Table 4.5 for all the compared stations.

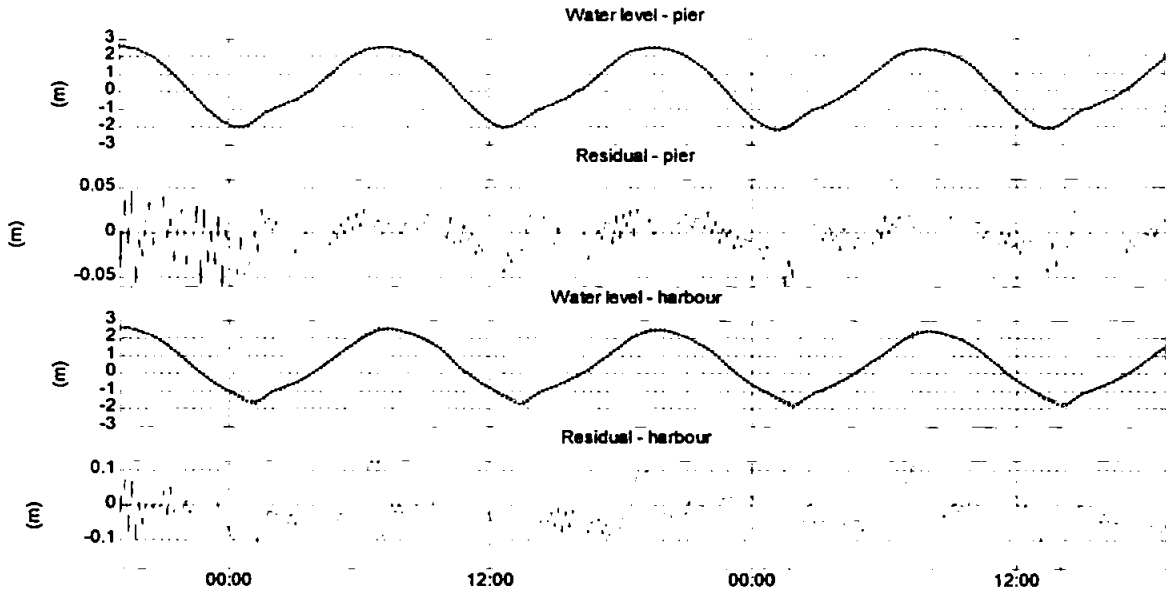

Figure 4.5. Time series of measured (dotted line) and predicted water level (solid line) with respective residual values for the calibration period 1 (25/10/1999 18:50 – 27/10/1999 18:50).

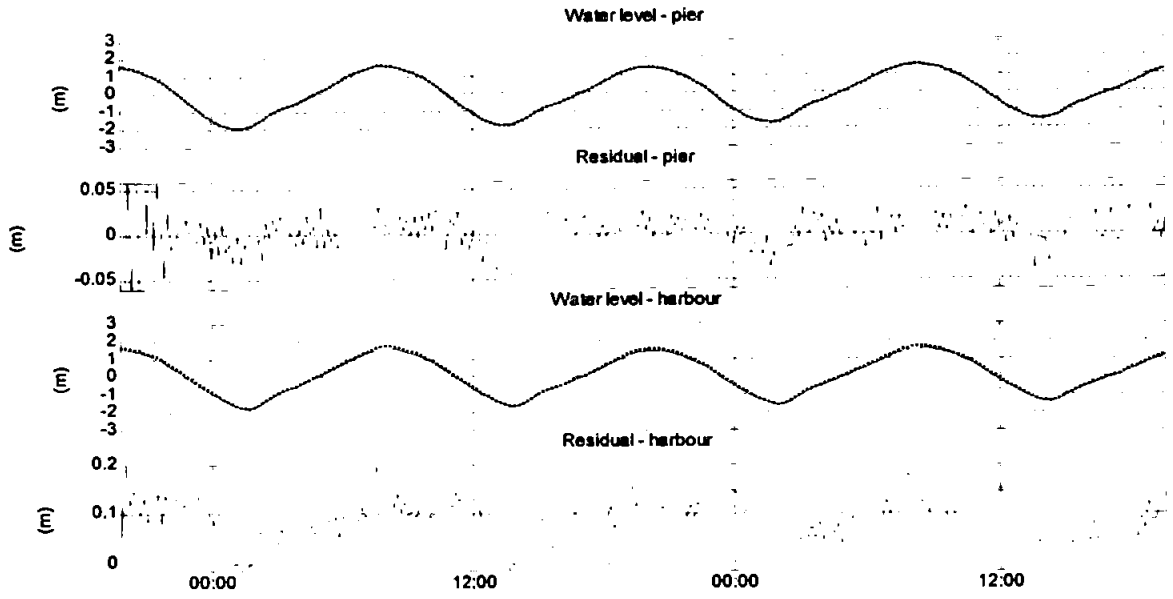

Figure 4.6. Time series of measured (dotted line) and predicted water level (solid line) with respective residual values for the calibration period 2 (10/11/1999 19:40 – 12/11/1999 19:40). RMAE pier: 0.0133; RMAE harbour: 0.099.

Figures 4.7 and 4.8 compare measured and modelled currents at station 14 for CP1 and CP2 respectively. Station 14 is located just outside of the sandbar system, being under the influence of the secondary channel that crosses the sandbars (Figure 3.6). Time series show a general good agreement for calm conditions (CP1), when the model only underestimates the northerly velocities. Scatter plots show similarity between measured and predicted currents and the linear regression between measured and calculated currents gives r^2 values of 0.84 and 0.86 respectively for x and y-velocities. Low values of RMAE confirm the good agreement between modelled and measured currents (Table 4.5). The same reproduction is not seen during CP2, when the presence of waves increases the eastward currents and decreases the northward currents. The model represents the main features of the current patterns but mainly the easterly currents are underestimated, as shown also in the scatter plots of measured and modelled current components. Correlation in the linear regression analysis decreases mainly for the east component of the currents during storm conditions. The RMAE value gives a reasonable/fair qualification of the model (Table 4.5).

Station 24 is in a similar position to station 14, but just inside the secondary channel that crosses the sandbar system (Figure 3.6). Figures 4.9 and 4.10 show the plots for CP1 and

CP2 at station 24. During CP1 the general features of the measured current components are reproduced by the model with some underestimation of the northwards currents, which can be seen in the time series plots and in the scatter plots. During CP2, as for station 14, the presence of waves in the model cause an underestimation of the cross-shore velocities (x-velocity). Scatter plots of measured and modelled current components show that the overall current pattern is well reproduced. According to the qualification proposed by Van Rijn et al. (2003), values of RMAE show a reasonable/fair qualification of the modelled currents at this location.

Measured data for station 28 is available only for part of the CP1 (Figure 4.11). This station is just outside the Ness sandbar (Figure 3.6). Time series and scatter plots show that the overall current climate is being reproduced, with some differences in the *y*-velocity magnitudes. Here, the current velocities are low increasing the importance of the measurement errors, favouring low RMAE values. A good agreement is given by the RMAE value (Table 4.5).

Station 25 is located at the inlet channel border of the Sprat Sand, an area that dries out during low tide conditions (Figure 3.6). In the model this point also dries out during virtually the same periods (straight dropping lines in the time series). Sufficient measured data for comparison is available only for CP2 and is shown in the plots of Figure 4.12. All plots of Figure 4.12 show that the model reproduces well the currents at this point. The RMAE value shows a good agreement between measured and modelled currents (Table 4.5).

Stations 5, 9, 26 and 33 are located in the outer region relative to the sandbar system (Figure 3.6). As these stations are not inside the region of interest, only their statistical parameters are shown (Table 4.4). At these outer points the current velocity components are small, with maximum velocities reaching 0.3 m s^{-1}. In general, the modelled currents reproduce well the measured flow patterns at the outer region as shown by the low RMAE values (Table 4.5). At these stations the correct current climate is being modelled, with some differences in magnitudes during individual events. However, even some differences in individual events are less important due to the relatively high influence of the measurement errors (0.05 m s^{-1}) in the low current values. Quality of the modelled results

for these locations varies from excellent (CP1 station 33, CP2 station 5) to poor (CP2 station 33).

Using the RMAE qualification ranges proposed by Van Rijn et al. (2003), the averaged RMAE values of all the compared stations (for current velocities) result in a good (0.25) modelled result during calm conditions (CP1) and reasonable/fair (0.35) result during stormy conditions (CP2). Considering that the proposed qualification ranges are based on a tough set of standards (Van Rijn et al., 2003), the calibration of the applied hydrodynamic module of the MIKE21 model can be considered well calibrated, providing reliable results under different forcing conditions.

Experiments for the same calibration periods using the "closed" north and south boundaries (as explained in section 4.2.1) with the use of flux boundaries extracted from the wave simulations result in only small differences when compared to the use of flux boundaries derived from the regional model. The modelled water levels present the same RMAE values of the ones obtained through the use of flux boundaries, showing an excellent agreement with the measurements. For the current velocities, in general results give similar RMAE values for the compared individual stations and for the average over each calibration period. The main differences are registered at the offshore stations (26 and 33) where the tidal currents are underestimated when "closed" boundaries are used. At the inlet and adjacent nearshore region the currents are still well reproduced by the model when the closed boundaries are used. Average RMAE values (0.35 for CP1 and 0.45 for CP2) result in a reasonable/fair classification of the current velocity results.

Based on the modelled wave parameters output of the NSW module, the measured and modelled waves are compared for the CP2, during the storm with significant wave heights of up to 1.8 m. Since during CP1 the significant wave heights are small (around 0.2 m), the comparison between measured and modelled are not shown, but were also well reproduced by the model. In Figure 4.13 three locations of measured wave heights and wave periods, with one of them including measured wave directions are compared with the modelled results. The most offshore location compared is the station 7 (Figure 3.6) at around 7 m depth (Figure 4.13a). Station 4 is located northwards of the inlet channel at around 5 m depth (Figure 3.6) and is compared with modelled results in Figure 4.13b. The most onshore wave comparison is made for station 25, which is located in the intertidal

region at the margin of the main inlet channel (Figure 3.6 and Figure 4.13c). The comparison plots show that the model reproduces well the measured wave parameters, with only small deviations being observed in wave heights, wave periods, and for station 7, wave direction. Statistics comparisons through the use of the RMAE shows that the model reproduces the significant wave heights with an excellent agreement (according to the qualification ranges proposed by Van Rijn et al., 2003 – Table 4.2), with values being lower then 0.03 for all compared stations (Table 4.6).

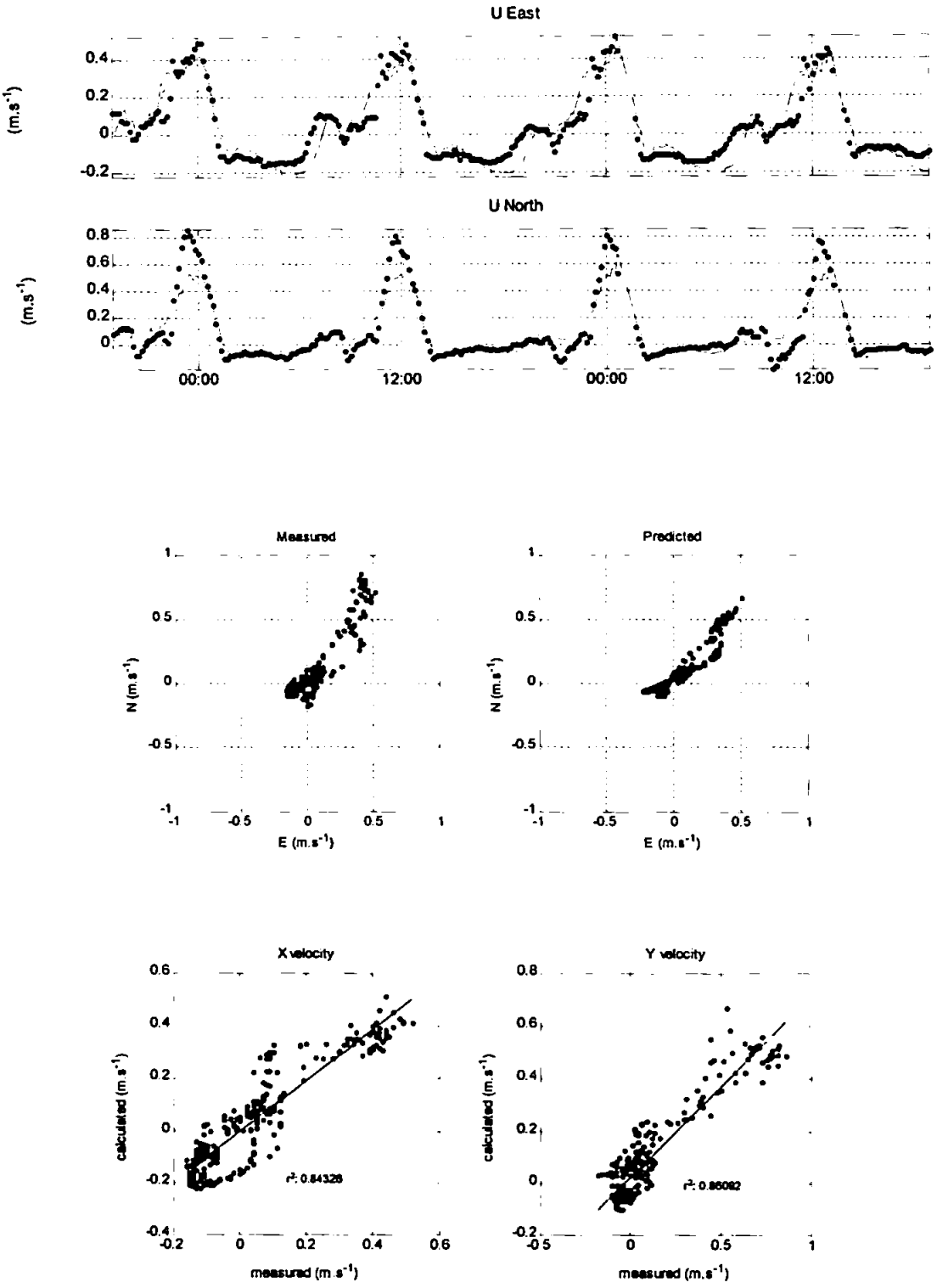

Figure 4.7. Station 14, CP1. Upper panel: Time series of flow velocities; measured (dots) and predicted (lines). Middle panel: scatter plots of measured and predicted velocity components. Lower panel: Linear regression between predicted and observed velocities.

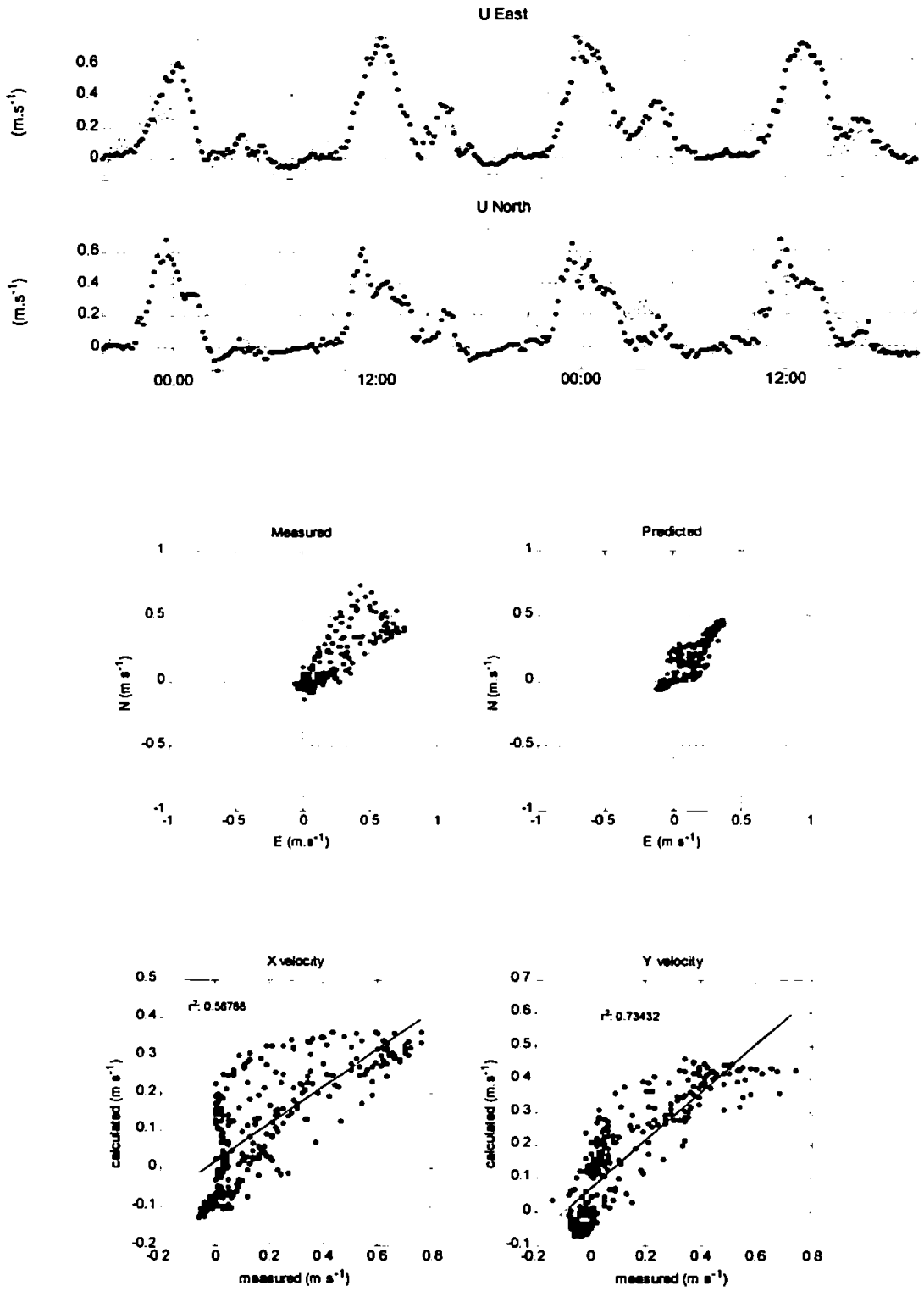

Figure 4.8. Station 14, CP2. Upper panel: Time series of flow velocities; measured (dots) and predicted (lines). Middle panel: scatter plots of measured and predicted velocity components. Lower panel: Linear regression between predicted and observed velocities.

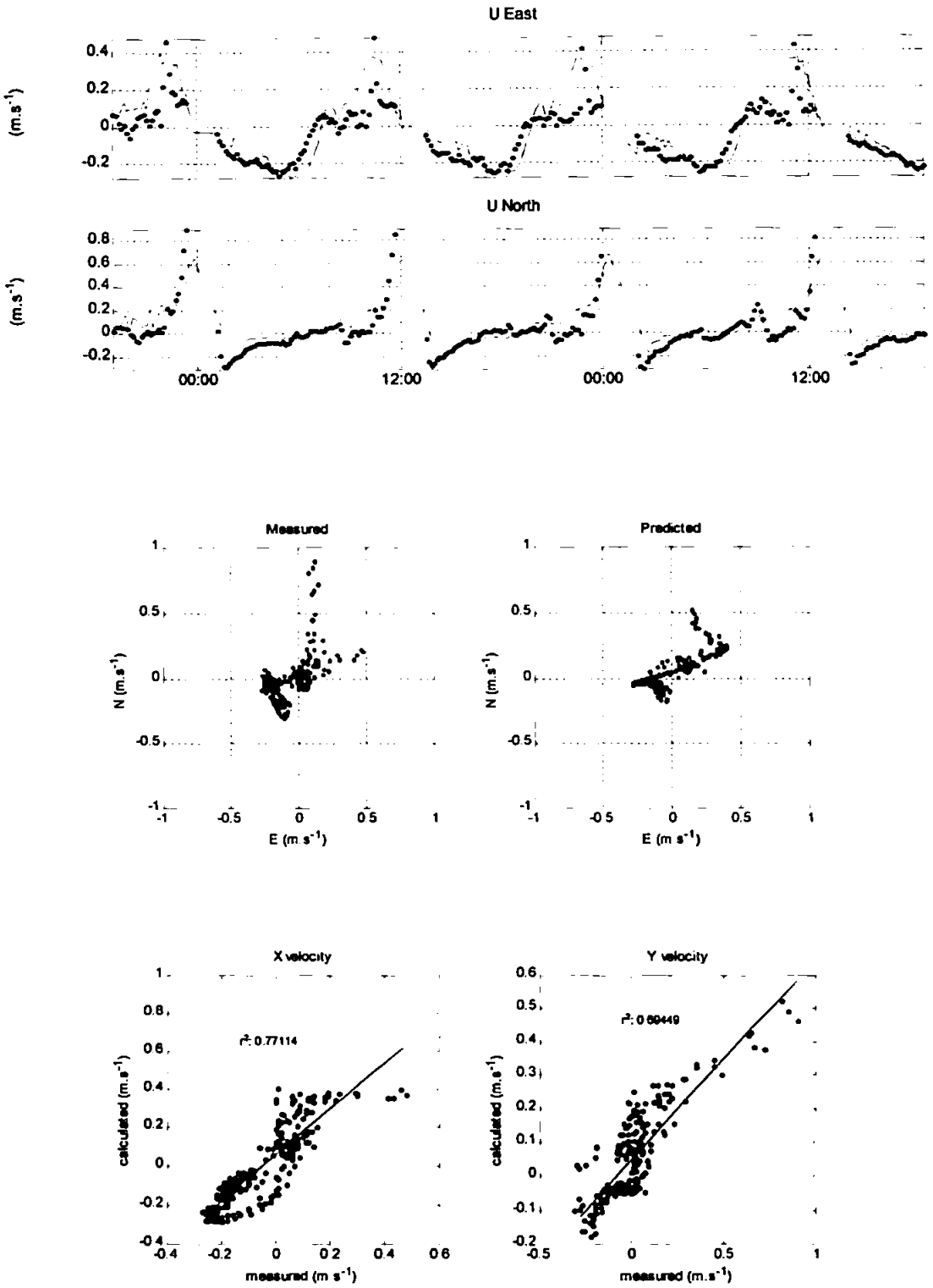

Figure 4.9. Station 24, CP1. Upper panel: Time series of flow velocities; measured (dots) and predicted (lines). Middle panel: scatter plots of measured and predicted velocity components. Lower panel: Linear regression between predicted and observed velocities.

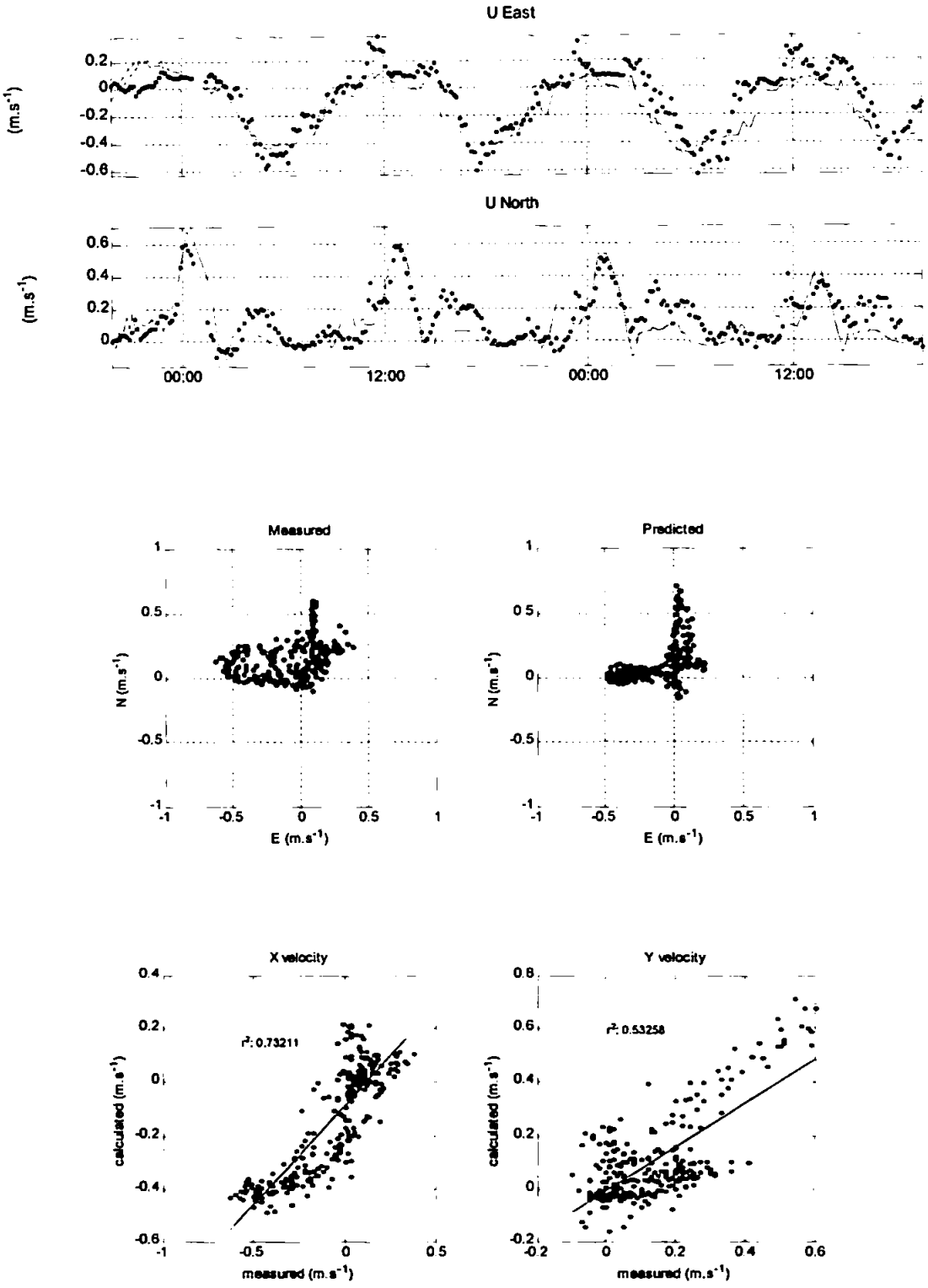

Figure 4.10. Station 24, CP2. Upper panel: Time series of flow velocities; measured (dots) and predicted (lines). Middle panel: scatter plots of measured and predicted velocity components. Lower panel: Linear regression between predicted and observed velocities.

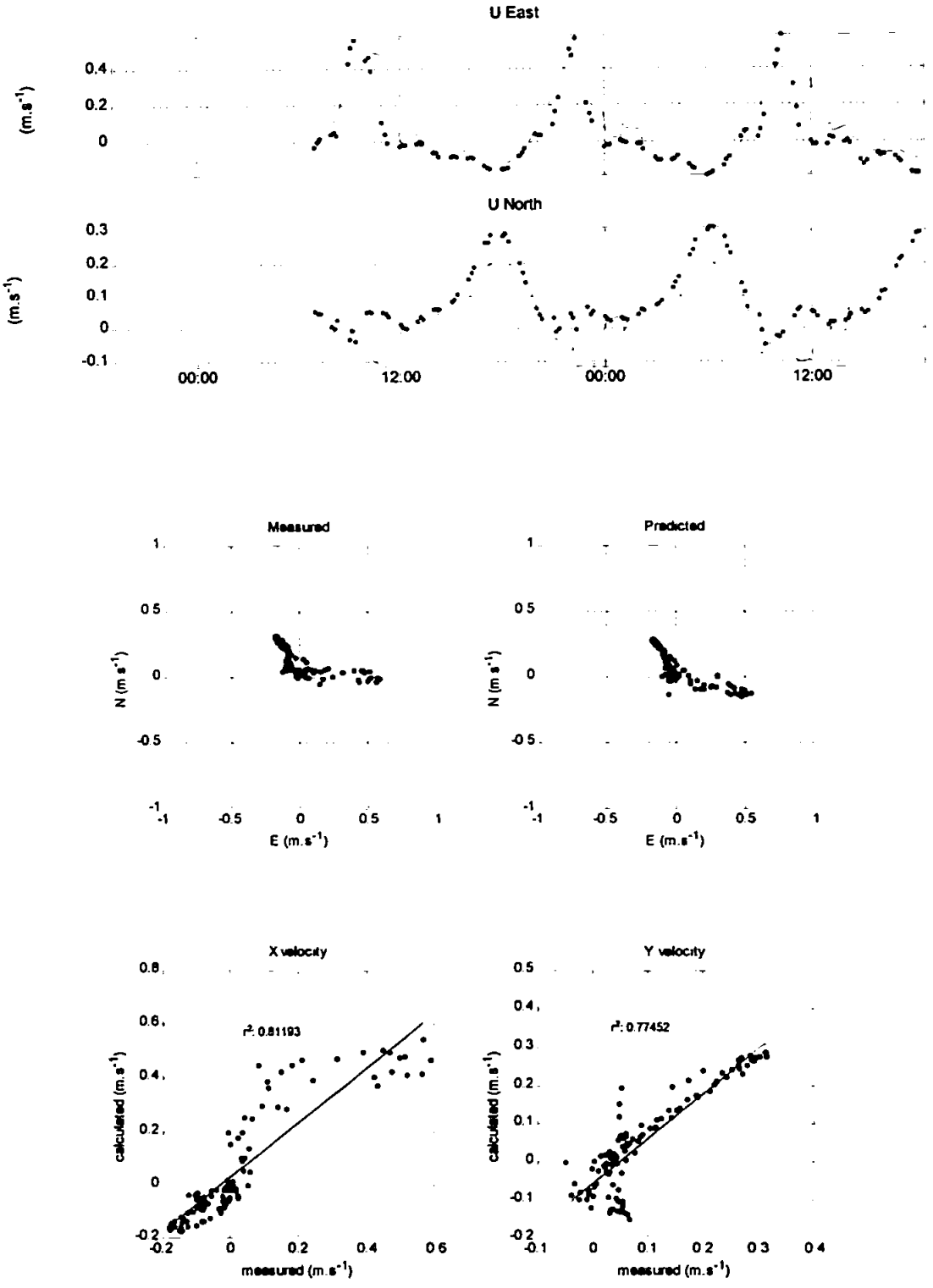

Figure 4.11. Station 28, CP1. Upper panel: Time series of flow velocities; measured (dots) and predicted (lines). Middle panel: scatter plots of measured and predicted velocity components. Lower panel: Linear regression between predicted and observed velocities.

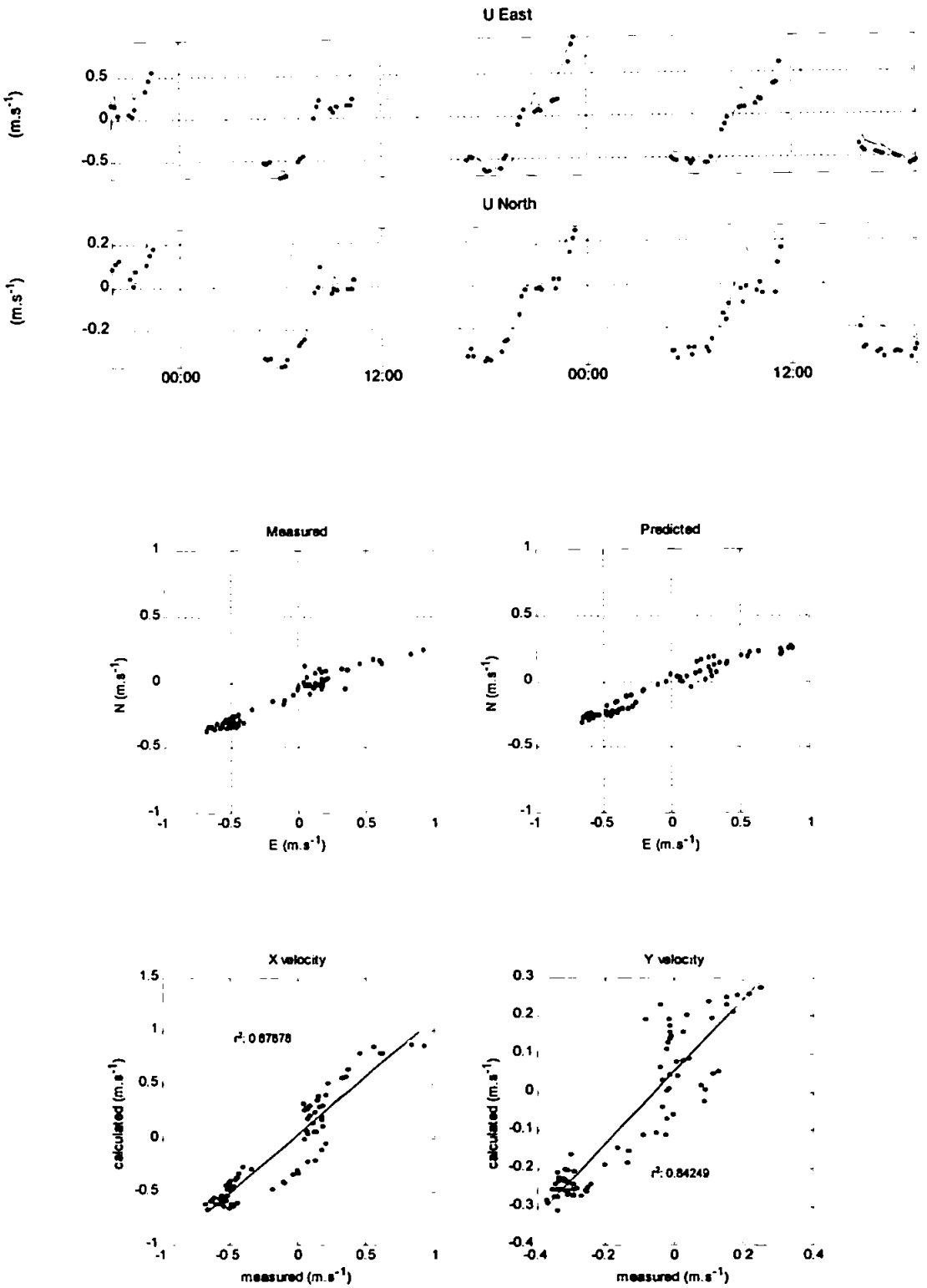

Figure 4.12. Station 25, CP2. Upper panel: Time series of flow velocities; measured (dots) and predicted (lines). Middle panel: scatter plots of measured and predicted velocity components. Lower panel: Linear regression between predicted and observed velocities.

Table 4.4. Statistical parameters for the water level at the pier and harbour for both calibration periods.

	Station	$\langle\|X\|\rangle$	$\langle\|Y\|\rangle$	MAE	RMAE
Calibration Period 1	pier	1.366	1.360	0.013	0.010
	harbour	1.234	1.212	0.048	0.039
	Average	1.300	1.286	0.030	0.024
Calibration Period 2	pier	0.961	0.955	0.015	0.013
	harbour	0.918	0.893	0.091	0.099
	Average	0.939	0.924	0.053	0.056

Table 4.5. Statistical parameters for the current velocity time series at the indicated stations for both calibration periods.

	Station	$\langle\|X\|\rangle$	$\langle\|Y\|\rangle$	MAE	RMAE	Qualification
Calibration Period 1	14	0.216	0.218	0.100	0.231	good
	24	0.194	0.216	0.130	0.415	reasonable
	26	0.141	0.096	0.099	0.351	reasonable
	9	0.091	0.091	0.088	0.420	reasonable
	28	0.179	0.211	0.087	0.208	good
	25	-	-	-	-	
	5	0.099	0.078	0.065	0.155	good
	33	0.077	0.056	0.045*	0.000*	excellent
	Average	0.142	0.138	0.087	0.254	good
Calibration Period 2	14	0.261	0.250	0.172	0.466	reasonable
	24	0.266	0.280	0.163	0.425	reasonable
	26	0.164	0.111	0.109	0.364	reasonable
	9	0.100	0.108	0.085	0.352	reasonable
	28	-	-	-	-	
	25	0.412	0.468	0.164	0.277	good
	5	0.091	0.083	0.049	0.000*	excellent
	33	0.082	0.080	0.091	0.509	poor
	Average	0.196	0.197	0.119	0.359	reasonable

* computed value is within error band range of the measured value (excellent agreement).

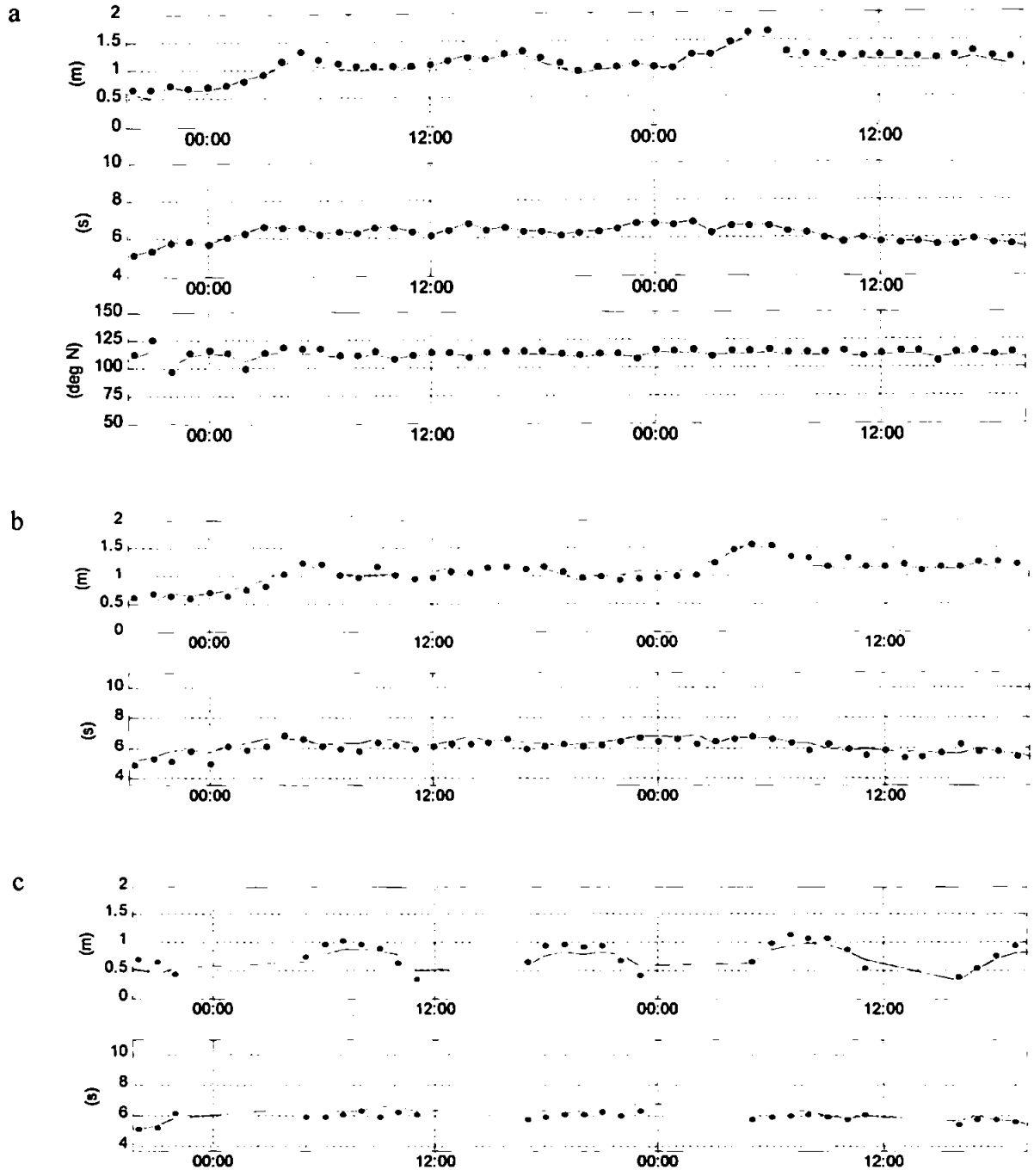

Figure 4.13. Comparison of measured (dots) and modelled (lines) wave parameters for a) station 7, significant wave heights (upper panel), significant wave period (middle panel), wave direction from true North (lower panel); b) station 4, significant wave heights (upper panel), significant wave period (lower panel); and c) station 25, significant wave heights (upper panel), significant wave period (lower panel).

Table 4.6. Statistical parameters for the significant wave heights time series at the indicated stations.

		Station	$\langle\|X\|\rangle$	$\langle\|Y\|\rangle$	MAE	RMAE	Qualification
Calibration Period 2		7	1.11	1.12	0.09*	0.00*	excellent
		4	1.06	1.12	0.12	0.02	excellent
		25	0.77	0.70	0.12	0.02	excellent
Validation		7	0.46	0.35	0.11	0.02	excellent
		4	0.46	0.36	0.10	0.01	excellent
		25	0.36	0.26	0.10	0.01	excellent

* computed value is within error band range of the measured value (excellent agreement).

4.4.2. Validation

In order to assess the quality of the calibrated HD and NSW modules, a validation experiment is set up including a variety of forcing conditions. The same values for the calibration parameters defined as optimal during the calibration experiments (for CP1 and CP2) are maintained for the validation experiment. The chosen validation period includes most of the COAST3D main experiment, with a one-month model run. Water levels, waves and river discharge during the modelled period are shown in Figure 4.14. Conditions are variable during the modelled period, including spring and neap tide conditions, with tidal ranges varying from 4.5 to 1.2 m, significant wave heights varying from 0.1 m during calm conditions to 1.7 m during stormy conditions, and river discharge generally low (under 15 $m^3 s^{-1}$) with the exception of one high river discharge peak of about 53 $m^3 s^{-1}$.

In the same way as for the calibration, *in situ* measurements are used to judge the quality of the modelled results through time series comparison and RMAE assessment. Water levels are modelled with an excellent agreement with the measurements throughout the whole validation period, giving low values of RMAE (Table 4.7). Flow velocities are also well reproduced by the model over the validation period, with RMAE values varying from excellent to reasonable/fair (according to Van Rijn et al., 2003 – Table 4.2) depending on

the compared station (Table 4.8). The averaged RMAE value over all stations during the validation shows that the model output gives a good (0.27) result if compared with the measurements. Time series of modelled current velocities are shown for four stations in Figure 4.15. Observation of these time series confirms that the model reproduces well the overall flow patterns, resulting in relatively low RMAE values.

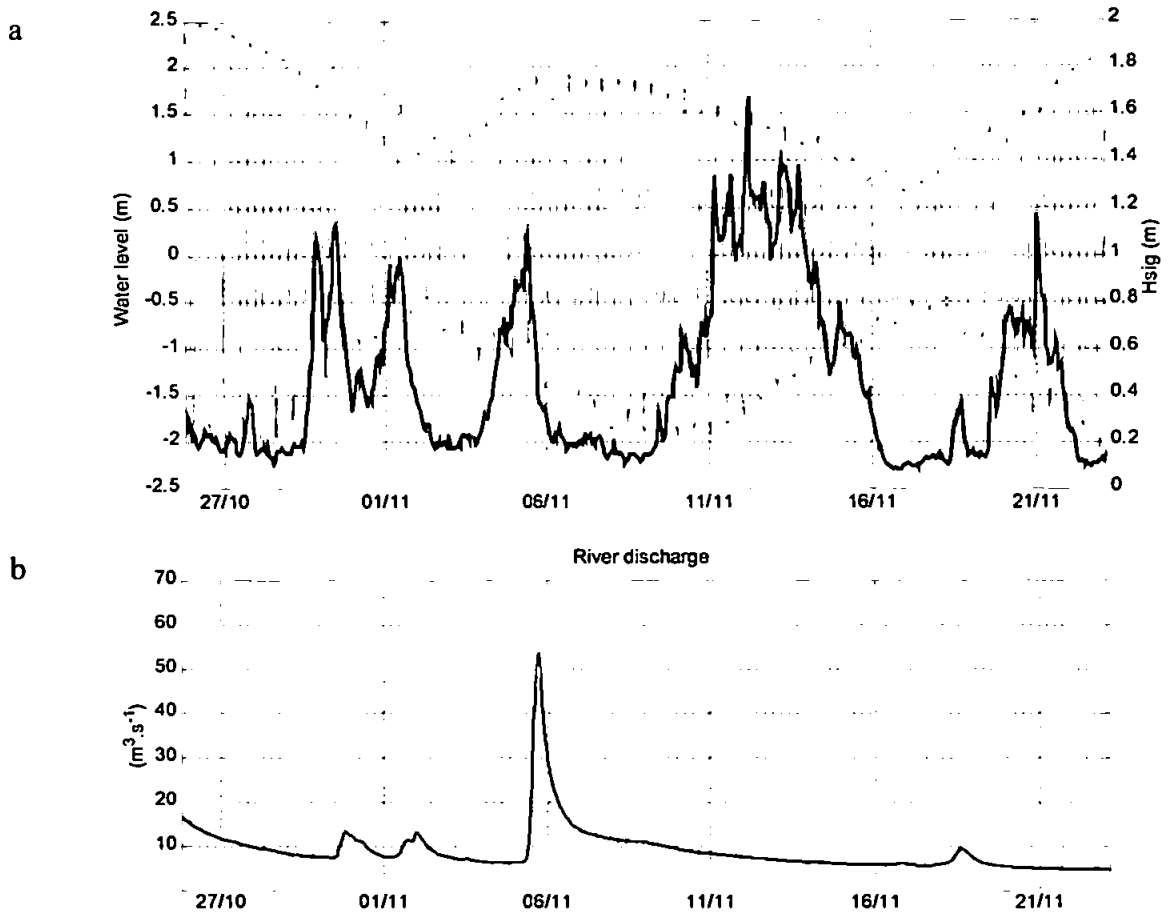

Figure 4.14. Water level and significant wave heights (a) and river discharge (b) during the validation experiment period.

Table 4.7. Statistical parameters for the water level at the pier and harbour for the validation period.

	Station	$\langle\|X\|\rangle$	$\langle\|Y\|\rangle$	MAE	RMAE
Validation Period	pier	0.894	0.890	0.011	0.012
	harbour	0.863	0.842	0.051	0.059
	Average	0.878	0.866	0.031	0.035

Table 4.8. Statistical parameters for the current velocity time series at the indicated stations for the validation period.

	Station	$\langle\|X\|\rangle$	$\langle\|Y\|\rangle$	MAE	RMAE	Qualification
Validation Period	14	0.156	0.164	0.104	0.346	reasonable
	24	0.159	0.173	0.118	0.429	reasonable
	26	0.134	0.083	0.093	0.326	reasonable
	9	0.070	0.071	0.071	0.296	good
	28	0.126	0.184	0.107	0.450	reasonable
	25	0.377	0.432	0.139	0.237	good
	5	0.083	0.066	0.055	0.066	excellent
	33	0.070	0.054	0.055	0.071	excellent
	Average	0.146	0.153	0.092	0.277	good

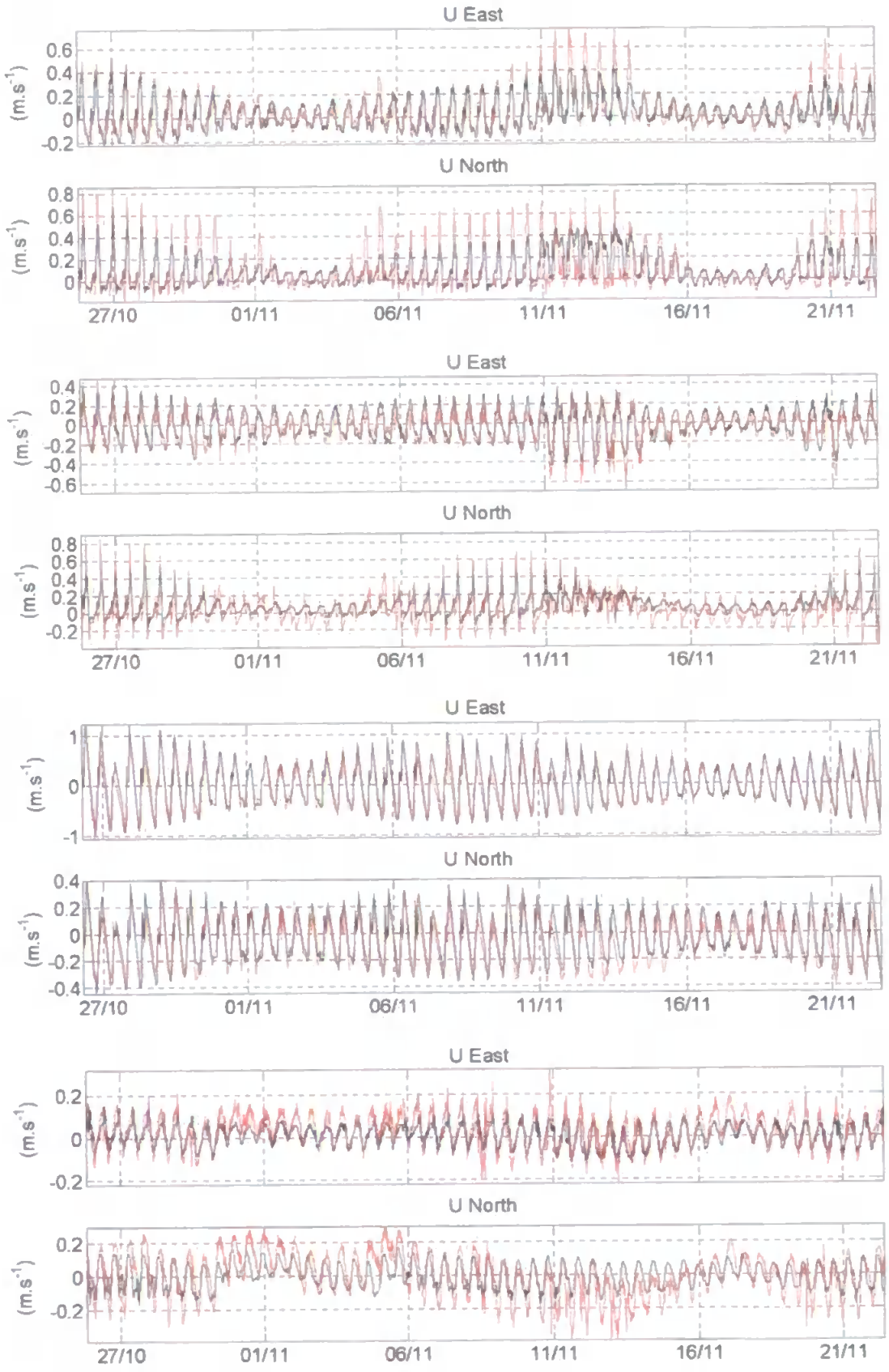

Figure 4.15. Time series of measured (red) and predicted (black) flow velocity components for a) station 14; b) station 24; c) station 25 and d) station 26.

4.4.3. Sediment Transport

The validation of the modelled sediment transport rates and assessment of both applied transport formulations were carried out through the use of the modelled initial sedimentation/erosion rates compared to the observed morphological evolution. As the applied numerical model does not include the feedback from the morphological evolution into the hydrodynamic module, the bed was only updated at the end of the run. The calibration period covers fourteen days, between surveys 2 and 4 of the COAST3D main experiment carried out on 6th to 8th and 16th to 19th November 1999. Varying grain size and sorting (based on samples collected during the COAST3D main experiment) was applied throughout the region of interest; however, the sensitivity of the applied transport formulations to the grain size was assessed by making additional model runs using constant sizes.

The quality of the modelled results of the morphological changes as a consequence of the sediment transport rates was assessed quantitatively through probabilistic assessments by the application of skill scores. Skill scores are measures of the accuracy of a prediction relative to the accuracy of a baseline prediction (Sutherland and Soulsby, 2003). In this study the Brier Skill Score was applied to assess the quality of the predicted morphological evolution.

4.4.3.1. Brier Skill Score

Developed for the quality assessment of weather forecast models, the Brier Skill Score (BSS) was first applied by Sutherland et al. (2001) and Brady and Sutherland (2001) with the objective of obtaining a quantitative judgement of the quality of morphodynamic models. Van Rijn et al. (2002), Van Rijn et al. (2003) and Sutherland and Soulsby (2003) carried out further applications to the modelling of coastal morphodynamics. A brief description of the Brier Skill Score and its decomposition in terms of amplitude, phase and mean are given below. More details and examples of its application can be found in the cited literature.

The BSS is a measure of the accuracy of a prediction (compared to the observed outcome) relative to the accuracy of a simple baseline prediction (compared to the observed outcome) (Sutherland and Soulsby, 2003). The BSS is given by:

$$BSS = 1 - \frac{\langle (Y - X)^2 \rangle}{\langle (B - X)^2 \rangle} \tag{4.8}$$

where B is a set of N baseline prediction depths, X is a set of N observed final depths and Y is a set of N predicted final depths, with the *nth* point in B, X and Y being at the same horizontal position. Perfect agreement gives a BSS of 1, while predicting the baseline condition gives a score of 0. If the model prediction is further away from the final measured condition than the baseline prediction, a negative score is obtained. The baseline in this case is the initial bathymetric survey (survey 2 of the COAST3D main experiment); i.e. model predictions are being assessed against a baseline prediction of no morphological change.

Murphy-Epstein decomposition of the Brier Skill Score

Murphy and Epstein (1989) decomposed the BSS for mean, phase and amplitude errors as repeated in Sutherland et al. (2001) and summarised here. The decomposition shows that the BSS can be decomposed in terms of the anomalies in the prediction ($Y'=Y-B$) and the measurements ($X'=X-B$). The variance in both predicted and observed anomalies are given by $\sigma_{X'}^2 = \langle X'^2 \rangle - \langle X' \rangle^2$ and $\sigma_{Y'}^2 = \langle Y'^2 \rangle - \langle Y' \rangle^2$ and the covariance between the anomalies is $s_{Y'X'} = \langle Y'X' \rangle - \langle Y' \rangle \langle X' \rangle$. The linear correlation between the anomalies in predicted and observed sets is the anomaly correlation coefficient ($r_{X'Y'}$)given by:

$$r_{X'Y'} = \frac{s_{X'Y'}}{\sigma_{X'} \sigma_{Y'}} \tag{4.9}$$

The Murphy and Epstein (1989) decomposition of the BSS shows that it can be written as:

$$BSS = \frac{A - B - C + D}{1 + D} \tag{4.10}$$

with the terms being:

$$A = r_{Y',X'}^2 \qquad B = \left(r_{Y',X'}^2 - \frac{\sigma_{Y'}}{\sigma_{X'}} \right)^2 \qquad C = \left(\frac{\langle Y' \rangle - \langle X' \rangle}{\sigma_{X'}} \right)^2 \qquad D = \left(\frac{\langle X' \rangle}{\sigma_{X'}} \right)^2 \qquad (4.11a, b, c, d)$$

with:

A = measure of phase error – when the sand is moved to the wrong position;

B = measure of amplitude error – when the wrong volume of sand is moved;

C = measure of the map mean error – when the predicted average bed level is different from the measured;

D = normalisation term.

Further details and comments on the decomposition can be found in Murphy and Epstein (1989) and Livezey et al. (1996). Ranges of BSS values for a classification of the quality of the model output are not available for morphodynamic modelling; however Sutherland et al. (2001) suggest that a BSS value greater than 0.2 represents a useful forecast.

As the BSS requires all three surface elevations (baseline, measured and predicted) to be at the same horizontal location, grids with the same size were created using the interpolation package SURFER (Golden Software, 1995) prior to the calculations.

4.4.3.2. Application of the Brier Skill Score

A set of numerical experiments was carried out for each of the applied sediment transport formulations. In the case of Bijker's (1967) formulation, the main adjustment factor is the bed-load transport coefficient, B, which is a proportionality factor in Bijker's formulation. Recommended values vary between 1 and 5, with B = 1 being suggested for the calculation of sediment transport outside the surf zone, whereas a value of B = 5 is suggested within the surf zone (DHI, 2000c). A spatially varying set of values can be defined for the model domain, being adjusted in order to obtain the best possible predictions of sediment transport. When applying the DHI's deterministic STP transport formulation, the main calibration factor is the critical value of the Shields parameter when generating the sediment transport tables in MIKE21 toolbox.

Within the region of interest, the area of the offshore sandbar is of particular interest for the sediment transport validation, due to its highly dynamic behaviour. Much of the validation shown here is based on the results of the sediment transport and morphological evolution of this sub-area. However, results also include the model performance for the region of the Ness sandbar (Table 4.9). Modelling experiments to assess the sensitivity of the formulations to the grain size were carried out by using constant grain size throughout the model domain. However, the best results were achieved when applying varying grain sizes which are closer to the real characteristics.

In Figures 4.16 and 4.17 the measured and modelled sedimentation/erosion rates are represented for the fourteen-day interval between surveys 2 and 4 of the COAST3D main experiment. Figure 4.16 shows the results for the STP formulation and Figure 4.17 for Bijker's formulation. A qualitative assessment from Figures 4.16 and 4.17 shows that the overall sediment transport patterns and initial sedimentation/erosion rates are similar for both formulations, mainly over the offshore sandbar. In this region, the morphological changes modelled with both formulations indicate the onshore transport of sediments, with erosion at the outer part of the sandbar and deposition on its onshore side. This is the same pattern shown by the measurements for the given period. The main differences between the formulations are found for the Ness sandbar, where the Bijker's formulation indicates an offshore (southwards) migration of the sandbar, which is the opposite of that indicated by the measured evolution. Using the STP formulation, the Ness sandbar evolution is better represented, with only small erosion on the offshore side of the sandbar.

The quantitative judgement of the modelled evolution through the application of the BSS shows that both formulations are able to predict the morphological evolution of the offshore sandbar, with BSS values higher than 0.2 (Table 4.10). However, the Ness sandbar evolution is not well predicted by either formulation, with negative value for Bijker's formulation and close to zero for the STP formulation (Table 4.10).

Table 4.9. BSS sensitivity to grain size and formulation.

	offshore sandbar ($N \approx 800$)	Ness sandbar ($N \approx 500$)
Bijker (1967)	0.24	-0.2
STP	0.36	0.003

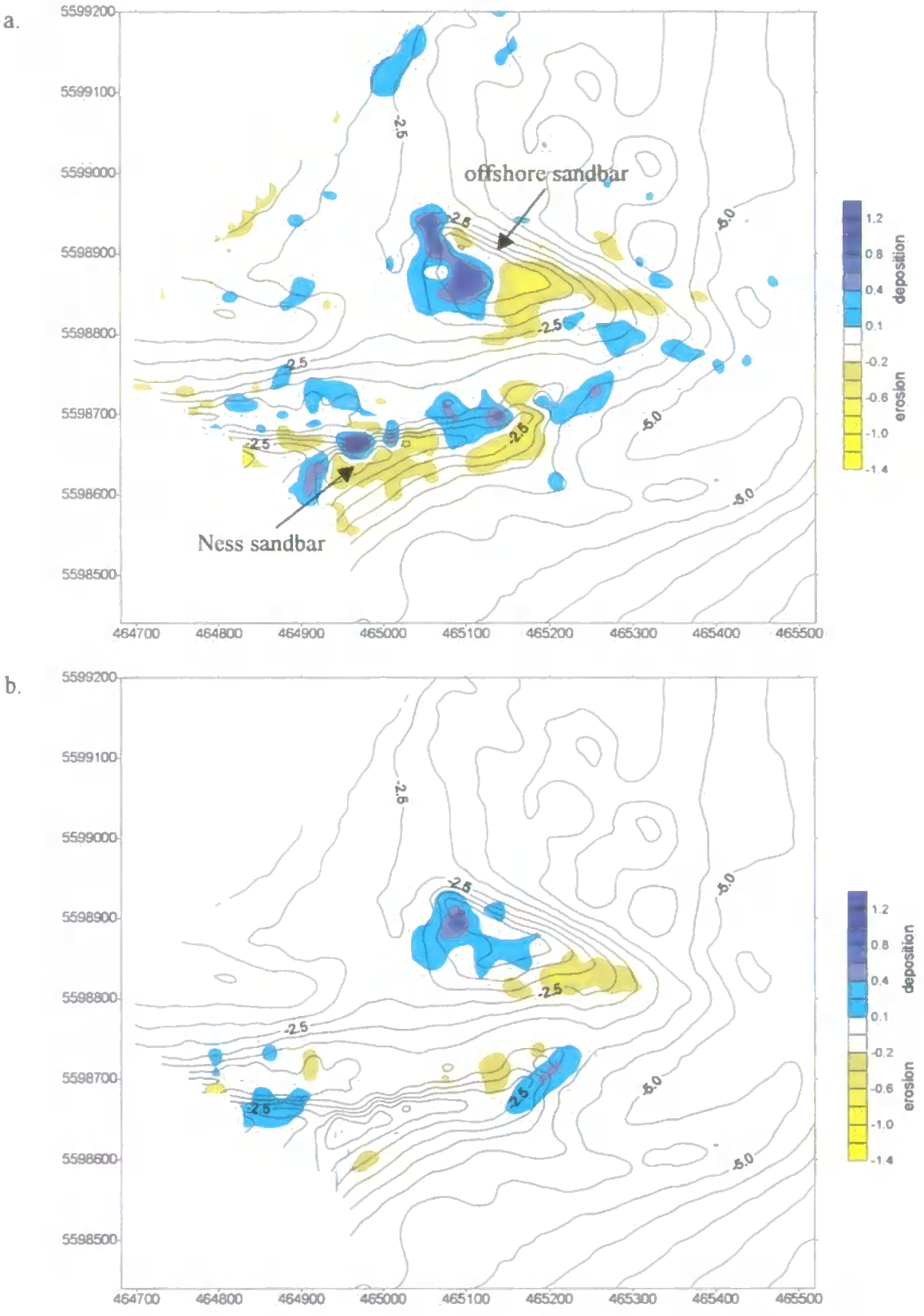

Figure 4.16. Measured (a) and modelled using the deterministic STP transport formulation (b) morphological changes over a 14 days period, between surveys 2 and 4 of the COAST3D main experiment.

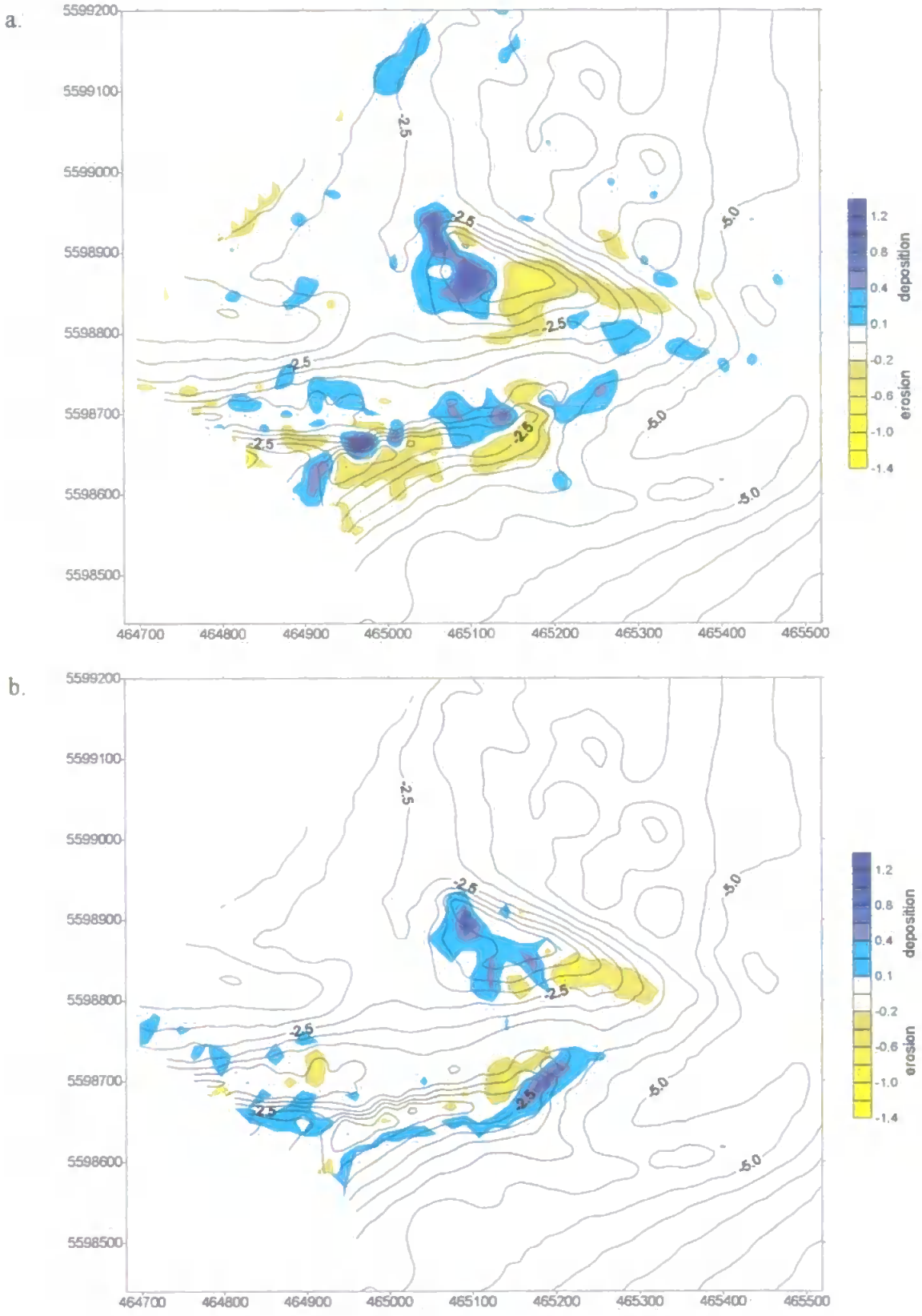

Figure 4.17. Measured (a) and modelled using Bijker's transport formulation (b) morphological changes over a 14 days period, between surveys 2 and 4 of the COAST3D main experiment.

These results are consistent with the ones found by Sutherland et al. (2001) and Sutherland and Soulsby (2003) when applying an area model (PISCES) at the same region and period. The offshore sandbar is also well reproduced in their experiments. However, negative BSS values for the Ness sandbar indicate a problem in reproducing the evolution of this region. The authors expected this problem to be due to the difference in grain sizes, since they applied spatially constant values of up to 0.5 mm in their experiments. In the present application, larger grain size values were applied, representing values closer to the reality, however, the spatial resolution of the grab samples is poor over this region (Figure 3.8), which may be one of the causes of the disparity between measured and modelled results.

In order to assess the main causes of the difference between both sediment transport formulations, the Murphy-Epstein decomposition of the BSS is applied for the offshore sandbar region. Through the use of Equations 4.11a, b, c and d the terms for phase error (A), amplitude error (B) and mean error (C) were calculated. The normalisation term (D) is 0.001 in both cases. As shown in Table 4.10, the main difference between the applied formulations is given by the phase error (term A), indicating that the STP formulation is more accurate in moving the sand to the right position.

Table 4.10. Decomposition of BSS (offshore sandbar)

	BSS	Term A	Term B	Term C
Bijker (1967)	0.24	0.28	0.03	0.01
STP	0.36	0.41	0.05	0.00

Despite the overall transport patterns and quantities of sediment displaced by each of the sediment transport formulation being similar, resulting in comparable morphological changes over the studied period (Figures 4.16 and 4.17), the BSS values indicate that the STP formulation results in better predictions. This was expected, since the STP formulation accounts for a range of processes that are not included in the Bijker's formulation (see Appendix I for details). Camenen and Larroudé (2003) comparing several sediment transport formulations also do not recommend the use of the Bijker's formulation for the application of morphodynamic models of the nearshore zone, since it integrates only the current related sediment transport. This quality assessment of the available sediment transport formulations in MIKE21 ST leads to the use of the deterministic STP

formulation in the numerical modelling experiments of sediment transport designed for Chapters 6 and 7.

One way of trying to reduce the differences between the measured and modelled evolution could be the application of a morphodynamic model, with feedback between the morphological evolution and the hydrodynamics. This limitation of updating the morphology only at the end of the simulation may be the cause of some of the discrepancies between measured and modelled morphologies. Another cause of discrepancies can also be the differences of the modelled velocities at some locations within the area of interest (as discussed in section 4.4.1).

4.6. Conclusions

In this Chapter, the MIKE21 numerical modelling system has been applied and validated for the inlet region of the Teign river at Teignmouth, UK. A unique database for the calibration and validation of the applied modules is derived from the COAST3D project, which included a dense spatial coverage of measurements within the area of interest. The complexity of the studied environment makes it a challenge for the application of numerical area models.

The hydrodynamic and waves modules were assessed through the traditional visual observation of time series comparing measured and predicted water levels, flow velocities and wave parameters. This gives a general evaluation of the quality of the modelling experiments, which can also be assessed quantitatively through the application of statistical parameters such as the relative mean absolute error (RMAE). It is only recently that model quality has been assessed through the use of such statistical parameters which provide a quantitative result in judging the quality of a numerical model (Brady and Sutherland, 2001; Sutherland et al., 2001; Van Rijn et al. 2003). Following the range of RMAE values recommended by these authors as a tough set of standards for models to achieve (Table 4.2) the hydrodynamic model applied here can be classified as being between "reasonable/fair" and "good". Following the same classification, the wave module can be

considered as "excellent" in reproducing the measured wave heights at three selected stations.

The quality of the sediment transport module was assessed through the comparison of measured and predicted morphological changes between two surveys carried out during the COAST3D main experiment. It was assessed qualitatively through the visual observation of the measured and observed morphological changes and quantitatively through the use of skill scores as proposed by Sutherland et al., 2001 and Sutherland and Soulsby, 2003. From the two sediment transport formulations applied, the deterministic STP formulation (DHI, 2000c) was chosen for further sediment transport experiments (Chapters 6 and 7) since it resulted in a better prediction of the overall morphological evolution.

Despite the validation of the numerical model, which shows that it reproduces well the overall observed phenomena, as with all numerical modelling experiments, one needs to be aware of some limitations that arise from its application. The main limitations of the present application are summarised below:

- the hydrodynamic model is depth averaged. This can be a limitation during simulations that include high river discharge values, since this can create a stratified water column at some regions. This aspect is discussed in Chapter 6 (section 6.3.1).
- the grid resolution of 10x10 m is a relatively fine resolution, but for such a complex region with a variety of morphological features, some of the features may be undersampled at some areas.
- the sediment data available for the region is limited in its spatial distribution and may result in some uncertainties when applied to the varying grain size in the sediment transport simulations.
- the applied modules do not form a morphodynamic model with feedback between the morphological changes and the hydrodynamics. At this complex and dynamic site where the morphological changes can be drastic and developing over short periods of time, this may lead to some misrepresentations of the actual morphological evolution.
- no internal checks on bed form size, bed and suspended concentrations, and bed load transport have been done.
- horizontal gradients in water density are not included in the hydrodynamic simulations.

Considering the limitations and advantages of the applied numerical model, a series of modelling experiments are conducted. These experiments and their results are described in Chapters 5, 6 and 7. In Chapter 5, hydrodynamic modelling experiments are combined with video imaging techniques for the intertidal mapping method that takes into account the pressure gradients across the region of interest. In Chapter 6 the numerical model experiments aim to assess the physical controls driving the local sediment transport and consequent morphodynamics of the system. And Chapter 7 combines numerical experiments of sediment transport with the morphological evolution observed from the video images.

Chapter 5

Video Imaging and Numerical Modelling

5.1. Introduction

In this chapter, the combined application of video imaging and numerical modelling experiments is described and applied in order to extract the intertidal morphology from video images. The coupling between these two techniques is fundamental for the application of the numerical model at different stages of the morphological cycle at Teignmouth.

Previous work and observations at the Teignmouth estuary and inlet (e.g. Nunney, 1980, COAST3D project measurements, visual observations) show the existence of large differences in water levels in the estuary and between the estuary and the adjacent nearshore region. As video image processing techniques depend on accurate water levels, and no measurements of the pressure gradients in the inlet channel are available, the modelled water levels are applied in the image processing. The use of numerical modelling results combined with the image processing techniques is a consequence of the need for accurate water levels across the field of view of the cameras in order to correctly process the video images. As shown in the following sections, the coupled application of video image processing techniques and numerical modelling is carried out iteratively, since the results of the numerical model are used as input for the image processing and vice versa.

This chapter starts with the description of the technique applied for the extraction of the intertidal morphology from video images, based on the photogrammetric techniques described in Chapter 3 (section 3.2.2). This is followed by a brief assessment of the water surface topography across the region of interest carried out through numerical modelling experiments (based on work carried out by the author and published in Siegle et al., 2002 – Appendix II). This leads to the coupling of both tools, with the modelled water levels being

used as input for the video imaging processing and its results being used in further numerical simulations. Prior to the application of the technique, it is validated against measurements obtained by traditional surveying techniques. Finally, advantages and limitations of the applied method are discussed in the context of using its results in the numerical model experiments at different stages of the morphological cycle.

5.2. Technique Applied to Extract Intertidal Morphology from Images

As described in the literature review (Chapter 2), there are several techniques that aim at the extraction of morphological information from images (e.g. Plant and Holman, 1997; Davidson et al., 1997; Holland and Holman, 1997; Janssen, 1997; Aarninkhof and Roelvink, 1999; Kingston et al., in prep.). These techniques are all based on the detection of the shoreline location at a number of instances during a tidal cycle, the shoreline being considered the contour line corresponding to the location of the local water level.

In this study a method of defining contour lines with the same pixel intensities in an image is used for the morphology extraction from the images. This is done through the use of the "imcontour" routine available in the MATLAB® Image Processing Toolbox. This routine draws contour plots of the intensity image, automatically setting up the axes so their orientation and aspect ratio match the image. The intensity level to be drawn and the number of intensity contours can be detected automatically or defined manually. The application of this technique is based on the photogrammetric techniques described in Chapter 3.

Applying this contouring technique to the Argus images involves the steps described below. The schematic diagram in Figure 5.1 illustrates the main steps:

- based on the oblique images, all the information related to the image is loaded, including the time, image geometry parameters, camera information and tidal level. As the "imcontour" tool works only with grey scale images, the image is converted to grey scale. This results in an image with 256 grey shades ranging linearly in value from 0

(black) to 255 (white). An oblique image consists of a 640 x 480 array of pixels ordered according to a pixel coordinates system (U_i, V_i);

- through the use of the "improfile" MATLAB® routine a sample profile of the pixel intensities is extracted so that the range of pixel intensity values that better represent the shoreline can be defined (Figure 5.1b);
- using the "imcontour" tool the pixel intensity value defined as being the shoreline (mid-point of the drop in intensity) is drawn (Figure 5.1c). The intensity that will best define the shoreline may change from image to image as a function of solar radiation incidence and the composition of the aimed material (e.g. wet/dry sand, water). However, the abrupt change in intensity values usually verified when comparing water pixels with sand pixels in the images allows the definition of the intensity values that represent the shoreline;
- this selected contour line of same intensity is saved with its U_i and V_i image coordinates, which are corrected for the lens distortion and then rectified using the geometrical parameters for the given image. The image is rectified using as vertical elevation the local tide level;
- the rectified points with their corresponding elevation are used to create the grid (x, y, z) of the intertidal morphology (Figure 5.1d).

Through the use of additional routines written for this purpose in MATLAB® most of these steps are carried out automatically.

When defining the rectification level (z), these techniques for morphology extraction from video images normally assume that the water surface is horizontal over the region of interest. However, as will be seen in the next sections, in regions influenced by high pressure gradients, the water level height is spatially variable. As it is difficult to measure these irregularities in coastal regions due to both the density and spatial extend of the measurements required, the use of numerical models provides valuable insight into the important physical processes. The next section discusses the combined application of the numerical model and the video image technique for the extraction of the intertidal morphology.

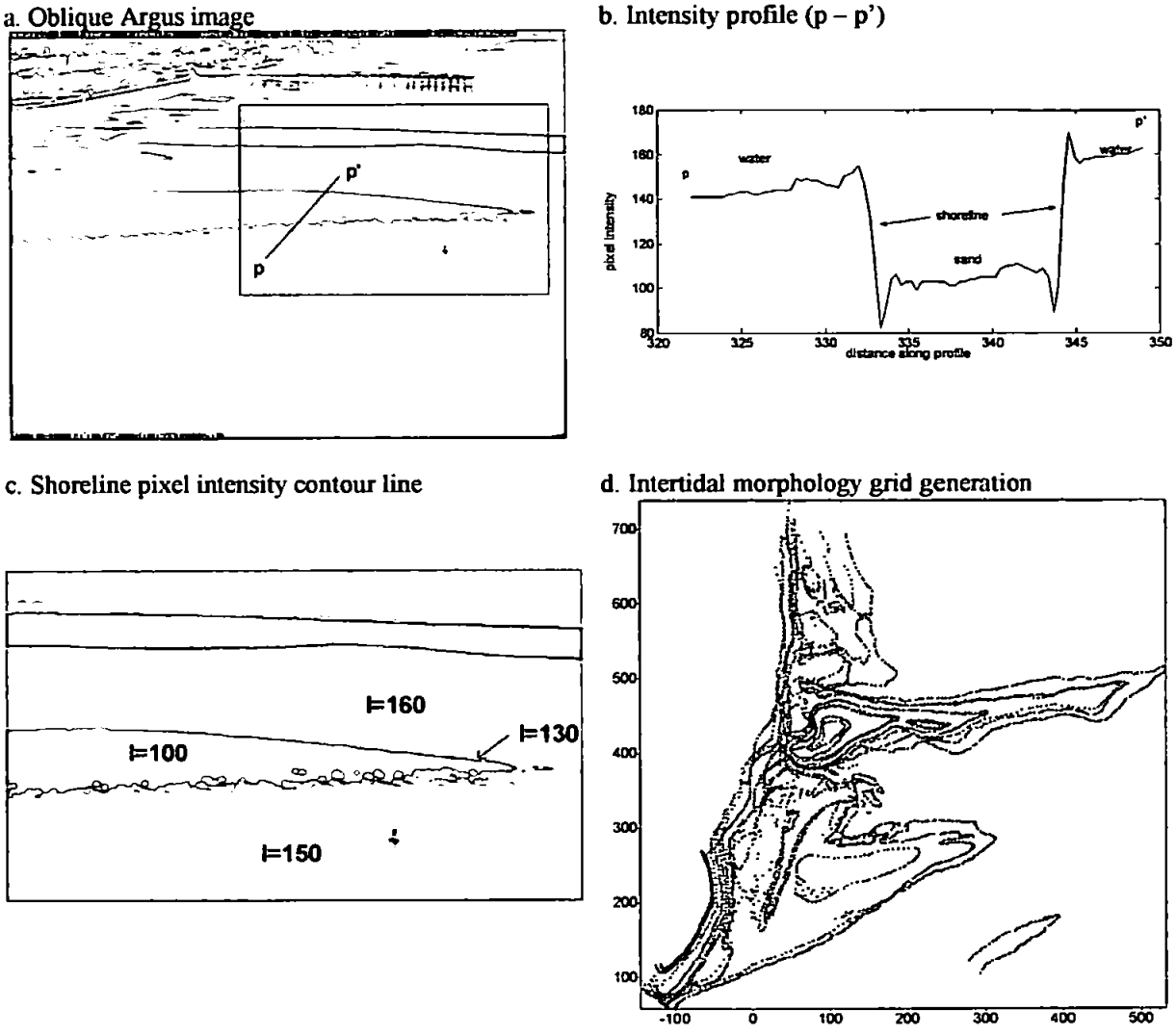

Figure 5.1. Diagram of the procedure applied for the extraction of the intertidal morphology from video images.

5.3. Combination of Numerical Modelling and Video Imaging

As described in the basic image processing (Chapter 3) and in the previous section, in the image processing techniques for the extraction of morphology from images, the water level information is needed twice: 1) for the rectification process of the image or selected contour lines, and 2) when defining the z values for the morphology grid.

All the previously cited techniques for the extraction of intertidal morphology from images (Plant and Holman, 1997; Davidson et al., 1997; Holland and Holman, 1997; Janssen, 1997; Aarninkhof and Roelvink, 1999; Kingston et al., in prep.) assume that the water surface is spatially horizontal, an assumption that is often invalid in shallow waters. In a region with high pressure gradients, such as inlet channels, if it is assumed that the water level is spatially horizontal, the detected shoreline and its vertical elevation are not necessarily correct. Differences in water levels for the rectification process for a given point (U_i, V_i) in the image will cause deviations of the horizontal position of its rectified ground coordinates (x, y) and by defining its vertical elevation values (z) as spatially constant a second error is generated. This highlights the importance of accurate water levels when processing images, since a small difference in water level may result in large deviations of the horizontal shoreline position and in its associated vertical elevation.

As it is difficult to obtain the necessary spatial resolution through measured water levels, the application of a numerical area model can help by providing the water surface topography across the region of interest. In this study the MIKE21 HD and NSW (Chapter 4) modules are applied for this purpose. Using the calibrated model a series of experiments were conducted aiming to quantify the relative importance of tidal range, wave conditions and river discharge on the water surface topography. Part of the results presented in section 5.3.1 are summarised from work carried out by the author and published in Siegle et al. (2002) (see article "Modelling water surface topography at a complex inlet system – Teignmouth, UK" by Siegle, E., Huntley, D.A. and Davidson, M.A. in Appendix II).

5.3.1. Water Surface Topography

Water surface topography is defined as the spatial water level distribution over the area of interest, and is quantified through the analysis of water level differences in relation to a fixed water level reference point. At Teignmouth, the reference water level used in the basic image processing is the data measured by the pressure sensor at the pier (station 8 in Figure 3.6).

Large variations in the water surface topography are found across the region, with levels of up to 0.9 m higher in the estuary channel than in the adjacent coastal region. This

difference can be seen in the time series of water levels measured at the pier (station 8 in Figure 3.6) and at the harbour (station 11), as shown by Figure 5.2 for the COAST3D measurements. It is during ebbing spring tides when the biggest differences are measured, with smaller differences occurring during neap tides.

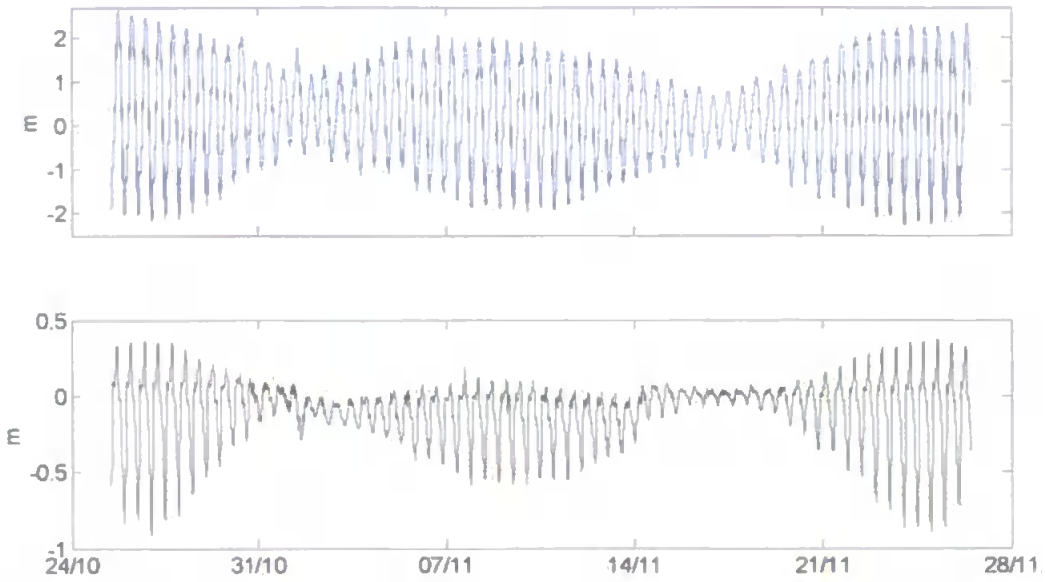

Figure 5.2. a) Measured tide levels at the pier (black line) and harbour (blue line), and b) measured difference (= pier–harbour) in tide level between the pier and the harbour. (October – November 1999).

Results of the water surface topography modelling experiments for the COAST3D period are summarised below and the relative influence of the main processes (tidal range, waves and river discharge) on the water levels is assessed (based on Siegle et al., 2002 – Appendix II).

5.3.1.1. Tidal Range

Water surface topography is directly related to the tidal range, with highest water level residuals during spring tide periods. During the modelled neap tide period, only small changes in water surface topography are registered, with a virtually flat surface across the

area. Maximum residual elevations in relation to the pier reference point are less than 5 cm. Conversely, water surface topography varies significantly during spring tide conditions, with maximum and minimum water level residuals in the inlet channel of 0.6 and -0.3 m, respectively. This is particularly important for the image processing, since it is during spring tide conditions that the coastline extraction from images is more important, as this permits shoreline detection over a wider intertidal area.

The emerged sandbars at low water spring tide periods play an important role in the funnelling and friction effects of the channel. This is clearly seen in the analysis of a sequence of contour plots of water surface topography over the modelled spring tide period, as shown by the example represented in Figure 5.3 for the time of maximum residuals (final stages of ebb tide). During the early stages of the ebb tide, the deeper water column and wider channel reduce these funnelling and friction effects in the channel. The observations and modelling experiments show that maximum residuals are registered at approximately local LW – 1 hour and minimum values at local HW – 1 hour, coinciding with ebb and flood peak currents. Figure 5.4 shows how the water level and mid channel current velocities are phase locked with the water level residuals, a response to the pressure gradient forces created by the difference in water level in the estuary and offshore. It is always when water level differences are at its maximum that the peak ebb flow velocities occur.

The water surface slope between the estuary and the open sea is shown at its maximum gradient in Figure 5.5a for a profile along the middle of the channel on 27/10/1999. Figures 5.5b and 5.5c present the cross and longshore velocities along the same profile, illustrating the relation between them and the surface slope. It shows the dominant along-channel velocities (x) in the funnelled channel associated with higher water level residuals that generate the slope. When it reaches the end of the channel, the flow spreads out and the slope reaches its end, with values of water level residuals close to zero. This is followed by a decrease in the along-channel velocity and a slight increase in the longshore velocity as the flow turns to the south as it leaves the channel. The channel slope cycle, from flat surface to the maximum slope and back to flat surface takes about 5 hours of the ebb tide period.

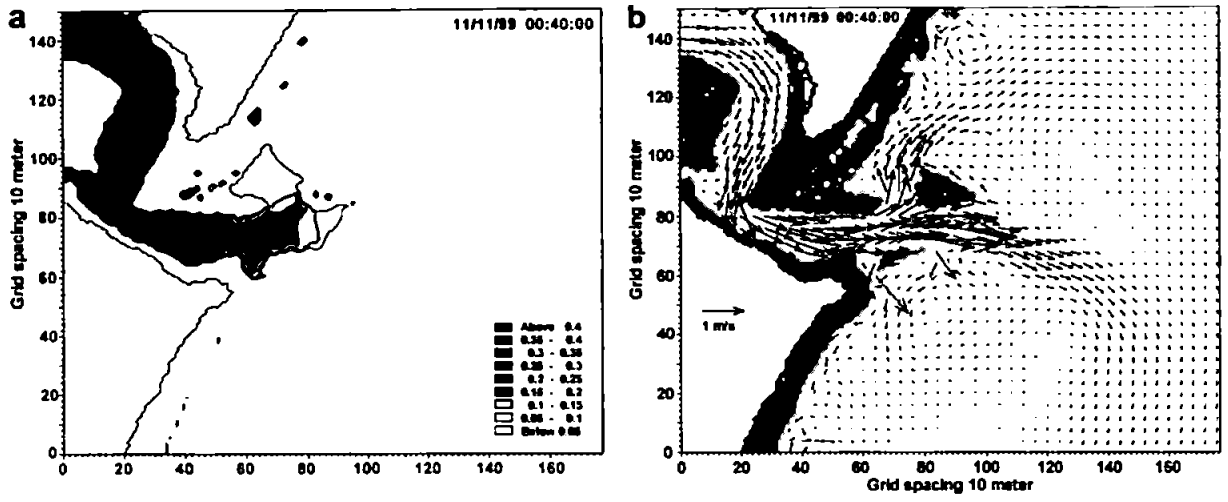

Figure 5.3. Contour plot of the water surface topography in relation to the pier water level (a) and velocity vector plot (b) at maximum ebb flow.

5.3.1.2. Waves

As shown by Siegle et al. (2002) the influence of waves is relatively small in the water level elevations at the channel region. Its influence is higher in the region outside the main inlet channel where high waves can cause an increase of up to 0.15 m in the local water levels (Appendix II). An example of the wave setup around the sandbars is shown in Figure 5.6.

5.3.1.3. River Discharge

River discharge values varying between the real conditions (of about 7 $m^3 s^{-1}$) during the modelled period and 100 $m^3 s^{-1}$ caused a maximum water level increase of about 12 cm coincident with the peak ebb tide currents. Average values over the 25 hour period for high discharge show an increase of about 5 cm compared to low discharge periods. The opposite is verified for the minimum residuals (negative), since the flood currents are reduced due to the residual flow during high discharge periods. This causes the water level residuals during high discharge events to be closer to zero at flood periods, while for low discharge events the residuals become negative in relation to the pier reference point.

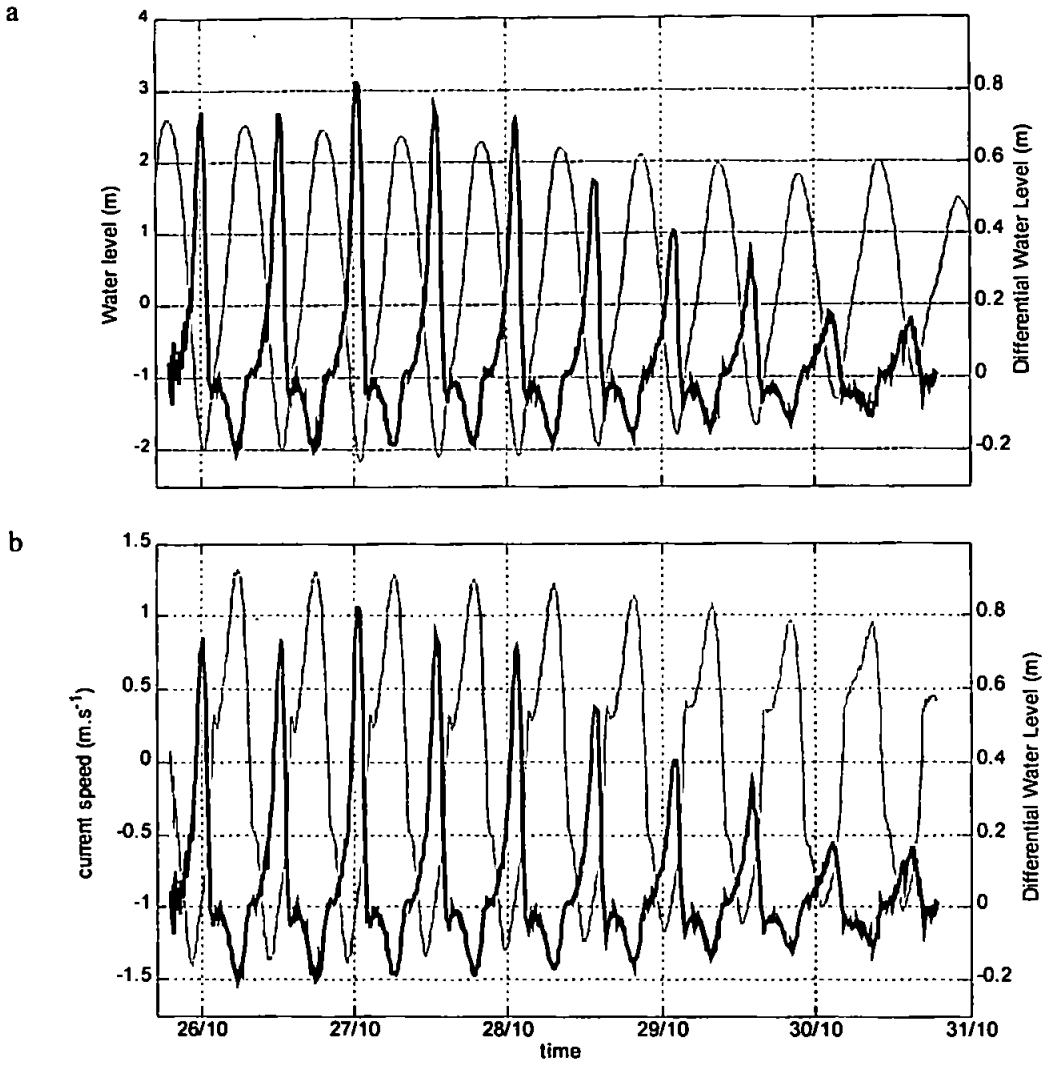

Figure 5.4. Time series of water level residuals (thick line) and water level (a – thin line) and current velocity (b – thin line) in the middle of the channel.

The water surface slope gradient in the inlet channel also shows an increase in residual water level during high discharge events. Figure 5.7 illustrates this for the slope along the middle of the channel for high and low river discharge. The slope gradient is significantly increased at high discharge, but the offshore end of the slope is the same for both conditions, being defined by the channel morphology. The channel and sandbar morphology defines the maximum extent of the water surface deviations across the area of interest. This highlights the importance of the channels and sandbar morphology for the water surface topography variability and distribution. The water surface slopes shown in

Figure 5.7 also show a flattening of the slopes at around 400 m, which is coincident with the secondary channel that guides the flow northwards (see Figure 5.3). This allows part of the flow to spread before it is funnelled again in the final part of the main channel.

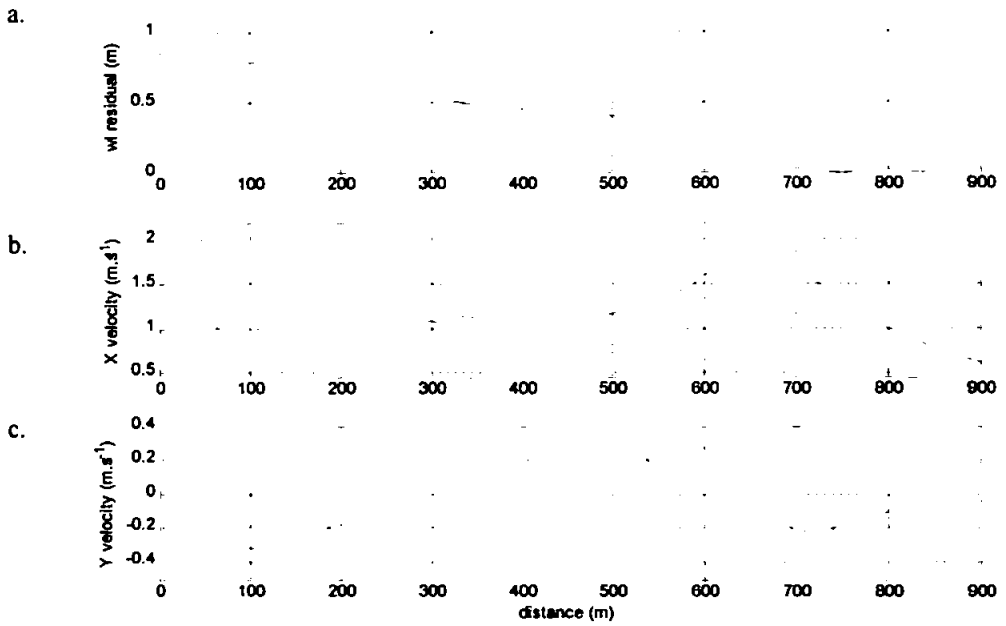

Figure 5.5. Along channel profile of water level differential (a), x-velocity (b) and y-velocity (c). The situation represented is at approximately LW – 1 hour during spring tide (27/10/1999 00:40:00).

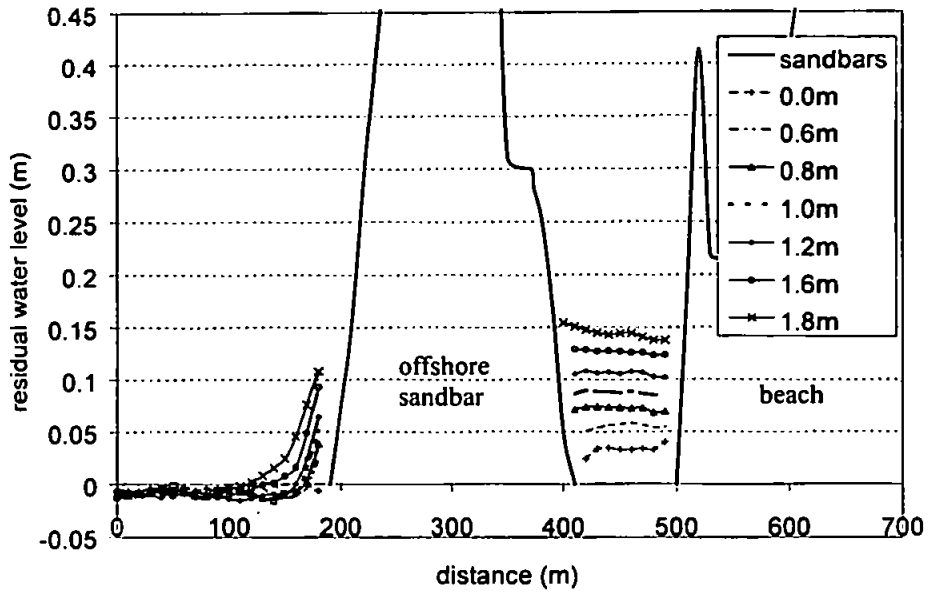

Figure 5.6. Wave effect on the water levels around the sandbars. The represented profile starts offshore (0 m) and ends onshore (700 m) and its exact position is given in Figure 1 in Appendix II (P3). The figure legend shows the modelled wave heights.

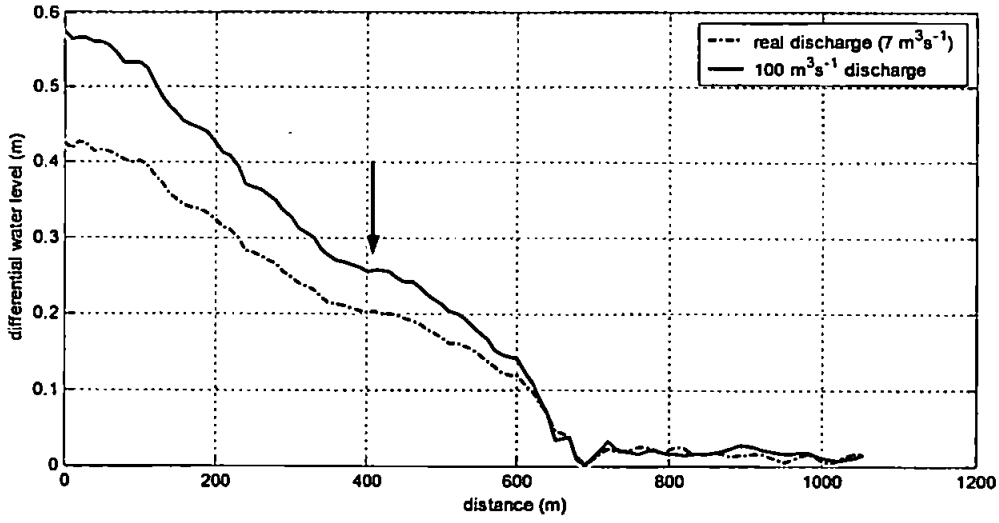

Figure 5.7. Mid channel water slope for real measured discharge and for high river discharge conditions. The arrow indicates the flattening in the curve at around 400 m distance.

5.3.2. Modelled Water Levels as Input for Video Imaging Techniques

In order to carry out the image processing with the best approximation of the real water level distribution, the spatially varying modelled water levels are applied. This process of using the modelled water levels for the morphology extraction requires the inclusion of an additional step in the applied extraction technique described earlier in section 5.2 and represented schematically in the diagram in Figure 5.1. The use of modelled water levels is included between the steps represented by "c" and "d" in Figure 5.1. As seen previously, the modelled water levels are used twice in the extraction process: 1) for the rectification of the U_i and V_i image coordinates into x, y and z ground coordinates, and 2) when defining the correspondent elevation values (z) for the extracted points for the morphology grid generation.

This additional step in the image processing consists of the segmentation of coastline stretches in an oblique image according to the modelled water level gradients. Figure 5.8 shows an example of how the coastline segmentation is defined for images from cameras 1 and 2 at 13:00h on the 27/10/1999. From the overlaid modelled water levels it is possible to define stretches of coastline, according to regions of similar water levels, and consider them separately during the shoreline extraction, processing each defined segment with its corresponding modelled water level. This segmentation is defined according to the balance between the accuracy of the applied technique and processing time, with differences of about 0.05 m to 0.1 m defining each segment. For the example shown in Figure 5.8, the measured water level at the pier at the given time is –1.98 m, resulting in differences of up to 0.78 m when compared to the water levels in the channel (Figure 5.8a). If these differences are taken into account in the image processing, improvements can be made when extracting the intertidal morphology (as seen later in the technique validation – section 5.4).

The modelled water surface topography described in the previous section and in Siegle et al. (2002 – Appendix II) is specific for one morphological stage (October 1999). However, in order to extract the morphology at different stages of the morphological cycle it is necessary to obtain the water levels around the region of interest under different morphological conditions. In order to do so, the numerical modelling experiments and the techniques to extract the intertidal morphology from images need to be carried out

iteratively, with model simulations under a given morphological condition providing water levels for the morphology extraction from the set of images representing the next morphological stage.

For this purpose, ten situations with distinct morphological characteristics were selected from the three-year observed sandbar evolution cycle (March 1999 to April 2002). The morphology used for the modelling experiments is based on two surveys (March and October 1999) and on the intertidal morphology extracted from images for the remaining eight modelled morphological conditions. These modelling experiments are conducted iteratively with the image extraction techniques, with model results from the previous situation providing water levels for the intertidal morphology extraction for the next stage.

When running the model to obtain the water level distribution, boundary conditions for the period corresponding to the next morphological situation are used (river discharge, water levels, wave data). This means that the morphology is considered constant between each of the ten represented stages. However, as the main influence of the pressure gradients on the water level occurs in the region of the inlet channel, which is relatively stable, this is a fair assumption. Water levels extracted from these numerical simulations are then used for processing the images from the following period (the period that provided the boundary conditions for the water level simulation). This process results in the morphology definition for the latter period, allowing further modelling experiments (including water level distribution for the following stage – as seen in item 5.3.3) to be carried out at each selected morphological stage of the cycle.

In order to reduce the errors in estimating the water levels based on the previous morphological stage, the number and temporal distribution of the modelled periods is chosen according to morphological changes observed in the rectified video images. Increasing the temporal resolution of the modelling experiments can always reduce errors. Despite some limitations, the technique validation (section 5.4) shows that the use of varying water levels allows the extraction of a more realistic intertidal morphology from images.

5.3.3. Extracted Intertidal Morphology as Input for Numerical Model Simulations

As one of the objectives of this study is to apply the numerical model to different stages of the morphological cycle at Teignmouth, the intertidal morphology extracted from the video images is used as an input to the numerical simulations. Following the process described in item 5.3.2, this also enables the use of the modelled water levels for the extraction of morphology from the next evolutionary stages, completing a loop between the numerical model and image processing outputs. The overall method approach is diagrammed in Figure 5.9.

Since only the intertidal morphology is extracted from images, the subtidal bathymetry is assumed to be constant in relation to the last existing survey (October 1999). Despite this being a limitation of the method used, this assumption is reasonable since only small changes were observed in the subtidal morphology during the measured interval (March – October 1999, surveys carried out by the COAST3D project).

a

b

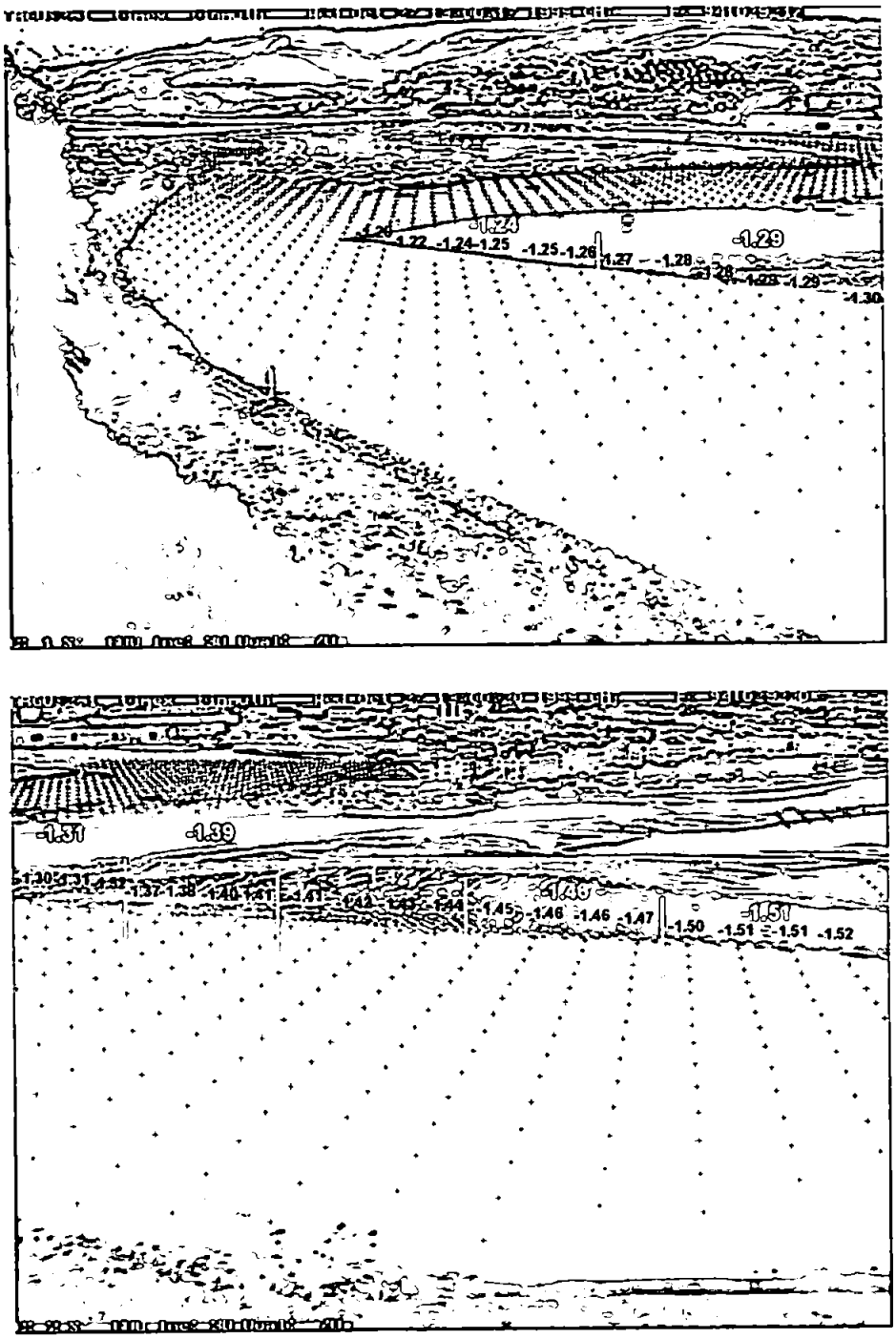

Figure 5.8. Example of coastline segmentation for the image processing using modelled water levels for: camera 1 (a) and camera 2 (b) at 13:00h on the 27/10/1999. Black crosses indicate positions (U_i, V_i) of water levels extracted from the model with elevation values indicated by black labels. Yellow lines show the stretches of coastline processed from average water level (yellow numbers). At the given time, the measured water level at the pier is –1.98 m.

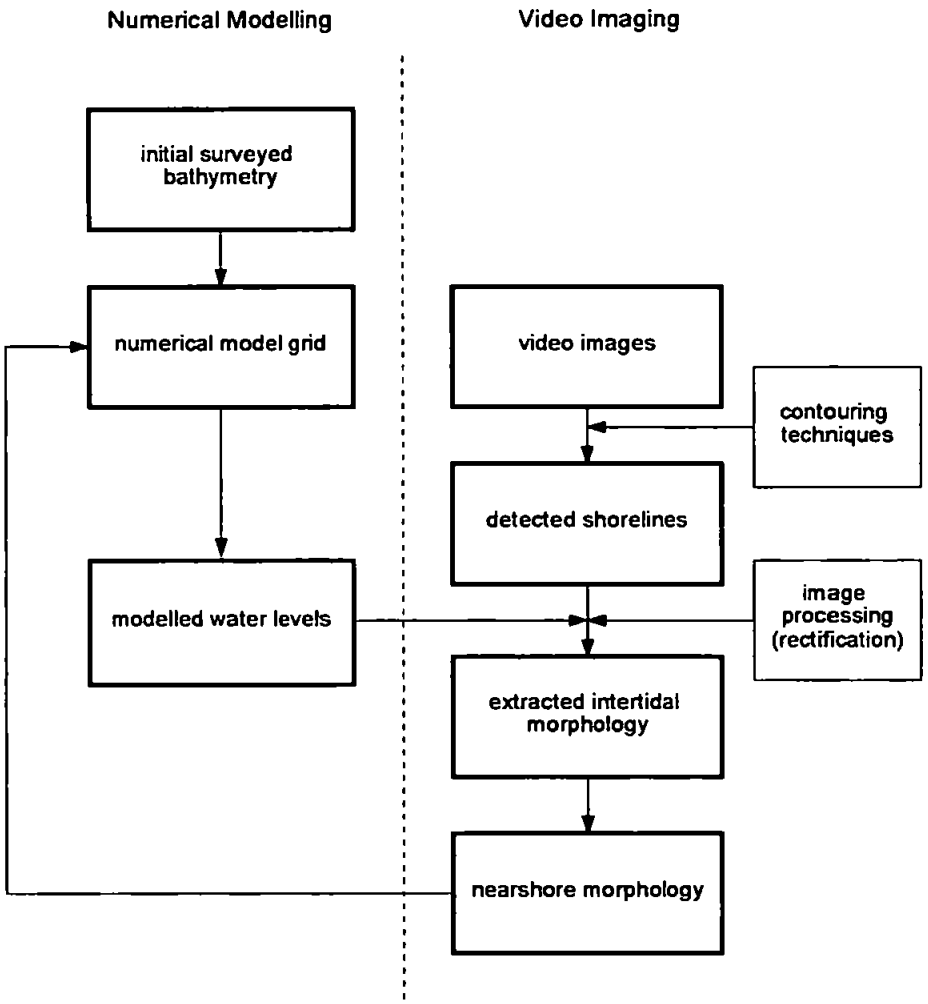

Figure 5.9. Diagram representing the framework of the applied method. Red arrows represent the links between the numerical modelling and video imaging techniques.

Based on the surveyed "background" bathymetry, the intertidal morphology extracted from the video images replaces the original data where information is overlapped and remaining data points of the previous intertidal morphology are removed. This process is carried out in the MIKE21 bathymetry editor, using the new intertidal data to create new bathymetries to be applied in the model simulations. The interpolation process fills the remaining gaps of data between the intertidal and subtidal morphologies. The applied interpolation method in the MIKE21 bathymetry editor is the "True Distance", which searches for data points in circles around a point. The final configuration of the intertidal morphologies is tested in the model simulations through plots of modelled hydrodynamics overlaid on images at given

times. Drying areas in the model simulations should coincide with the dry intertidal areas in the images at the same tidal level, as shown in the example in Figure 5.10. Some small differences are expected since the comparison is made using time exposure images (averaged over 10 minutes) and the model output is representing one snapshot of the given time. Examples of these differences can be seen at hours 10:00, 11:00 and 12:00 in Figure 5.10, where the modelled velocity fields appear overlaid to some parts of the exposed sandbar in the images.

In the next section the applied technique is validated for periods with data available from traditional surveying techniques and in section 5.5 the application of the technique to the studied morphologies is described, providing the basis for the model application at different stages of the morphological cycle of the sandbars.

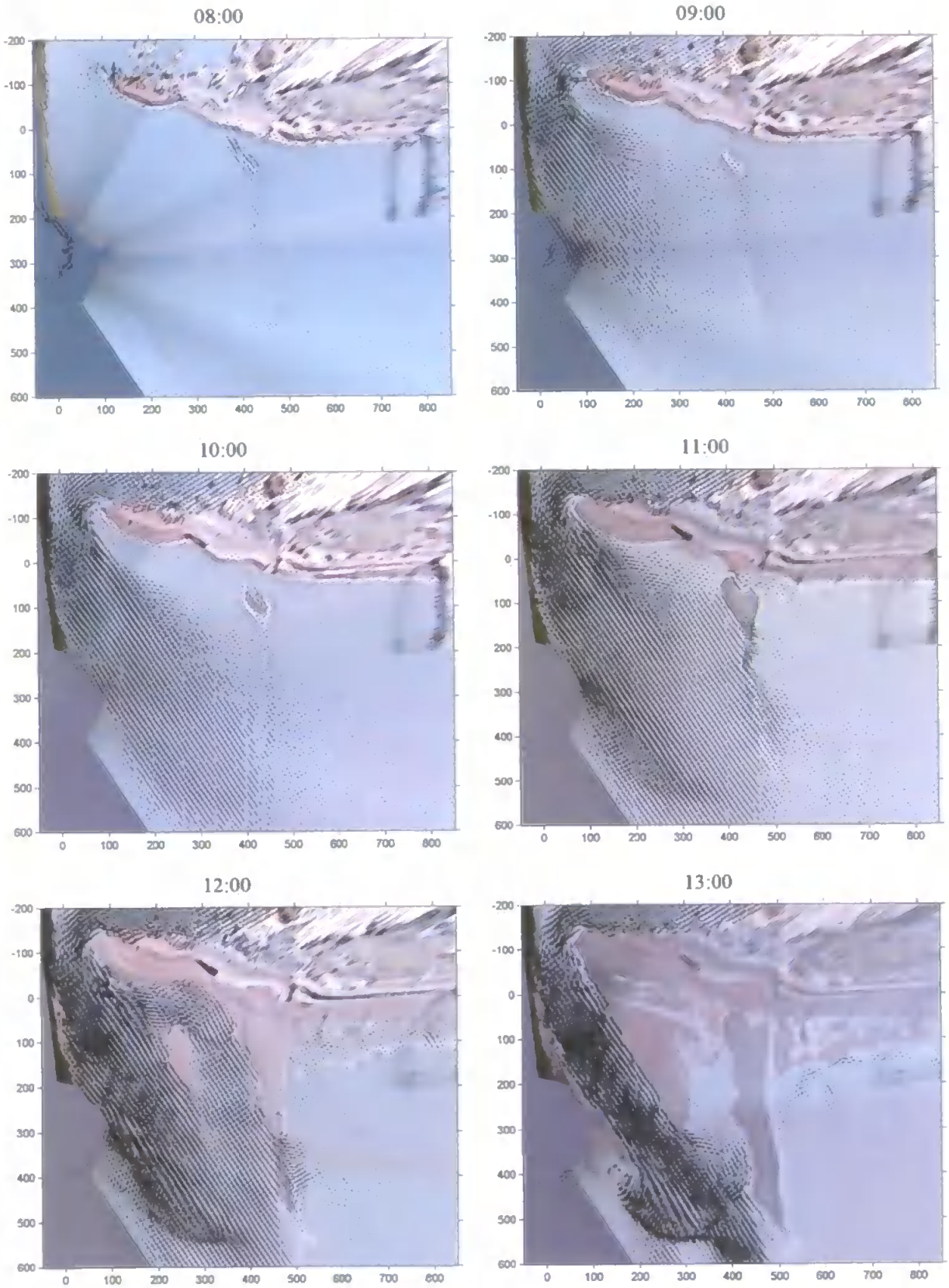

Figure 5.10. Example of modelled hydrodynamics overlaid on video images at different tidal levels in order to test the intertidal morphology applied in the simulations through the wetting and drying areas. Example for 31/08/2000. Continued on next page.

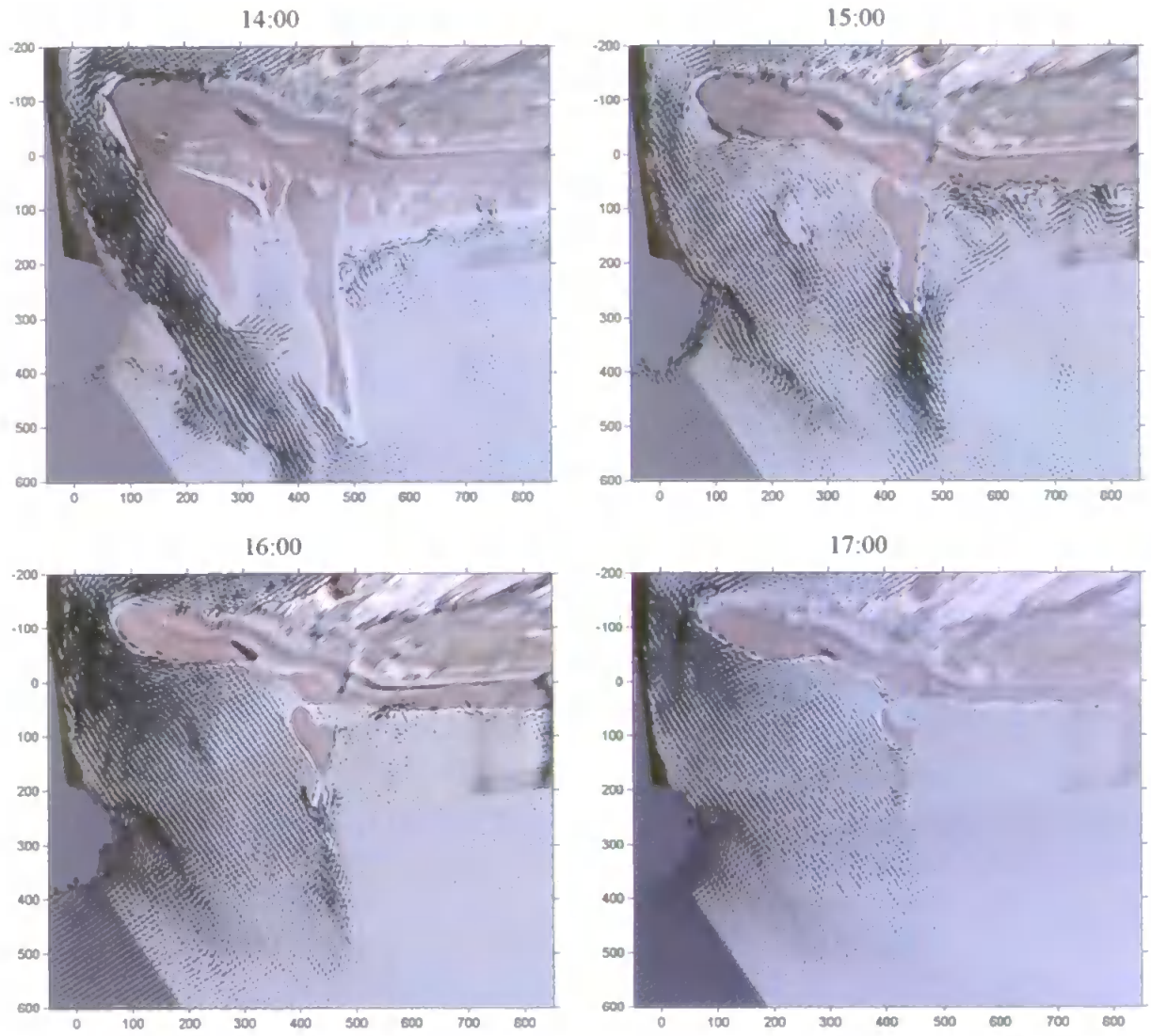

Figure 5.10 (Cont.). Example of modelled hydrodynamics overlaid on video images at different tidal levels in order to test the intertidal morphology applied in the simulations through the wetting and drying areas. Example for 31/08/2000.

5.4. Technique Validation

In order to validate the technique applied for the morphology extraction from the video images, periods with available data obtained through traditional surveying techniques are compared for the region of interest. In this study, three available surveys of the intertidal region are used for the morphology extraction technique. One period is the COAST3D

main experiment survey (25 – 27 October 1999 – Figure 5.11). The second is a survey carried out on the 5th of July 2000, covering mainly the long straight attached sandbar (Figure 5.15); and the third survey was carried out through three cross-sections over the Sprat sandbar on the 30th of August 2000. The accuracy of the COAST3D topographic and bathymetric surveys was assessed by Van Rijn et al. (2000) (Chapter 3).

The comparison of the measured morphology with that extracted from images is carried out using the interpolated intertidal maps for the periods with available data (e.g. October 1999, July 2000 and August 2000). Results from the comparison for the October 1999 period are presented in Figures 5.11 to 5.14. In Figure 5.11 the compared profiles are plotted over the merged video image representative of the surveyed period. The comparison between surveyed data and morphology extracted from the images is represented in Figures 5.12, 5.13 and 5.14.

In the comparison shown in Figure 5.12 both spatially constant and varying water levels are applied for the morphology extraction. In general, all the compared profiles present a better result when using the varying modelled water levels, and this improvement is increased for profiles close to the inlet mouth, where higher pressure gradients control the water levels. The use of spatially horizontal water levels results in large differences in the extracted morphology when compared to the surveyed data. As shown by the compared profiles, this difference is significantly reduced when applying the modelled water levels in the shoreline extraction technique.

Quantifying the vertical errors through the use of Root Mean Square Error (RMSE) values also shows the gain in accuracy when using the varying modelled water levels for the image processing. RMSE values are summarised in Table 5.1 for the compared profiles. Extending the comparison to the map generated by all extracted and surveyed points over the Sprat sandbar (yellow dots in Figure 5.11) the RMSE values are 0.373 m when using constant water levels and 0.144 m when applying the varying modelled water levels. The RMSE values present an even further reduction when comparing some particular profiles at the region under the channel influence (Table 5.1 – page 123).

As shown by the modelling experiments, the main changes in water level in relation to the measured pier water level occur close to the channel region where the pressure gradients

are high. Only small deviations (<0.05 m) affect the region further northward in the cameras field of view. At this region the water level considered in the image processing is the one measured at the pier. Example comparison profiles at this region are Profiles 7, 8 and 9 (Figure 5.13, with positions indicated in Figure 5.11).

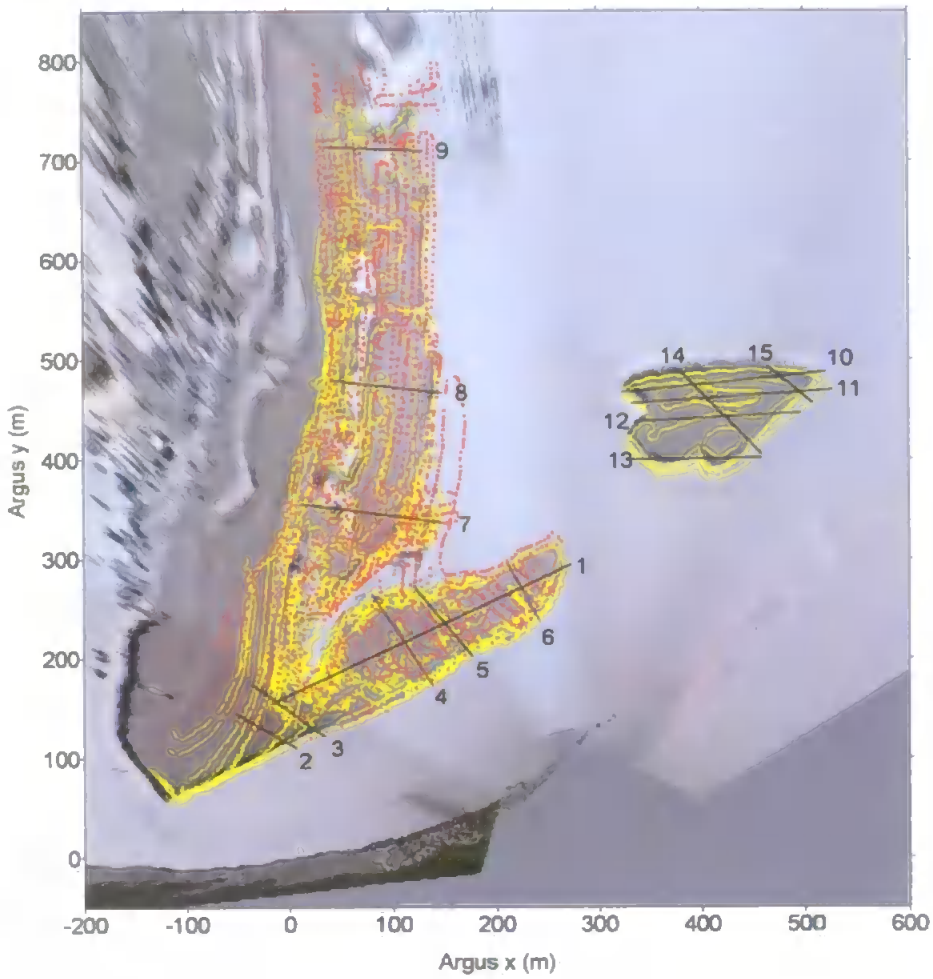

Figure 5.11. Validation profiles of the morphology extraction technique from the video images. Yellow contour lines are the shorelines extracted from the images; red dots are the surveyed points; and black lines are the compared profiles indicated by the numbers. Survey carried out on 25 – 27/10/99 and image from the 26/10/1999. Contour lines were extracted from images covering a two day interval (26 – 27/10/1999).

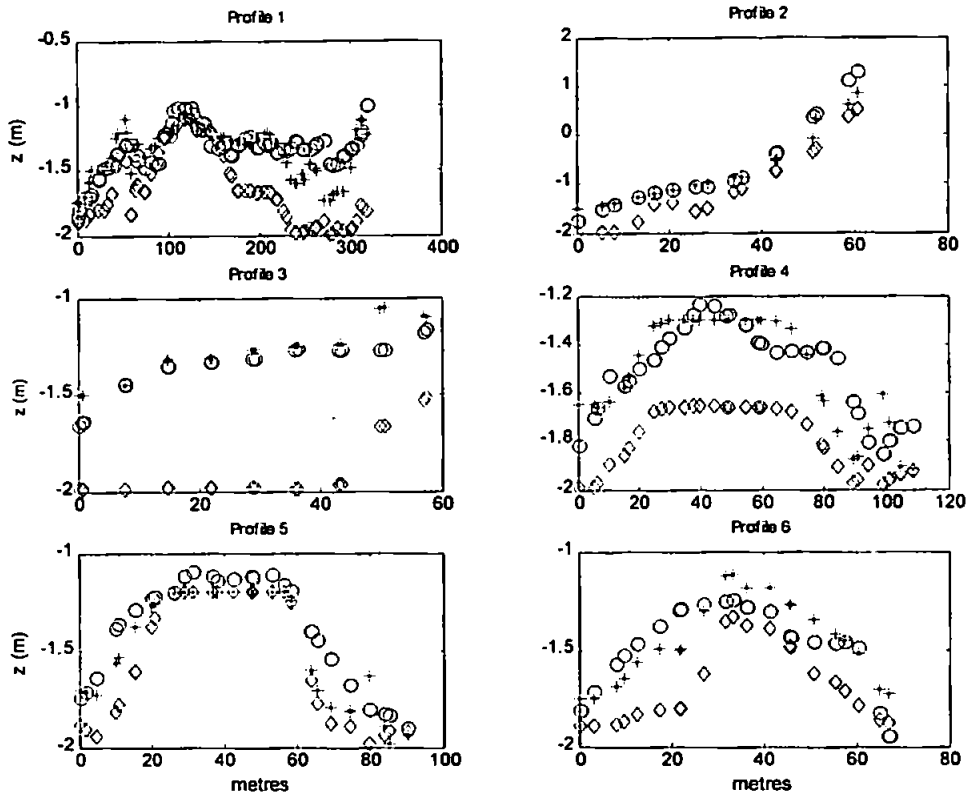

Figure 5.12. Comparison of measured morphology profiles (circles) and extracted from images using the modelled water level (stars) and a constant water level (diamonds) at the Sprat sandbar for the 26-27/10/1999. Profile locations are shown in Figure 5.11.

Morphology comparison over the offshore sandbar is based on the COAST3D ship survey of the region. For this comparison it is important to be aware of the relatively high measurement errors that can occur at this region, with values of up to 0.25 m (Van Rijn et al. 2000 – Chapter 3). Compared profiles are 10 to 15 indicated in Figure 5.11 and compared with measurements in Figure 5.14. Profiles over the sandbar are approximately overlaid to the measurement transects.

The offshore sandbar is also under the influence of the channel pressure gradients, and both constant and modelled water levels are applied in the comparison. The southern side of the sandbar is the most influenced by the channel water slope, while at the northern side only small variations are detected. RMSE values are slightly lower for all compared profiles when using the varying water levels (Table 5.1), with major improvement in accuracy for Profiles 13 and 14 (RMSE values are approximately halved). The transects of

these profiles include the region under the influence of the channel water levels, resulting in a better profile estimate from the images when applying the modelled water levels.

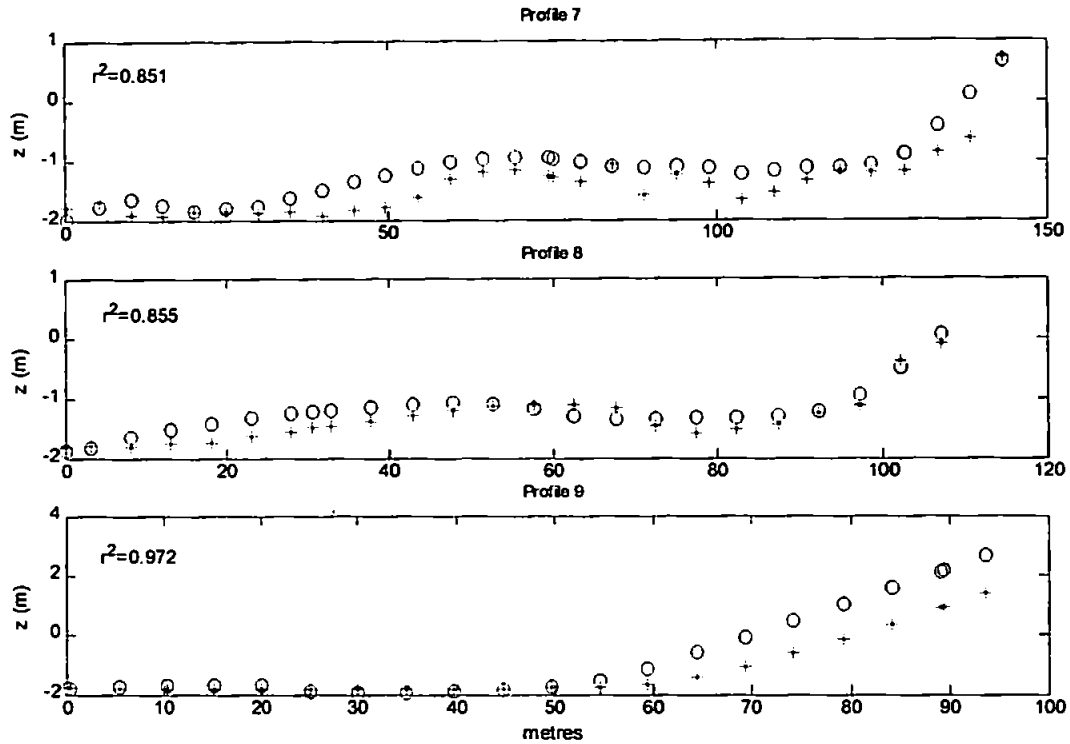

Figure 5.13. Comparison of measured morphology profiles (circles) and extracted from images (stars). Profile locations are shown in Figure 5.11.

Another opportunity to assess the accuracy of the technique applied to extract the intertidal morphology from images is the survey carried out in July 2000. This survey covers in detail the straight sandbar attached to the beach, distant approximately 450 m from the cameras (Figure 5.15). As the modelling experiments for this morphological situation show that this region is under only small differences in water level in relation to the levels measured at the pier, the water level is assumed to be spatially horizontal for the image processing at this region.

Profiles represented in Figure 5.15 and 5.16 show the compared morphology of the attached sandbar. The extracted morphology represents well the surveyed one, with low

RMSE values (Table 5.1) and high r^2 values for the compared points (Figure 5.16). The excellent agreement between measured morphology and the one extracted from images confirms that, when considering this region, the use of spatially constant water levels represents reality well.

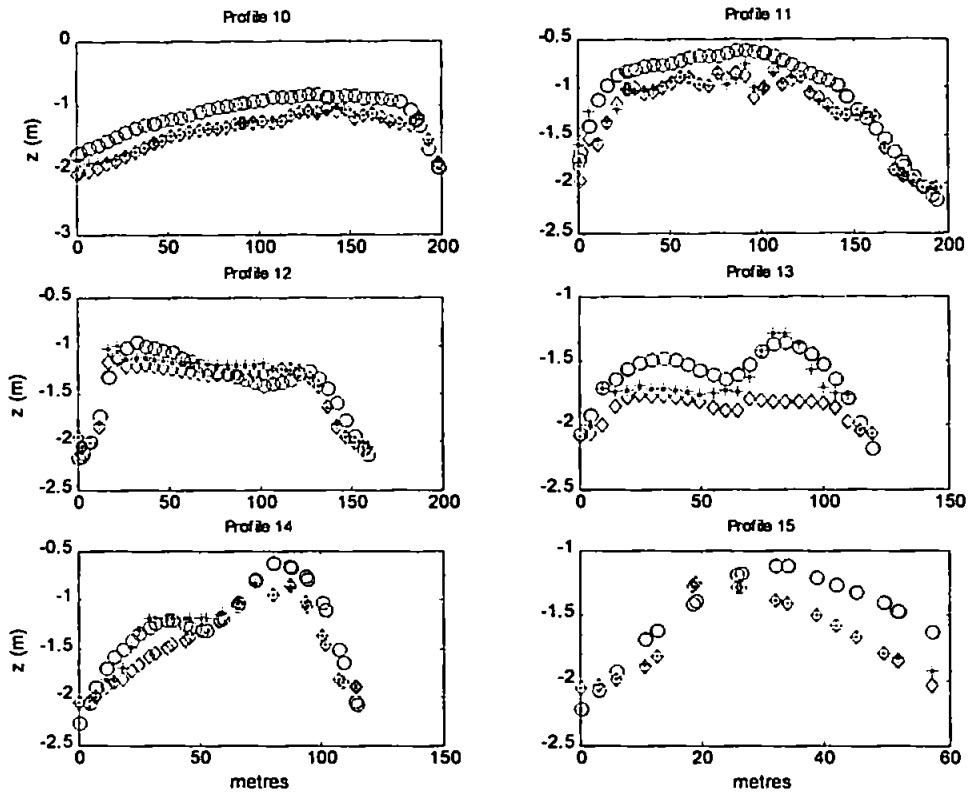

Figure 5.14. Comparison of measured morphology profiles (circles) and extracted from images using the modelled water level (stars) and constant water level (diamonds) at the offshore sandbar for the 26-27/10/1999. Profile locations are shown in Figure 5.11.

The only opportunity to test the accuracy of the application of modelled water levels based on the previous morphological stage for the image processing (applying the method described in items 5.3.2 and 5.3.3) are three surveyed profiles over the Sprat sandbar at the 30th of August 2000. For the extraction of the intertidal morphology at this stage, the water levels modelled for the May 2000 situation are used. Boundary conditions used in the numerical model represent the August 2000 period; however, the previous morphological

conditions (May 2000) are used, completing the loop between the image processing and numerical modelling. Results are shown in Figure 5.17 for the three profiles under the influence of the channel, and show an overall good agreement when compared to the measurements, with high r^2 values. RMSE values are also low for these comparisons (Table 5.1).

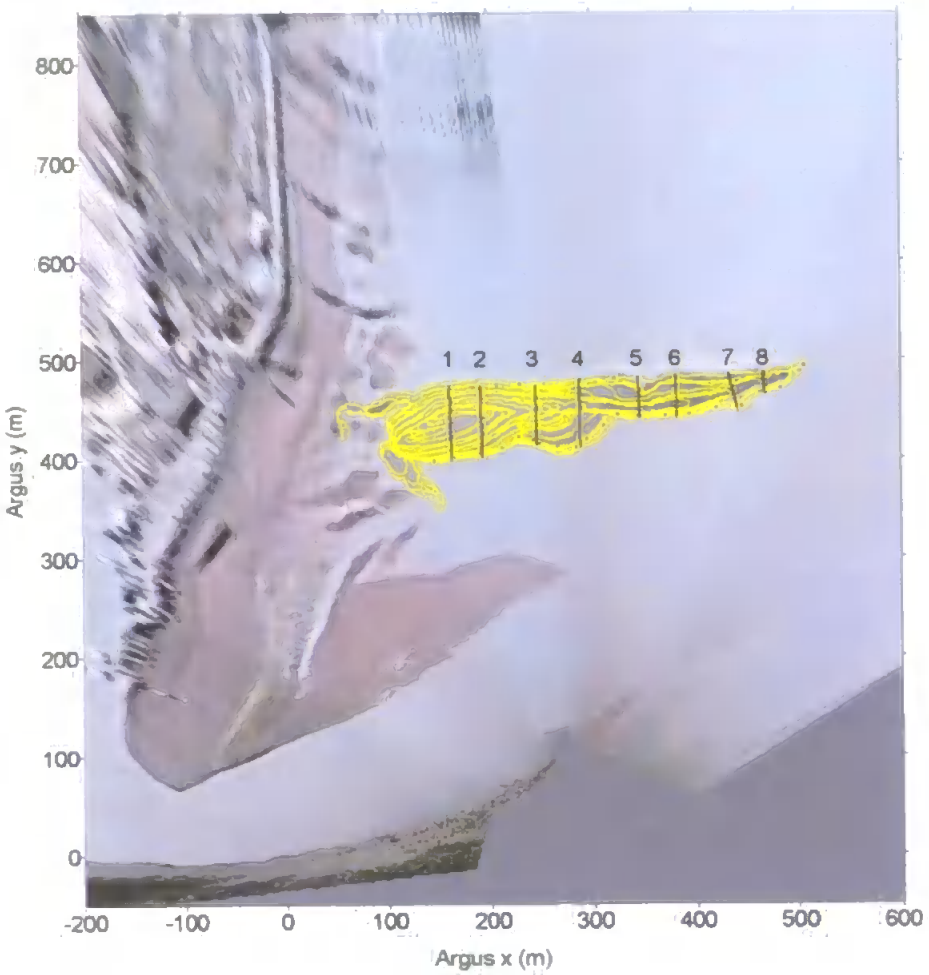

Figure 5.15. Validation profiles of the morphology extraction technique from the video images. Yellow contour lines are the shorelines extracted from the images; red dots are the surveyed points; and black lines are the compared profiles indicated by the numbers. Survey and image from the 05/07/2000. Contour lines were extracted from images covering a three day interval (04 – 06/07/2000).

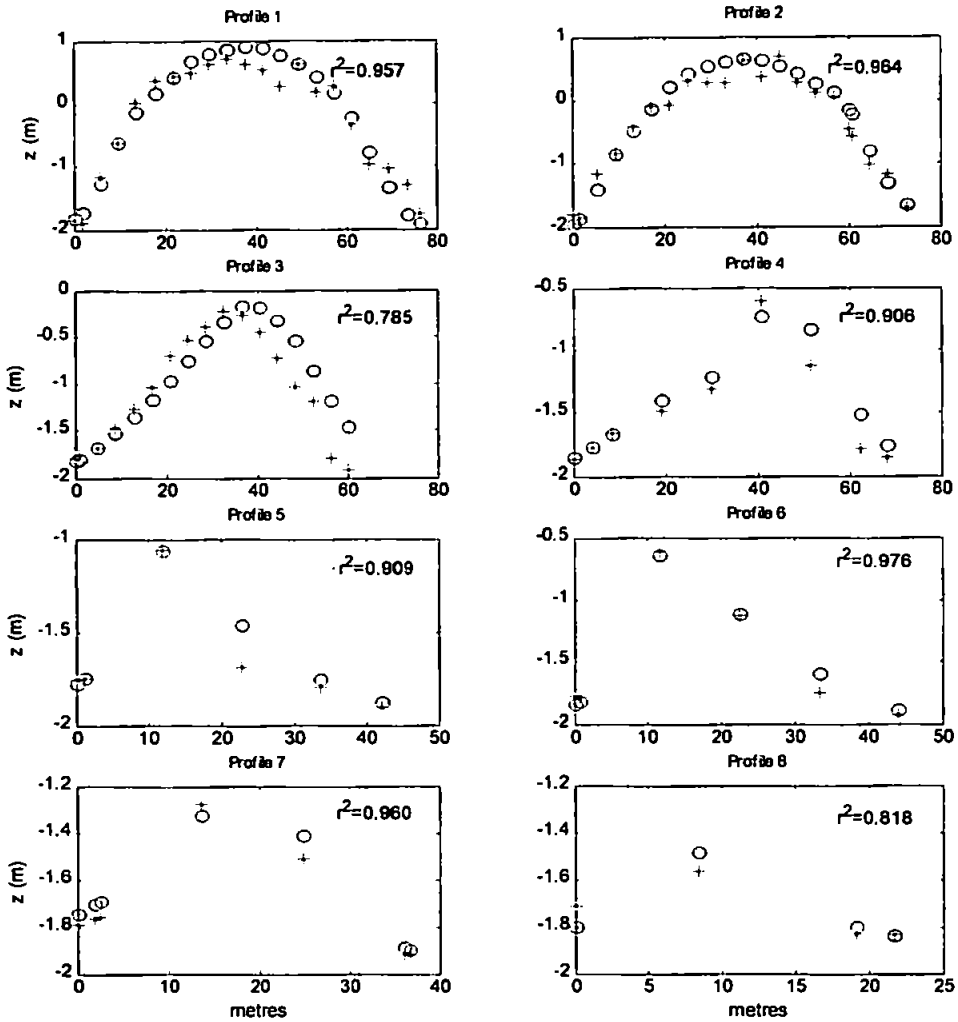

Figure 5.16. Comparison of measured morphology profiles (circles) and extracted from images (stars) at the attached sandbar for the 05/07/2000. Profile locations are shown in Figure 5.15.

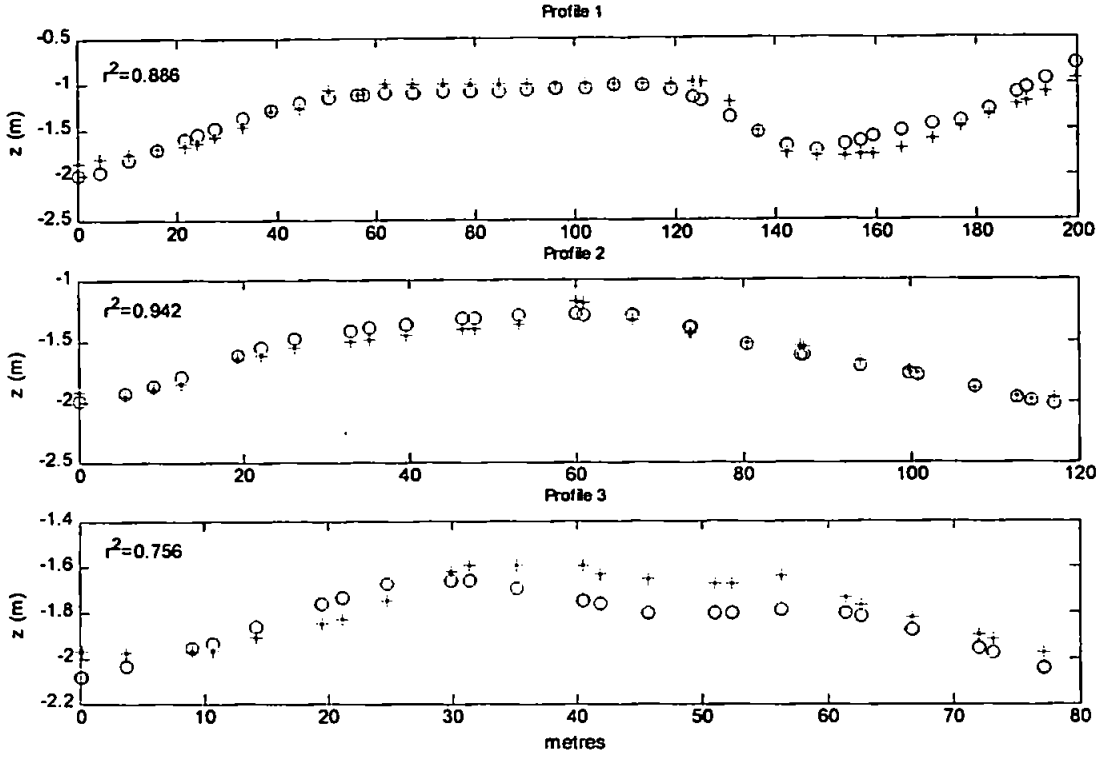

Figure 5.17. Comparison of measured morphology profiles (circles) and extracted from images (stars) using the modelled water levels with the previous morphology. These profiles were extracted from 30/08/2000 images using modelled water levels from the previous model runs (May 2000 morphology).

These results show that the contouring technique applied for the morphology extraction from images results in good approximations of the measured intertidal morphology, representing the overall morphology with relatively small errors (with averaged RMSE of about 0.15 m). The application of varying modelled water levels results in an increased accuracy in the image processing at regions under the influence of high pressure gradients (e.g. the inlet channel). Water level differences of up to 0.80 m at the channel region highlight the importance of the use of spatially varying water levels when extracting the morphology from images at such regions.

Table 5.1. RMSE* (m) values of the compared profiles.

	Sprat sandbar, beach and offshore sandbar (26/10/1999)		Attached sandbar (05/07/2000)	Sprat sandbar (30/08/2000)
	modelled water level	constant water level	constant water level	modelled water level
profile 1	0.152	0.382	0.227	0.111
profile 2	0.226	0.508	0.191	0.062
profile 3	0.096	0.565	0.282	0.090
profile 4	0.128	0.300	0.143	
profile 5	0.120	0.202	0.094	
profile 6	0.124	0.266	0.072	
profile 7	N/A	0.330	0.058	
profile 8	N/A	0.201	0.064	
profile 9	N/A	0.709		
profile 10	0.285	0.296		
profile 11	0.229	0.237		
profile 12	0.131	0.132		
profile 13	0.135	0.283		
profile 14	0.183	0.226		
profile 15	0.242	0.253		

* Root Mean Square Errors (RMSE) of the compared profiles were calculated through $RMSE = \sqrt{\sum (z_e - z_m)^2 / n}$, where z_e are the extracted elevations, z_m are the measured elevations and n is the number of compared points.

5.5. Application

As described in the previous sections, the application of the combined use of numerical modelling and video imaging is carried out in order to obtain a number of morphological stages that represent the main changes in the sandbar configurations at Teignmouth. The nearshore morphology generated from merging the changing intertidal morphology with the constant subtidal bathymetry is then used for a series of modelling experiments. From the observed morphological evolution through rectified video images (Chapters 6 and 7), four morphological stages are identified that represent the main configurations in the evolutionary cycle. However, in order to apply the video imaging techniques with improved accuracies due to the modelled water surface topography, ten stages of the three-year cycle are chosen (see Table 5.2).

The first two stages are based on surveys carried out during the COAST3D project (March and October 1999), and the remaining eight (January, May, August 2000; February, May, September 2001; January, April 2002) are based on the intertidal morphology extracted from the video images. These stages were selected in order to allow the application of the loop between the numerical model and video images (Figure 5.9). In Table 5.2 the selected stages are indicated with a summary of the available boundary conditions for the numerical model application.

The nearshore morphology of the eight stages extracted from the interactive application of modelled water levels and image processing are represented in Figure 5.18. These nearshore morphologies are the "changing" part of the model grid, with the estuary and remaining offshore bathymetry being considered constant over the studied period. Separate numerical modelling experiments carried out in Chapter 7 apply these morphologies in order to study the sediment transport and its controlling processes for each morphological stage.

Table 5.2. Stages chosen for the numerical modelling and image processing.

		Bathymetry	Modelled water levels for image processing based on	Model boundary conditions		
				water lev.	waves	river disch.
1999	March, 24	survey		meas.	meas.	meas.
	October, 26	survey		meas.	meas.	meas.
2000	January, 23	image	October 1999 morphology	pred.	meas.	meas.
	May, 7	image	January 2000 morphology	pred.	N/A	meas.
	August, 31	image	May 2000 morphology	meas.	meas.	meas.
2001	February, 11	image	August 2000 morphology	pred.	meas.	meas.
	May, 08	image	February 2001 morphology	pred.	N/A	meas.
	September, 19	image	May 2001 morphology	meas.	meas.	meas.
2002	January, 1	image	September 2001 morphology	meas.	meas.	meas.
	April, 28	image	January 2002 morphology	meas.	meas.	meas.

meas. = measured; pred. = predicted; N/A = not available.

January 2000

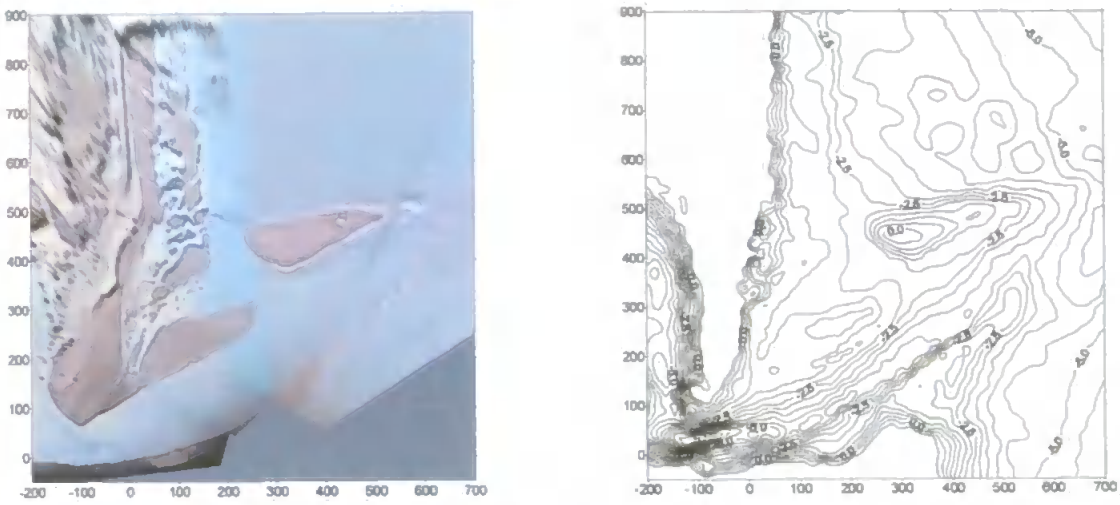

May 2000

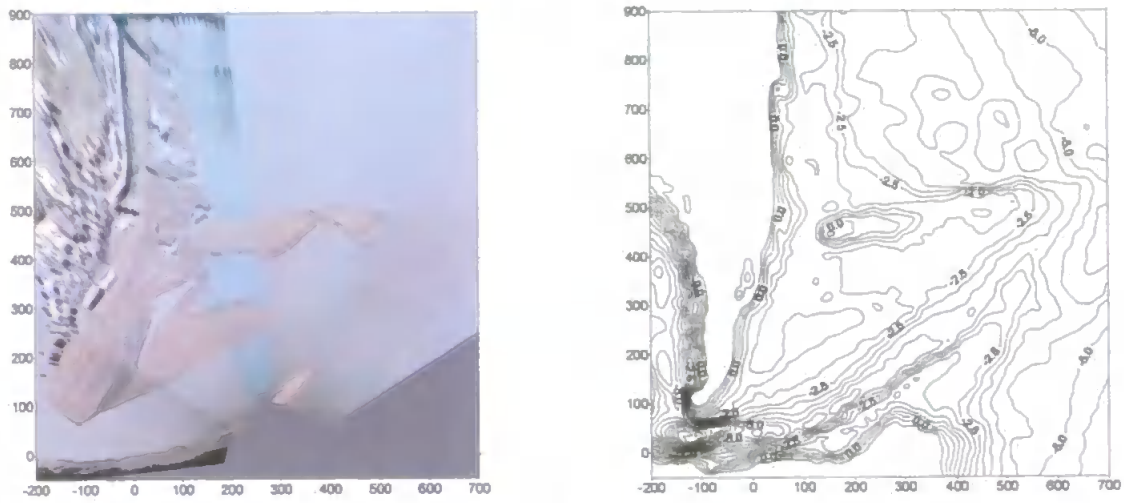

August 2000

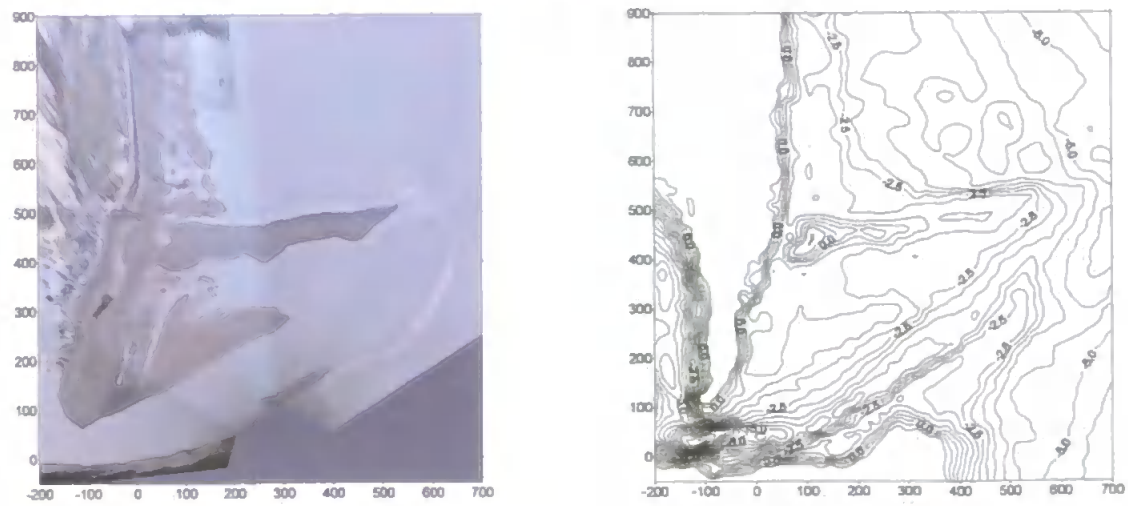

Figure 5.18 (continued next page).

February 2001

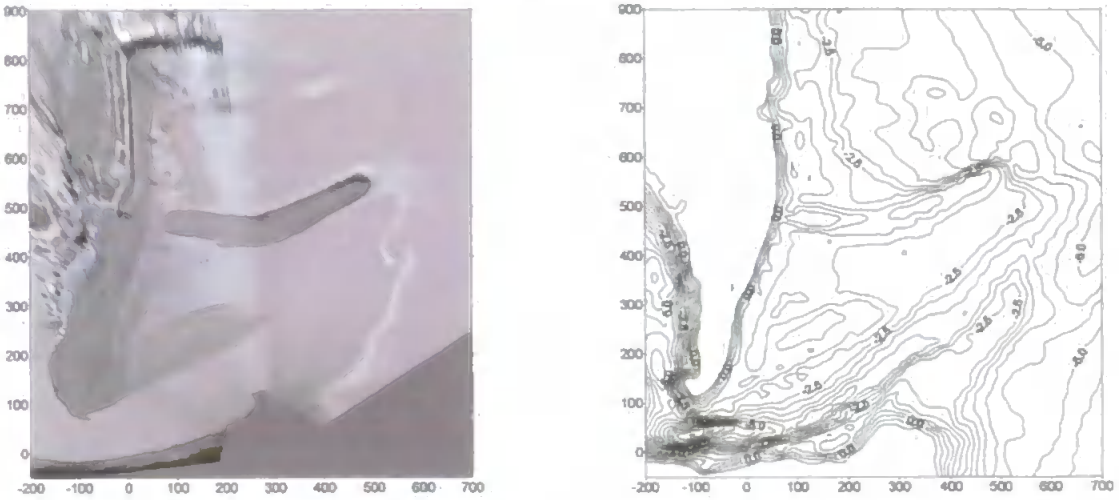

May 2001

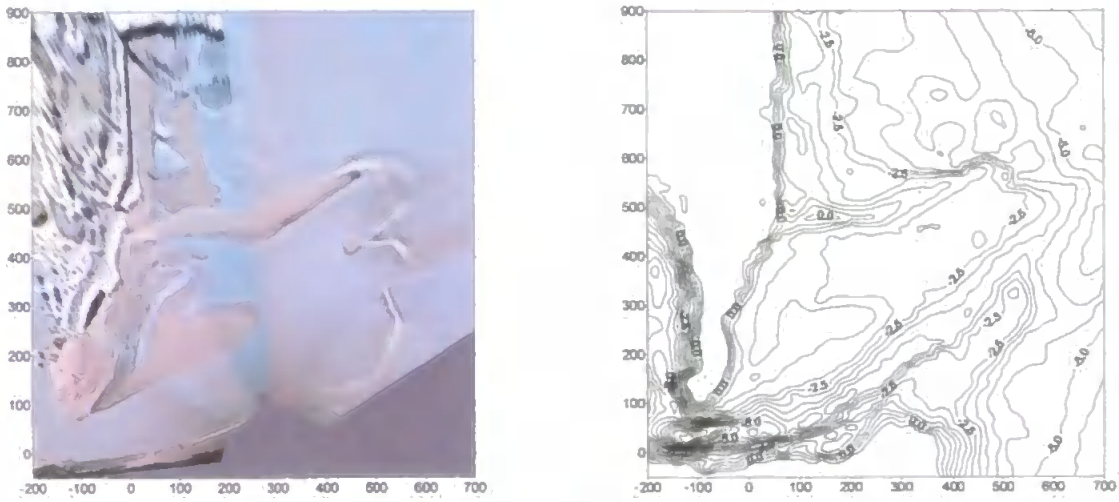

September 2001

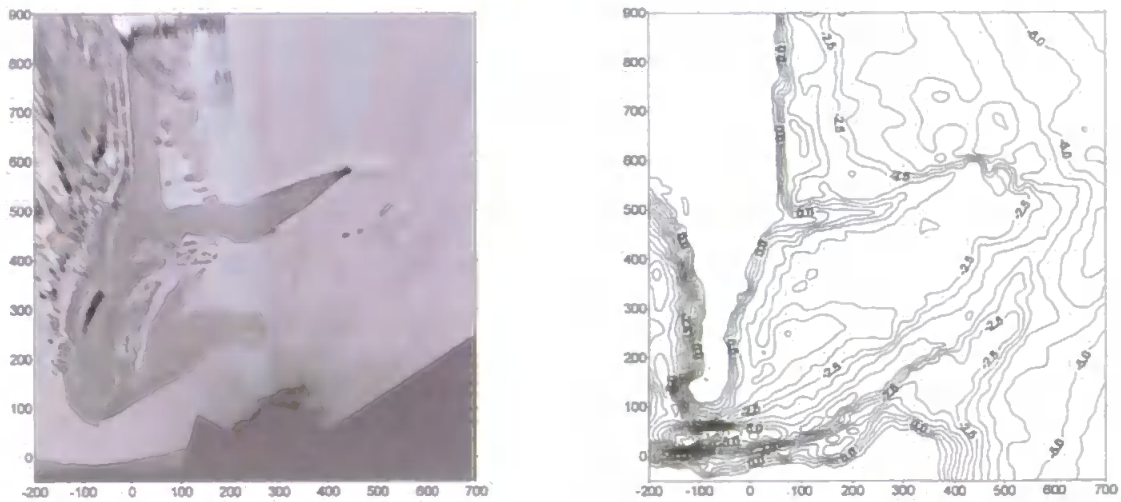

Figure 5.18 (continued next page).

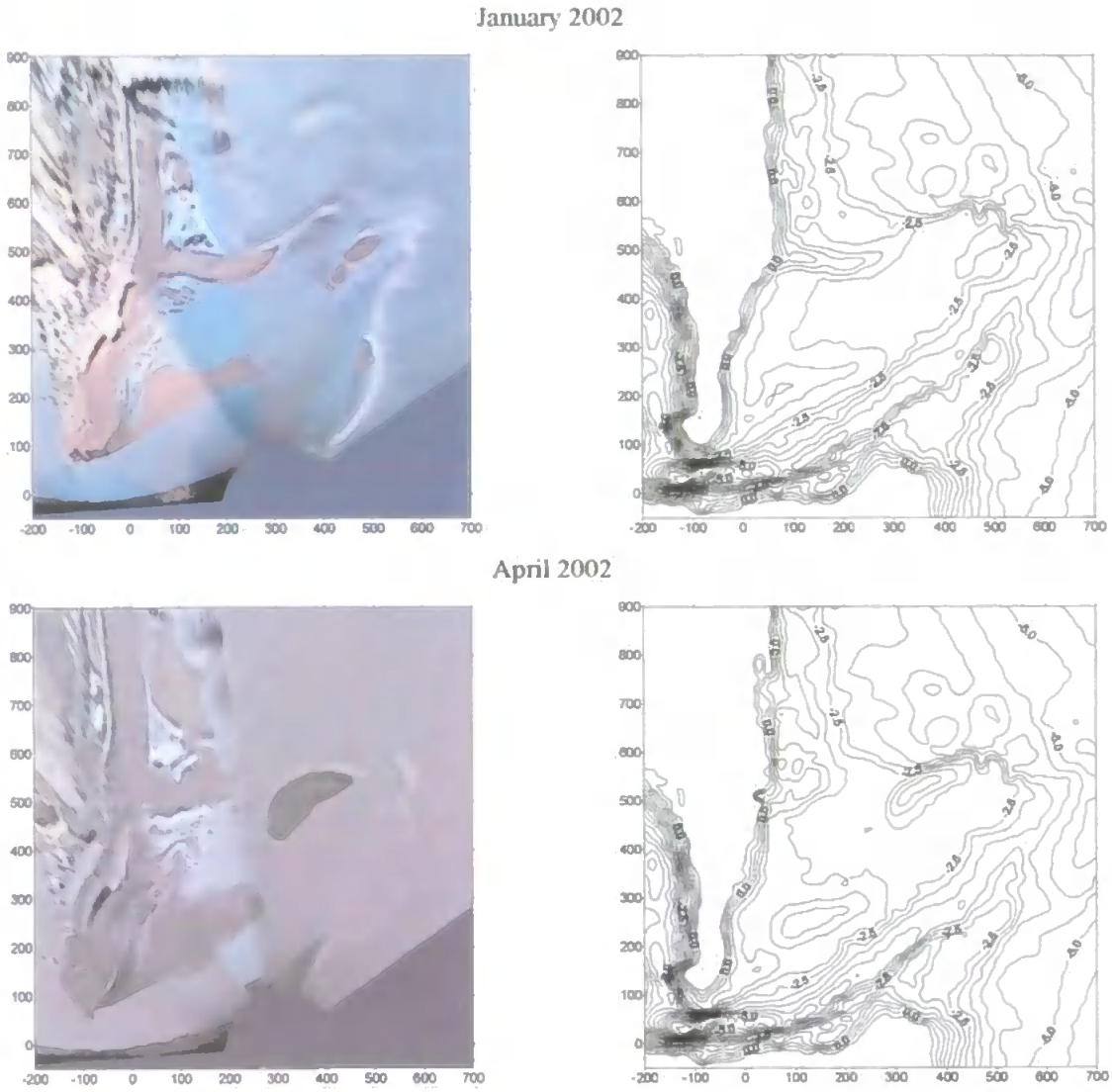

Figure 5.18 (continued). Rectified images and nearshore morphology for each of the modelled periods using the extracted intertidal morphology with constant subtidal morphology. These morphologies are applied in the modelling experiments (Chapter 7).

5.6. Discussion and Conclusions

The overall aim of this chapter was to describe and apply a technique to extract the intertidal morphology from video images with the purpose of applying it in a numerical area model, thus increasing the time-scale of its application. The applied technique is based on the same principle of previous techniques applied for the shoreline extraction from

images (e. g. Plant and Holman, 1997; Davidson et al., 1997; Janssen, 1997; Aarninkhof and Roelvink, 1999; Kingston et al., in prep.). This principle is the detection of the shoreline location at a number of instances during a tidal cycle, assuming the vertical elevation of the shoreline as being the local water level. However, the main difference in the method applied in this study is the application of modelled spatially varying water levels across the region of interest for the image processing.

As shown by measurements (COAST3D project) and numerical modelling experiments (section 5.3.1 and Siegle et al., 2002) the inlet channel at Teignmouth is highly influenced by the pressure gradient existent between the estuary and the adjacent nearshore region. As the processing of images is dependent on the local vertical elevation, the inclusion of differences in the water level across the channel region is shown to be very important to obtain the correct horizontal position of the shoreline and its associated vertical elevation.

Despite the contouring technique being simple and limited to greyscale images, it is able to define well the contours that best represent the shoreline in most cases. This means that it is able to solve part of the problem of morphology extraction from images, by locating the U_i and V_i coordinates of the shoreline in an oblique image. The second part of the process is the application of the photogrammetric relations to convert the detected U_i, V_i positions in the oblique image into x, y, z ground coordinates. This part is considerably improved by applying accurate water levels, since they are used in the photogrammetric relations to rectify the coordinates and for the intertidal map definition of vertical elevations.

When the morphology extraction is aimed at regions out of the influence of the inlet channel pressure gradients, the assumption of spatially horizontal water levels is accurate and results in good estimates of the morphological features from the images. Examples of this case are shown in the profiles compared over the straight attached sandbar (Figure 5.16). At this case the intertidal map can be reproduced with an overall residual error of about 0.19 m. However, at regions where the water levels present high differentials in relation to the level measured at the pier, large variations in the horizontal and vertical position occur if these differences are not considered in the image processing. This problem is clearly verified through the compared profiles over the Sprat sandbar, where the use of the measured water level at the pier resulted in a residual error of 0.37 m for the extracted intertidal morphology. At some locations (profiles 2 and 3 – Figure 5.11 and

5.12) this error can reach values of over 0.5 m. Applying the modelled water levels results in an improved reproduction of the intertidal morphology, with the overall error being 0.14 m over the Sprat sandbar (for all compared points). At profiles 2 and 3 (which presented errors larger than 0.5 m when using constant water level) the errors are reduced to 0.22 and 0.09 m respectively (Table 5.1).

The iterative application of the numerical model and image processing for the temporal extension of the modelling experiments uses as a start point the model calibration and validation period (October 1999 – Chapter 4). It is then applied at eight different stages of the cycle, and at each stage, the morphology extracted from the images is dependent on the water surface topography modelled using the previous nearshore morphology (Table 5.2). Limitations arise from the assumption of constant subtidal morphology and constant morphological conditions between the eight analysed stages. However, the validation of the extracted morphology from images using this principle shows an excellent agreement between measured and image derived morphology. An overall residual error of 0.09 m is found for the three profiles compared in August 2000, based on modelled output using the May 2000 morphology (Figure 5.17 and Table 5.1). This is the only situation with available measurements for the validation of the temporal extension of the modelling experiments. A different way of assessing the accuracy of the application is an indirect validation carried out through the comparison of sediment transport patterns and the general movement of the sandbars (as discussed in Chapter 7).

Despite some limitations, the application of the described technique to obtain the nearshore morphology for numerical modelling simulations at different stages of the evolutionary cycle at Teignmouth shows promising results. In the absence of *in situ* surveyed data from the region of interest at short time intervals, this application provides a good approximation to the observed morphological changes. In order to summarise, a list of advantages and limitations of the application is given below.

Advantages:

- the contouring technique applied to define the U_i and V_i coordinates of the shoreline is simple and available in the MATLAB® image processing toolbox;

- through the application of modelled water levels, spatially varying levels can be applied in the image processing;
- by merging the extracted morphology with the surveyed subtidal bathymetry, the resultant nearshore morphology can be applied in the numerical model;
- the intertidal mapping of relatively large areas can be achieved on a daily basis;
- the loop between the numerical model and image processing in the applied method allows the temporal extension of the application of the numerical model;
- errors in the estimates of water levels across the region applying the model interactively with images can always be reduced by increasing the temporal resolution of the application;
- the method reproduces well the main measured morphological features.

Limitations:

- the efficiency of the contouring technique depends on the contrast in the images;
- intertidal maps extracted from images present larger errors than the ones expected by traditional surveying techniques;
- vertical coverage of the extraction technique depends on the tidal range;
- when merging the extracted morphology with the surveyed subtidal bathymetry, the subtidal morphology is assumed to be constant since the last available survey (October 1999);
- when extending the application of the technique to different stages of the evolutionary cycle, the modelled water levels applied for the next stages are modelled under slightly different morphological conditions to the ones of the day of the image processing;
- the use of modelled water levels increases the amount of user input in order to apply the technique.

The nearshore morphologies obtained here are applied in the modelling experiments carried out to study the processes controlling the local sediment transport and sandbar dynamics. The modelled sediment transport patterns discussed in Chapter 7 also provide an indirect validation of the applied model when compared to the observed morphological changes from video images.

Chapter 6

Physical Controls on the Sandbar Dynamics

6.1. Introduction

Previous chapters have defined the tools and analysis techniques used to model the Teign inlet sandbars. These techniques are used in this chapter and in Chapter 7 to investigate the processes that control the local sediment transport and morphodynamics.

The objectives of this chapter are to identify and assess the relative importance of the controlling processes across the complex sandbar dynamics at the inlet system. This allows the determination of the regions dominated by wave processes or by tidal processes and to define the variability of these regions under different wave, tide and run-off conditions. Knowledge of the main physical processes acting at the inlet system forms the basis for the study of the system at different stages of the evolutionary cycle (Chapter 7). Part of this chapter has been published by the author in Siegle et al. (in press).

The chapter structure includes a brief description of the numerical experiments carried out in order to assess the relative importance of different physical forcing conditions. This is followed by the results of the modelled hydrodynamics and sediment transport, with emphasis on the driving forces. Finally, the conclusions of the chapter with a summary of the findings are given, forming the background for Chapter 7.

6.2. Numerical Simulations

Through the application of the MIKE21 HD, NSW and ST modules, several combinations of simulations are carried out.. In this exercise, the experiments are carried out for one stage (October 1999) of the morphological evolution of the system, which is that

encountered during the COAST3D main experiment period (numerical modelling validation period – Chapter 4).

The numerical modelling experiments were designed in order to cover a range of conditions found at the region. They include sets of simulations with different boundary conditions over short period of times (two tidal cycles) and one longer simulation (thirteen days) under measured forcing conditions. The short period simulations include several combinations of forcing conditions, with spring or neap tides combined with waves varying from 0 to 1.8 m (with 0.2 m intervals) and river discharge varying from 5 to 150 $m^3 s^{-1}$ (with 20 $m^3 s^{-1}$ intervals - these values vary between the minimum and maximum measured values over a four year data set). The thirteen-day simulation covers a period with tidal range varying from spring to neap and wave conditions varying from calm to stormy. The measured river discharge over this period was low and constant (of about 8 $m^3 s^{-1}$). Exact forcing conditions during this period are shown later in the chapter.

The short period simulations were designed in order to assess the relative influence of the tidal range, waves and river discharge on the sediment transport. The influence of the tidal range is assessed through simulations with different tidal amplitudes, while keeping the other forcing conditions constant. The same process is carried out for the assessment of the wave influence, where the varying parameters are the significant wave heights (H_{sig}) and wave directions of incidence. In these cases the parameters governing wave breaking were set as suggested by Holthuijsen et al. (1989): γ_1=1.0 (maximum steepness parameter), γ_2=0.8 (maximum *H/d* parameter; *H* is wave height and *d* is water depth) and α=1.0 (adjustable constant).

As described in Chapter 4, the non-cohesive sediment transport formulation chosen for the modelling experiments of sediment transport under currents and waves is the deterministic STP formulation (see Chapter 4 and Appendix I for details).

6.3. General Hydrodynamics

6.3.1. Tidal circulation

The analysis of the *in situ* data and results of the model simulations allow the description of the circulation patterns at the inlet and adjacent nearshore region during a range of distinct conditions. The flow velocity field represented in Figure 6.1 shows the inlet circulation pattern during maximum ebb and maximum flood tide currents at spring tide. Currents in the channel can reach up to 2.0 m s^{-1} during spring ebb and flood tides. Maximum ebb flow occurs during low-tide, with smaller water depths constricting the flow within the main channel, resulting in a jet-like outflow with an associated circular flow pattern on its southern side (Figure 6.1a). In contrast, maximum flood tidal flows occur late in the flood tidal cycle (high tides) when water depths are greater, so the flow is more regularly distributed across the channel and over the sandbars. In the inner part of the inlet, in the curved channel, a gyre is observed in the flood flow, with currents flowing parallel to the sandy spit towards the inlet (Figure 6.1b).

Tidal flow asymmetry varies along the channel with flood dominance close to the estuary mouth and ebb dominance seawards to the inlet entrance. Time series of modelled flow velocities extracted at four points in the main channel including spring to neap tidal conditions show this along-channel asymmetric variability (Figure 6.2). At station 1 (indicated in Figure 6.1a) the maximum flood current exceeds the maximum ebb current by about 40 %, while at station 4, the opposite occurs, with maximum ebb current exceeding maximum flood current by about 75 %. At the intermediate stations 2 and 3, the ebb current is also dominant, exceeding the maximum flood currents by 10 and 50 % respectively, showing the gradual increase in the ebb dominance at the outer part of the channel. This will be reflected in the sediment transport patterns as discussed later in this chapter.

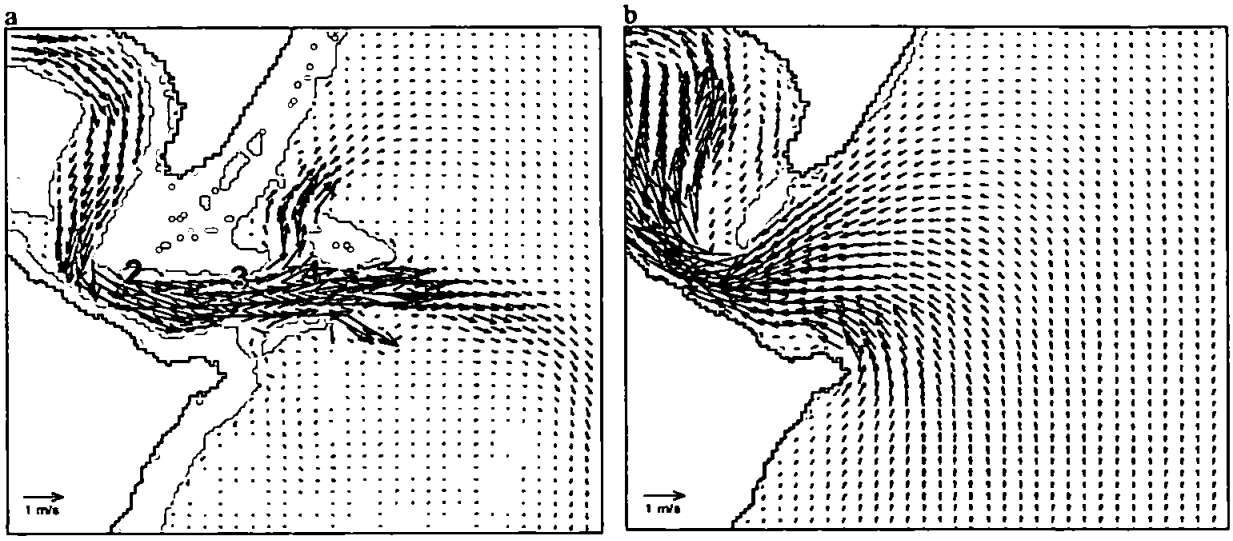

Figure 6.1. Example vector plots indicating the modelled velocity field at the inlet region for maximum ebb (a) and maximum flood (b) conditions. Red numbers in (a) represent the position of the extracted time series shown in Figure 6.2.

6.3.2. River discharge

During the relatively short periods of high river discharge at the Teign river, the freshwater input plays an important role in the Teign inlet, with the tidal prism and river discharge controlling the hydraulics of the system. Model results show that high river discharge events, which are frequent over winter months, may change the hydraulics of the system. The main changes occur during neap tides, when the weaker tidal currents are largely influenced by the run-off, with an increase in the mid-channel ebb flow velocity by approximately 40 % and decrease the flood flow velocity by up to 60 %. During spring tides, when the relative influence of the river discharge on the tidal currents is smaller, high run-off values cause an increase in the mid-channel ebb flow velocity by approximately 20 % and decrease the flood flow velocity by approximately 15 %.

Estimates of quantified classifications of estuarine structure, such as the flow ratio (Simmons, 1955, in Dyer, 1997), provide a general statement of the estuarine structure under the influence of river discharge effects. Simmons (1955) found that when the flow ratio (ratio of river flow per tidal cycle to the tidal prism) is 1.0 or greater, the estuary is

highly stratified, when about 0.25 the estuary is partially mixed, and when it is less than 0.1 it is well mixed. For spring tide conditions, this relation results in a partially mixed (flow ratio of 0.52) classification of the Teign estuary during high river discharges (of about 150 $m^3 s^{-1}$) and well mixed (flow ratio under 0.03) for low discharge (5 $m^3 s^{-1}$) and mean discharge (10.5 $m^3 s^{-1}$ – averaged over four years of observations). During neap tide conditions, high river discharge values result in a stratified estuary, and low and mean discharge result in well mixed conditions. Considering this classification, the Teign estuary can be considered partially mixed (flow ratio of 0.25) when the river discharge is higher than 70 $m^3 s^{-1}$ during spring tides and higher than 30 $m^3 s^{-1}$ during neap tides. Lower river discharges result in a well mixed estuary.

As a consequence, during ebb tides with high river discharges, it is likely that a plume is formed by the buoyant outflow of brackish water from the estuary (Pritchard and Huntley, 2002). However, this does not necessarily mean that a stratified structure is present in the channel region; as it is believed that the plume is formed as the mixed brackish water leaves the main channel when it flows into Lyme Bay (Pritchard*, pers. comm.). From the analysis of X-Band radar images, Pritchard (2000) observed that the first detection of the plume front occurs at approximately 700 m offshore, which is outside of the region of interest of this study.

These considerations are important since the model applied in this study is vertically homogenous. However, as the region of interest is the inlet channel and adjacent nearshore region, one would not expect large influences of vertical stratification in the hydrodynamics and sediment transport in this region.

* Dr Mark Pritchard – School of the Environment/University of Leeds.

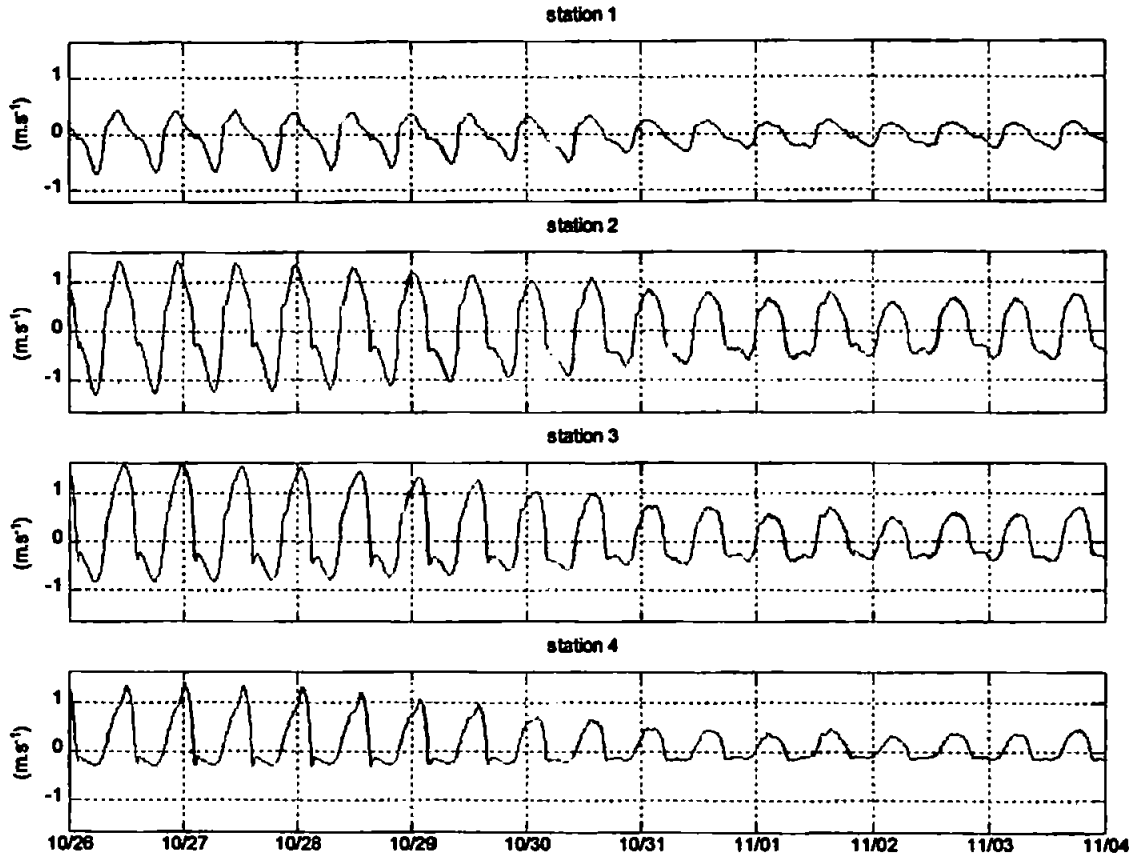

Figure 6.2. Channel *x*-component of modelled current velocities from the mouth to the outer part ranging from spring (26/10/1999) to neap tide (04/11/1999) conditions. Positive values indicate ebb flow and negative represent flood flow. Station positions are indicated in Figure 6.1a.

6.3.3. Wave driven circulation

Teignmouth is protected from the Atlantic swell and the local wave climate is dominated by infrequent periods of relatively small and short period wind-driven waves. These short period waves can be organised in well-defined groups and present swell-like characteristics. Significant wave heights are greater than 0.5 m for 10 % of the year (Miles, 1997). The direction of incidence of the waves is shown in Figure 6.3 for the available directional wave data (measured at 1.5 km offshore during the COAST3D experiments). For the observed period, waves with significant heights greater than 0.5 m reach the coast at an approximately shore-normal angle (115-150°).

High wave energy during storm periods changes considerably the hydrodynamics at the inlet region and beach. In the vector plots in Figure 6.4 some of the main changes in the flow patterns can be seen. The plots show an example of a snapshot of the modelled hydrodynamics during ebb tide with low- and high-energy wave conditions. Comparing these plots, it is clearly visible that the complex circulation in the nearshore region is a consequence of wave action. The regular flows during calm conditions are transformed into complex gyres due to the wave action. At both sides of the sandbars, the breaking waves generate longshore currents (in relation to the sandbar) with an overall onshore direction.

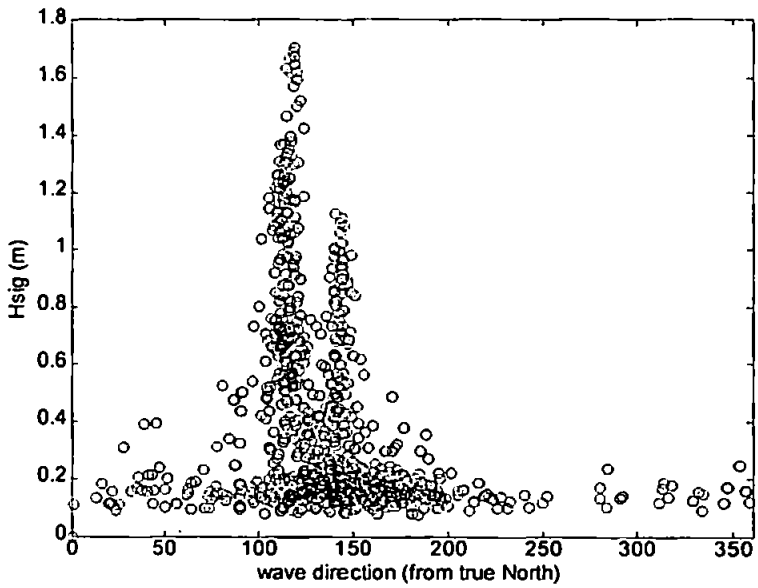

Figure 6.3. Incident wave direction scatter plot.

The wave-current interaction at the ebb tidal jet is also visible, and one of the consequences is the deflection of the main ebbing flow. Depending on the incoming wave direction, the ebb jet can be deflected to either south or north. Figure 6.5 shows an example of flow deflection due to the wave-current interaction during the 12/11/1999 storm, with incoming waves being approximately shore-normal. During low wave energy periods, the ebb jet flows approximately straight out into the bay (Figure 6.5a), while the influence of wave generated currents causes the southwards deflection of the flow (Figure 6.5b).

a. H_{sig} = 0.0 m

b. H_{sig} = 1.25 m

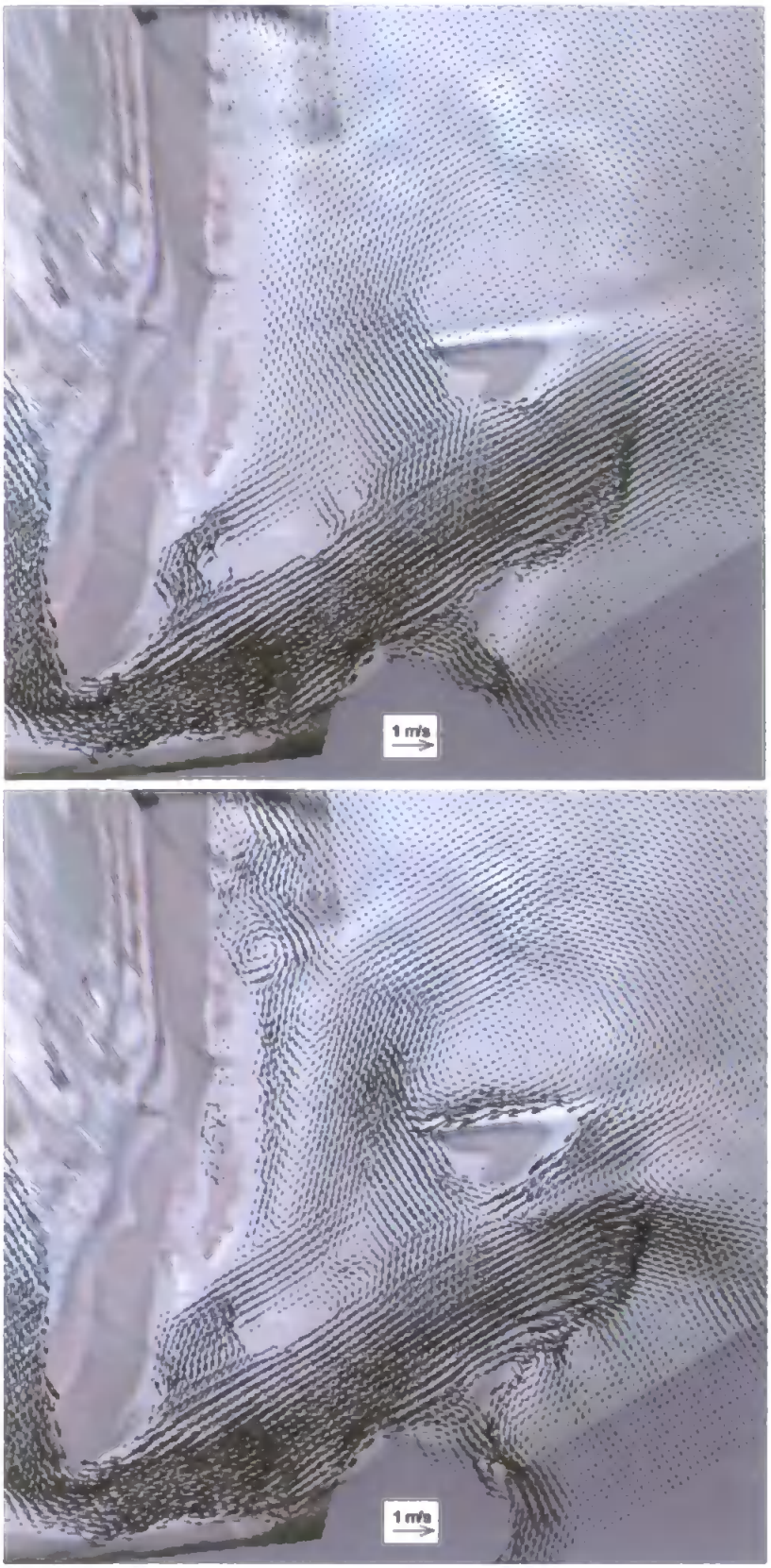

Figure 6.4. Example vector plots indicating the modelled velocity field without (a) and with (b) the presence of waves (12/11/1999 13:00h). Vectors are plotted over the rectified video image of the inlet region for this time.

Another factor that is observed in the modelled wave-current interaction at the outflow of the main channel is the wave shoaling due to the opposing current. When the incoming waves encounter the opposing ebb-flow the peak of the wave height increases and becomes sharper. The position of the peak also moves further offshore, indicating that the wave-current interaction causes the waves to shoal earlier than they normally would, as shown in the example of Figure 6.6. These effects also affect the local sediment transport, with their combined bottom stresses causing sediment mobilisation and hence determining the amount of sediment available for transport (Lyne et al., 1990; Vincent and Downing, 1994; Pan et al., 2001).

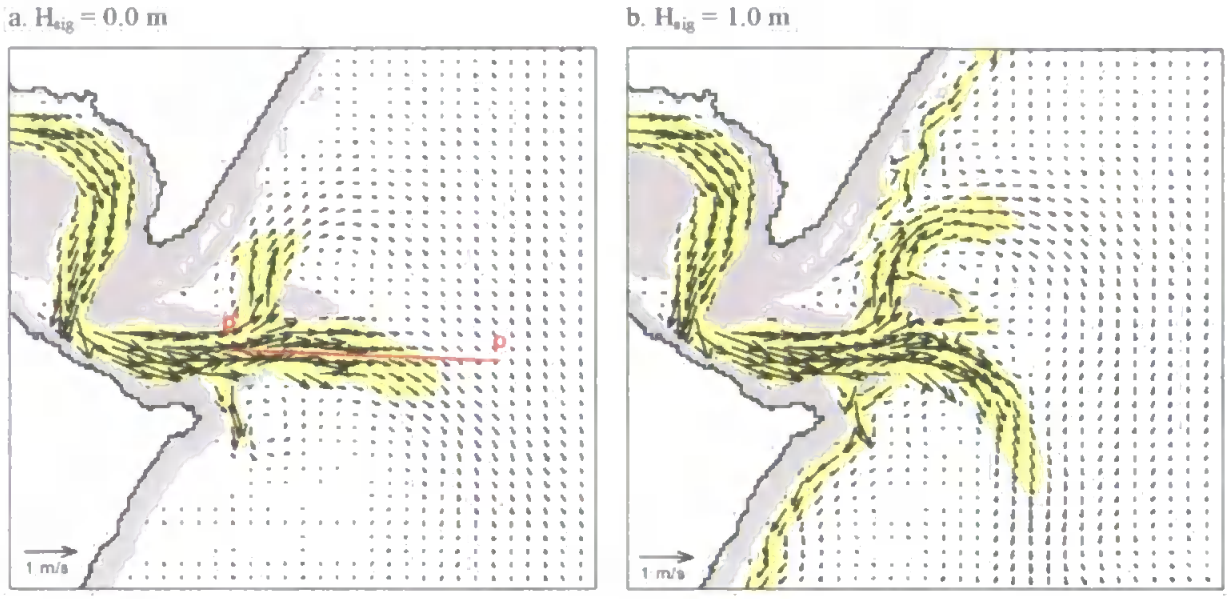

Figure 6.5. Vector plots showing the ebb flow deflection due to the wave action 12/11/1999 00:40h). Yellow shading represents the region where current velocities are higher than 0.2 m s^{-1}. The profile p-p' (a) indicates the position of the profile in Figure 6.6.

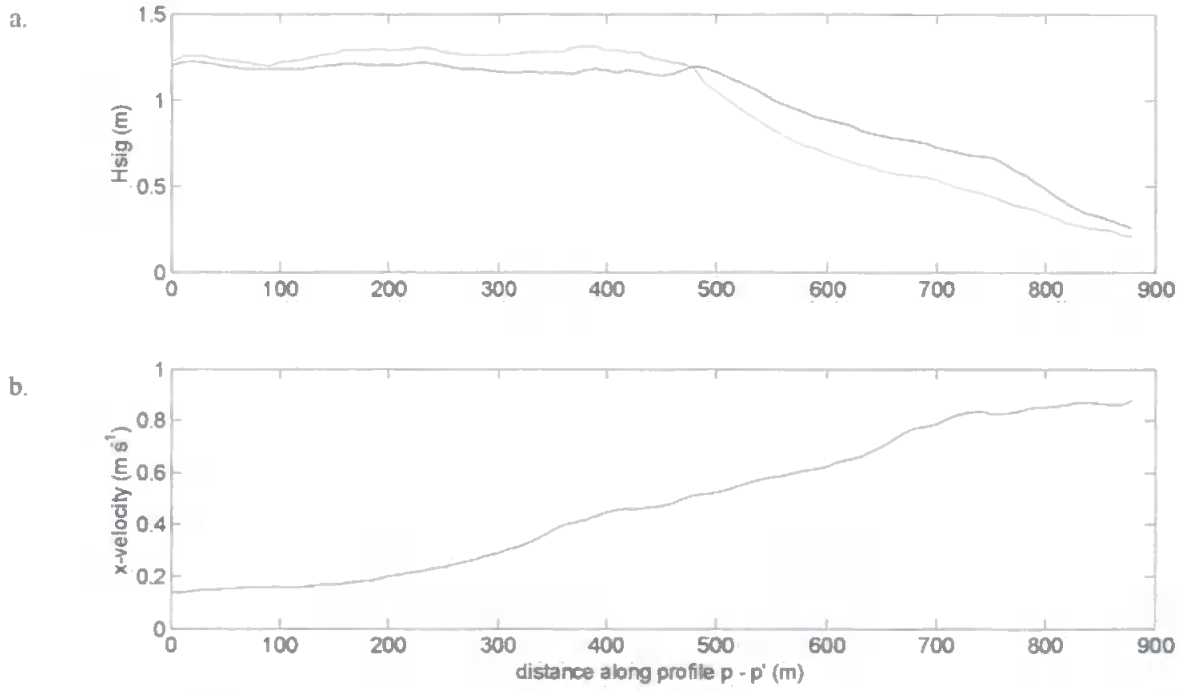

Figure 6.6. Significant wave height for simulations without considering the wave-current interaction (a - black line) and considering the wave-current interaction (a - blue line) and the *x*-velocity component along the profile (b) along the profile p-p' indicated in Figure 6.5 (12/11/1999 11:00h). The profile starts offshore.

6.4. Sediment Transport

The overall physical controls that drive the sediment transport at the sandbar system are described for the October/November 1999 situation surveyed during the COAST3D main experiment. The understanding of the processes driving the sediment transport derived from this specific morphological state allows the definition and spatial distribution of the main acting processes across the region.

6.4.1. General Sediment Transport Patterns

Sediment transport patterns across the region are described based on model simulations under different conditions. Tidal range, waves, and river discharge were the main parameters varied to determine their influence on the sediment transport and consequent morphodynamics. Modelled results show that, independent of the nearshore morphology, the overall sediment transport pattern at the inlet region is controlled by the interaction of tidal currents, waves, and river discharge. Figure 6.7 shows schematic diagrams based on the model outputs of the general sediment transport patterns over two tidal cycles (25 hours) of spring tide (tidal range of 4.4 m) and neap tide (tidal range of 1.2 m) under different wave conditions.

Simulations during spring tide (tidal range of about 4.2 m) with low wave energy conditions (significant wave heights ≤ 0.2 m) and low river discharge (8 $m^3 s^{-1}$) show that sediment transport is restricted to the main channel (Figure 6.7a). As shown in bedload transport studies at other inlets, flow asymmetries in tidal channels produce large net transport rates (e.g. Dalrymple et al., 1978; Pickrill, 1986; Smith and FitzGerald, 1994; FitzGerald et al., 2000a; Williams et al., 2003). In Teignmouth, the flood dominance close to the inlet mouth and ebb dominance in the channel seaward to the inlet entrance is reflected in the sediment transport rates, which are divided into a main seaward transport and a secondary landward transport at the inlet mouth. The flood dominance at the inlet mouth allows part of the sediment that reaches the channel to be transported into the estuary, providing sediment to the flood tidal delta. However, due to the predominant ebb dominance in the channel, the majority of sediment transported to the channel is redirected

seawards and deposited on its offshore end. This deposition that occurs with the decrease in the ebb flow velocities in the outer part of the channel results in the formation of the "U" shaped submerged ebb shoal.

The main sediment input to the channel during low wave energy conditions occurs through the flood channel that is directed parallel to the sandy spit at the inlet mouth (location D in Figure 6.8). No sediment transport is registered outside the channels of the inlet system during calm conditions. During storm conditions, with significant wave heights of up to 1.8 m, the sediment transport pattern changes outside the main channel. Wave induced longshore currents add sediment to the system from the north and south, providing more sediment to be transported by the tidal currents in the main channel. This result contradicts the idea of the system being a closed self-contained unit of sediment as proposed by Robinson (1975). From the modelled sediment transport patterns it is clear that there is an exchange of sediments between the sandbar system and adjacent regions. Addition of sediment to the system via longshore currents and offshore loss of sediment through the channel during high-river discharge in the winter months seem to control the sediment volume in the system. Exchange of sediment also occurs between the ebb- and the flood-tidal delta. As discussed earlier, under low-river discharge conditions, part of the sediment in the main channel is redirected landwards being deposited on the flood tidal delta. However, with increasing river discharge, net sediment transport in the channel occurs only in the seaward direction and part of the flood tidal delta sediment is transported seawards back to the ebb tidal delta system. Weaker tidal flows during neap tide conditions (with tidal range of about 1.2 m) cause only little sediment transport in the main channel. The general sediment transport patterns are similar to those registered during spring tide conditions, but due to the weaker tidal flows, they occur in much smaller magnitudes in the channels (Figure 6.7b). During storm conditions, sediment transport outside the main channel is mainly concentrated over the wave dominated shoals (sandbars), as the small water level variation reduces the effects of wave action across the deeper marginal regions.

Wave generated currents also redistribute the sediment deposited by the tidal currents at the outer part of the channel (submerged sandbar) transporting it mainly northwards in the direction of the offshore sandbar. Under these conditions, the south to north sediment bypass through the channel is also adding sediment to the offshore sandbar. Net sediment transport over the offshore sandbar is shorewards (as discussed later in section 6.4.2).

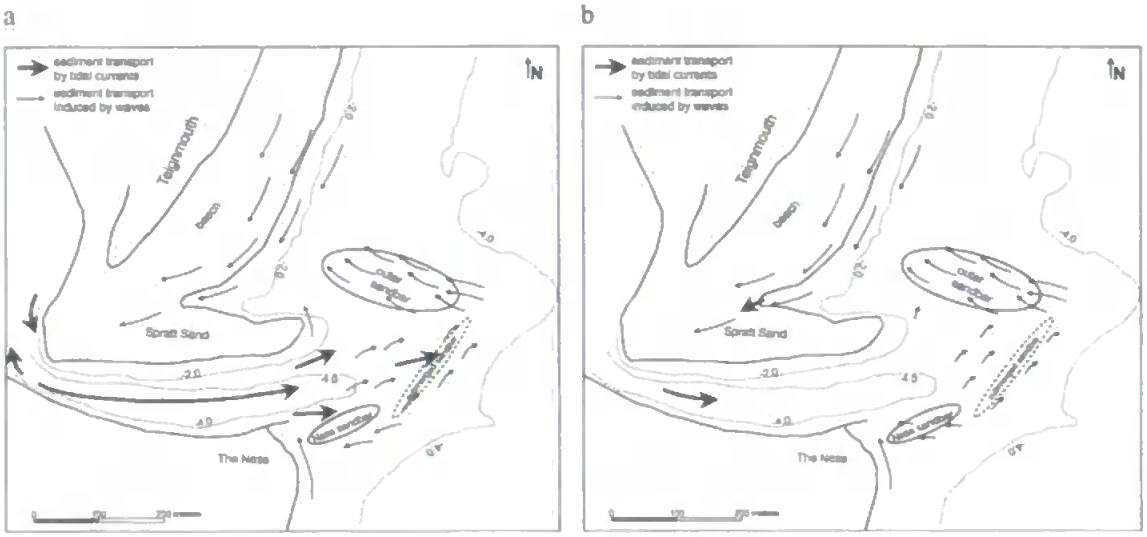

Figure 6.7. Schematic diagrams of calculated sediment transport patterns averaged over two tidal cycles for a) spring tide and b) neap tide. Arrow lengths are schematically related to strength of transport.

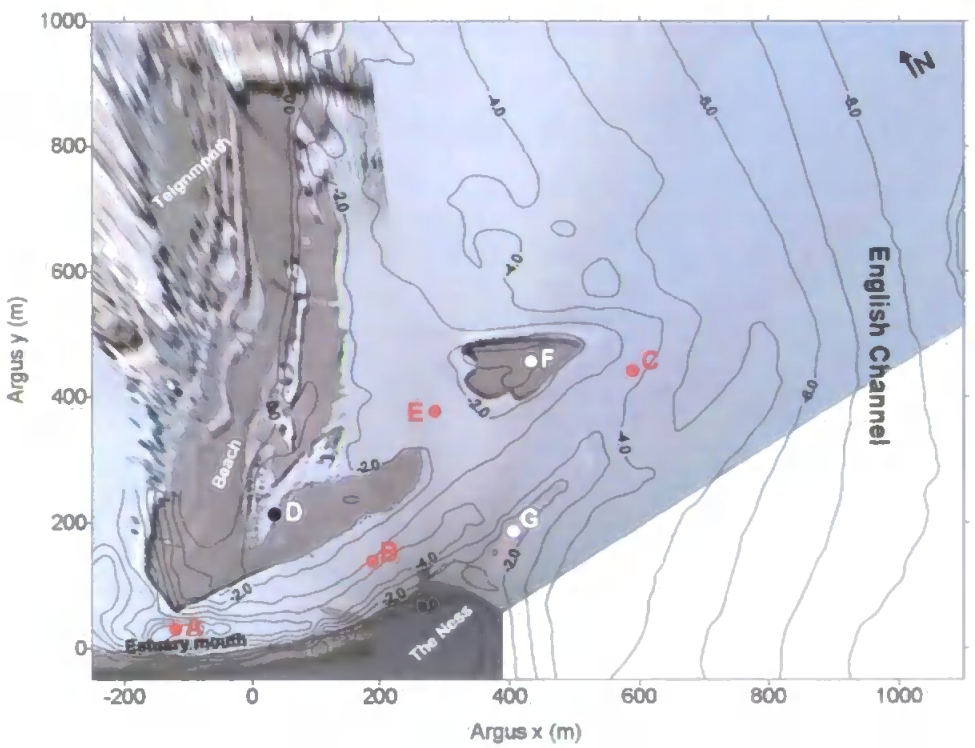

Figure 6.8. Locations of extracted time series of modelled sediment transport. The nearshore bathymetry is plotted over a rectified Argus image.

A thirteen-day numerical simulation with realistic varying forcing conditions gives an averaged sediment transport pattern for the inlet system. Modelled conditions include tides varying from spring to neap and significant wave heights ranging from 0.2 to 1.7 m. Boundary conditions used in the simulation are real conditions for the period (07/11 – 19/11/1999) and are represented in the time series of Figure 6.9a. River discharge is low during the period with average values of about 8 $m^3 s^{-1}$.

The resultant sediment transport patterns for the channels are similar to those found during spring tide simulations, while net transport over the shoals is defined by high wave energy conditions. It is during these dynamic periods that most of the sediment transport takes place, defining the resultant sediment transport paths over the whole thirteen days period. These results indicate that the magnitude and speed of the morphological changes of the sandbars are a function of the intensity and frequency of high wave energy events. Extending this idea to a larger temporal scale, one would expect major morphological changes at the sandbar system during the winter months (with frequent storms) and a more stable system during the summer months.

The sediment transport patterns for the modelled stage of the cyclic sandbar behaviour (October – November 1999) are consistent with progression towards the next stages of the sandbars morphological evolution. The expected growth and onshore migration of the offshore sandbar, as indicated by the numerical simulations for the given period, can be observed during the following months (as discussed in Chapter 7 when the numerical modelling experiments are extended to several stages of the evolutionary cycle).

6.4.2. Driving forces on the sediment transport

To analyse the relative influence of the acting processes on the sediment transport across the area, sediment transport time series were extracted from the thirteen days simulation (from 07/11 to 19/11/1999) at different locations (Figure 6.8). Stations A, B and C are located in the channel, under dominant tidal flow influence, while stations D, E, F and G

are located over the shoals and secondary channels where sediment transport is controlled by the combined tidal currents and wave action or mainly due to wave action.

6.4.2.1. Relative tidal range/wave height influence

Sediment transport at stations A and B is dominated by tidal currents, with sediment transport occurring mainly during spring tides with waves having virtually no effect (Figure 6.9b, c). Over the submerged sandbar (station C), at the outer part of the channel, the sediment transport is controlled by a combination of both tidal flows and wave-generated currents (Figure 6.9d). As shown in the time series in Figure 6.9d, the seawards sediment transport persistent during calm spring tide conditions starts to decrease with the reduced tidal range. However, it reaches its maximum peaks with the increasing wave energy while the tidal range is still high (day 11/11) showing the importance of the sediment mobilisation effects due to the interaction between tidal flows and wave generated currents over the submerged sandbar. From day 12 when the tidal range becomes smaller, the sediment transport also becomes smaller despite the increasing wave heights, showing that at this location the sediment transport is defined by the interaction between waves and tidal currents.

In the region of the flood channel (station D), the relatively strong flood flows during spring tides control the sediment transport that is directed towards the inlet mouth (Figure 6.9e). When progressing towards smaller tidal ranges, sediment transport is reduced and the weak tidal flows during neap tides are not able to displace any sediment at this region. However, the effect of the storm on the sediment transport is also registered at this region, when despite the reduced tidal range breaking waves generate longshore currents that enhance the dominant tidal flood currents at this region, displacing and transporting sediment towards the inlet (Figure 6.9e).

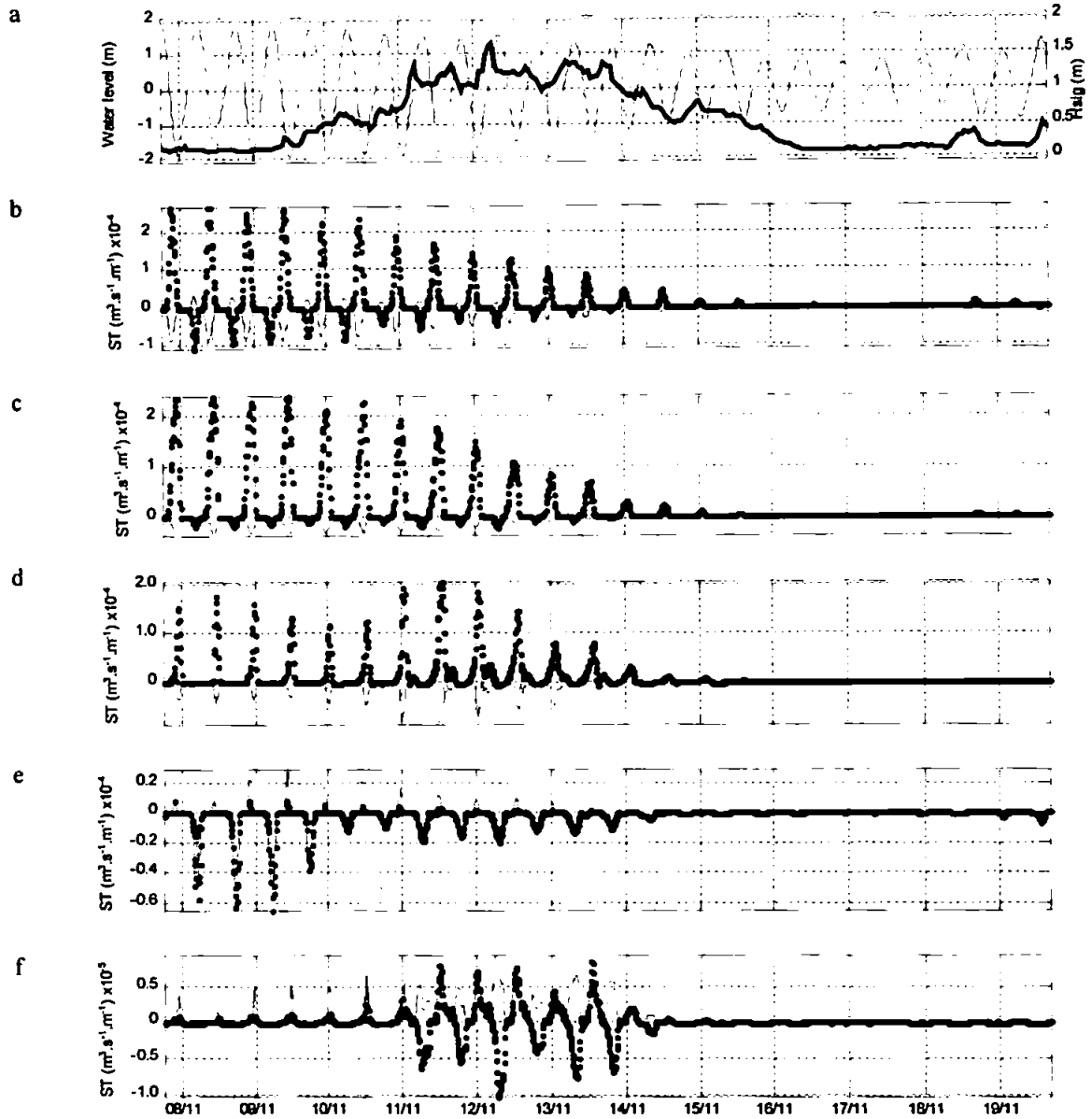

Figure 6.9. Time series of boundary conditions (a), sediment transport (ST) at station A (b), station B (c), station C (d), station D (e) and station E (f). *x*-components (dots), *y*-components (line).

Sediment transport time series taken from the region encompassing the shoals outside the main channel (stations E, F and G in Figure 6.8) show the importance of the waves on the sediment transport, with the majority of transport occurring during higher significant wave heights. In the secondary channel (station E – Figure 6.9f) a small amount of sediment is transported northwards by the ebb flow during low wave conditions. However, this

transport is increased when waves become higher and the tidal range is still large (days 10 and 11). With the gradual decrease in tidal range and increase in wave heights the cross-shore transport becomes dominant with sediments being moved mainly shorewards, showing the dominance of wave generated sediment transport over the transport by tidal flows in the region.

Over the offshore sandbar (station F – Figure 6.10) almost no sediment is transported until waves become higher than 0.5 m, when the onshore wave-generated currents reach values of about 0.6 m s^{-1} over the sandbar. These onshore currents reach values of about 1.2 m s^{-1} over the sandbar when waves reach heights of 1.7 m (day 12). Over the sandbar onshore wave generated currents are dominant over the ebb flow currents causing currents to be constantly onshore during storms (Figure 6.10b).

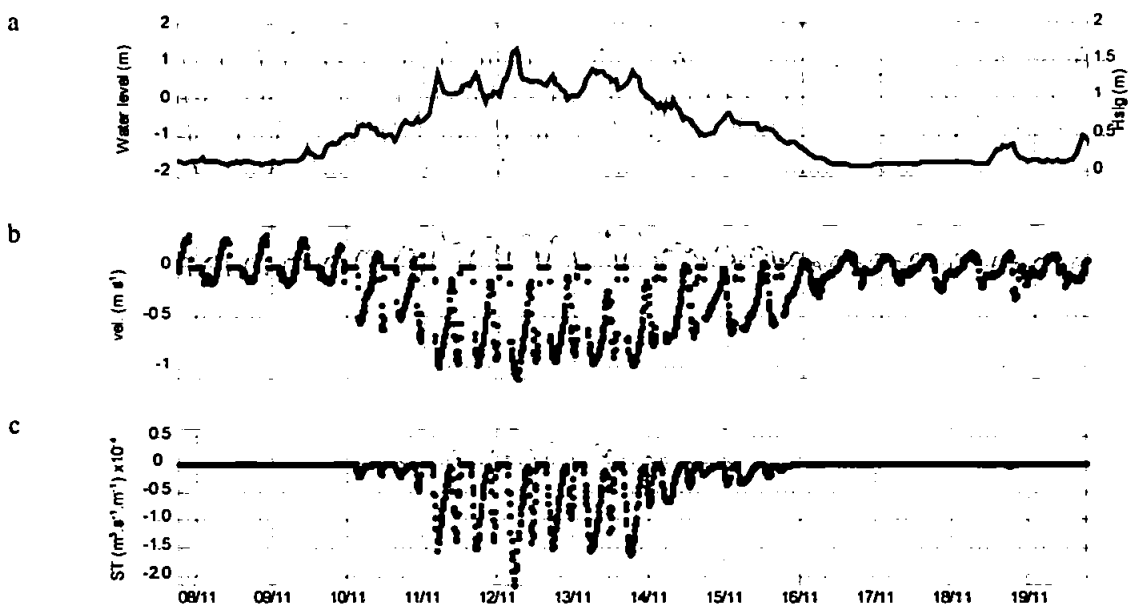

Figure 6.10. Time series of boundary conditions, current velocity and sediment transport over the offshore sandbar (station F). x-components (dots), y-components (line).

With different levels of exposure and submersion of the sandbar, the relative importance of mechanisms controlling the hydrodynamics and sediment transport differ during a tidal cycle (Oertel, 1972; Smith and FitzGerald, 1994; Komar, 1996). A schematic diagram

representing different stages of the interaction that drives sediment transport over the intertidal sandbar is represented in Figure 6.11. At low tide, when the sandbars are exposed, waves breaking at shoal margins produce onshore currents and consequent onshore sediment transport. When the rising tide submerges the sandbars, wave generated currents and tidal flows transport sediment shorewards. During the ebbing tide, it is the interaction of the seaward tidal currents and the onshore wave-generated currents that define the sediment transport pattern. With the presence of waves, cross-shore currents over shallow areas (sandbars) are constantly onshore, with wave-generated currents being dominant over the seaward ebb flow (Figure 6.10b). This circulation pattern forms gyres of sediment transport similar to those described by Oertel (1972), resulting in a accumulation of sediment over the shoals. The combination of these processes results in an overall shoreward net sediment transport over the offshore sandbar.

Simulations of storm wave conditions (H_{sig} = 1.8 m) combined with both neap and spring tidal conditions, indicate that during neap tides the quantities of sediment transported over the offshore sandbar are slightly higher and more regularly distributed. This is expected for two reasons: 1) weaker tidal flows are opposing the onshore wave-generated transport during this situation, and 2) due to the smaller tidal range the sandbar is submerged over longer periods of time, becoming exposed to the wave action. The main difference between both tidal conditions is visible on the southern side of the sandbar, which is exposed to the channel flows. During spring tide conditions, the onshore wave generated transport opposes a stronger offshore-directed flow at this side of the sandbar, resulting in an asymmetric onshore transport. This situation is represented by the sediment transport vectors over the offshore sandbar in Figure 6.14 (in section 6.4.2.3).

- high tide
- flood flow in the channel and over the sandbar
- wave shoaling and refraction over the sandbar re-suspend sediment which is transported onshore

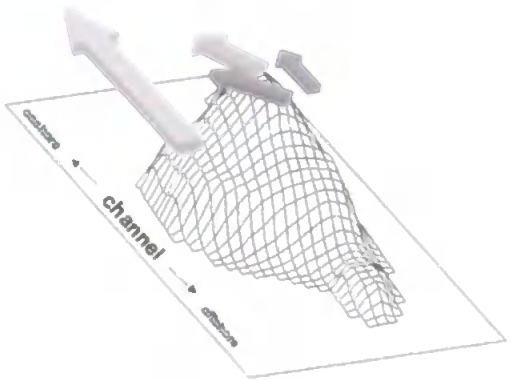

- early ebb tide
- ebb flow in the channel
- wave – tide interaction causing sediment transport gyres

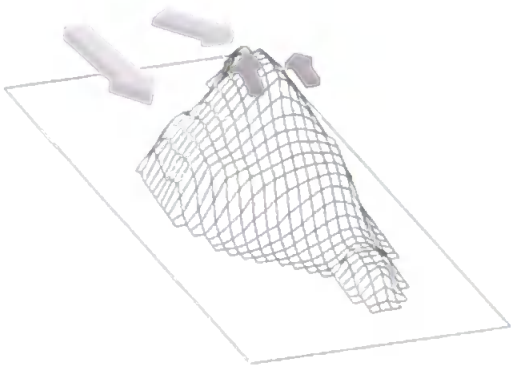

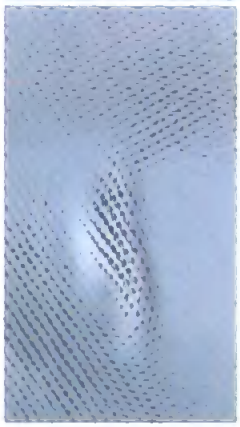

- intermediate ebb tide
- ebb flow in the channel
- wave generated onshore directed longshore currents around the sandbar

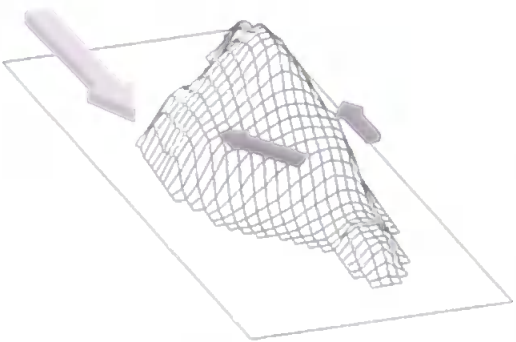

- low tide
- maximum ebb flow in the channel
- wave generated onshore directed longshore currents around the sandbar

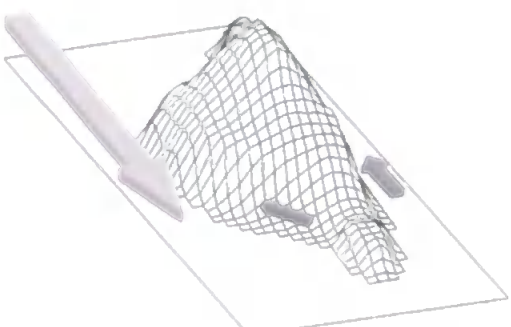

Figure 6.11. Diagrams showing different stages of wave – current interaction driving the sediment transport over the intertidal sandbar (centre) and the modelled hydrodynamic over the sandbar (right hand side). Tidal currents (light arrows), wave driven currents (dark arrows).

In Figure 6.12 the modelled sediment transport patterns over the sandbar are shown for the storm period (day 12/11; H_{sig} = 1.2 m) at different tide levels during an intermediate tide (tidal range of about 3.2 m). As represented schematically in Figure 6.11, the flows that control the sediment transport are the result of the interaction of wave generated and tidal currents over the intertidal sandbar (Figure 6.12). During the late periods of the flood tide, both wave and tidal currents drive the sediment shorewards (Figure 6.12a, b). With the beginning of the ebb tide, the interaction of opposing tide and wave generated currents deflect slightly northwards the overall transport over the submerged sandbar. At the southern part of the sandbar, exposed to the channel ebb currents, some sediment is transported offshore, resulting in a gyre of sediment transport over the sandbar. (Figure 6.12c). At lower tidal levels, the exposed sandbar acts as a divisor of flow and sediment transport, with sediment being transported offshore in the main channel and alongshore in the secondary channel (Figure 6.12d, e). Breaking waves (indicated by the white pattern in the image – Figure 6.12d) generate longshore currents on the north face of the sandbar, which is protected from the ebb flow. The result is an onshore sediment transport at this side of the exposed sandbar (Figure 6.12d, e). These stronger onshore flows at the protected side of the sandbar are also reflected in the shape of the offshore sandbar, which is extended shorewards at this side. During the early stages of the flood tide, the sediment transport over the recently submerged sandbar is mainly onshore and towards the inlet mouth, due to the interaction between breaking waves and onshore tidal flow (Figure 6.12f).

A similar influence of the wave-generated currents is observed over the Ness sandbar at the opposite side of the channel (station G in Figure 6.8). Time series of modelled flow velocities and sediment transport for this station are represented in Figure 6.13. During spring tides and low wave energy, small quantities of sediment are transported in the offshore direction. It is however when the wave heights increase, that larger quantities of sediment are displaced (Figure 6.13). During storm conditions, the wave-generated currents are predominantly directed northwards and onshore over the Ness sandbar. The combination of this north-west wave generated current and the dominant ebb tidal flow, results in sediment being transported towards the channel and offshore, providing sediment to the channel and to the submerged sandbar at the outer part of the main channel. Depending on the tidal range and run-off conditions, part of this sediment can be bypassed to the offshore sandbar or transported offshore through the outer part of the channel. The

bypass of sediment northwards through the channel and/or through the submerged outer sandbar is likely to occur during higher wave energy events that coincide with neap tides, when the weaker tidal currents in the channel are less efficient in transporting sediment offshore.

6.4.2.2. Angle of incident waves

During this thirteen-day period the incident wave direction was approximately shore-normal, with an average angle of 115 degrees from the true North, resulting in the transport patterns described in the previous sections. Simulations with different angles of wave incidence during high energy events (H_{sig} = 1.8 m) were carried out in order to assess the sensitivity of the region to these changes. As expected, the main changes in the sediment transport directions are mainly reflected at the direction of the transport over the offshore sandbar and on the intensity of the longshore transport (Figure 6.14). Over the offshore sandbar, the quantities of sediment transported remain approximately constant, however the direction of transport changes according to the direction of the incoming waves. The experiments show that the longshore sediment transport at the beach region is highly influenced by the angle of the incident storms, with low quantities of sediment being transported at this region under south-easterly storms. Independent on the incident wave direction, the longshore transport at the southern end of the beach is always southwards, with the incidence angle defining only the quantities of transport. The amount of sediment transported is sharply increased when the region is faced by a north-easterly storm. High energy events from the north-east are responsible for large quantities of sediment being transported towards the inlet channel, through the longshore and cross-shore (over the shoals) transport. The predominant shore-normal storms that affect the area also result in the longshore transport being directed to the south, towards the inlet mouth, though smaller quantities of sediment are transported under these conditions at the beach region.

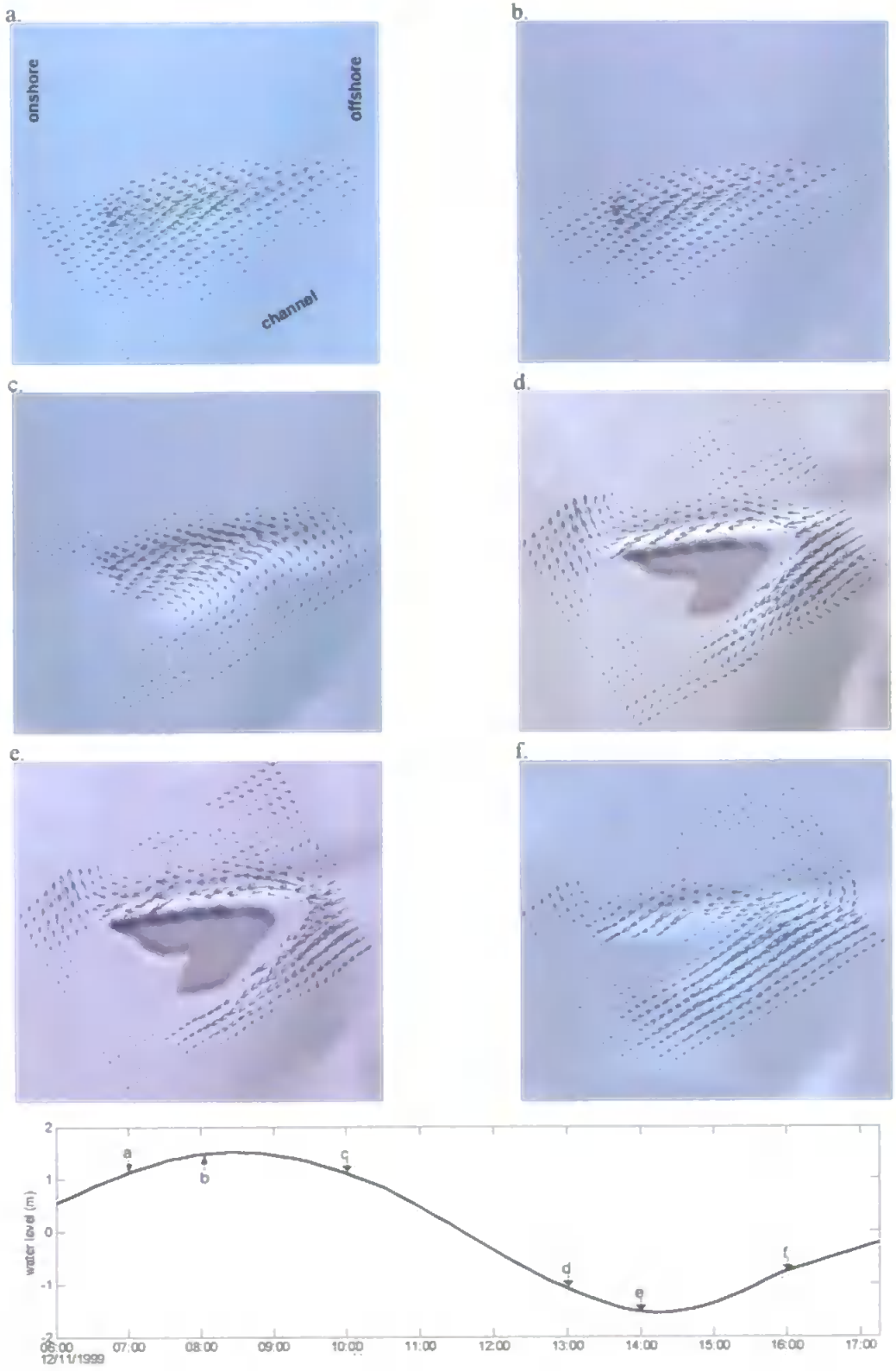

Figure 6.12. Modelled sediment transport patterns over the intertidal offshore sandbar. The correspondent tidal phase of each plot is indicated in the lower plot.

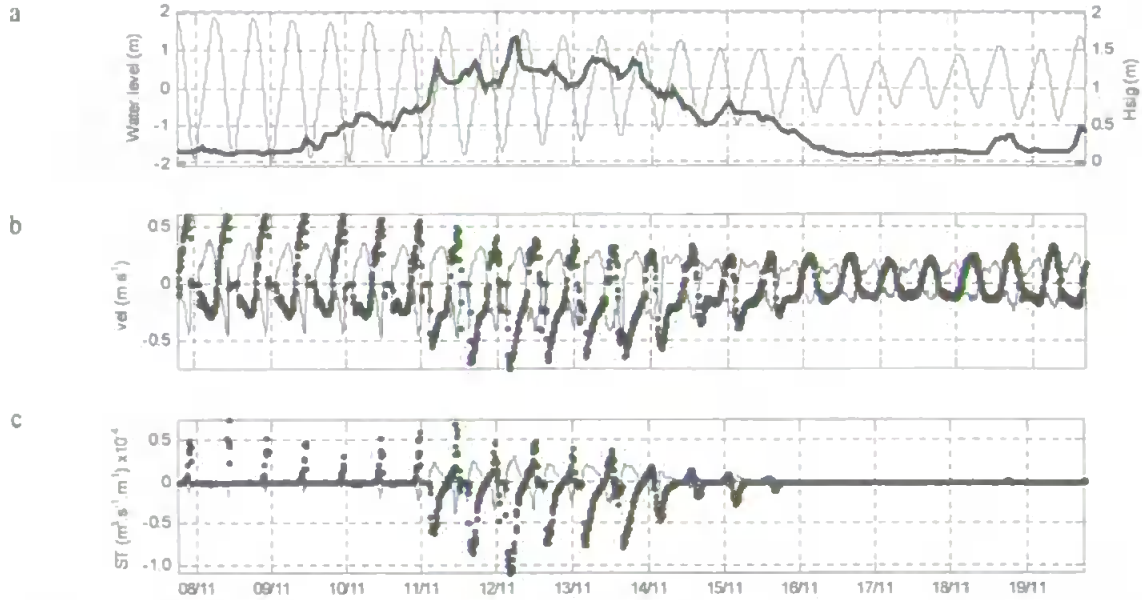

Figure 6.13. Time series of boundary conditions, current velocity and sediment transport over the Ness sandbar (station G). x-components (dots), y-components (line).

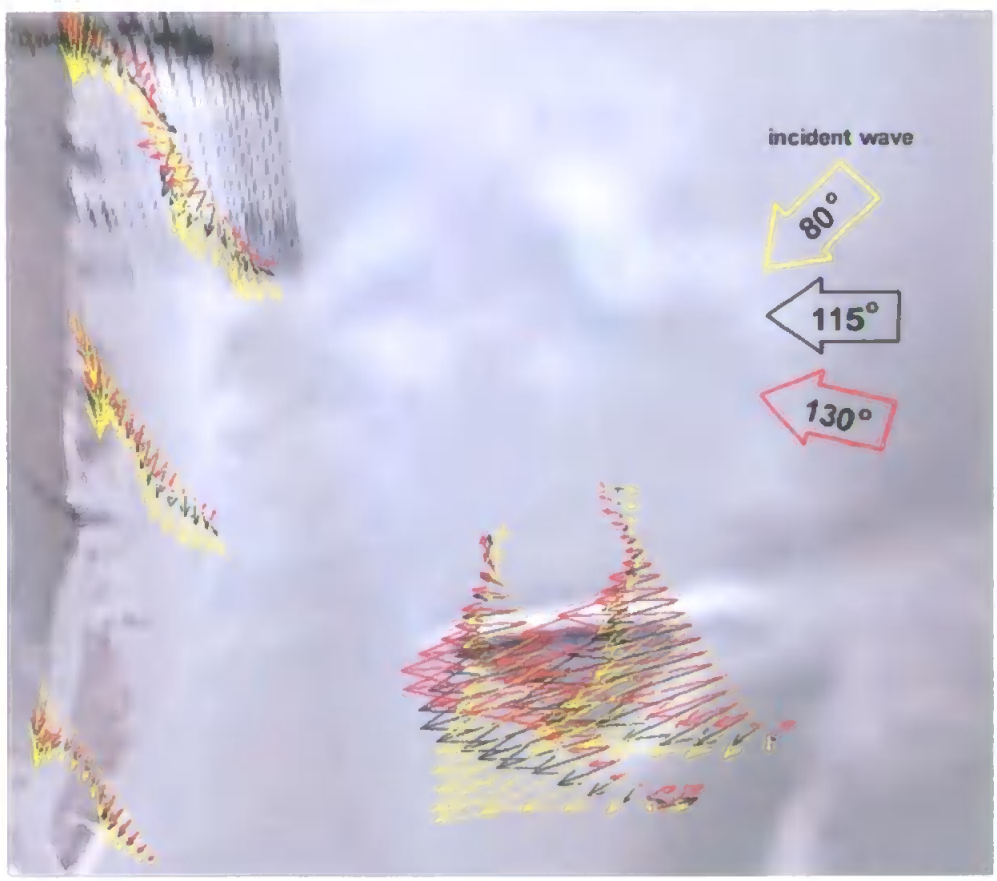

Figure 6.14. Sediment transport patterns for different angles of incident waves (H_{sig} = 1.8 m). Yellow vectors (80°); black vectors (115°); and red vectors (130°). Angles are given in relation to the true North, with the beach on the left and offshore on the right.

6.4.2.3. River discharge

A subject treated less frequently in studies of tidal inlets/estuaries is how the influx of freshwater affects the sediment transport patterns at its mouth. As discussed in the previous section, the Teign estuary is influenced by relatively small freshwater input. However, during winter periods these values can reach peaks that become significant in altering the hydraulics of the system. Numerical simulations with different run-off values used as forcing condition showed changes in the sediment transport patterns across the area, including the shoals that form the ebb-tidal delta. During high river discharge events the interaction of the ebb-flow and wave-generated currents over the shoals changes, as the seaward flow becomes stronger. Simulations with different river discharge values show the gradual increase in the northwards deflection of the resultant sediment transport with increasing ebb flow currents. Extreme cases of low and high run-off values are represented in Figure 6.15 for neap and spring tide conditions.

As shown by the transport patterns in Figure 6.15, the most affected areas are the ones under close influence of the main channel strong flows (e.g. the Ness sandbar and the submerged sandbar at the outer part of the channel). The vectors shown in Figure 6.15a represent simulations with low (about 8 m^3 s^{-1}) and high (150 m^3 s^{-1}) river discharge conditions, both under high incoming wave energy (H_{sig} of 1.8 m) over two neap tidal cycles. Sediment transport pattern over the Ness sandbar is most affected during neap tides, when high river discharges sharply deflect southwards the normally onshore wave-generated sediment transport. During spring tides the general transport pattern remains similar under the varying river discharge, with only higher quantities of sediment being transported by the stronger flows due to the increasing river discharge. The region of the Ness sandbar presents these large differences in transport patterns between spring and neap tides due to its varying wave/tide dominance. The weak tidal currents during neap tides allow the onshore wave generated transport to dominate, while the opposite occurs during spring tides, with the ebb-flows being dominant over the wave generated currents.

At the region of the submerged sandbar at the outer part of the main channel, the increasing river discharge results in larger quantities of offshore directed sediment displacement independent of the tidal condition (Figure 6.15). This process may result in

larger quantities of sediment being removed from the system to deeper waters. As shown in Figure 6.15a, during neap tides a northward deflection of the transport is also registered as a consequence of changes in the wave-current interaction. With low river discharge values, the resultant transport is bent southwards by the incoming waves (as seen in section 6.3.2 and Figure 6.4). As the river discharge increases, the balance between the ebb flow and incoming waves changes resulting in a transport normal to the channel axis.

In similar ways to the Ness sandbar, the sediment transport over the offshore sandbar is directed by the interaction of incoming waves and tidal flows. However, as this region is wave dominated independent of the tidal conditions, it is less affected by the channel flows. The degree of deflection of the sediment transport is given by the balance between the relative forces of the onshore wave-generated transport and the offshore flows, with the northward deflection becoming larger than the ones represented by the example of Figure 6.15 when the incoming waves are smaller.

The sensitivity of the local sediment transport to the river discharge, mainly during neap tidal conditions, can be an important factor for the local sediment transport. In the same way as for the temporal storm distribution, the high river discharge events occur normally over the winter periods, resulting in an additional controlling process in the dynamics of the system over winter months.

a. neap tide; H_{sig} = 1.8 m

b. spring tide; H_{sig} = 1.8 m

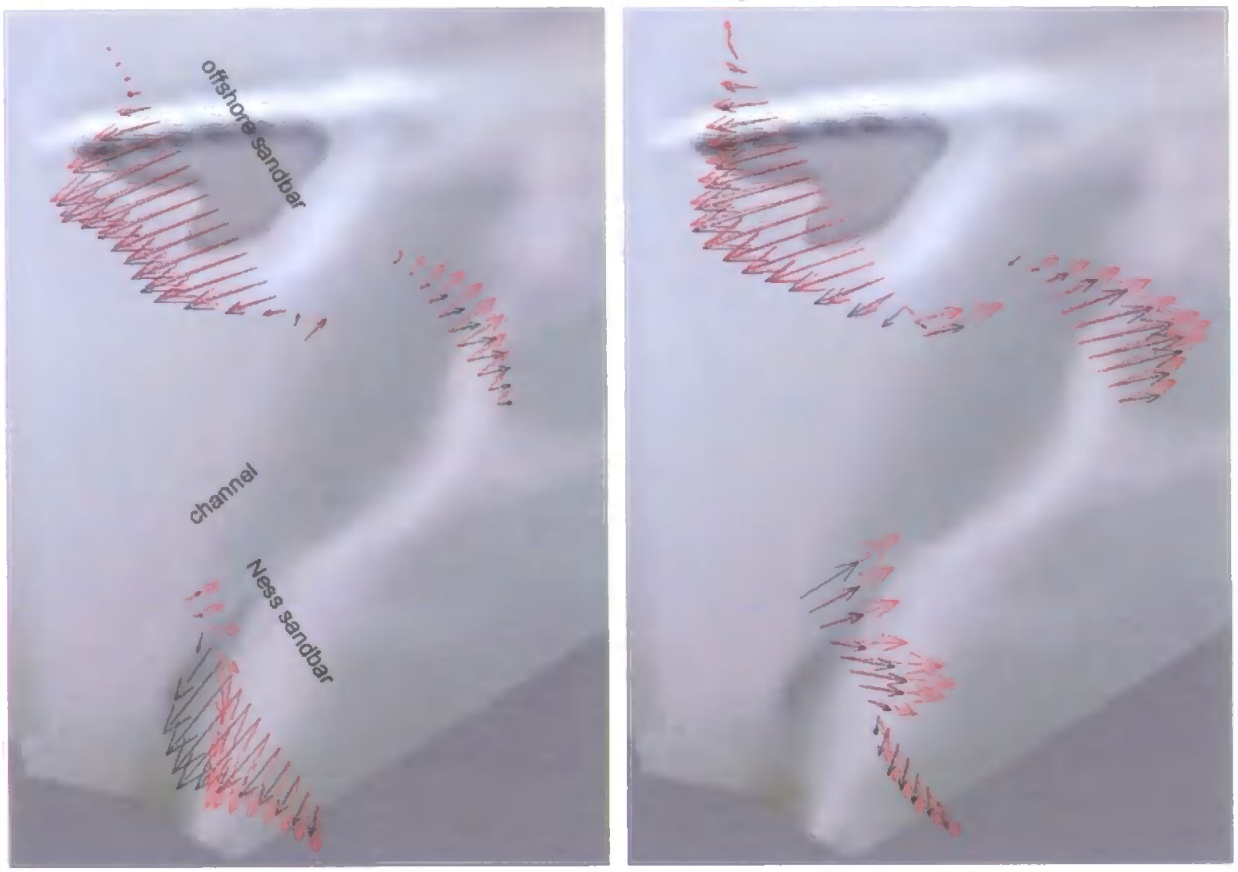

Figure 6.15. Vectors of sediment transport along profiles over the Ness sandbar, the submerged sandbar at the outer part of the channel and the offshore sandbar during high energy wave event at neap tide conditions (a) and spring tide conditions (b). Black vectors represent sediment transport during low river discharge (8 $m^3 s^{-1}$) and red vectors represent results for high river discharge events (150 $m^3 s^{-1}$).

6.4.2.4. Sediment supply

As described in Chapter 3 (section 3.1.1) only qualitative information regarding sediment supply to the Teign inlet system is available, with the main sources of sediment being related to cliff erosion at both sides of the inlet, from the north and south coastline stretches (Robinson, 1975; Carter and Bray, 2003). Based on the numerical modelling simulations of sediment transport in the region, some quantitative estimates of the sediment budget can be obtained for the analysed period. It is however important to be aware of the limitations of such quantitative estimates, one of them being related to the

constant drag-dredging operations across the region of the main inlet channel which are not taken into account in the modelling experiments. These dredging operations are not thought to be removing sediment from the system, but it may result in increased volumes of sediment leaving the main channel and also affecting the sediment bypass through the channel. Limitations of the numerical model should also be considered in such experiments (as discussed in Chapter 4).

In order to estimate the sediment budget of the sandbar system, the total sediment discharge volume was calculated for transects enclosing the system, providing the balance of sediment input/output to the region. Using the MIKE21 sediment discharge tool, the volume of sediment that crossed each transect over the studied period was calculated. Limitations arise in the analysis of the sediment transport rate through the inlet mouth, which despite being known to transport offshore the majority of sediment that reaches it, may provide an overestimate of the actual rates of transport. This is a consequence of the deeper parts of the main channel being incised in stable sandstone bedrock. In order to minimise unrealistically high sediment transport rates they are set to zero in the deeper parts of the channel. There is no data available about the exact limits of the bedrock, and here it is assumed that regions of the main channel deeper than 5 m (below ODN) are stable.

The modelled sediment transport rates during the given period of thirteen days are summarised in Figure 6.16. The overall sediment balance indicates that during the analysed period a sediment volume of approximately 2,000 m^3 is added to the system. The main sources of sediment input are the longshore wave generated currents, which add sediment to the system from both sides. There is also a net seaward sediment transport registered at the inlet mouth, which also provides sediment to the system. It is not clear however if the estuary can be considered a source of sediments to the system or if this input would be a consequence of the exchange of sediment between the flood and ebb tidal deltas, redistributing sediments within the system. As described in Chapter 3, Nunney (1980) found that the net transport of medium sands is always down the estuary, with more sediment being carried during ebb than flood tides. However, most important in the sediment dynamics of the lower estuary seems to be the ebb/flood dominance controlling the transport over the flood tidal delta (Salty Flat). This study by Nunney (1980) also

suggests a two-way exchange of material through the estuary entrance, supplying the sand circulation system within the lower part of the estuary.

Within the system, the main exchanges of sediment occur between the channel and the ebb shoals, including the bypass of sediment across the channel. In order to estimate the volume of sediment that bypassed the channel from south to north, the sediment discharge through an along channel transect was calculated. During the storm period, an estimated sediment volume of 300 m^3 crossed the channel transect, providing additional sediment to the offshore sandbar at the northern side of the channel.

The addition of sediment to the system over the analysed period is mainly a consequence of the storm event that lasted for approximately three days during intermediate tide conditions, as shown in the time series of sediment transport across the region (Figures 6.9, 6.10 and 6.13). Under calm wave conditions, a small but constant net loss of sediment from the system will occur through the outer part of the main channel. These quantities of sediment removed from the system may also depend on the freshwater discharge, which can increase the hydraulic efficiency of the main channel.

For the analysed period, the modelled addition of sediment to the region is consistent with the observed increase in volume of the offshore sandbar. Figure 6.17 shows the rectified video images for spring tides over an approximately one-month interval that includes the modelled period. Applying the morphology extraction techniques described in Chapter 5, volume estimates of the intertidal sandbar were carried out showing an increase in the intertidal area and volume of the sandbar of approximately 500 m^2 and 2,200 m^3 respectively (at low tide of –2.05 m). As discussed later in Chapter 7, the observation of video images show that this drastic change in the morphology of the offshore sandbar happens mainly during the storm period that is covered in the numerical simulation.

This net accumulation of sediment at the inlet area during the studied period cannot, however, be considered an average situation for the region. Sediment transport patterns outside the channels are clearly dominated by the storm event, whose relative importance would be reduced by extending the period to be analysed. As discussed in the previous sections, during low wave energy periods, several factors can remove sediments from the system. Added to the fact that very little sediment is carried to the system through

longshore transport during calm periods, strong ebb currents at spring tides are more efficient in transporting sediments offshore to deeper waters, removing them temporarily or even permanently from the system. This process can also be enhanced by higher river discharges. It seems that the balance between the slow and gradual removal of sediments during calm periods and the addition of sediment during drastic storm events controls the overall sediment budget of the system.

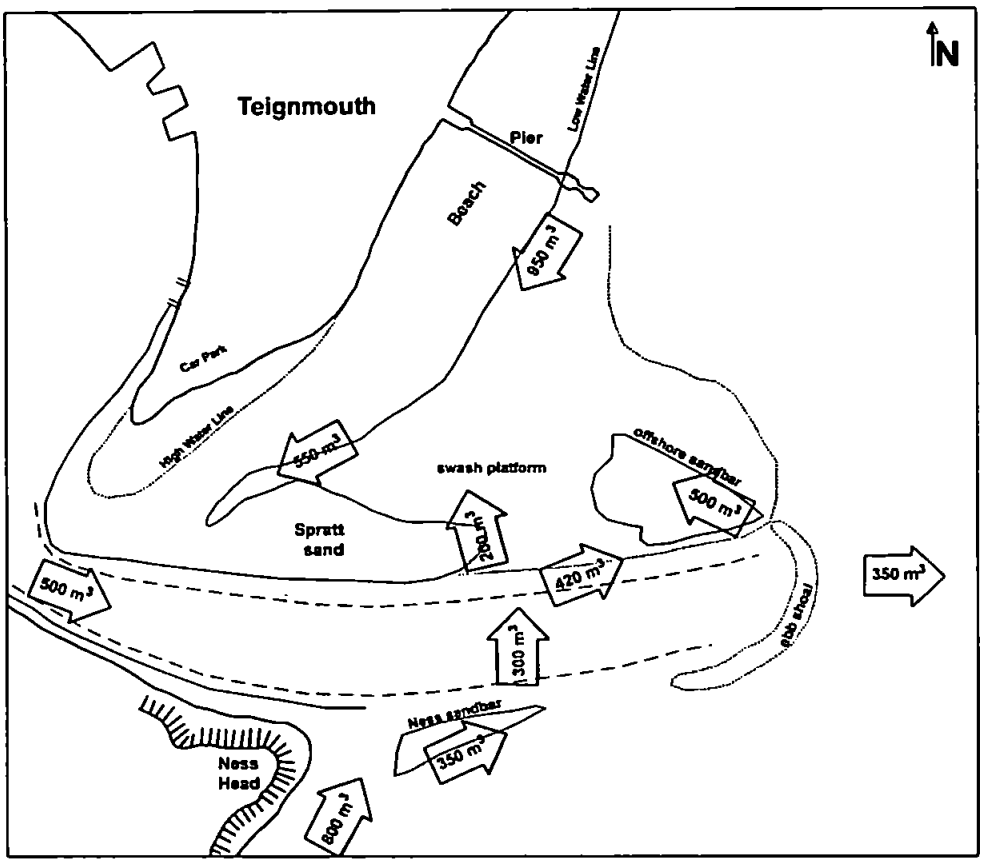

Figure 6.16. Modelled sediment transport rates across the sandbar system for the thirteen-day simulation.

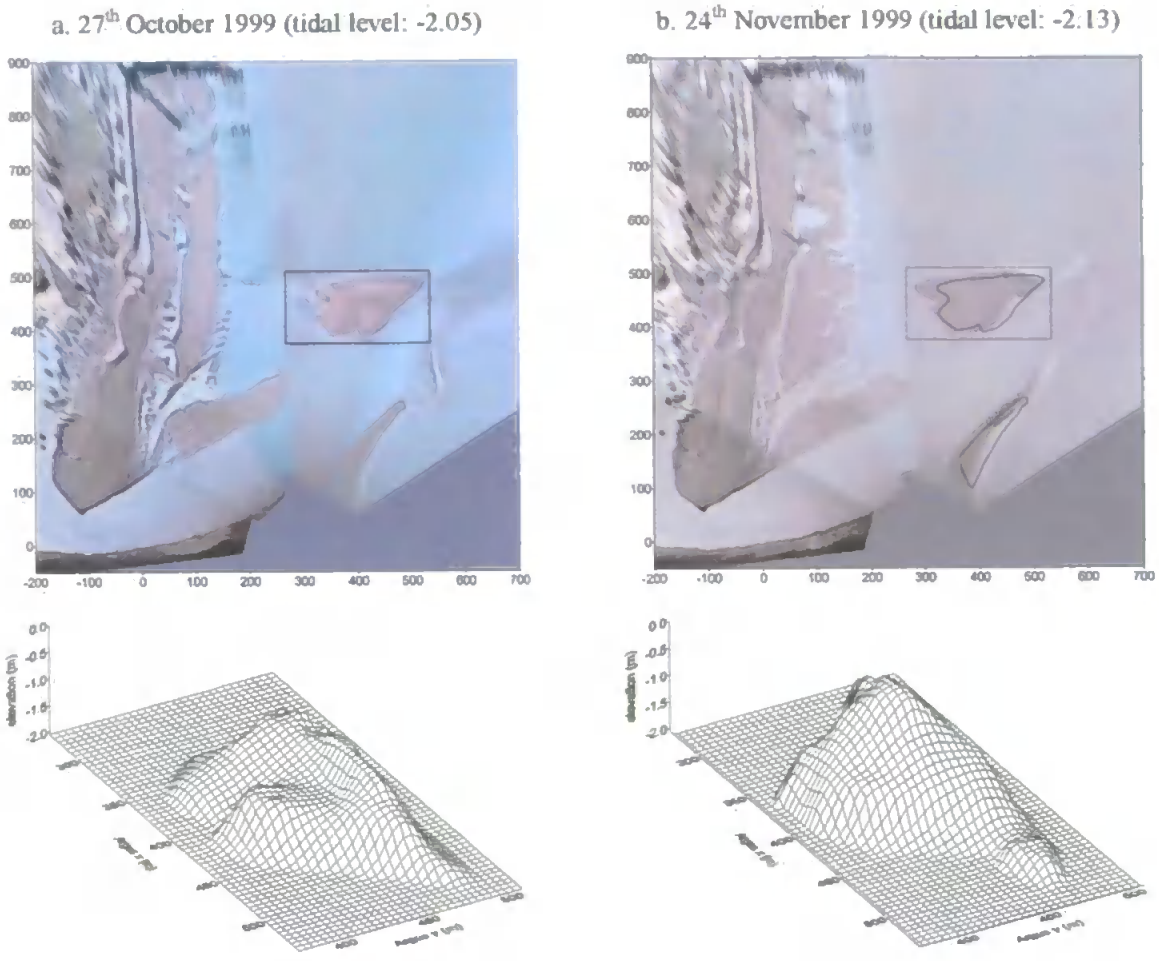

Figure 6.17. Morphological changes of the offshore sandbar over a one-month period represent the pre- and post-storm situation. The block diagrams represent the morphology of the sandbar (extracted from video images) detailed by the box in the rectified image. The October (a) digitised sandbars shoreline is overlaid on the November (b) image.

6.5. Discussion and Conclusions

In this chapter, the calibrated and validated numerical model is used to simulate the relative importance of the processes controlling the sandbar dynamics at the complex inlet system. The interaction of tidal currents, waves, and river discharge at the mouth of the Teign River produces a cyclic morphological behaviour of the sandbars that form the ebb-tidal delta. This cyclicity is controlled by the great temporal and spatial variability of the processes governing the local sediment dynamics. The majority of the sediment

displacement in the channels occurs during spring tide periods, while transport over the shoals is dependent on the presence of waves. Addition of sediment to the system via longshore currents and offshore loss of sediment through the channel during high-river discharge events seem to control the sediment volume in the sandbars, characterising a non-closed system.

Based on the modelling experiment results, waves seem to be of fundamental importance in the formation, maintenance and evolution of the sandbars that form the ebb tidal delta. The instability of the sandbars is controlled by the competition between cross- and onshore migration and offshore sediment transport due to the ebb tidal flow. This type of cyclic behaviour with constant volume changes of ebb tidal deltas is a characteristic of mixed-energy (tide dominated) coasts according to the classification proposed by Hayes (1979) and exemplified in several studies (e.g. FitzGerald, 1982; Smith and FitzGerald, 1994, FitzGerald et al., 2000a). At Teignmouth, the presence of a structural control (the Ness headland) adds to the complexity of the environment by anchoring the ebb shoals, causing an increase in sediment availability to the system by providing a relative protection from incident waves and longshore currents. This results in asymmetric ebb shoals, with typical triangular or elongate wave-dominated swash platforms of shore-normal orientation built in the lee of the headland (as observed also by Hume and Herdendorf, 1992 and Hicks and Hume, 1996). This delta morphology is akin to that described by Oertel (1977) and suggests that inlet currents rather than longshore currents are the dominant factor influencing the accumulation of sediments at the inlet. Typically a marginal flood tidal channel separates the ebb tidal delta from the beach. The size of the ebb tidal delta varies as a function of the headland shelter (Hume and Herdendorf, 1992). Based on the Teignmouth ebb delta morphology and following the classification proposed by Hicks and Hume (1996) (described in Chapter 2), it can be classified as being between the "constricted ebb delta" and "high-angle half delta" (types "b" and "c" in Figure 2.2).

The relative importance of each physical process on the sediment transport varies across the region, and is summarised in Figure 6.18. The channel region is dominated by the tides, directing the sediment transport as a consequence of the tidal flow asymmetry in the channel. Part of the sediment transported by these tidal flows is deposited at the outer part of the channel forming a submerged sandbar that is controlled by the interaction between tidal flows and wave generated currents. The shoals and secondary channels at both sides

of the channel are dominated by wave related processes. Sediment transport in these areas occurs only under the influence of wave generated currents. High river discharge events may change sediment transport patterns across most parts of the area, causing changes to the relative importance of seaward flows on the interaction with the onshore wave generated currents.

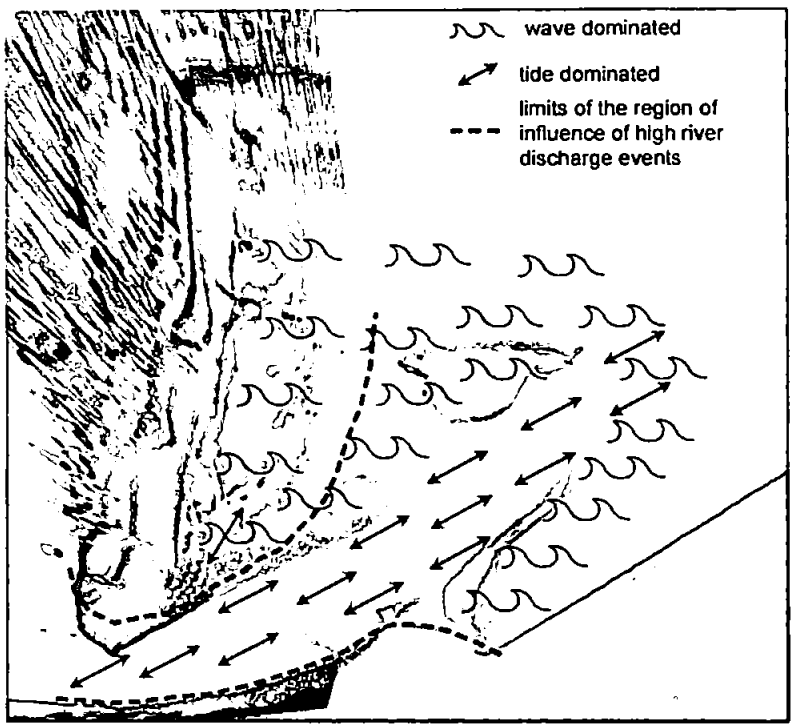

Figure 6.18. Summarised areas of relative dominance of tides, waves and river discharge over the sediment transport.

Chapter 7

Sediment Transport Patterns and Morphodynamics

7.1. Introduction

Teignmouth's ebb tidal shoals that form the sandbar system have been studied since the 19th century when Spratt (1856) described the movement of the sandbars. Further observations supported by some hydrological and sedimentological measurements were made by Robinson (1975) (see Chapter 3 for further details). Previous studies (Spratt, 1856; Robinson, 1975) and observations suggest that the movement of the sandbars follows a cyclical sequence.

Bringing together the calibrated numerical model (Chapter 4), the method that couples the hydrodynamic numerical model with video images in order to extract the intertidal morphology (Chapter 5), and the assessment of the driving forces in the sandbar dynamics (Chapter 6), this chapter aims to better understand the morphodynamics of the system and to evaluate the overall technique applied in this study. Through the application of short period modelling experiments at different morphological stages of the sandbar system, qualitative predictions of the evolution are given as a function of its causing processes. The comparison of the predicted and observed evolution through the video data also provides an alternative validation of the applied techniques. A reduced version of part of this chapter was published by the author in Siegle et al. (2003).

Starting with the knowledge of the main driving forces acting on the local sediment transport (Chapter 6), this chapter assesses the morphological evolution of the sandbar system at Teignmouth using three years of rectified Argus video images (March 1999 to June 2002). This qualitative analysis of the available video data is combined with modelling experiments, allowing comparisons between the modelled sediment transport rates, with the resulting initial sedimentation/erosion patterns, and the observed

morphology at each stage of the evolution. For the numerical modelling experiments throughout the evolutionary cycle, the morphologies applied are those previously defined in Chapter 5. Some references are also made to the available field data. During the COAST3D project experiments for example, the intensive field campaigns provide information that can be related to the morphological evolution over a given event (e.g. one storm event). However, during most of the observed period only limited measured data is available (pier measured water levels and non-directional waves). River discharge information is available over the whole period. Details of the available data can be found in Chapter 3.

The description of the morphological evolution is based mainly on the observation of rectified video images (Chapter 5). Using digitisation techniques, the evolution of the main features visible in the images is analysed throughout the cycle. Some area and volume estimates of morphologic features are carried out using the gridding facilities in the SURFER© software (Golden Software, 1995). The nomenclature and definition of the main morphological features observed throughout the evolutionary cycle are given in Chapter 3 (Figure 3.5).

The chapter structure includes a brief description of the model setup and the numerical simulations carried out, highlighting some adjustments needed in order to apply the model at each morphological stage. This provides the background for the main section of the chapter, which combines the observed morphological evolution with the numerical experiments. This section is sub-divided according to the main stages of the evolutionary cycle. In order to summarise the knowledge obtained from the observations and numerical modelling experiments, a conceptual model of the evolutionary cycle is also proposed.

7.2. Model Setup

Based on the validation model setup (Chapter 4), the numerical experiments at different stages of the morphological cycle need some adjustments related to the updating of the original bathymetry using the video imaging technique (Chapter 5). As no *in situ* measurements are available to calibrate and validate the model at each stage, the

calibration parameters of the validated model for October/November 1999 are maintained throughout the experiments. This means however that the depth dependent bed resistance needs to be adjusted to the varying morphology. The sediment grain size distribution is also adapted for the experiments, as given below.

7.2.3. Bed resistance

For the calibration and validation of the numerical model, bed resistance values (Chézy number) were defined as a function of depth, using the same combination as for the calibration (Table 4.3 – Chapter 4). The same range of values was applied to each of the "new" bathymetries, resulting in specific bed resistance distributions for each morphological stage.

7.2.4. Sediment data

The varying sediment data applied for the numerical model experiments is based on samples obtained during COAST3D experiment period. However, as the sandbars are very dynamic throughout the studied period, it is believed that grain sizes are equally variable throughout the cycle. Since there is no sediment data available for most of the duration of the observed evolution, areas and morphological features of similar grain size were defined for the October/November 1999 period based on the available sediment samples. These areas with similar grain characteristics are the inlet channel, the beach, the sandbars, and the offshore area. Assuming that the grain sizes remain approximately constant at each defined area or morphological feature, the applied spatial distributions of sediment characteristics were adapted to each stage of the cycle. This was done by tracking the main morphological features throughout the cycle and defining their grain characteristics as constant. This assumption may not always be correct, though it is a good approximation in the absence of measured data. The main limitations may be related to some differences in the magnitudes of the modelled sediment transport and initial sedimentation/erosion rates. The overall transport patterns are not expected to be affected by these variations in grain size, as shown by the grain size sensitivity tests during the sediment transport calibration (Chapter 4).

7.3. Numerical Simulations

Numerical modelling experiments were designed using the set of different morphologies in order to inter-compare the modelled sediment transport patterns and initial sedimentation/erosion rates with the observed morphological evolution of the inlet sandbar system. Several runs under a range of forcing conditions were carried out with each of the ten morphological stages described in section 5.5 in order to assess the variability of the controlling processes and the consequent predicted morphological evolution.

Limitations on the longer-term, quantitative predictability of the system arise from the use of an initial sedimentation/erosion model (as discussed in Chapter 2) and from the limited amount of available measured data outside the COAST3D periods to be used as boundary conditions. Since the knowledge about the forcing conditions is fundamental for the accuracy of such predictions, measurements or the understanding of the sequencing of the forcing conditions would be needed throughout the simulations. Therefore, the model runs were designed in order to cover two tidal cycles, giving an indication of the importance of the key processes and the tendencies in the morphological evolution. Usually the most energetic periods are reproduced, as it is during these situations that most of the sediment transport happens, as shown in Chapter 6. The results of each numerical experiment are presented according to the pre-defined stages of morphological evolution in the next sections.

The comparisons described in this chapter between the predicted sedimentation/erosion rates and the observed morphological evolution through video images can be considered also an alternative way of validating the numerical model against observations. If the numerical model is reproducing the tendency of the observed evolution with a certain degree of accuracy, it adds confidence to the predicted results.

7.4. Sediment Transport and Morphological Evolution

The morphological evolution of the three-year observed cycle (Figure 7.1) is described for separate stages of the cycle, defined according to diagnostic observed morphological

characteristics. Over the three-year observed period, three main stages can be defined with approximately the same length, and a smaller fourth stage is defined for the period of completion of the cycle, when the morphology returns to being similar to the initial condition.

Stage 1 (March to December 1999 – Figure 7.1a, b) is characterised by the growing offshore sandbar. The continuous growth and onshore migration until it becomes attached to the beach defines **Stage 2** (January to December 2000 – Figure 7.1c). **Stage 3** (January to November 2001 – Figure 7.1d, e) is characterised by the northward migration of the attached sandbar and consequent reduction of its size, while a new offshore sandbar is formed. Finally, **Stage 4** (December 2001 to April 2002 – Figure 7.1f) represents the completion of the evolutionary cycle, with the destruction of the beach-attached sandbar and growth of the offshore sandbar. A schematic diagram of the main features characteristic of each stage is given in Figure 7.2.

In the following sections the characteristics of each stage and its evolution are further described. More detailed observations of some dramatic changes in morphology can be made when field data is available, helping in the understanding of the dynamic agents acting on the system.

7.4.1. Stage 1

In March 1999, the first spring tide period recorded by the Argus system installed in February 1999 shows the sandbar morphology that is considered the starting point in this description (Figure 7.1a). At this time, the morphology is defined by a relatively small offshore sandbar and by the remains of a shore-normal attached sandbar on the beach. The Ness sandbar, whose position is revealed by the breaking waves, is submerged at the outer part of the channel.

The main observed morphological change during this first stage of the description is the continuous growth of the offshore sandbar and the spreading of the remains of the attached sandbar on the beach. The three separate shoals visible in March gradually merge to form

one larger sandbar in September (Figure 7.3). This seven months period is characterised by the deposition and accumulation of sediment at the offshore sandbar, with an estimated increase in intertidal area of about 2,500 m^2, doubling its area from 2,400 m^2 in March to 4,900 m^2 in September 1999. At the same time, the previously shore-normal attached sandbar decreases in size being spread along the beach, leading to a gradual increase in the beach area. This is clearly visible in Figure 7.3b, when despite the higher tidal level at the time of the gathered image the beach is wider than in April 1999.

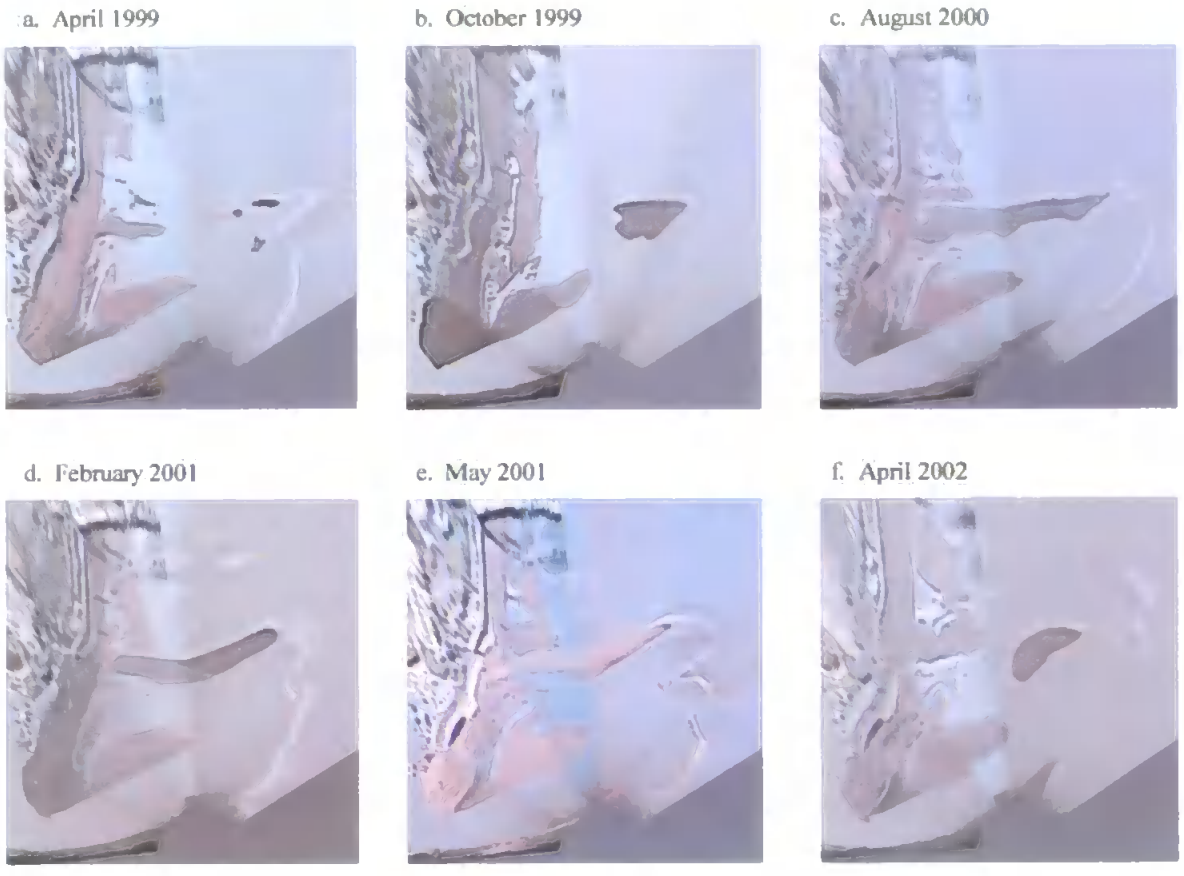

Figure 7.1. Rectified video images showing the evolution of the sandbar system from March 1999 to April 2002. Images were gathered at similar tide levels of about –1.90 m.

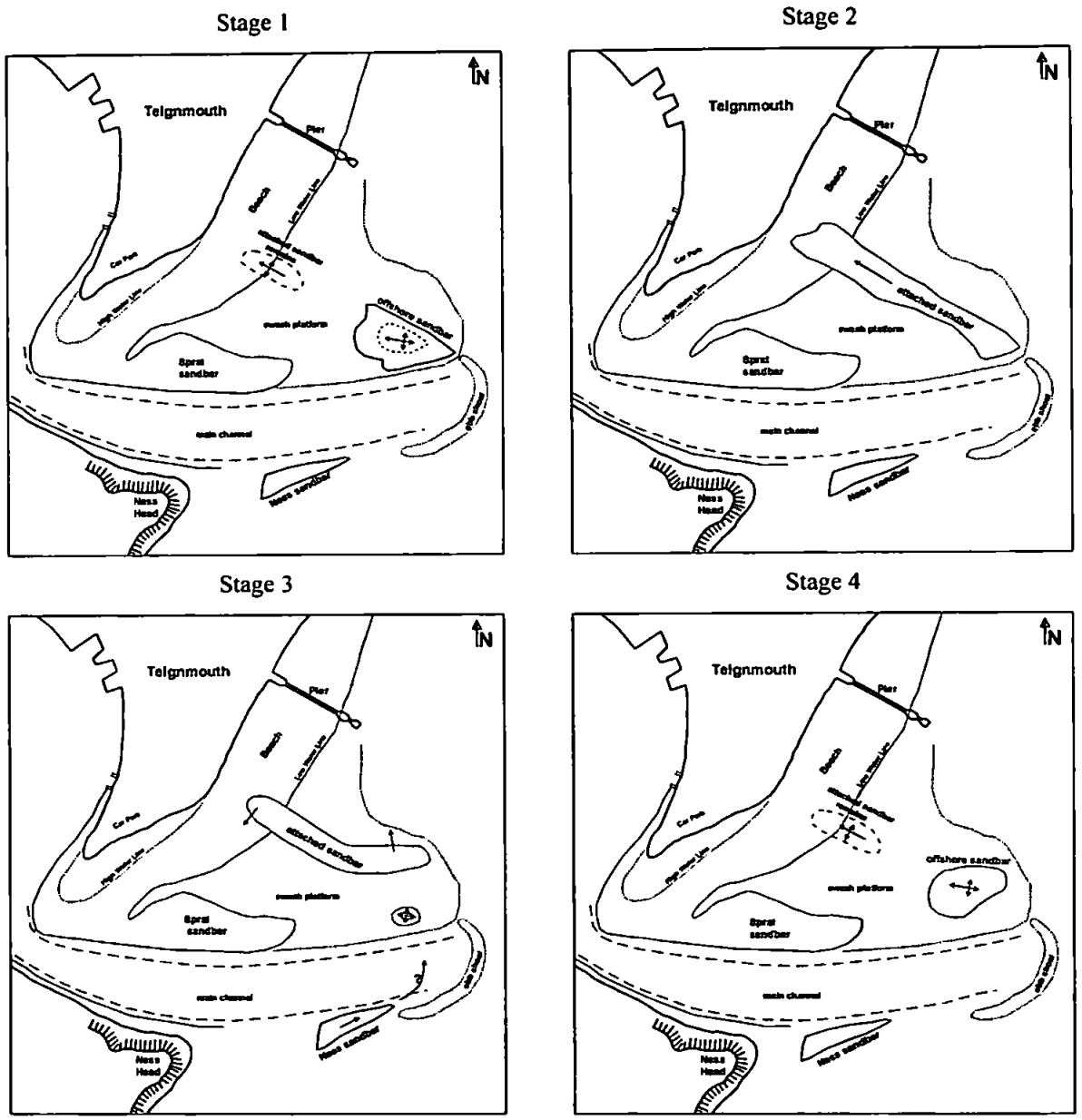

Figure 7.2. Schematic diagrams with the diagnostic morphologic features of each evolutionary stage. Arrows indicate the direction of the sandbars migration.

Measurements for this period are mainly from the COAST3D pilot experiment, which show a storm (with H_{sig} of up to 1.8 m) during the 10-12/03/1999. However, since the video system was installed at the end of February 1999, no video data of the previous spring tide period is available to determine the morphological changes caused by this specific storm. The two available bathymetric surveys were also carried out after the storm,

at the 12/03 and 24/03/1999, covering a spring-tide period with small waves (H_{sig} of about 0.2 m). Between these two surveys only small changes over the offshore sandbar were measured, with differences usually laying in the range of the measurement errors (of up to 0.25 m – Van Rijn et al., 2000). The Ness sandbar, whose approximate position is estimated through breaking waves in the images, remains approximately constant (with a convex shape) from March to July. In August the submerged sandbar appears deformed, becoming more parallel to the main channel, remaining constant until September (Figure 7.3).

Numerical experiments covering the March 1999 morphology indicate that the physical forces act in a similar way to the October/November 1999 situation (as described in Chapter 6). A gradual deposition of sediment occurs over the growing offshore sandbar when significant wave heights are higher than 0.5 m (Figure 7.4). The sediment transport patterns and initial sedimentation/erosion rates in Figure 7.4a represent the transport over two tidal cycles with high energy incoming waves (H_{sig} = 1.8 m; dir. = 115°). Lower wave energy results in similar transport patterns, though with a smaller sediment displacement. Although no wave data is available for the period between March and September 1999, the seasonal variation in the frequency and intensity of storms would suggest that on average lower wave energy was affecting the region. This less energetic situation may explain the relatively slow increase in volume and area of the offshore sandbar observed during this period. Model results for the beach region, suggest that the shore-attached sandbar is spread alongshore, mainly southwards, with its sediment being transported towards the inlet channel. This is a result of the dominant southwards longshore currents at this region, as shown by the experiments in Chapter 6.

From September to October 1999, the offshore sandbar grows rapidly reaching an area of 11,500 m^2 at the –1.90 m reference level (same as in September 1999 – Figure 7.3b). This implies an area increase of about 6,600 m^2 over a one-month period. Unfortunately, no measured data for comparisons is available for this period. However, from the observation of the video images, higher waves are visible during the 15-21 of October period. Despite not being possible to quantify the wave action during this period, wave shoaling and breaking are clearly visible over the sandbar. Another visible change is on the previously submerged Ness sandbar, which emerges at low tide in October 1999 (Figure 7.1).

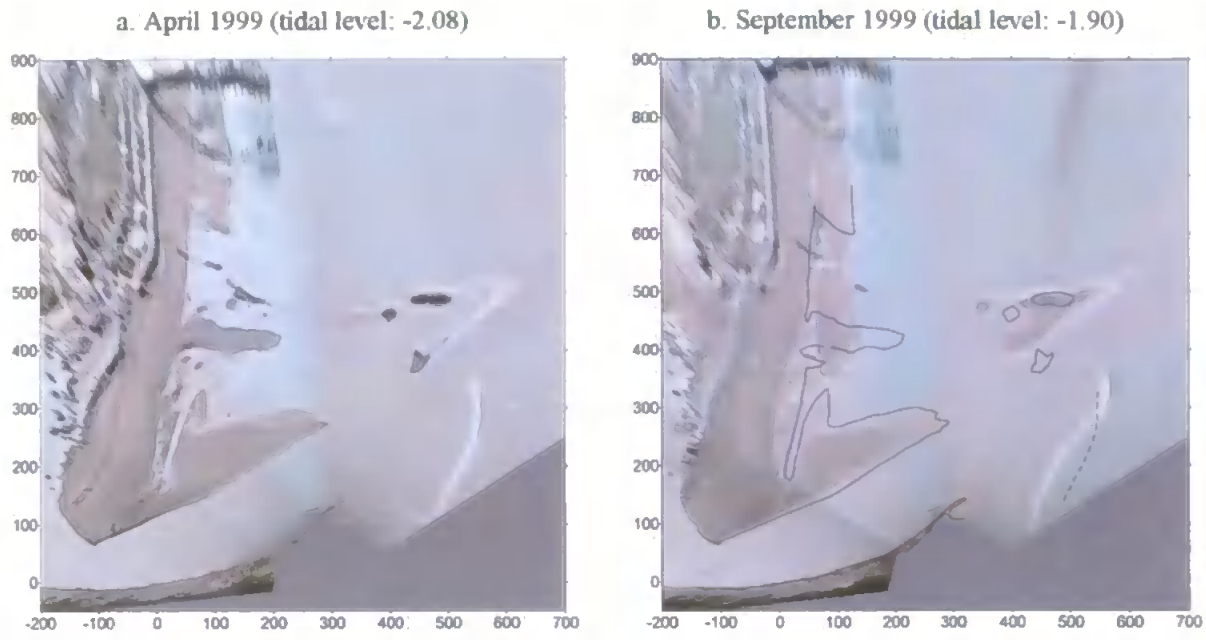

Figure 7.3. Rectified images for April and September 1999. Continuous black lines in b represent the digitised shoreline in a, and the dotted line represents the estimated location of the submerged sandbar through the breaking waves.

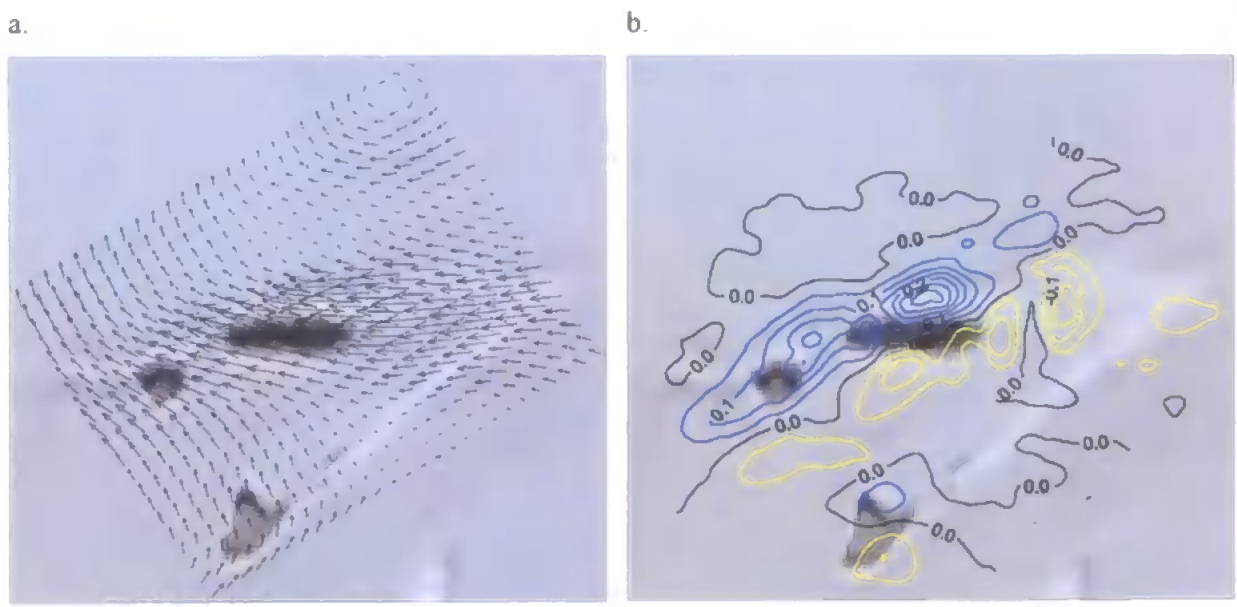

Figure 7.4. Detail of the modelled sediment transport for a high-energy event (H_{sig} = 1.8 m) over the offshore sandbar in March 1999. Sediment transport patterns (a) and initial sedimentation/erosion rates (b), where deposition is represented by blue lines and erosion by yellow lines.

The October – November 1999 period is covered by the COAST3D project main experiment measurements, allowing a more detailed assessment of the morphological evolution. The main changes during this one-month period are registered over the offshore sandbar. Following the growth tendency from September, it is increased further in area and volume during this period. From the visual observation of the video images, the sandbar remains approximately constant from the 27th October until the 10th of November. During the 11-13 November a high-energy storm (Figure 4.3b – calibration period 2) caused the increase of the intertidal sandbar volume and area.

The importance of this storm in reshaping the morphology of the sandbar can be seen in the video images that cover this period. Images gathered at similar tide levels just before and after the storm show a considerable increase in its area. As the images soon after the storm (15/11) were gathered at neap tide conditions, they are limited in the intertidal coverage area. However, when compared to images at the same tidal level (-0.89 m) before the storm, an increase of 950 m^2 in area is verified (Figure 7.5).

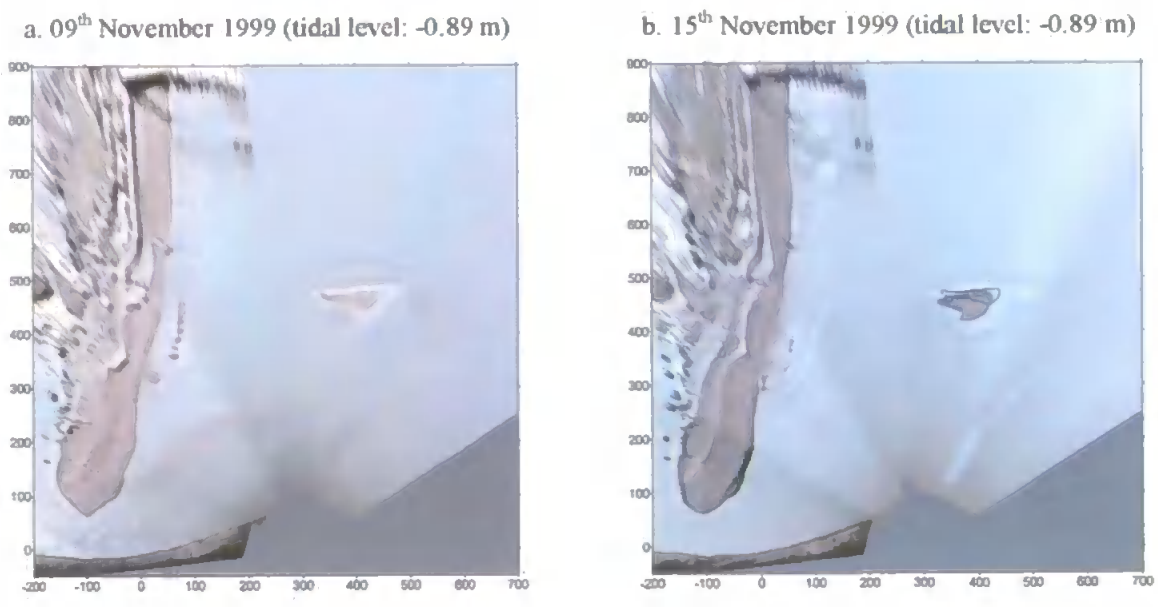

Figure 7.5. Pre- and post-storm images at the same tidal level showing the increase in area. Shoreline of the sandbar before the storm (a) is overlaid on the image gathered after the storm (b).

As shown also in Chapter 6, better estimates of the morphological changes can be obtained by comparing the morphology extracted from the images (applying the method described in Chapter 5) at spring tide conditions before and after the storm. It includes a larger period of time, but as seen in Figure 7.5, the most drastic changes occurred during the high-energy event. The area and volume of the sandbar over this one-month period increased by approximately 500 m^2 and 2,200 m^3 respectively (at low tide of –2.05 m). The shape of the offshore sandbar shows that the main sediment deposition and consequent volume increase occurs at its shoreward side (Figure 6.17 and Figure 7.6).

The same behaviour is observed from the numerical simulations covering the thirteen-day period that includes the storm that reshaped the sandbar morphology (see Chapter 6), where the onshore sediment transport results in erosion at the outer end of the sandbar and deposition at the onshore flank (Figure 7.7).

The increase in height of the sandbar may be a consequence of the November storm being coincident with a relatively high tidal range (of about 3 m), as opposed to the high-energy event that acted over the sandbar during the 15-21 October period, which occurred during neap tide. The occurrence of the storm during low tidal ranges (of about 1.7 m) appears to provide large amounts of sediment to the sandbar, whilst waves acting at a similar level over the storm have a "flattening" effect over the sandbar. With the increased tidal range, this flattening effect is reduced, since at low tide the deposited sediment emerges, resulting in an overall reduced wave action over the sandbar.

This can also be verified through the numerical experiments, with simulations of high wave energy events at different tidal conditions. Results confirm that the rate of sediment deposition over the sandbar is higher when combined with larger tidal ranges. Typical time series of modelled water level, cross-shore velocity and magnitudes of sediment transport over the sandbar (station F in Figure 6.8) are shown in Figure 7.8 for neap and spring tides. Average sediment transport at this point is higher during smaller tidal ranges when compared to the spring tide transport. This is mainly related to the fact that the sandbar is permanently submerged during neap tides, resulting in a slightly higher average sediment transport. During spring tides, two factors are responsible for the smaller quantities of sediment transported: a) Cross-shore flow velocities over the sandbar are always higher

than 0.6 m s^{-1} during neap tides; b) the large variation in water depth during spring tides results in abrupt changes in the flow velocity. With the sandbar exposed during low tide, no sediment is being transported and as shown by the time series in Figure 7.8, the onshore wave generated currents are reduced by the strong opposing ebb flows, reducing consequently the amount of sediment transported mainly during the beginning of the ebb tide. As discussed earlier in Chapter 6, and shown in Figure 7.8, it is at the beginning of the ebb tide that the relative dominance of the wave-generated onshore flow over the opposing channel ebb flow is at its minimum, resulting in the reduction of sediment transported at this stage. The example shown in Figure 7.8 is of extreme tidal ranges and wave energy. In reality, the combination of different relative wave height/tidal range values result in a range of sediment transport patterns over the sandbars. Further details of the behaviour of the sandbar under these conditions for the October/November 1999 morphology are given in Chapter 6.

The shape of the Ness sandbar remains approximately constant over this month, with a slight northward migration (in the channel direction) after the measured storm (Figure 6.9a). This change is confirmed by the bathymetric surveys carried out during this period. The beach and the Sprat sand showed only small morphological changes over this period.

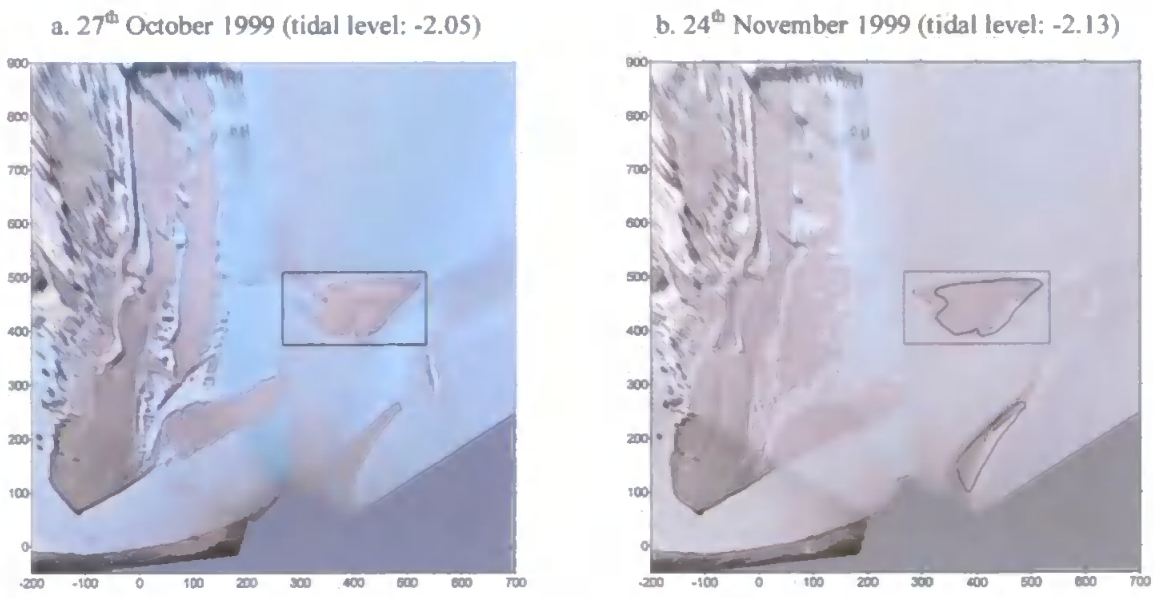

Figure 7.6. Morphological changes of the offshore sandbar over a one-month period represent the pre- and post-storm situation. The October (a) digitised sandbars shoreline is overlaid on the November (b) image.

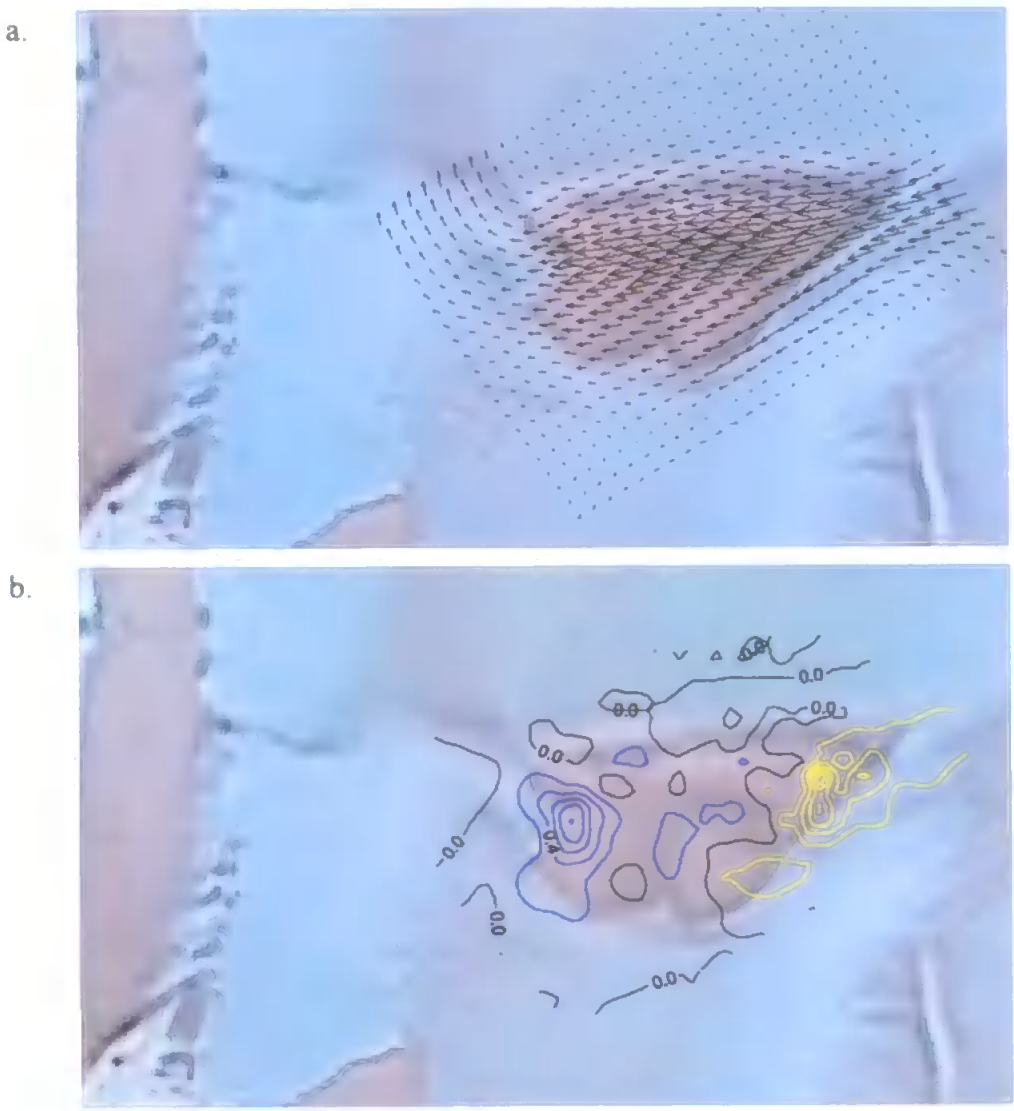

Figure 7.7. Detail of the modelled sediment transport over a thirteen-day simulation covering the storm that reshaped the offshore sandbar in October 1999. Sediment transport patterns (a) and initial sedimentation/erosion rates (b), where deposition is represented by blue lines and erosion by yellow lines (interval between lines is 0.20 m).

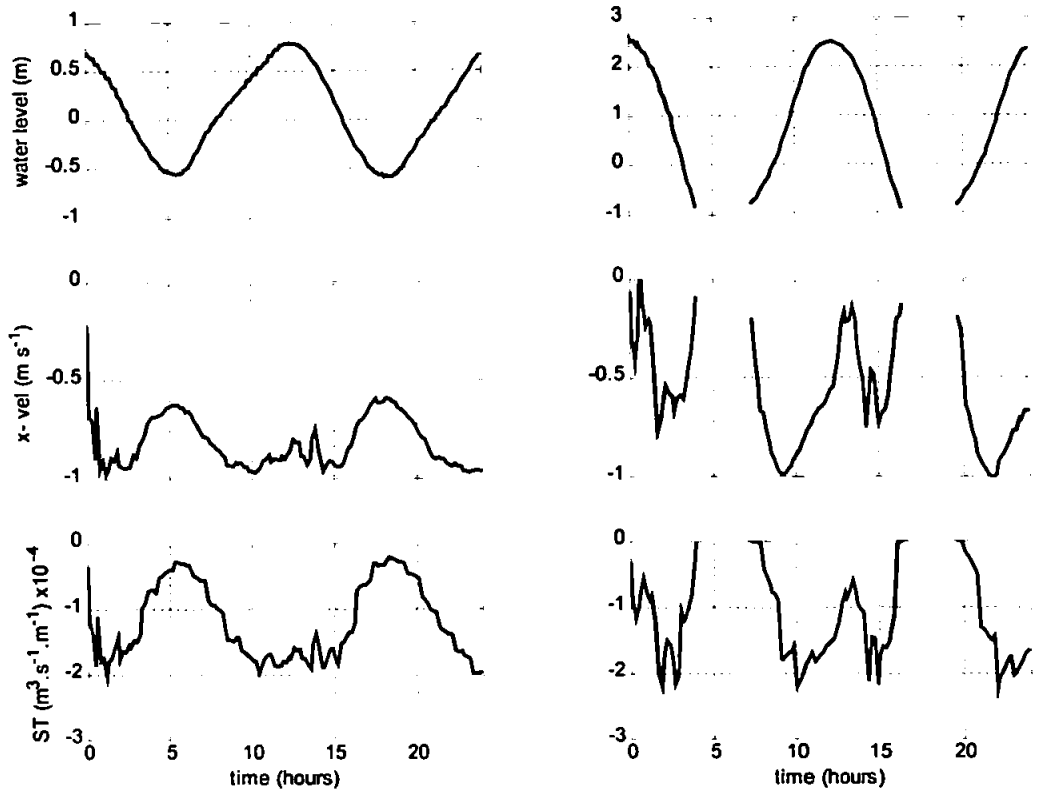

Figure 7.8. Time series of water level, cross-shore velocity and magnitudes of sediment transport over the offshore sandbar for neap (left) and spring (right) tide during high wave energy conditions (H_{sig} = 1.8 m) for the October/November 1999 situation.

7.4.2. Stage 2

During the following nine months (December 1999 – August 2000) the offshore sandbar presents a continuous growth and onshore migration, reaching its maximum size in August 2000 (Figure 7.9). Over this period, again only small changes are visible on the beach and Ness sandbar morphology. Stage 2 is characterised by the long straight shore-attached sandbar.

In January 2000 (Figure 7.9a) the offshore sandbar is elongated growing mainly in the onshore direction. From January to March (Figure 7.9b), the shape of the offshore sandbar is approximately constant, despite the whole sandbar being moved slightly northwards. The submerged sandbar, whose approximate position is indicated through the breaking

waves patterns in the time-averaged images, becomes more convex and moves offshore. Waves breaking at the outer end of the offshore sandbar indicate sediment deposition and the beginning of the formation of a smaller sandbar at this portion. This new sandbar is visible in April 2000 (Figure 7.9c) and with its continuous growth it merges to the main offshore sandbar which is attached to the beach in May (Figure 7.9d). From May to August, the offshore sandbar continues to increase in size becoming more linear and shore-normal. In the following months, from August to December 2000, the attached sandbar area is gradually reduced (Figure 7.9f).

The rapid onshore growth of the offshore sandbar during this period is probably a consequence of the constant onshore sediment over the sandbar by the wave action and the reduction in the sediment transport efficiency of the secondary channel that separates the sandbar from the beach. The reduction of the channel width is accompanied by an onshore shift of the channel axis, causing it to become sheltered from the main ebb flows by the Sprat sand. The modelled hydrodynamics shows a reduction of up to 50 % in the maximum spring tide flow velocities along the secondary channel from October 1999 to January 2000, with ebb flow peaks of about 1 m s^{-1} in October being reduced to maximum velocities of about 0.5 m s^{-1} in January. This gradual reduction in flow velocity enhances the sediment deposition at the shoreward flank of the sandbar, as shown by the modelled sediment transport at this stage (Figure 7.10). During high wave energy conditions, sediment is transported onshore over the sandbar (Figure 7.10a) with the consequent initial sedimentation/erosion rates showing the tendency of sediment deposition at the shoreward flank of the sandbar (Figure 7.10b). This deposition and the erosion that occurs mainly at the channel side of the sandbar are consistent with the evolution of the sandbar, which grows onshore and is shifted northwards during the following months (Figure 7.9).

The result of the numerical simulation shown in Figure 7.10 is representative of a high wave energy event coincident with spring tide conditions. Similar high wave energy during neap tides would result in higher rates of deposition at the shoreward flank of the sandbar, since the high onshore sediment transport would be combined with weaker tidal flows in the secondary channel. Unfortunately, there is no measured wave data for this period in order to verify the exact magnitudes and timing of the acting processes.

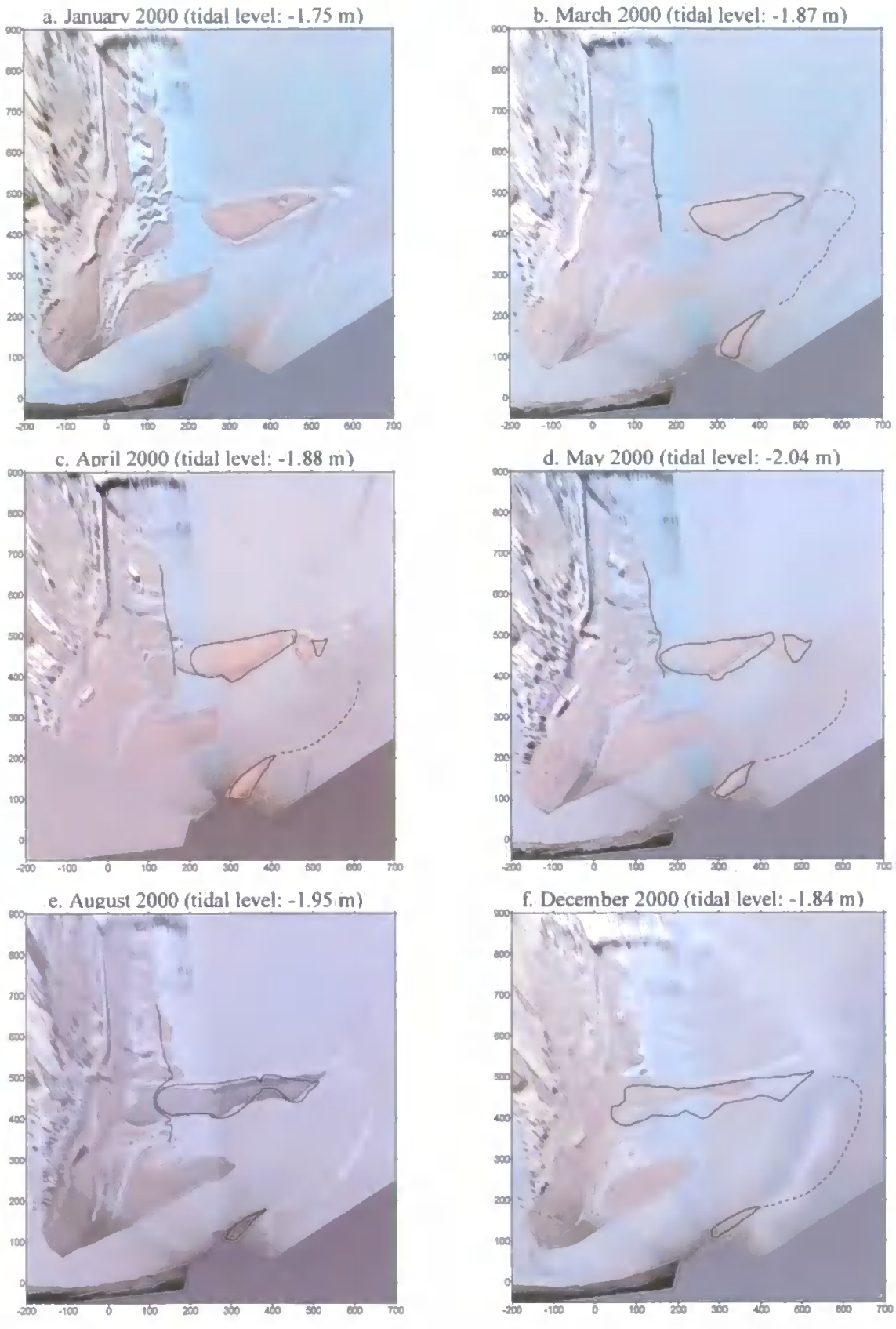

Figure 7.9. Morphological evolution from January to December 2000. Continuous black lines represent the sandbar shoreline from the previous image and dotted line represents the approximate position and of the submerged sandbar. Tidal levels vary between images.

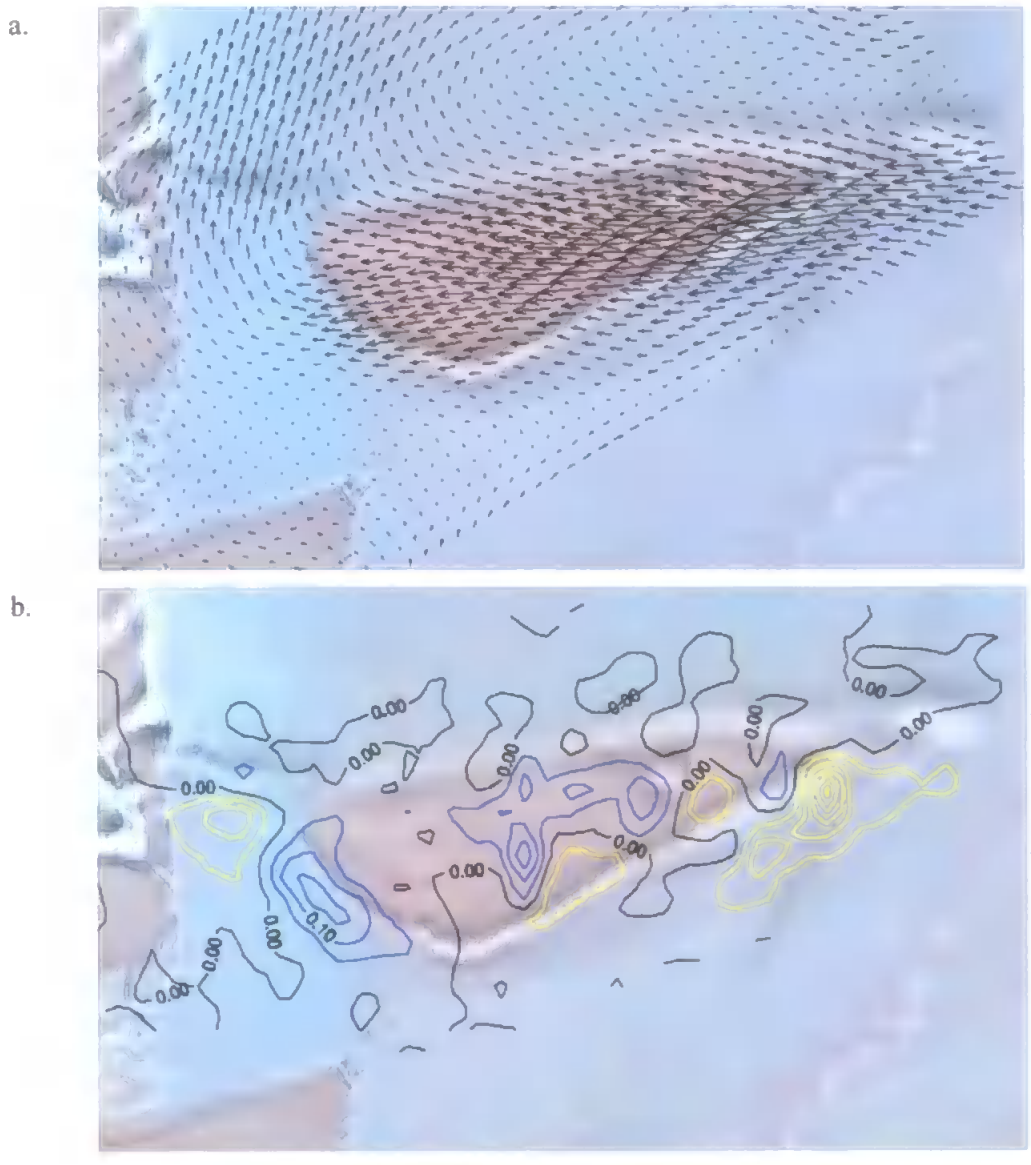

Figure 7.10. Detail of the modelled sediment transport for a high-energy event (H_{sig} = 1.8 m) over the offshore sandbar in January 2000. Sediment transport patterns (a) and initial sedimentation/erosion rates (b), where deposition is represented by blue lines and erosion by yellow lines (interval between lines is 0.05 m).

This process of growth and onshore migration of the offshore sandbar from October/November 1999 onwards results in the attachment of the sandbar to the beach in April/May 2000, reaching its maximum size in August 2000 (Figure 7.9). Numerical experiments for the August 2000 morphology show the same wave dominance over the attached sandbar, with the onshore generated sediment transport during high wave energy

events (Figure 7.11). With this morphological situation there is also a differentiation in sediment transport between spring and neap tides for shore-normal incident waves. Modelled flow velocities over the outer part of the sandbar are directly related to the tidal range, with northward currents (y-component) over the sandbar reaching maximum peaks of 0.6 m during spring tides and 0.15 m during neap tides. This difference will result in variable sediment transport patterns depending on the tidal range, with shore-normal transport during neap tides and a northward deflected transport when the high wave energy coincides with larger tidal ranges. However, as for the previous simulations for other morphological stages, the final direction of sediment transport will be defined by the balance of the opposing tidal and wave generated currents and also by the direction of the incident wave.

At the inner portion of the attached sandbar, an inversion in the direction of sediment transport occurs, with the net southwards longshore current at the beach region driving the sediment transport (Figure 7.11a). The predicted initial sedimentation/erosion rates for this situation are represented in Figure 7.11b, indicating the southwards deposition of sediment at the inner portion of the sandbar. This deposition coincides with the sandbar morphology observed in the background image for August 2000 (Figure 7.11).

From the video images, the main observed change at the beach region is due to the attachment of the offshore sandbar. This results in local effects, with an increased beach volume at the location where the sandbar becomes attached, and a secondary effect, which is the increase in beach width northwards of the attached sandbar. The increase of over 20 m is clearly seen between May and August 2000 (Figure 7.9d and 7.9e). This may be a confirmation of the resultant longshore transport being southwards, with the large attached sandbar acting as a barrier to the sediment transport resulting in this deposition on its northern side. The numerical simulations show the presence of a gyre of sediment transport at the beach region northward of the attached sandbar (Figure 7.11) as a result of the complex circulation at this region with the sandbar acting as a barrier to the flow. This complex circulation can be seen in the example in Figure 5.10 (Chapter 5) showing snapshots of the flow fields during a spring tidal cycle under high incident wave energy. The gyre of transported sediment may result in a gradual deposition at this region, resulting in the widening of the beach at this portion. The deposition at this region is not clear in the predicted morphological evolution, which is probably a consequence of the relatively small

quantities of sediment carried over the simulation time (two tidal cycles). However, considering larger time scales, it can be expected that this process would lead to sediment deposition at this region, which is confirmed by the observations (Figure 7.9).

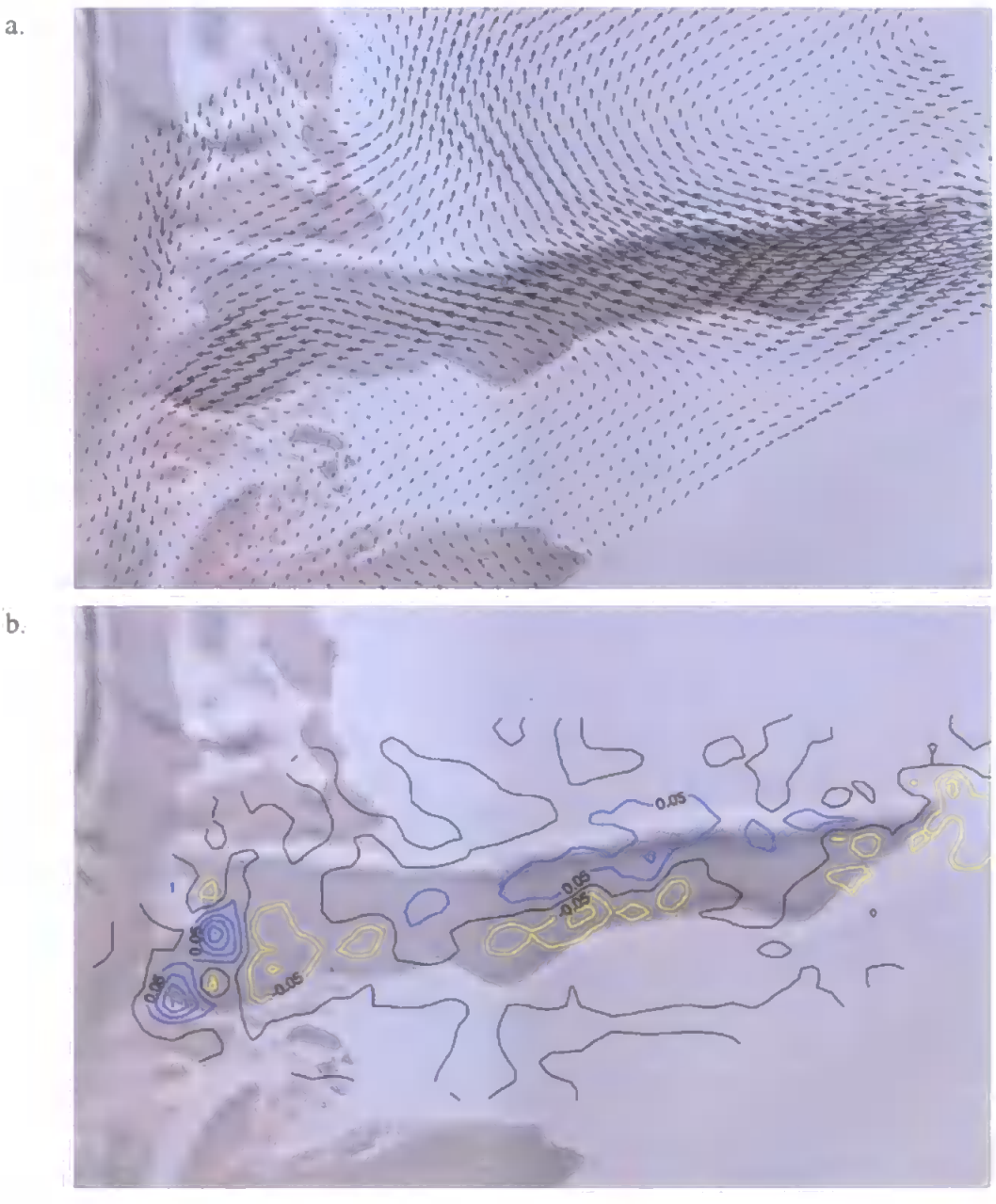

Figure 7.11. Detail of the modelled sediment transport for a high-energy event (H_{sig} = 1.8 m) over the offshore sandbar in August 2000. Sediment transport patterns (a) and initial sedimentation/erosion rates (b), where deposition is represented by blue lines and erosion by yellow lines (interval between lines is 0.05 m).

Sediment transport patterns at the outer portion of the attached sandbar are also affected by events of high river discharges, with an increased northward deflection of the sediment transport direction displacing larger amounts of sediment in this direction. An example of this process is shown in Figure 7.12, where the vectors show the northwards deflection of the transport and the resultant profile of initial sedimentation/erosion rates shows the consequence of larger amounts of sediment being transported northwards due to the higher river discharge. The deflected transport results in larger erosion at the southern side of the sandbar and consequently in larger deposition at its northern flank.

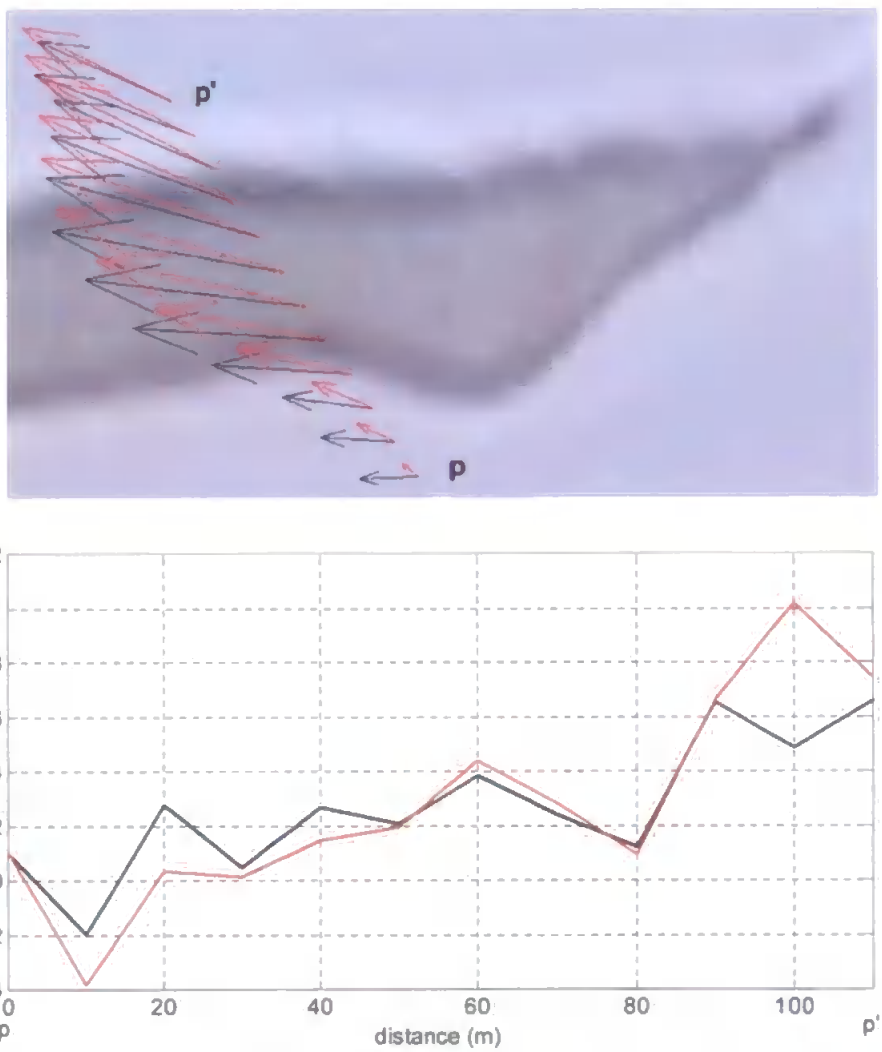

Figure 7.12. Top: predicted patterns of sediment transport along the indicated profile for low river discharge (black vectors) and high river discharge ($100m^3\ s^{-1}$) (red vectors). Bottom: initial sedimentation/erosion rates along the indicated profile (p-p') for low river discharge (black line) and high river discharge (red line).

Comparing these predicted processes with the observed evolution of the sandbar may indicate the cause of the evolution to the Stage 3 of the morphological cycle. From August to December 2000, only small changes in morphology can be seen through the analysis of the video images (Figure 7.9). This is probably the consequence of relative low wave energy conditions over this period. Non-directional wave data measured at the Teignmouth pier shows that from August to November 2000 only one event of significant wave height higher than 1 m took place. River discharge during this period is also low, with an average discharge of about 10 $m^3 s^{-1}$. It is only in December that the frequency and intensity of storms increased, coinciding also with higher river discharge values, creating much more energetic conditions that will be reflected in the sandbar morphology.

7.4.3. Stage 3

Following the evolutionary tendency of the morphological Stage 2, the outer portion of the previously straight attached sandbar is bent northwards in February 2001 (Figure 7.13a). This change in the sandbar shape happened over a relatively short period of time, between December 2000 and February 2001. Due to technical problems with the video system no images were recorded in January 2001, a period during which this change in morphology happened. Based on the observations of measured conditions during this period it is expected that the drastic morphological change of the sandbar is associated with a high wave energy event coincident with spring tide and a period of high river discharge (Figure 7.14). The storm event that hit the region was relatively long, lasting for approximately five days (10-15/01/01) with significant wave heights of up to 2.0 m. The tidal range at the time was of about 4 m resulting in strong ebb flows which combined with river discharge peaks of up to 70 $m^3 s^{-1}$ are able to enhance the northward transport over the sandbar (as discussed in the previous section).

Based on the predicted sediment transport patterns of the August 2000 period (Stage 2), this combination of a storm event with spring tides and high river discharge seems to be the most likely cause of the change in morphology that happened over this short period of time. No directional wave data is available for the period; however, the simulations show that waves approaching the region at angles higher than 110 degrees from true North

(approx. shore-normal) would cause sediment to be transported northwards over the outer portion of the sandbar. Maximum quantities of sediment being transported and maximum northward deflection in the transport direction occur if the storm reaches the region from the south-westerly quadrant.

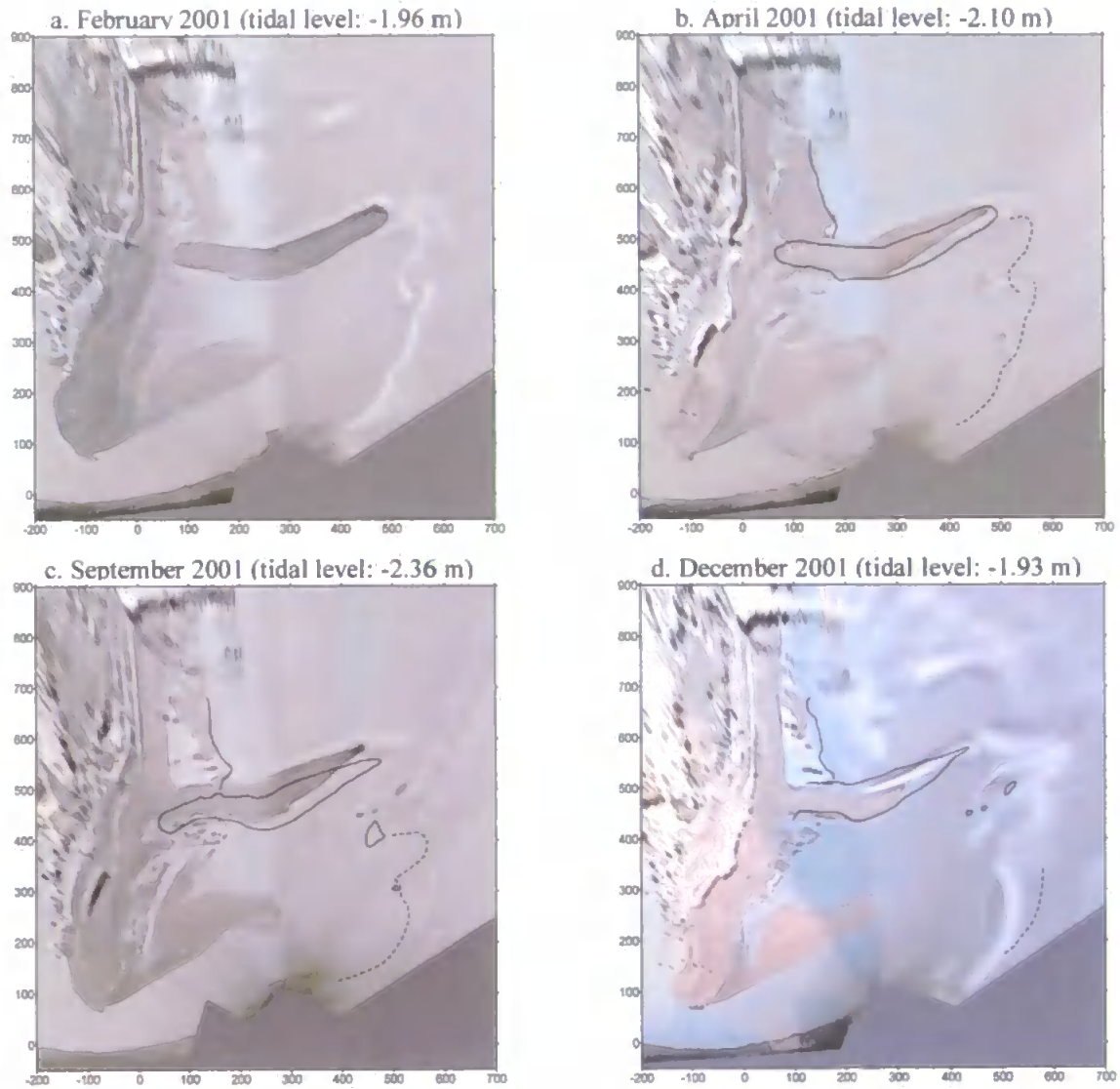

Figure 7.13. Morphological evolution from February to December 2001. Continuous black lines represent the sandbar shoreline from the previous image and dotted line represents the approximate position and of the submerged sandbar. Tidal levels vary between images.

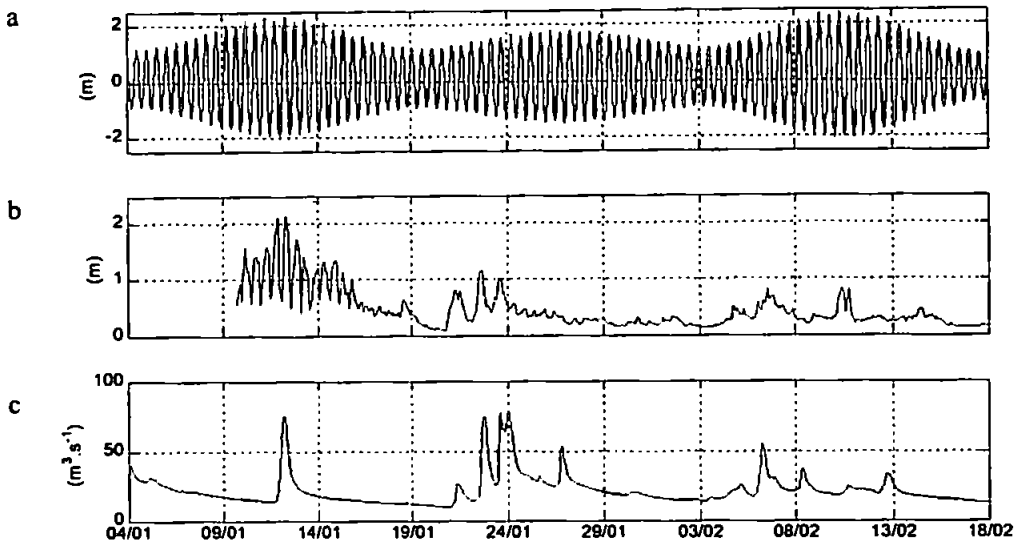

Figure 7.14. Predicted water level (a), measured waves at the pier (b), and river discharge (c) for January/February 2001.

Similar simulations for the February 2001 morphology, with the bent attached sandbar, indicate the continuation of the northward migration of the outer portion of the sandbar and a slow southward displacement of the inner part of the sandbar (Figure 7.15). This anti-clockwise "rotation" of the sandbar is also verified in the video images over the following months (Figure 7.13b). In the numerical experiment of a storm situation this rotation process is shown by the strong onshore and northwards transport over the bent portion of the sandbar and by the constant southwards longshore transport (Figure 7.15a). Large amounts of sediment being transported at the exposed outer portion of the sandbar result in rapid morphological changes, as indicated by the predicted rates of erosion and deposition over two tidal cycles (Figure 7.15b). Smaller amounts of sediment displaced by the longshore current result in slower morphological changes at the inner portion of the sandbar, and are not evident in the short-term predicted initial sedimentation/erosion rates.

The observed evolution of the sandbar indicates that after it is bent northwards, a relatively rapid northward migration takes place, with a consequent reduction in area of the sandbar (Figure 7.13). This process occurs even during calmer summer months, indicating that the sandbar is destabilised, probably due to its larger exposure to the incoming waves. This process is also reflected in the numerical experiments for both straight and bent attached

sandbar. If considering the sediment transport through the main axis along the middle part of the sandbar, it is mainly parallel to the axis when the sandbar is straight (August 2000 – Figure 7.11), with the dominant onshore transport meaning that little sediment is removed from the sandbar. With the bent sandbar, the sediment crosses through the main axis of the outer portion, meaning that larger quantities of sediment are being removed from the sandbar (e.g. February 2001 – Figure 7.15). Predicted sediment transport patterns, under the same forcing conditions, over two tidal cycles show that an increase in sediment volume crossing the sandbar axis of about 120 m^3 is expected when the sandbar is bent. In August 2000, the sediment volume crossing the sandbar axis during two tidal cycles is of about 360 m^3, while in February 2001 it is increased to about 480 m^3. This process of increased quantities of sediment being removed from the sandbar shows the importance of sporadic events for the development of the cycle, controlling the speed of its development. Without the northward bend of the sandbar due to the combination of high energy events during the winter months (e.g. January 2001), the sandbar would probably remain approximately constant over the summer months, since it would have been relatively "protected" from the action of waves.

The gradual reduction of the attached sandbar coincides with the origin of a new offshore sandbar, which is visible in April 2001 when it emerges at low water (Figure 7.13b). When comparing the predicted sediment transport and initial sedimentation/erosion rates for the morphology in February 2001 with the observed morphology in the April image, it is shown that the offshore sandbar is formed in the region between opposing directions of sediment transport (Figure 7.16). This contradicts Robinson's (1975) idea of the offshore sandbar being originated by the northward growth and breaching of the Ness sandbar. Model results show that the offshore sediment transport driven by the ebb flow in the channel and the wave driven onshore transport over the shoals seem to be responsible for the initial sediment deposition that generates the sandbar. The initial sedimentation/erosion rates shown in Figure 7.15 and 7.16 indicate the region of sediment deposition between these two opposing flows. Although this modelled deposition region is relatively small and slightly offshore in relation to the formed sandbar (Figure 7.16) it indicates that there is indeed sedimentation at this region. This example is the result of a short period simulation (two tidal cycles) of storm conditions, therefore it is expected that over longer periods of high wave energy or periods with higher frequency of storm events (e.g. winter months) this process will be enhanced.

This process is controlled by the flow asymmetry resultant from the wave action (Figure 7.17). Under the influence of waves, the flow over the shoals becomes flood dominant, with an onshore residual current of about 0.38 m s^{-1} and peaks close to 0.8 m s^{-1}. In the channel, stronger offshore flows characterise its strong ebb-dominance, independent of the intensity of the incident waves. The shear originated from these two opposing flows would create a deposition area, where the sandbar can be formed (Figure 7.16). During calm conditions, both channel and shoals are ebb dominant, despite the small residual offshore currents over the shoals (of about 0.1 m s^{-1} – Figure 7.17). Extending the idea of this process to a larger time scale it can be expected that during storm situations a initial sediment deposition would occur, while during calmer spring tide periods the dominant but weaker offshore flows would slowly spread the deposited sediment by moving it offshore and northwards. During calm neap tides, the weak tidal currents would displace only small amounts of sediment, with the sediment deposits remaining relatively stable.

From the observed morphological evolution following the origin of the new offshore sandbar in April 2001, this idea of the formation and initial evolution of the sandbar seems to be consistent. In September 2001, after the less energetic summer months, the sandbar is less evident and spread offshore and northwards. This is clearly seen in the corresponding video image (Figure 7.13c), where only small remains of the sandbar are visible despite the lower tidal level in relation to the previous image. The opposite is observed with the presence of more dynamic conditions in the beginning of the winter (December 2001 - Figure 7.13d), where the sandbar volume seems to have increased considerably, with a larger intertidal area despite the higher water level at the time of the image. At the southern side of the channel, the same process is verified by the evolution of the Ness sandbar. The Ness sandbar is not evident during the calmer summer months, emerging only in December 2001 showing its large volume increase. The wave dominance on its formation can be seen also by its evident onshore migration (Figure 7.13d).

A similar process of sandbar origin can be related to the Sprat sandbar (indicated by "f" in Figure 3.5), which extends offshore from the sandy spit constricting the inlet channel. The dominance of the ebb tidal flows at its south margin contrasts with the wave and flood tide onshore generated flows at the northern flank. Despite being formed and maintained by the same process, the Sprat sandbar is much more stable than the offshore sandbar due to its relative protection from the incident waves.

On the other hand, due to the dominant wave action over the attached sandbar, it is gradually spread and reduced in size. Numerical simulations for the May and September 2001 morphologies result in similar sediment transport patterns as for February 2001, indicating the gradual erosion and northward migration of the outer part of this sandbar.

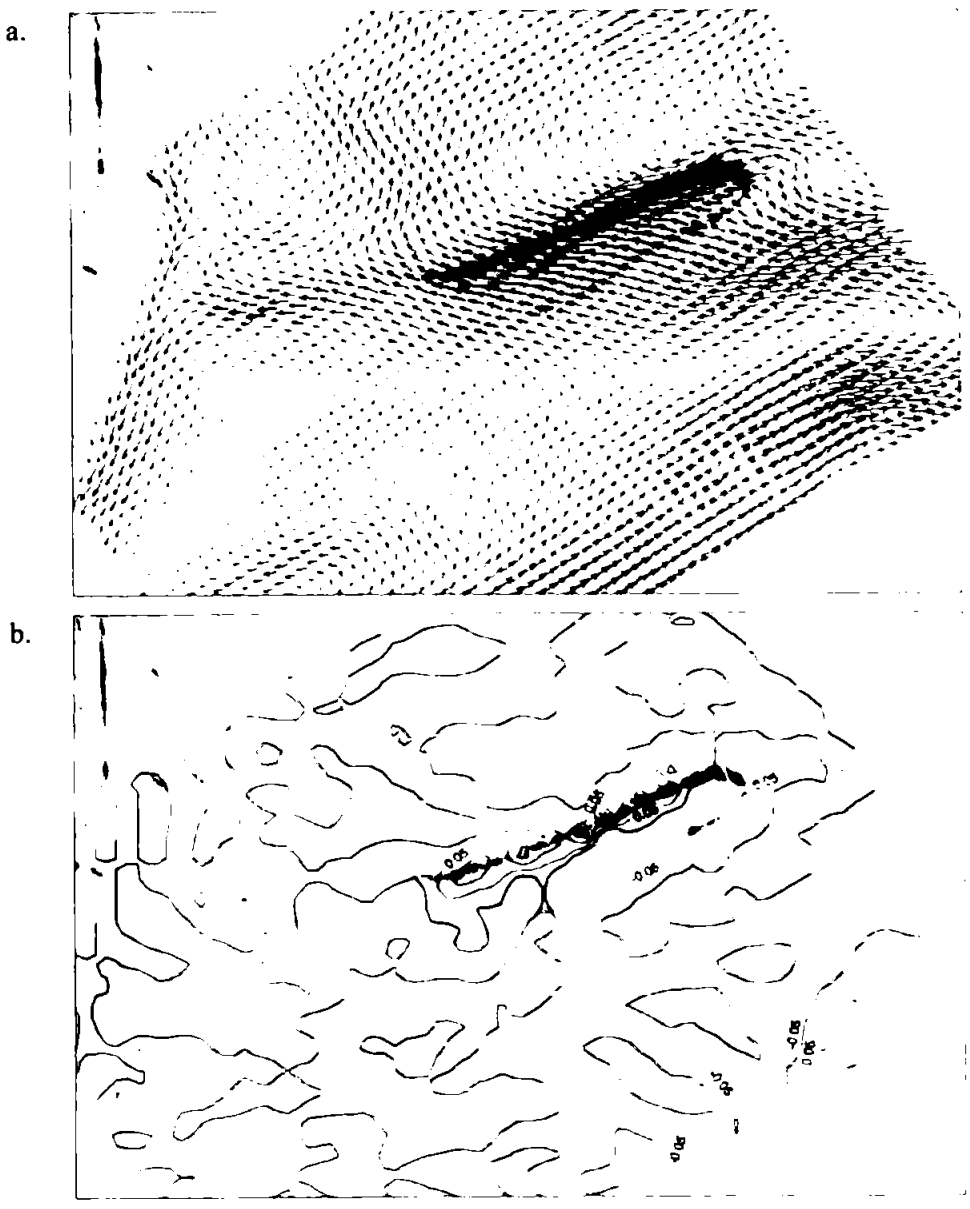

Figure 7.15. Detail of the modelled sediment transport for a high-energy event (H_{sig} = 1.8 m) over the offshore sandbar in February 2001. Sediment transport patterns (a) and initial sedimentation/erosion rates (b), where deposition is represented by blue lines and erosion by yellow lines (interval between lines is 0.05 m).

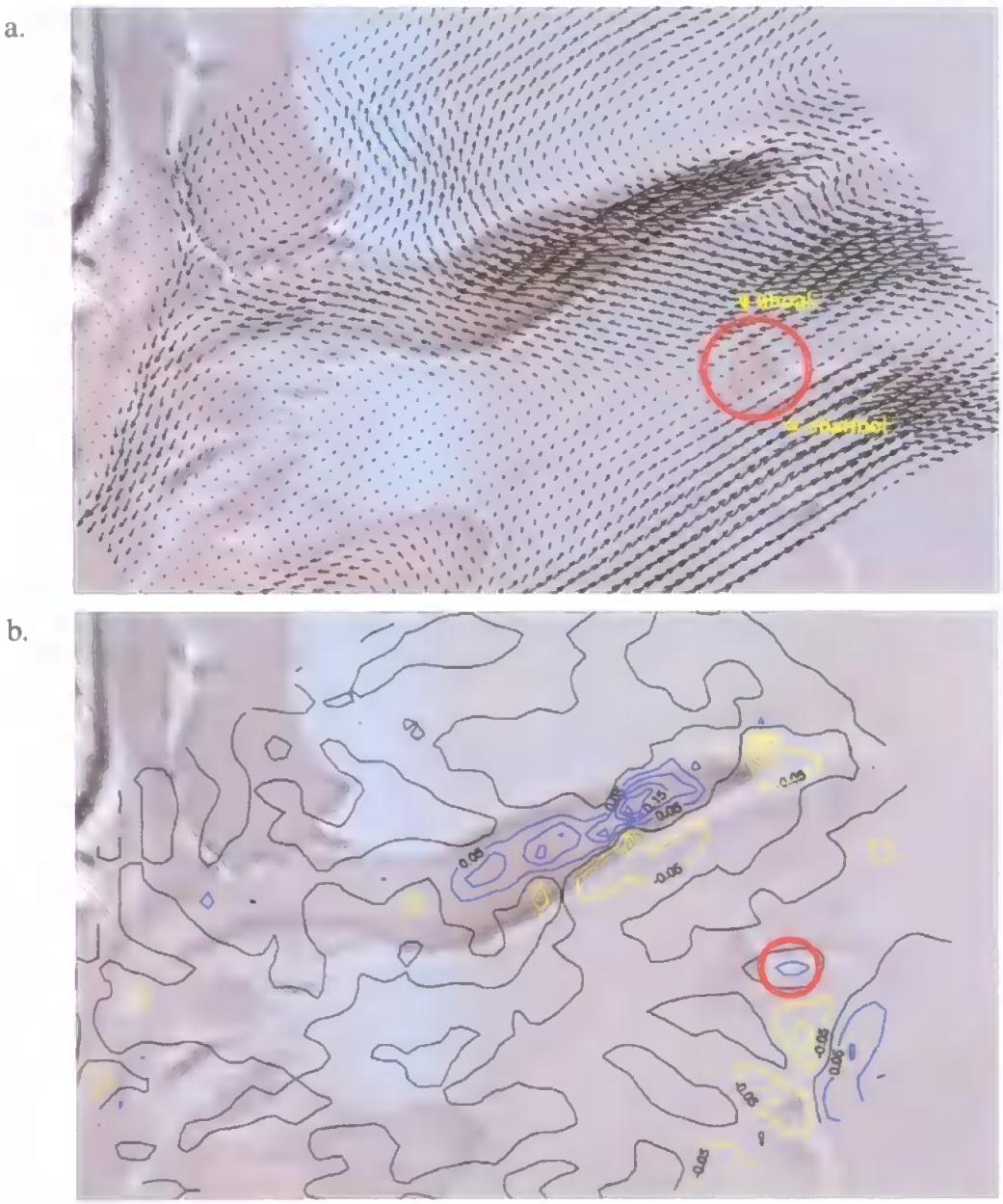

Figure 7.16. Predicted sediment transport (a) and initial sedimentation/erosion patterns for February 2001 overlaid on the April 2001 image. In (a) the red circle highlights the new offshore sandbar and the yellow dots indicate the location of the channel and shoal velocity time series represented in Figure 7.17. In (b) the red circle indicates the location of the modelled sedimentation region.

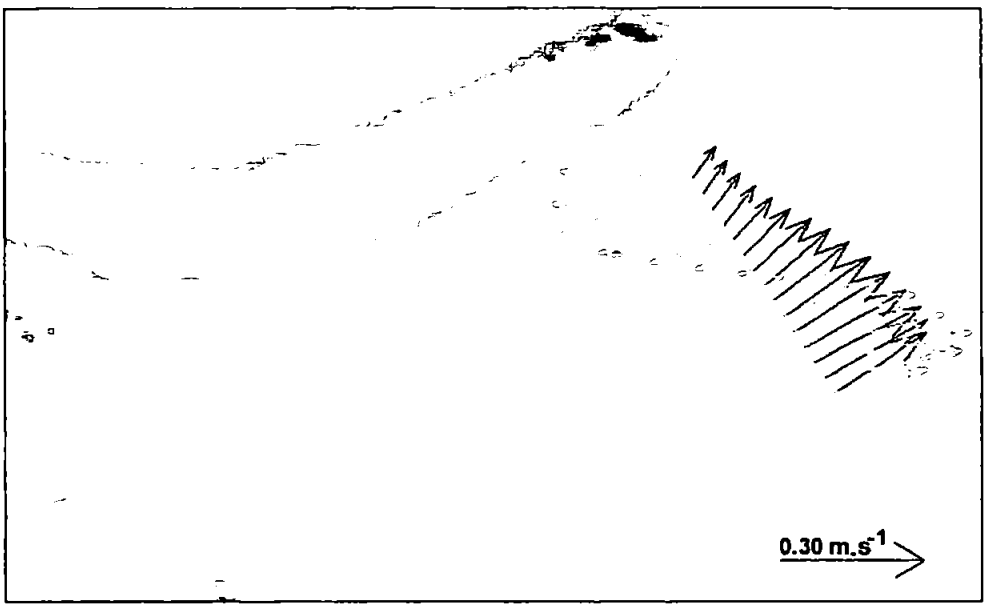

a. no waves

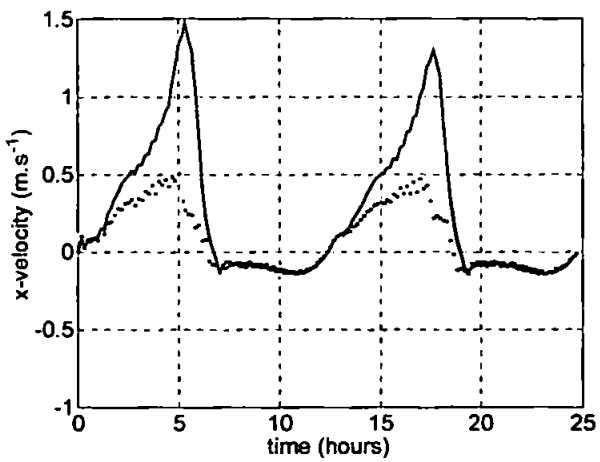

b. H_{sig} = 1.8 m

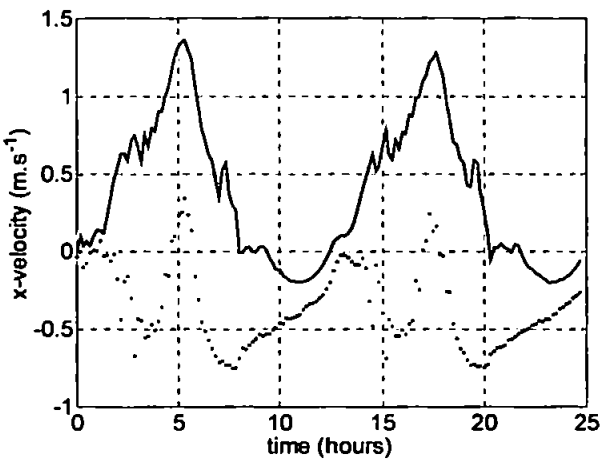

Figure 7.17. Top: residual flow vectors for only tide simulation (black) and under the influence of waves (H_{sig} = 1.8 m – yellow) over two spring tidal cycles in February 2001. Bottom: time series of modelled cross-shore component of the velocities over the two-tidal cycles at the channel (line) and shoal (dots) locations indicated in Figure 7.16 for both wave energy situations. Negative values = onshore; positive = offshore.

7.4.4. Stage 4

During the following month, from December 2001 (Figure 7.13d) to January 2002 (Figure 7.18a), an increase in the new offshore sandbar can be observed, with the attached sandbar remaining approximately constant. In the following three months, drastic changes in

morphology can be observed. The attached sandbar decreases in size and volume, and the offshore sandbar grows rapidly and moves shoreward (Figure 7.18b), producing a configuration reminiscent of the morphology observed at the beginning of the observations (Figure 7.3), suggesting the completion of a cycle in the evolution of the sandbars over this approximately three-year period.

The Ness sandbar that emerges further offshore from December 2001 to January 2002, is visible only at its onshore portion, attached to the Ness point in April 2002 (Figure 7.18b). Part of the sediment that composed the sandbar may have been bypassed through the channel due to the wave action over this period, being a possible source of sediment for the growing offshore sandbar.

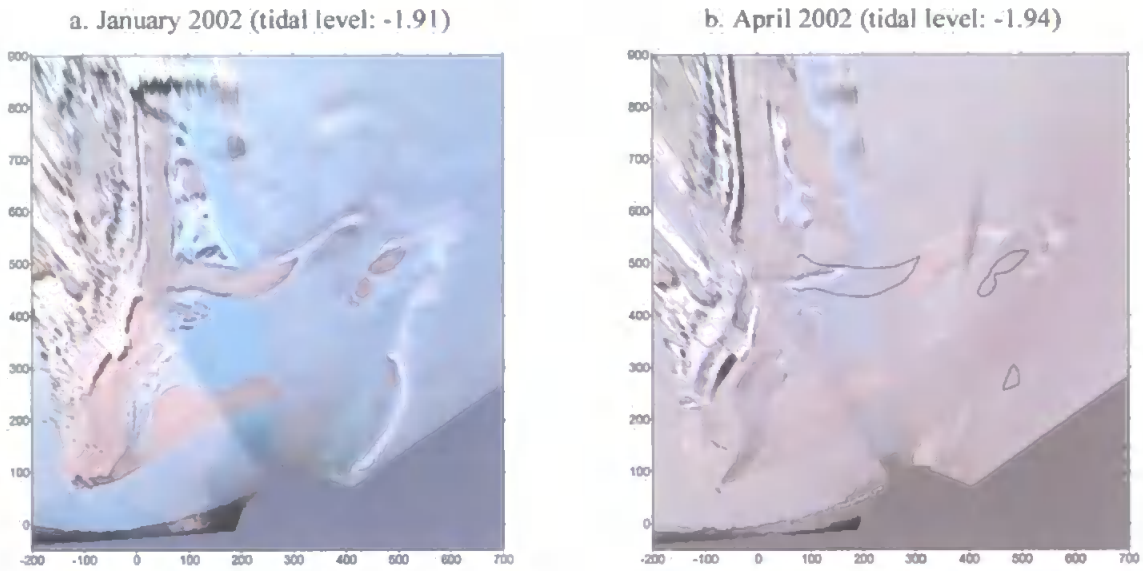

Figure 7.18. Morphological evolution from January to April 2002.

Numerical experiments using both January and April 2002 morphologies produced similar sediment transport patterns over the forming offshore sandbar. These are also similar to those obtained for the March and October/November 1999 simulations discussed in section 7.4.1. Sediment transport over the offshore sandbar is directed onshore and northwards under energetic situations (H_{sig} = 1.8 m and tidal range of about 4 m), resulting in an increased deposition at the northern side of the sandbar (as shown in the example for the

April 2002 simulation in Figure 7.19). The main difference in the morphology at the beginning of the cycle is the sandbar shape and orientation. In April 2002 the offshore sandbar is more exposed to the wave action due to its main axis being rotated in relation to the shoreline. This may increase the sediment transport over the sandbar resulting in an accelerated onshore migration. Observations of the following months show that the sandbar becomes attached to the beach in September 2002.

a.

b.

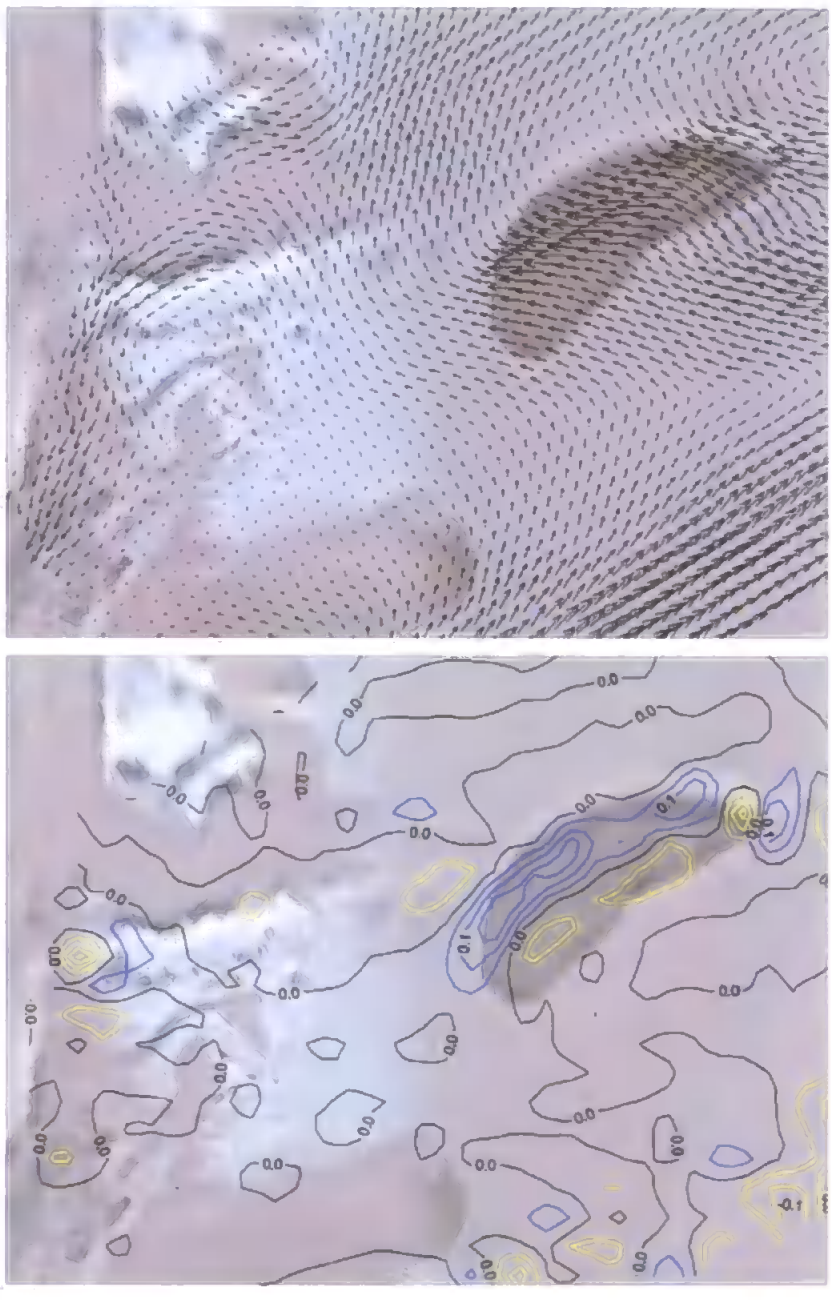

Figure 7.19. Detail of the modelled sediment transport for a high-energy event (H_{sig} = 1.8 m) over the offshore sandbar in April 2002. Sediment transport patterns (a) and initial sedimentation/erosion rates (b), where deposition is represented by blue lines and erosion by yellow lines (interval between lines is 0.05 m).

7.5. Conceptual Model of the Cyclic Evolution at Teignmouth

Based on the observed evolutionary cycle of the sandbar morphology at Teignmouth and the knowledge obtained about the physical processes controlling the system through the model application at each of the previously described stages, a simplified conceptual model for the cyclic sandbar behaviour is proposed. The previously described results show that despite the relatively low frequency and intensity of high energy events that hit the region, these sporadic events control the local morphodynamics by catalysing the morphological changes. The main features of each morphological stage are summarised starting with the origin of the sandbar and following its evolution until its spreading and the possible beginning of a new cycle.

7.5.1. Origin of the sandbars

The flow asymmetry around the Teign estuary mouth seems to be the process responsible for the origin and maintenance of the sandbars. There are three main intertidal sand bodies at Teignmouth: the Sprat sandbar; the Ness sandbar; and the offshore sandbar (Figure 3.5).

The Sprat sandbar, is a relatively stable sandbar formed as an offshore extension of the sandy spit that limits the inlet channel. The main sediment supply to this sandbar is probably the dominant southward longshore transport. This sandbar is stable due to its relative protection from the incoming waves, being controlled mainly by the tidal flows. Its origin is probably related to the sediment being gradually trapped at the region between the dominant ebb channel (main channel) and the flood channel that separates the sandbar from the beach (Figure 7.20a). During the three-year observed cycle only small morphological changes are observed at the Sprat sandbar, indicating a longer-term morphological evolution.

The origin and morphodynamics of the Ness sandbar and the offshore sandbar seem to be directly related to the wave action, presenting as a consequence a seasonal behaviour with the most drastic changes occurring during winter months. Nonetheless, the same principle of flow asymmetry around the sandbars is expected to be responsible for their formation. As shown in section 7.4.3, the onshore wave generated currents over the shoals opposing

the main ebb flows in the channel create deposition zones that will be responsible for the origin of these sediment accumulations over the shoals, as represented in the schematic diagram in Figure 7.20. These two intertidal sand bodies are linked by the submerged "U" shaped sandbar at the outer part of the channel, which is controlled by the interaction of channel tidal flows and the reworking of sediments by the incoming waves. The on- or offshore migration of this submerged sandbar is a function of the relative importance of waves or tides.

This process of generation of new sandbars over the shoals is constant throughout the cycle, with newly formed sand accumulations being added to the already existent sandbars. An example of merging of sandbars is shown in Stage 2 (Figure 7.9b, c and d).

In this study no direct estimates of the influence of the drag-dredging in the channel region were made. However, as the dredging is concentrated at the outer part of the channel and is constantly (independent of the tidal phase) resuspending sediment, it is believed that little sediment is removed from the system through this process. The main affected sandbar is the submerged sandbar at the outer part of the channel and consequently the Ness sandbar. Pictures of the sandbars previous to the dredging activities show that at periods the Ness sandbar grew northwards crossing the inlet channel, being responsible for the bypass of sediment from south to north. Nowadays this process is probably minimised due to the dredging activity.

7.5.2. Onshore migration of the sandbar

Once formed, the sandbars continue to grow due to the gradual sediment addition from both sides, the channel (mainly during spring tides) and the shoals (during higher wave energy periods). The magnitude of this process is also controlled seasonally, with increased growth rates during more energetic periods (e.g. winter months).

Combined with the sediment addition, the sandbar tends to move onshore, due to the large quantities of sediment transported by the wave action over the sandbar (Figure 7.20b). This process occurs during high energy events independent of the tidal range. The onshore migration of the sandbar is accelerated when the secondary channel that separates the

offshore sandbar from the beach reduces its competence for sediment transport. Due to the gradual landward migration of the sandbar, the main axis of the secondary channel is shifted becoming "protected" from the main tidal flows, leading to its abandonment and increased sedimentation at the shoreward flank of the sandbar.

Additional sediment to the sandbar may come from newly formed sandbars over the shoals, which will migrate onshore and merge at the outer portion of the growing sandbar. This process is verified during Stage 2 (Figure 7.9b, c and d).

The process of the sandbar attachment to the beach is driven mainly by wave action, which reshapes the sandbar so that it becomes thinner and elongated (Figure 7.20c). Interaction with tidal currents results in the slow northward migration of the sandbar while it is growing onshore.

7.5.3. Spreading of the attached sandbar and formation of a new offshore sandbar

Due to the wave action over the attached sandbar, it is expected that the reshaping process of the sandbar will continue, driving sediment constantly onshore and resulting in a gradual reduction in width and length of the outer portion of the sandbar (Figure 7.20c, a). Depending on the angle of wave incidence and the interaction with tidal currents a resultant northward component in the sediment transport is also expected over the outer portion of the sandbar. The longshore wave generated currents, with a southward resultant, control sediment transport at the inner portion, attached to the beach. In the observed cycle, the outer portion of the sandbar is bent northwards, and this is the probable cause of an accelerated spreading process. As discussed previously, the reorientation of the sandbar to face the incoming waves more directly results in larger quantities of sediment being removed from the sandbar. The velocity of the spreading process of the attached sandbar is also dependent on the frequency and magnitude of incoming storms and the balance between erosion over the sandbar and deposition of sediments through the merging of the newly formed depositions.

As a result of the gradual spreading and northward migration of the outer portion of the attached sandbar, the sandbars formed over the shoals are not able to merge with the

remains of the attached sandbar. This results in the formation of a secondary channel between the attached sandbar remains and the "new" sandbar, which will then grow as an isolated new offshore sandbar. This process completes the evolutionary cycle as illustrated in Figure 7.20.

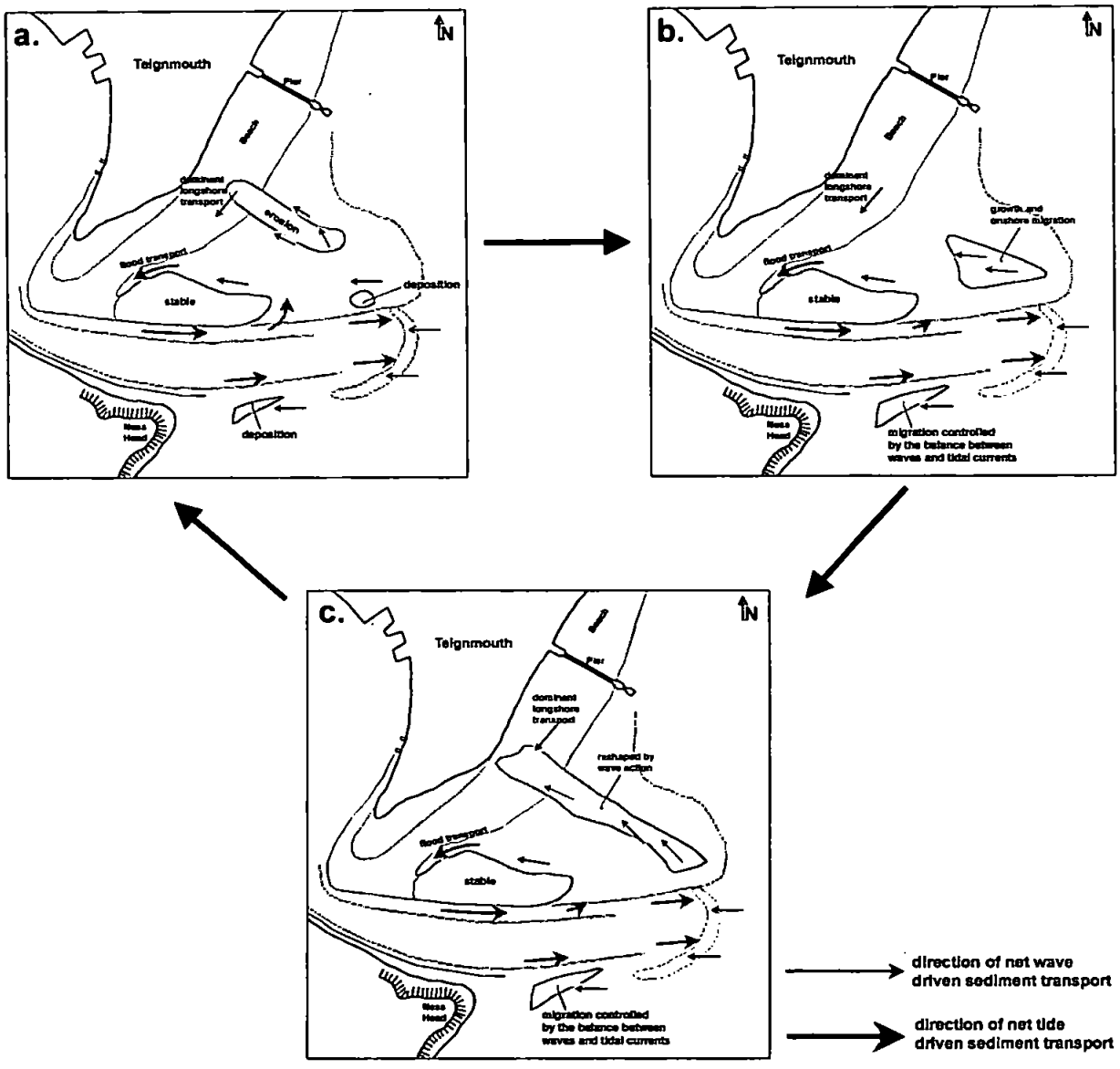

Figure 7.20. Conceptual model for the evolutionary cycle of the ebb tidal delta sandbars at Teignmouth.

7.6. Conclusions

The coupled use of video imaging and numerical modelling proved to be a very powerful tool in order to assess the morphodynamics of this complex site. In the absence of *in situ* field measurements, the technique proposed in Chapter 5 to obtain the morphology of the region of interest at different stages of the morphological evolution complements the numerical modelling experiments. Following the assessment of the sensitivity of the region to the several key forces (Chapter 6), the application of the numerical model at different stages of the evolutionary cycle brings a valuable insight into the local morphodynamics.

The complex interaction between tidal currents and waves controls the dynamics of the sandbars. Wave action over the shoals is particularly important to the local dynamics and defines the most drastic morphological changes of the system. High wave energy events are responsible for the displacement of great quantities of sediment over relatively short periods of time (days). This makes the system more dynamically active over the winter months, when a higher frequency and intensity of storms reshape the morphology. It is also during this period that river discharge values reach high peaks, increasing the capacity of the ebbing tidal flows and interacting with the opposing waves. The opposite occurs during summer periods, when less energetic conditions lead to slower morphological changes. Despite the relatively low frequency of high wave energy events that reach the region they can catalyse some drastic morphological changes that define the local morphodynamics.

The main difference between the observed evolutionary cycle and those previously described by Robinson (1975) is probably related to human influence. The constant drag-dredging at the region of the main channel keeps the orientation of the channel relatively constant and minimises the sediment bypass through the northward growth of the Ness sandbar. The cycle observed by Robinson (1975) includes the bypass of large amounts of sediment through the growth of the Ness sandbar, which would cross the channel adding sediment to the offshore sandbar.

The present application of an initial sedimentation/erosion model proved to be useful in giving qualitative predictions of the morphological evolution of the sandbar system. The short period simulations were carried out in order to test the effects of different forcing

conditions on the sediment transport patterns and initial morphological changes. These changes represent the first morphological adjustments of the system as a response to the presence of the sandbars. As discussed in Chapter 2, according to De Vriend (1994) these primary transport phenomena are predominant in shaping the morphology of the system, resulting in a reliable indication of this process. Each of the modelled morphological stages of the sandbar system resulted in the tendency in the morphological evolution dependent on the forcing conditions, and thereby predict its behaviour.

For the longer-term predictability of this system (e.g. the whole evolutionary cycle), this study highlights the importance of the knowledge of the external forcing conditions or a good understanding of their sequencing. High wave energy events for example, which are relatively rare at this region, are shown to play a major role in the morphological evolution and cyclic behaviour of the system. Therefore, the knowledge of the frequency and intensity of such events throughout the entire cycle is of fundamental importance in order to predict its evolution.

Chapter 8

Conclusions and Future Directions

8.1. General Conclusions

The coupled application of a validated numerical area model and video images has been used to provide a better understanding of the driving forces that control sandbar dynamics at the inlet system of Teignmouth. The method applied here is an innovative way of iteratively combining the results of a numerical model with the information extracted from video images. In this process, the modelled water levels are used as input to the image processing, which then provides the intertidal morphology that is used in further modelling experiments, closing the loop that can be repeated several times depending on the required temporal resolution. This coupled technique allowed the application of modelling experiments to different stages of the evolutionary cycle, resulting in a quantitative assessment of the relative influence of the key processes that control the environment and in initial steps towards the prediction of its evolution.

The Teign river inlet system was chosen for this study due to its challenging nature, with complex and active morphodynamic behaviour. In addition, this site has been the subject of a series of studies and field campaigns, providing a unique database with *in situ* measurements and video images.

The objectives proposed in this study aim to provide a better understanding of the balance of driving forces in the vicinity of an inlet system. The main conclusions of this study are given below in accordance to the specific objectives.

Application, calibration and validation of a numerical area model

For this purpose, three modules of the MIKE21 modelling system were applied at the Teignmouth region: the two-dimensional hydrodynamic module; the nearshore spectral wave module, and; the non-cohesive sediment transport module. The adjustable parameters during the calibration procedure were the bed resistance (Chézy numbers) and the eddy viscosity. Both were defined as varying across the model grid. Chézy numbers were set as being depth dependent and eddy viscosity values were dependent on the modelled region. The hydrodynamic module and the wave module were validated against measured water levels, current velocities and wave parameters obtained during the COAST3D main experiment. This unique database includes a dense spatial coverage of measurements within the area of interest, including a range of forcing conditions. The validation procedure included the qualitative time series comparison of measured and calculated values and the application of statistical parameters (relative mean absolute error – RMAE) in order to quantify the quality of the model. The quality of the sediment transport module was assessed using the COAST3D morphological surveys. This was carried out in an indirect way, by comparing the measured and modelled morphological changes over a given period. The visual observation of the morphological changes provides a qualitative assessment of the model quality, which is complemented by the quantitative measure through the use of skill scores. It is only recently that the quality of numerical models has been assessed through the use of such statistical parameters (Brady and Sutherland, 2001; Sutherland et al., 2001; Van Rijn et al., 2003; Sutherland and Soulsby, 2003) and their validity has been confirmed in this study.

As with all numerical modelling experiments, one needs to be aware of some limitations that arise from its application. In addition to the inherent limitations of numerical models, the main limitations of the present application are related to the depth averaged calculated flows, the grid resolution, the limited resolution of the available sediment data and the use of an initial sedimentation/erosion model. The depth averaged calculated flows, which may not always represent the actual circulation at regions where stratification is important is not believed to affect the region of interest, since evidence shows that a stratified water column is formed only when the flow leaves the main channel. The applied grid resolution (10x10 m), which may not represent some of the features of the complex bathymetry, is the best possible representation of the surveyed bathymetry. The limited resolution of the

available sediment data may result in misrepresentations of the quantities of sediment displaced, but the definition of regions of sedimentation or erosion is expected to be less affected. And finally, the fact that the present application is based on an initial sedimentation/erosion model, without the feedback between the morphological changes and the hydrodynamics is minimised by the application of the model over short periods, reproducing the initial adjustment of the morphology to the forcing conditions. Despite some uncertainties attached to the application of numerical models, the partial validation of the numerical model shows that the applied model reproduces well the overall observed phenomena at this complex site.

Combining Numerical modelling and video imaging in order to extract intertidal morphology from images

The model application served two separate functions throughout this study, first with the hydrodynamics results being used for the image processing and second, combined with the sediment transport module, with the full model being used to understand the relative importance of the driving forces at the region. As one of the objectives was to apply the model to different stages of the morphological evolution of the system and only two surveys were available, an alternative way of obtaining the morphology was applied. This involves the use of the Argus video images available for the region. However, one complicating factor is the requirement of accurate water levels for the image processing. At inlet systems, where pressure gradients result in large horizontal differences in water levels, these need to be taken into account. Therefore, the modelled water levels were used when defining the intertidal morphology from the video images, solving the problem of highly variable water levels in the cameras' field of view. Combined with the shoreline detection method, these water levels were used twice in the processing: when converting the image co-ordinates into ground co-ordinates; and when defining the vertical elevation values corresponding to each section of the coastline. This added step in the image processing has been proved to considerably increase the accuracy of the extracted intertidal morphology, doubling the average accuracy of the extracted morphology, to an average value of about 0.15 m.

These intertidal morphologies obtained through the application of this method were merged with the original surveyed bathymetry in order to be applied in the numerical model. Thereby, the modelling experiments can be extended for different evolutionary stages of the sandbar system, and the comparison with observations gives a further qualitative validation of the numerical model.

This technique has been shown to be a good alternative in the absence of *in situ* surveyed data. However, some limitations arise from the application, being related to the assumption of constant subtidal morphology during the studied period and constant intertidal morphology between each of the stages. Although this limitation is not thought to cause large deviations in modelled water levels, reducing the time intervals between the studied stages may reduce these errors. Since the limited measured data available throughout the three-year cycle, the optimal time intervals between the modelled stages can not be defined here. Nevertheless, in order to minimise possible errors arising from this assumption, ten stages of the morphological cycle were used, comprehending most of the morphological variability of the area of interest.

Identify and assess the relative importance of the key processes across the sandbar system

Following the development and the application of the method of coupling the numerical model and video images, several experiments were carried out in order to assess the relative importance of the driving processes at the inlet system. A more detailed assessment of the driving forces was carried out for the surveyed situation (model validation period), when detailed bathymetric surveys and boundary condition data were available (Chapter 6) and shorter experiments were carried out for each of the analysed morphological stages (Chapter 7). Results provide valuable information about the interaction of forces and the resultant morphological evolution of the sandbar system.

The controlling factor of such systems is the interaction of tidal currents, waves, and river discharge that produce a cyclic morphological behaviour of the sandbars forming the ebb-tidal delta. This cyclicity is controlled by the temporal and spatial variability of the processes governing the local sediment dynamics. Throughout the entire observed cycle, there is a clear difference in the spatial distribution of the dominant processes. Over deeper

regions the tides dominate the sediment transport, whilst over the shoals the waves are dominant. Based on the numerical model results and the observation of video images, it is suggested that the sandbars are formed in the region between the offshore ebb tidal currents and the onshore wave generated currents in the area that defines the limit between the channel and the shoal. These opposing flows result in a gyre of sediment transport, with deposition taking place in the middle. Therefore, the genesis of the offshore sandbar is associated with high wave energy events. Once formed, the dynamics of the sandbars are controlled mainly by wave action, with the mean onshore flows driving it onshore, and by the ebb tidal currents, which have the opposite effect, driving sediment offshore. As a consequence, during low wave energy periods (e.g. summer months) the forming sandbar may be spread in the offshore direction and during periods with higher intensity and frequency of energetic events (e.g. winter months) the sandbar tends to grow and move in the onshore direction. A similar process of opposing flows may be responsible for the generation and maintenance of the other sandbars that compose the system (e.g. Sprat Sand, Ness sandbar), however their dynamics are controlled according to the level of exposure to the wave action. The more protected sandbars are relatively stable, while the sandbars exposed to the action of waves are very dynamic, with changes in shape and volume defined by the incoming wave energy. As a consequence, the magnitude of the morphological changes is also controlled seasonally, with increased modifications during the more energetic periods. Sandbars migrate landwards due to the wave generated onshore transport over the sandbars, resulting in a thinner and shore-normal elongated sandbar. This shape, which is not typical of a wave dominated sandbar, is a consequence of the wave action at different tidal levels. At lower tides, when the sandbar is partially exposed, wave action generates strong longshore (in relation to the sandbar) currents on both sides of the sandbar, moving sediment in the onshore direction. The spreading of the shore-normal attached sandbar occurs as a consequence of the wave generated transport over the sandbar, with the spreading rate being defined by the relative angle of the incident waves in relation to the sandbar.

Waves play a major role in the sandbar morphodynamics. Despite the relatively low frequency of high wave energy events that reach the region they are responsible for large amounts of sediment displacement, catalysing some dramatic morphological changes. This is represented in the diagram in Figure 8.1, which summarises the main controlling factors of the sandbars morphodynamics. High wave energy events are dominant in the

morphological changes, with their temporal distribution defining the cyclic behaviour of such environments. The main physical process responsible for the onshore transport due to the wave action is the gradient in the radiation stresses generating strong onshore mean flows. Results indicate that river discharge may also significantly affect the morphological evolution, with the river discharge adding another variable to the system. High discharge values increase the relative importance of the ebb flows, affecting the sediment transport in the channel and over the adjacent shoals.

Initial steps towards assessing the predictability of the environment

The present application of an initial sedimentation/erosion model proved to be useful in providing qualitative predictions of the morphological evolution of such a complex sandbar system. Based on short period simulations of the system's evolution under different forcing conditions, the general tendency of evolution to the next morphological stage is reproduced. As shown quantitatively through the application the Brier Skill Scores during the validation period (Chapter 4), the model showed an ability to reproduce correctly the evolution of the offshore sandbar when compared to measurements over the same period. However, the same level of prediction was not achieved in the region of the Ness sandbar. This may be a consequence of the limited resolution of the sediment samples at the region or limitations in the model capabilities of reproducing correctly the balance between the ebb tidal flows and the wave generated flows. Due to its location, the Ness sandbar is under stronger influence of the channel flows than the offshore sandbar, and as a consequence, reproducing correctly the interaction of these processes is more important in this region than at the wave dominated offshore sandbar. Based on video observations, it can be seen that the Ness sandbar is less dynamic than the offshore sandbar, with a seasonal on- and offshore migration pattern. During periods characterised by high wave energy the Ness sandbar is moved onshore, towards the channel, and during periods of tidal flow dominance this sandbar migrates offshore.

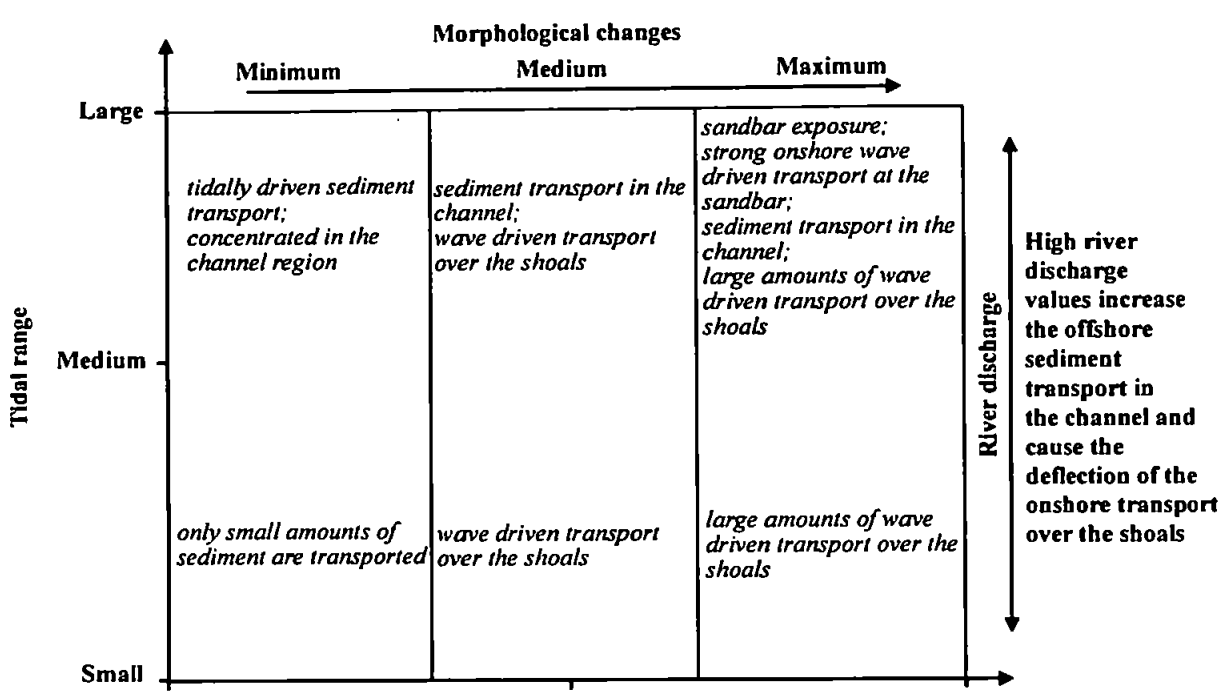

Figure 8.1. Degree of sandbar morphological changes as function of tidal range and wave height.

Comparing the modelled sedimentation/erosion patterns with the observed changes of the dynamic offshore sandbar shows that the model is able to reproduce consistently its overall evolutionary tendency. The morphological adjustment of the system to the forcing conditions shows the progression towards the next morphological stage, allowing the initial steps towards predicting the evolution to be taken. Due to limitations in the time-scale of the application of such models (as discussed in De Vriend, 1994; De Vriend and Ribberink, 1996), only qualitative predictions can be obtained based on the first "adjustment" of the distorted system. At short time-scales, the model provides the initial morphological response to the forcing conditions, but without the feedback between the evolution and the hydrodynamics the interpretation of such a model is limited at larger time-scales.

The technique of coupling the numerical model with the video images applied here, has been shown to be of great value in providing a better understanding of the processes that control the dynamic of inlet systems. At short time-scales (e.g. one tidal cycle), quantitative information about the acting processes and how they interact was provided by

the modelling experiments, and at medium time-scales, the combined application resulted in qualitative predictions of the evolution of the system.

8.2. Future work

It is recommended that future studies include, where possible, the combination of *in situ* measurements, numerical modelling and video imaging. As shown in this study, the high quality data sets originated from these combined studies are of great help in understanding the processes involved in such environments.

Future work at Teignmouth should include the application of a full morphodynamic model, in order to assess the quantitative predictability over the whole evolutionary cycle. With such application, the model should also be coupled with the video images in order to validate its predictions and to make adjustments in the morphology if necessary. One problem that may arise from the application of a morphodynamic model is the required computer time to simulate the whole cycle, since the grid resolution would need to be high in order to include the complex morphological variability and the time steps need to be relatively small, since small-scale processes drive the local morphodynamics. The accuracy of these predictions would also rely on knowledge about the forcing conditions. Measurements or the understanding of the sequencing of the forcing conditions (e.g. wave parameters, water level, river discharge) would be needed throughout the duration of the simulation.

Additionally, the understanding of larger scale sources and sinks of sediment that sustain the system would help in understanding the system and obtaining quantitative predictions of its evolution. As shown in this study, the system is open, with sediment being added or removed through longshore and cross-shore transport. This makes the regional sediment balance an important "boundary condition" for long-term simulations.

In situ measurements of the processes and consequent sediment transport in the vicinity of the sandbars would bring additional information about the system. At present, such

measurements are being made as part of the COASTVIEW[1] project, through the use of a variety of instruments positioned at the intertidal regions of the sandbars. These measurements are complemented with complete bathymetric and topographic surveys. These data will certainly result in interesting information about the processes that control sediment transport at this region and will also form a good database for model validation.

A continuous program of bathymetric and topographic surveys and measurement of forcing conditions would be necessary for any attempt of modelling the system's long-term evolution. This would create a database that could be used for the long-term modelling and video based techniques validations. Due to its interesting behaviour, available database, and strategic facilities, Teignmouth is certainly an excellent location for such studies.

[1] for details see the project website at http://www.thecoastviewproject.org

Appendix I – Numerical Model Description

AI.1. Model Description

The numerical model used in this study is the well-known MIKE21 model developed by the Danish Hydraulic Institute. The development of MIKE21 started at DHI in 1970 and has since been extended for different applications (e.g. Abbott et al., 1981; Abbott and Larsen, 1985). In this study three modules of the MIKE21 system are used, the Hydrodynamic module (HD), the Nearshore Spectral Wind-Wave module (NSW) and the non-cohesive Sediment Transport module (ST). Each of these modules is described in the next sections.

As this modelling system has been described in detail numerous times before in the literature, much of the description provided here is summarised from the MIKE21 HD scientific documentation (DHI, 2000a).

AI.1.1. MIKE21 Hydrodynamic Module (HD)

The hydrodynamic model component of MIKE21 is a general numerical modelling system for the simulation of water levels and flows in estuaries, bays and coastal areas (Warren and Bach, 1992). It simulates unsteady two-dimensional flows in one layer (vertically homogeneous) fluids in response to a variety of forcing functions. The water levels and flows are resolved on a square or rectangular grid covering the area of interest. The main inputs to the model are bathymetry, bed resistance coefficients, wind fields, and water level and/or flux boundary conditions. The model allows flooding and drying over the computational grid during the simulation.

AI.1.1.1. Two-dimensional Flow Equations

In the hydrodynamic module the flow and water level variations are described by the differential equations that govern the conservation of mass and momentum in the

horizontal plane. These are obtained through the vertical integration of the Navier-Stokes equations:

continuity:

$$\frac{\partial \zeta}{\partial t} + \frac{\partial p}{\partial x} + \frac{\partial q}{\partial y} = 0 \tag{AI.1}$$

x-momentum:

$$\frac{\partial p}{\partial t} + \frac{\partial}{\partial x}\left(\frac{p^2}{h}\right) + \frac{\partial}{\partial y}\left(\frac{pq}{h}\right) + gh\frac{\partial \zeta}{\partial x}$$

$$+ \frac{gp\sqrt{p^2+q^2}}{C^2 \cdot h^2} - \frac{1}{\rho_w}\left[\frac{\partial}{\partial x}(h\tau_{xx}) + \frac{\partial}{\partial y}(h\tau_{xy})\right] - \Omega p \tag{AI.2}$$

$$- fVV_x + \frac{h}{\rho_w}\frac{\partial}{\partial x}(p_a) = 0$$

y-momentum:

$$\frac{\partial q}{\partial t} + \frac{\partial}{\partial y}\left(\frac{q^2}{h}\right) + \frac{\partial}{\partial x}\left(\frac{pq}{h}\right) + gh\frac{\partial \zeta}{\partial y}$$

$$+ \frac{gq\sqrt{p^2+q^2}}{C^2 \cdot h^2} - \frac{1}{\rho_w}\left[\frac{\partial}{\partial y}(h\tau_{yy}) + \frac{\partial}{\partial x}(h\tau_{xy})\right] + \Omega p \tag{AI.3}$$

$$- fVV_y + \frac{h}{\rho_w}\frac{\partial}{\partial y}(p_a) = 0$$

At closed boundaries, the flow perpendicular to the boundary is set to zero. At open boundaries, the surface elevation along the boundary and/or the flux through the boundary have to be prescribed. Using these boundary conditions and defining initial values for surface elevations and flux densities, the system of Equations AI.1 through AI.3 forms a well-posed boundary value problem. Horizontal water density effects are not included in the above equations, which can result in errors in the surface gradients (up to 15 cm) when the density effects are important.

AI.1.1.2. Numerical Formulation

MIKE21 HD solves the vertically integrated equations of continuity and momentum in two horizontal dimensions. The Equations AI.1 through AI.3 are solved by implicit finite difference techniques with the variables defined on a spatially staggered grid. MIKE21 HD makes use of an Alternating Direction Implicit (ADI) technique to integrate the equations for mass and momentum conservation in the space-time domain. Second order accuracy is ensured through the centring in time and space of all derivatives and coefficients.

The variables are defined on a space-staggered rectangular grid with elevation and fluxes midway between grid points (Leendertse, 1964). The three equations are centred at $t+½$ and they are solved in one-dimensional sweeps alternating between the x and y directions.

In the x-sweep the continuity and x-momentum equations are solved, taking ζ from t to $t+½$ and p from t to $t+1$. For the terms involving q, the two levels of old, known values are used, i.e. $t-½$ and $t+½$ (Figure AI.1). The mass and momentum equations for the x-sweep for a sequence of grid points are:

$$A_j \cdot p_{j-1}^{t+1} + B_j \cdot \zeta_j^{t+\frac{1}{2}} + C_j \cdot p_j^{t+1} = D_j|_k$$

$$A_j^* \cdot \zeta_j^{t+\frac{1}{2}} + B_j^* \cdot p_j^{t+1} + C_j^* \cdot \zeta_{j+1}^{t+\frac{1}{2}} = D_j^*|_k \qquad \text{(AI.4)}$$

In the y-sweep the continuity and y-momentum equations are solved, taking ζ from $t+½$ to $t+1$ and q from $t+½$ to $t+3/2$, while terms in p use the values just calculated in the x-sweep at t and $t+1$ (Figure AI.1). The mass and momentum equations for the y-sweep for a sequence of grid point are:

$$A_k \cdot q_{k-1}^{t+1} + B_k \cdot \zeta_k^{t+\frac{1}{2}} + C_k \cdot q_k^{t+1} = D_k \mid_j$$

$$A_k^* \cdot \zeta_k^{t+\frac{1}{2}} + B_k^* \cdot q_k^{t+1} + C_k^* \cdot \zeta_{k+1}^{t+\frac{1}{2}} = D_k^* \mid_j \qquad \text{(AI.5)}$$

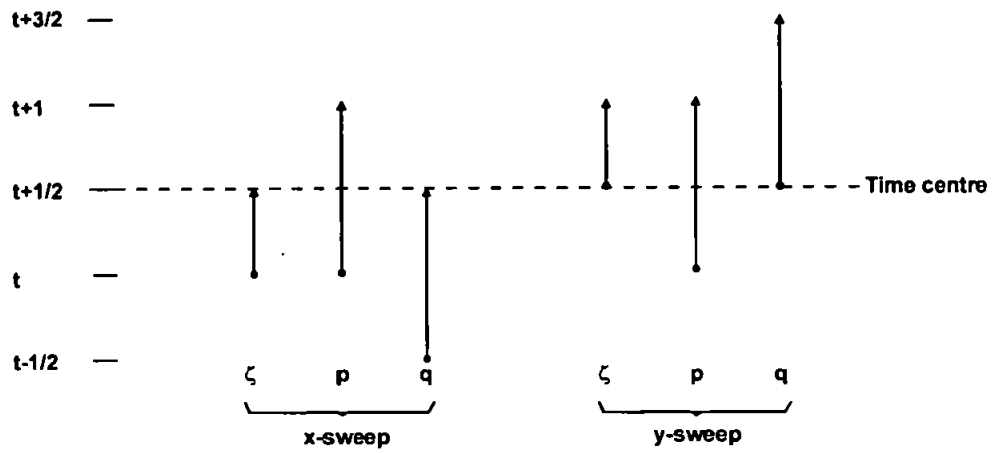

Figure AI.1. Time centring.

The coefficients A, B, C, D and A*, B*, C*, D* in Equations AI.4 and AI.5 are all expressed in known quantities. The application of the finite difference scheme results in a three-diagonal system of equations for each grid line in the model. The solution is obtained by inverting the three-diagonal matrix using the double-sweep (DS) algorithm (Abbott and Minns, 1998), which corresponds to a very fast and accurate form of Gaussian elimination.

AI.1.1.3. Boundary Conditions

The main purpose of the MIKE21 HD is to solve the partial differential equations that govern nearly-horizontal flow. Like all other differential equations they need boundary conditions. In general, the following boundary data are needed:

Surface elevations and/or Flux densities

These are the primary boundary conditions, which are defined as the boundary conditions sufficient and necessary to solve the linearized equations. The fully linearized x-momentum equation reads:

$$\frac{\partial p}{\partial t} + gh\frac{\partial \zeta}{\partial x} = 0 \tag{AI.6}$$

The corresponding terms in the x-momentum equation are:

$$\frac{\partial p}{\partial t} + ... + gh\frac{\partial \zeta}{\partial x} + ... = 0 \tag{AI.7}$$

A "dynamic case" is defined as a case where

$$\frac{\partial p}{\partial t} \approx -gh\frac{\partial \zeta}{\partial x} \tag{AI.8}$$

i.e. a case where these two terms dominate over all other terms of the MIKE21 HD x-momentum equation.

It is then clear that the primary boundary conditions provide "almost all" the boundary information necessary for MIKE21 HD when it is applied to a dynamic case. The same set of boundary conditions maintain the dominant influence (but are in themselves not sufficient) even in the opposite of the "dynamic case", namely the steady state (where the linearized equations are quite meaningless). This explains why these boundary conditions are called "primary". They must be given at all boundary points and at all time steps.

Secondary boundary conditions are given by the discharge or flux density parallel to the open boundary. The necessity for secondary boundary conditions arise because one cannot close the solutions algorithm at open boundaries when using the non-linearized equations.

As a consequence of the transport character of the convective terms, a "true" secondary condition is needed at inflows, whereas at outflow a "harmless" closing of the algorithm is required. This closing may either be obtained by defining the flow direction at the boundary or by extrapolation of the flux along the boundary from the inside. Furthermore, the fluxes outside the boundaries are needed (for the convective momentum term, the eddy term and the non-linear dissipation term).

The success of a particular application of MIKE21 HD is dependent upon a proper choice of open boundaries more then anything else. More details about the MIKE21 HD model can be found in Abbott et al. (1981) and DHI (2000).

AI.1.1.4. Calibration Factors

Bed resistance

In MIKE21 HD the bed shear stress is represented by the Chézy formulation,

$$\frac{gp\sqrt{p^2+q^2}}{C^2h^2} \tag{AI.9}$$

which is approximated as

$$\frac{gp_{j,k}^{t+1}\sqrt{p^{*2}+q^{*2}}}{C^2h^{*2}} \tag{AI.10}$$

where

$$p^* = p^t_{j,k}$$

$$q^* = \frac{1}{8}\left(q^{t-\frac{1}{2}}_{j,k} + q^{t-\frac{1}{2}}_{j+1,k} + q^{t-\frac{1}{2}}_{j,k-1} + q^{t-\frac{1}{2}}_{j+1,k-1} + q^{t+\frac{1}{2}}_{j,k} + q^{t+\frac{1}{2}}_{j+1,k} + q^{t+\frac{1}{2}}_{j,k-1} + q^{t+\frac{1}{2}}_{j+1,k-1} \right) \quad \text{(AI.11)}$$

$$h^* = \frac{1}{2}\left(h_{j+1} + h_j\right)^t_k$$

It is also possible to use Manning numbers in MIKE21 HD and they are converted to Chézy numbers as follows:

$$C = M \cdot h^{*\frac{1}{6}} \quad \text{(AI.12)}$$

Eddy viscosity

The effective shear stresses in the momentum equations contain momentum fluxes due to turbulence, vertical integration and subgrid scale fluctuations. The terms are included using an eddy viscosity formulation to provide damping of short-wave length oscillations and to represent subgrid scale effects (see e.g. Madsen et al., 1988; Wang, 1990).

The formulation of the eddy viscosity in the equations is implemented in two ways:

flux based formulation

$$\frac{\partial}{\partial x}\left\{E\frac{\partial P}{\partial x}\right\} + \frac{\partial}{\partial y}\left\{E\frac{\partial P}{\partial y}\right\} \quad (x - momentum) \quad \text{(AI.13)}$$

where P is the flux in the x-direction and E is the eddy viscosity coefficient.

velocity based formulation

$$\frac{\partial}{\partial x}\left\{h \cdot E\frac{\partial u}{\partial x}\right\} + \frac{\partial}{\partial y}\left\{h \cdot E\frac{\partial u}{\partial y}\right\} \quad \text{(AI.14)}$$

where u is the velocity in the x-direction and h the water depth.

Strictly speaking the first formulation is only correct at a constant depth and should be applied carefully in order to avoid falsification of the flow pattern. The velocity based formulation, which is more correct, is also more difficult to implement in the numerical algorithm. This is because the system uses the fluxes as the unknown parameters, and not the velocities. Therefore the velocity-based formulation is implemented by using the velocities from the previous time-step. This can lead to stability problems when the eddy viscosity coefficient becomes large.

The eddy viscosity in MIKE21 HD can be given as a time-varying function of the local gradients in the velocity field. This formulation is based on the Smagorinsky concept, which yields:

$$E = C_s^2 \Delta^2 \left[\left(\frac{\partial U}{\partial x} \right)^2 + \frac{1}{2} \left(\frac{\partial U}{\partial y} + \frac{\partial V}{\partial x} \right)^2 + \left(\frac{\partial V}{\partial y} \right)^2 \right] \tag{AI.15}$$

where U, V are depth averaged velocity components in the x- and y-direction, Δ is the grid spacing and C_s is a constant (Smagorinsky factor) to be chosen in the interval of 0.25 to 1.0. The Smagorinsky facility is combined with the following formulation of the shear stresses:

$$\frac{\partial}{\partial x} \left(hE \frac{\partial U}{\partial x} \right) + \frac{\partial}{\partial y} \left[\frac{1}{2} hE \left(\frac{\partial U}{\partial y} + \frac{\partial V}{\partial x} \right) \right] \tag{AI.16}$$

which is in agreement with Rodi (1980) and Wang (1990). More details of the formulation can be found in Smagorinsky (1963), Lilly (1967), Leonard (1974), Aupoix (1984) and Horiuti (1987).

AI.1.1.5. Other Driving Factors

Wind speed, direction and shear coefficient

The driving force due to wind effects over the model area is calculated from the wind friction term:

$$f(v) \cdot V \cdot V_x \tag{AI.17}$$

where all variables are known in each grid point. The wind friction factor is calculated in accordance with Smith and Banke (1975):

$$f(v) = \begin{cases} f_0 & \text{for } V < V_0 \\ f_0 + \dfrac{V - V_0}{V_1 - V_0} \cdot (f_1 - f_0) & \text{for } V_0 \le V \le V_1 \\ f_1 & \text{for } V > V_1 \end{cases} \tag{AI.18}$$

where

$$f_0 = 0.00063 \quad , \; V_0 = 0 \;\; m/s$$
$$f_1 = 0.0026 \quad , \; V_1 = 30 \;\; m/s \tag{AI.19}$$

Wave radiation stresses

The inclusion of the wave-induced flow in the model area is done through the specification of wave radiation stresses. By averaging the equations of motion over depth and time (wave period) wave radiation stress terms are included in the momentum equations. The additional terms are:

x-momentum

$$\frac{\partial S_{xx}}{\partial x} + \frac{\partial S_{xy}}{\partial y} \tag{AI.20}$$

y-momentum

$$\frac{\partial S_{yy}}{\partial y} + \frac{\partial S_{xy}}{\partial x} \tag{AI.21}$$

where S_{xx}, S_{xy} and S_{yy} are the three components of radiation stress.

Coriolis Term

In MIKE21 HD the Coriolis term $\Omega \cdot q$ is approximated explicitly by using q^* as defined in Equation AI.11.

AI.1.2. MIKE21 Nearshore Spectral Wind-Wave Module (NSW)

MIKE21 NSW is a spectral wind-wave model, which describes the propagation, growth and decay of short period waves in nearshore areas. The model includes the effects of refraction and shoaling due to varying depth, wave generation due to wind and energy dissipation due to bottom friction and wave breaking. The effects of current on these phenomena are included. Wave diffraction effects are not included in the applied model formulation. The basic equations in MIKE21 NSW are derived from the conservation equation for the spectral wave action density based on the approach proposed by Holthuijsen et al. (1989). The various wind formulations in MIKE21 NSW are discussed and compared in Johnson (1998).

MIKE21 NSW is a stationary, directionally decoupled, parametric model. To include the effects of current, the basic equations in the model are derived from the conservation equation for the spectral wave action density. A parameterisation of the conservation equation in the frequency domain is performed introducing the zeroth and the first moment of the wave-action spectrum as dependent variables. This leads to the following coupled partial differential equations:

$$\frac{\partial(c_{gx}m_0)}{\partial x}+\frac{\partial(c_{gy}m_0)}{\partial y}+\frac{\partial(c_\theta m_0)}{\partial \theta}=T_0 \tag{AI.22}$$

$$\frac{\partial(c_{gx}m_1)}{\partial x}+\frac{\partial(c_{gy}m_1)}{\partial y}+\frac{\partial(c_\theta m_1)}{\partial \theta}=T_1 \tag{AI.23}$$

The moments $m_n(\theta)$ are defined

$$m_n(\theta)=\int_0^\infty \omega^n A(\omega,\theta)d\omega \tag{AI.24}$$

where ω is the absolute frequency and A is the spectral wave action density.

The propagation speeds c_{gx}, c_{gy} and c_θ are obtained using linear wave theory. The left-hand side of the basic equations takes into account the effect of refraction and shoaling. The source terms T_0 and T_1 take into account the effect of local wind generation and energy dissipation due to bottom friction and wave breaking. The effects of current on these phenomena are included.

In MIKE21 NSW, the source terms for the local wind generation are derived from empirical growth relations, see Johnson (1998) for a detailed description.

In MIKE21 NSW, boundary conditions, in form of wave parameters, must be specified for the incoming waves at the offshore boundary (x=0). Typically, no information is available regarding the wave condition at the lateral boundaries (y=y_{max} and y=0). In this case, a symmetry boundary condition is usually applied indicating that the depth contours are assumed to be straight and parallel at these boundaries. Alternatively, absorbing boundary conditions can be applied. The wave field near the model north and south boundaries will only be correct in simple cases. Therefore, it is important in a real application that the area of interest is lying well inside the model area. The wave field propagating into the area of interest should enter the model through the offshore boundary. In general, the offshore boundary and the model north and south boundaries should be placed in areas where the wave field is reasonably uniform.

The formulation in MIKE21 NSW of wave breaking due to large wave steepness and limiting water depth is based on the formulation of Battjes and Janssen (1978). They introduced the following expression for the rate at which the energy is dissipated due to wave breaking:

$$\frac{dE}{dt} = \frac{-\alpha}{8\pi} Q_b \omega H_m^2 \tag{AI.25}$$

where

$$\frac{1-Q_b}{\ln(Q_b)} = -\left(\frac{H_{rms}}{H_m}\right)^2 \tag{AI.26}$$

E is the total energy, ω is the frequency, H_{rms} is the *rms*-value of the wave height, H_m is a maximum allowable wave height, Q_b is the fraction of wave breaking waves and α is an adjustable constant. Q_b controls the rate of dissipation, and the maximum wave height is calculated by

$$H_m = \gamma_1 k^{-1} \tanh(\gamma_2 kd / \gamma_1) \tag{AI.27}$$

where k is the wave number, d is the water depth and γ_1 and γ_2 are two wave breaking parameters. γ_1 controls the wave steepness condition and γ_2 controls the limiting water depth condition. The effect of wave breaking on the mean wave period can also be included. Here, the assumption is that the dissipation of energy due to wave breaking is concentrated on the low frequency side of the frequency spectrum. Hence, the wave breaking has the effect that the mean wave period is reduced.

AI.1.2.1. Numerical Solution

The spatial discretization of the basic partial differential equations is performed using Eulerian finite difference technique. The zeroth and the first moment of the action spectrum are calculated on a rectangular grid for a number of discrete directions. In the x-direction, linear forward differencing are applied while in both the y- and θ-directions it is

possible to choose between linear upwinded differencing, central differencing and quadratic upwinded differencing. The best results are usually obtained using linear upwinded differencing in both the y- and θ-directions.

The source terms due to local wind generation are introduced explicitly while the source terms due to bottom dissipation and wave breaking are introduced implicitly. Hence, a nonlinear iteration is performed in each grid point.

The nonlinear algebraic equation system resulting from the spatial discretization is solved using an once-through marching procedure in the x-direction (the predominant direction of wave propagation) restricting the angle between the direction of wave propagation and the x-axes to be less than 90°. Due to stability considerations the angle is further restricted depending on the discretization.

AI.1.3. MIKE21 Sediment Transport Module (ST)

MIKE21 ST is the sediment transport module of the MIKE21 modelling system for the assessment of the sediment transport rates and related initial rates of bed level changes of non-cohesive sediment due to current or combined wave-current flow. Five different transport theories are available for the computation of sediment transport rates in pure current (Engelund and Hansen, 1976; Engelund and Fredsøe, 1976; Zyserman and Fredsøe 1994; Meyer-Peter and Muller, 1948 and Ackers and White, 1973), while two methods are available in the case of combined waves and current (Bijker, 1968 and DHI, 2000c). In this study only the transport formulations for combined waves and currents were applied and thereby described below.

MIKE21 ST calculates the sediment transport rates on a rectangular grid covering the area of interest on the basis of the hydrodynamic data obtained from a simulation with MIKE21 HD and the wave parameters calculated by MIKE21 NSW, together with information about the characteristics of the bed material. The model accounts for the influence of the following phenomena on the computed sediment transport rates: a) pure current or combined wave-current flow, b) arbitrary direction of wave propagation with respect to the

flow direction, c) breaking/non-breaking waves, d) graded/uniform bed material, and e) plane/ripple covered bed.

The MIKE21 ST current and waves module allows the inclusion of the combined action of current and waves in the sediment transport. In this case, the currents may be tidal, wind-driven, wave-driven or a combination of the three. The effects of both breaking and non-breaking waves on the transport rates are also accounted for in one of the two used formulations (in this case, STP formulation). The transport capacity at each node of a rectangular grid covering the area of interest is determined using the bathymetry, the water depth, the sediment size and gradation, and the current and wave characteristics as input data. Erosion and deposition rates in the model are estimated from the computed sand transport.

As mentioned before, two transport formulations for combined waves and currents are available in MIKE21 ST: a) Bijker's total-load transport method (Bijker, 1967), and b) the theory based on the application of DHI's deterministic sediment transport model STP. Whereas the sediment transport rates are calculated directly at every grid point of the simulation area and for every time step if Bijker's method is used, the transport rates are determined by interpolation in the sand transport tables generated by the utilitary program STBASE if the deterministic program STP is used. STBASE is an interface that performs repeated calls to DHI's sediment transport program STP according to the requirements. As in the pure current module, the wave and current conditions are provided by the other modules of the MIKE21 system. In this study, both formulations were applied and some details of each formulation are given below.

AI.1.3.1. Deterministic Sediment Transport Model – STP

The model of Fredsøe (1984) provides the basis for the hydrodynamic description of the combined wave-current flow for the turbulent boundary layer. In combined waves and current, the non-linear interaction between the current and the wave-induced flow that takes place near the bed is of fundamental importance for the bed shear stresses and for the vertical structure of eddy viscosity. Fredsøe's model for the turbulent boundary layer

accounts for the variation in time of both the bed shear stress and the turbulence in the wave boundary layer. Fluxes of non-cohesive sediment transport are calculated through an intra-wave period approach (Deigaard et al., 1986). This involves solving the one-dimensional (vertical) diffusion-advection equation at various phases of the wave period, combining the resulting concentration profiles with the associated velocity profiles to yield the instantaneous sediment fluxes and then averaging the latter over a wave period.

The mean current above the boundary layer is assumed to have a logarithmic profile. The high levels of turbulence that exist near the bed due to the presence of the wave boundary layer, that acts as an increased resistance for the current, are accounted for by means of an apparent wave-related roughness k_w, larger than the geometric roughness k_N related to the grain diameter d.

The total transport rate of non-cohesive sediments is calculated according to the ideas of Engelund and Fredsøe (1976), extended to cover the combined waves and current situation, and surf zone conditions.

The rate of bed load transport is calculated as a function of the dimensionless bed shear stress related to skin friction θ':

$$\theta' = \frac{U_f'^2}{(s-1)gd_{50}} \tag{AI.28}$$

where s is the relative density of the sediment, g is the acceleration of gravity, d_{50} is the median grain size and U'_f is the instantaneous shear velocity related to skin friction. It is assumed that the bed load responds immediately to the bed shear stress under unsteady flow conditions, i.e. in the presence of waves.

The instantaneous rate of suspended load transport q_s is calculated as:

$$q_s = \int_0^h u(z,t)c_s(z,t)d_{50}z \tag{AI.29}$$

where t is time, h is the water depth, z is the vertical co-ordinate that is measured upwards from the bottom, c_s is the volume concentration of suspended sediment and u is the velocity of the combined wave-current flow. The instantaneous concentration of suspended sediment is determined by solution of the diffusion equation

$$\frac{\partial c}{\partial t} = \frac{\partial}{\partial z}\left(\varepsilon_s \frac{\partial c_s}{\partial z}\right) + w_s \frac{\partial c_s}{\partial z} \tag{AI.30}$$

where ε_s is the diffusion coefficient for suspended sediment and w_s its settling velocity. The bed boundary condition for the solution of Equation AI.30 is given in terms of bed concentration c_b defined as a level $z=2d_{50}$. Two alternative formulations for c_b are also implemented in the model: a) the deterministic formulation of Engelund and Fredsøe (1976), in which c_b is determined as a function of θ' from dynamic considerations regarding the way in which the shear stress is transferred to the bed, and b) the empirical formulation of Zyserman and Fredsøe (1994).

These formulations are only valid for plane beds, under sheet-flow conditions which occur for θ'>0.8-1.0. For smaller values of θ', the bed will be covered by ripples. The influence of ripples on the suspended sediment transport is accounted for in STP by modifying the bed concentration, the value of the diffusion coefficient close to the bed, and the bed roughness. The modified values of c_b and ε_s are based on the experimental results of Nielsen (1979), whereas the roughness related to the presence of ripples is calculated according to Raudkivi (1988). STP converges gradually towards a plane-bed description for increasing bed shear stress or current velocity.

The sediment diffusion coefficient contained contained in the diffusion-advection equation is assumed to be synonymous with the eddy viscosity, this quantity being derived by solving the transport equation for turbulent kinetic energy. Inside the surf zone, an additional source of turbulence related to the intense dissipation of wave energy by breaking exists. This is taken into account by the use of a one-equation turbulence model as described by Deigaard et al. (1986a, 1986b). For irregular waves, the effect of breaking/broken waves coexisting with non-broken, smaller waves is accounted for through an equivalent breaking wave that acts as source for turbulence in the one-equation

model. This wave has a height H_m equal to the maximum wave that will not break for the water depth h and wave period T considered according to the formulation of Battjes and Janssen (1978), see also Battjes and Stive (1985). The period of equivalent wave (called "dissipation period T_{diss}") is defined as:

$$T_{diss} = \frac{T}{Q_b} \tag{AI.31}$$

where Q_b is the fraction of waves that break at the location being considered according to Battjes and Janssen (1978).

The effect of graded bed material on the total load transport rate is accounted for through a reformulation of the relationship between the bed concentration c_b and the bed shear stress θ', a criterion for the entrainment of sediment into suspension, and the consideration of each fraction of suspended sediment separately, by using a revised version of the method described in Zyserman and Fredsøe (1992). Thereby, the sediment settling velocity is defined for each sediment fraction and Eq. AI.30 is solved for every size fraction of sediment in suspension.

AI.1.3.2. Bijker's Sediment Transport Method

Bijker (1967) proposed one of the first sediment transport formulations that is still often used in engineering applications. This formulation is derived from a current only formulation (Frijlink, 1952) with a modification of the bottom shear stress using a wave-current model. When selecting the Bijker (1967) formulation, the total load rate of sediment transport is calculated as the sum of bed-load transport (q_b) and suspended load transport (q_s):

$$q_t = q_b + q_s = q_b(1 + 1.83Q) \qquad m^3\,s^{-1}\,m^{-1} \tag{AI.32}$$

q_t is given in units of solid volume of bed material per unit time and unit width. Q is a dimensionless factor given by:

$$Q=\left[I_1 \ln\left(\frac{33h}{r}\right)+I_2\right] \tag{AI.33}$$

where h is the water depth, r is the bed roughness and I_1 and I_2 are Einstein's integrals that must be evaluated numerically on the basis of the dimensionless reference level $A=r/h$ and z_*.

$$z_* = \frac{w}{\kappa U_{f,wc}} \tag{AI.34}$$

w is the settling velocity of suspended sediment, κ is von Karman's constant and $U_{f,wc}$ is the shear velocity for the combined wave-current case. The roughness r can be related to the Chézy number C through

$$C = 18\log\left(\frac{12h}{r}\right) \tag{AI.35}$$

According to Bijker (1967) the shear velocity for combined waves and currents is calculated as

$$U_{f,wc} = U_{f,c}\sqrt{1+\frac{1}{2}\left(\xi\frac{\hat{u}_b}{V}\right)^2} = \frac{\sqrt{g}V}{C}\sqrt{1+\frac{1}{2}\left(\xi\frac{\hat{u}_b}{V}\right)^2} \tag{AI.36}$$

where $U_{f,c}$ is the shear velocity associated with the current, V is the depth averaged current velocity, $\hat{u}_b$ is the maximum value of the wave-induced velocity at the bottom and ξ is a dimensionless factor that can be expressed in terms of the wave friction factor f_w and the Chézy number C:

$$\xi = C\sqrt{\frac{f_w}{2g}} \tag{AI.37}$$

The wave friction factor f_w is calculated according to Swart (1974) as:

$$f_w = \exp\left[-5.977 + 5.213\left(\frac{a_b}{r}\right)^{-0.194}\right] \qquad if \quad 1.47 < \frac{a_b}{r} < 3000$$

$$f_w = 0.32 \qquad if \quad \frac{a_b}{r} \le 1.47 \tag{AI.38}$$

where a_b is the amplitude of the wave-induced motion at the bottom:

$$a_b = \frac{\hat{u}_b T}{2\pi} \tag{AI.39}$$

with T being the wave period. $\hat{u}_b$ and a_b are evaluated using linear wave theory. q_b in equation AI.32 is calculated according to

$$q_b = B d_{50} U_{f,c} \exp\left(-\frac{0.27 \Delta d_{50} g}{\mu U_{f,wc}^2}\right) \tag{AI.40}$$

B is a dimensionless coefficient for bed-load transport, Δ is the relative density for sediment, and μ is the "ripple-factor".

$$\Delta = s - 1 = \frac{\rho_s}{\rho} - 1 \tag{AI.41}$$

$$\mu = \left(\frac{C}{C'}\right)^{\frac{3}{2}} \tag{AI.42}$$

ρ_s is the density of the sediment, ρ_w is the density of water and C' is the Chézy number related to the geometric characteristics of the bed material. C' can be obtained from

$$C' = 18 \log\left(\frac{12h}{d_{90}}\right) \tag{AI.43}$$

d_{90} is the sediment size for which 90 % of the bed material is finer. For uniform sediment d_{90} is replaced by d_{50}. It is interesting to note that the influence of the waves on the bed

load transport q_b is included through the "stirring term" in AI.40 (the exponential). The "transporting term" is only related to the current. The influence of the waves on the suspended sediment transport is accounted for through the inclusion of $U_{f,wc}$ in z_* (see eq. AI.34).

Appendix II

Article presented at the International Coastal Symposium 2002, Templepatrick, Northern Ireland, and published in the Special Issue 36 of the Journal of Coastal Research.

Siegle, E., Huntley, D.A. and Davidson, M.A. 2002. Modelling water surface topography at a complex inlet system – Teignmouth, UK. Journal of Coastal Research, SI 36: 675-685.

Journal of Coastal Research	SI 36	675-685	(ICS 2002 Proceedings)	Northern Ireland	ISSN 0749-0208

Modelling Water Surface Topography at a Complex Inlet System – Teignmouth, UK

Eduardo Siegle†; David A. Huntley and Mark A. Davidson

Institute of Marine Studies
University of Plymouth
Drake Circus
Plymouth, PL4 8AA
United Kingdom
esiegle@plymouth.ac.uk

ABSTRACT

Accurate water surface topography data and its spatial and temporal variability provide information about the interaction of physical processes acting in coastal regions. At the inlet system in Teignmouth, UK, these data complement methods for the extraction of nearshore morphology using remotely sensed video techniques. The video methods normally assume that the water surface is horizontal over the region, an assumption that is often invalid in shallow water. The study area is a complex macro-tidal inlet system bounded by a rocky headland and a 2 km-long beach. In order to predict the water surface topography and its response to different tide, wave and river discharge conditions, a calibrated and validated numerical model (MIKE21 HD, NSW) was applied. The water surface topography at the inlet and adjacent coast exhibits high spatial and temporal variability, mainly related to the tidal phase. It is the interaction between the tidal phase and the sandbar morphology, defining the velocity field in the channels, which drives the water surface topography distribution across the region. Since a small, unaccounted, difference in water level may result in significant deviations of the horizontal shoreline position, this study highlights the importance of using numerical modelling in conjunction with the video image techniques for the extraction of nearshore morphology.

ADDITIONAL INDEX WORDS: *Nearshore hydrodynamics, waves, MIKE21, water elevation.*

INTRODUCTION

Spatial and temporal changes in water surface topography in coastal regions are a response to the balance of pressure gradient forces due to combined effects of irregular bathymetry (e.g. sandbars, channels), varying bed resistance (dependent on depth, grain size, bedforms), wave effects (run-up and set-up) and freshwater discharge. Accurate water surface topography data and information on its spatial and temporal variability can provide important information about the interaction of these physical processes. At the inlet system in Teignmouth, UK, these data complement the application of remotely sensed video methods for the study of nearshore morphology. Teignmouth is one of the sites included in the international Argus programme (LIPPMANN and HOLMAN, 1989; HOLMAN, 1994), with five video cameras overlooking the inlet and the sandbar system. Recently, several different techniques of shoreline identification and subsequent extraction of intertidal topography from video images have been developed (e.g. PLANT and HOLMAN, 1997; DAVIDSON *et al.*, 1997; HOLLAND and HOLMAN, 1997; JANSSEN, 1997; AARNINKHOF and ROELVINK, 1999; KINGSTON *et al.*, submitted). The basis of all these video methods is the detection of the shoreline location at a number of instances during a tidal cycle, the shoreline being considered the contour line corresponding to the location of the local water level. Therefore, determination of the shoreline comprises its horizontal spatial location and the associated vertical elevation (KINGSTON *et al.*, submitted). One source of inaccuracy in these methods comes from the assumption of a spatially horizontal water surface, an assumption that is often invalid in shallow water.

As it is difficult to measure these irregularities in coastal regions due to both the density and spatial extent of the measurements required, the use of numerical area models provides valuable insight into the important physical processes. The model applied in this study is the MIKE21 Hydrodynamic model (HD) and the Nearshore Spectral Wind-wave model (NSW).

Data used in this study originated from the European COAST3D project, in which Teignmouth was one of the studied areas. A detailed description of the COAST3D project and its achievements can be found in SOULSBY (2001).

The motivation of this work is the need for accurate spatial and temporal surface elevation data for the application of methods for the extraction of nearshore morphology using remotely sensed video techniques. The objective of this paper is to describe the varying water surface topography in the complex coastal region of Teignmouth, UK, and to evaluate the relative importance of the various physical processes acting in this area.

STUDY AREA

The dynamic estuarine inlet of river Teign is located in the southern portion of Teignmouth's beach (Figure1). This coastal region has a strongly 3-dimensional nature, with a rocky headland (The Ness), an estuary mouth and nearshore sandbars (Poles) all adjacent to a 2 km-long beach, backed by a seawall (WHITEHOUSE and WATERS, 2000). It has been suggested that complex interaction between waves and currents lead to a cyclic movement of sandbars systems in the mouth of the estuary (CRAIG-SMITH, 1970; ROBINSON, 1975).

Tides are semi-diurnal with tidal range varying between 1.7 to 4.2 m. Both nearshore tidal currents and waves are known to have large influence on sediment transport processes at this site. Offshore currents are generally low (0.2 to 0.4 m s^{-1}) but within the ebb shoal system influenced by the tidal outflow from the estuary the current speed is locally enhanced, with values exceeding 0.5 m s^{-1} and flowing in variable directions (WHITEHOUSE, 2001). Circulation around and over the sandbars is complex due to wave refraction and diffraction effects. River discharge varies between less than 20 m^3 s^{-1} in summer to 50-100 m^3 s^{-1} in autumn and winter. These river discharges can enhance the current speeds in the channel, which can reach up to 2 m s^{-1}. The channel width varies from up to 300 m at high tide to just 80 m at low tide, funnelling the flow. Storm wave heights greater than 0.5 m are present 10% of the year, and are due to easterly gales (MILES *et al.*, 1997).

MODEL DESCRIPTION

MIKE21 Hydrodynamic Module (HD)

The hydrodynamic model component of MIKE21 is a general numerical modelling system for the simulation of water levels and flows in estuaries, bays and coastal areas (WARREN and BACH, 1992). It simulates unsteady two-dimensional flows in one layer (vertically homogeneous) fluids in response to a variety of forcing functions. The water levels and flows are resolved on a square or rectangular grid covering the area of interest. The main inputs to the model are bathymetry, bed resistance coefficients, wind fields, and water level and/or flux boundary conditions. The model allows flooding and drying over the computational grid during the simulation.

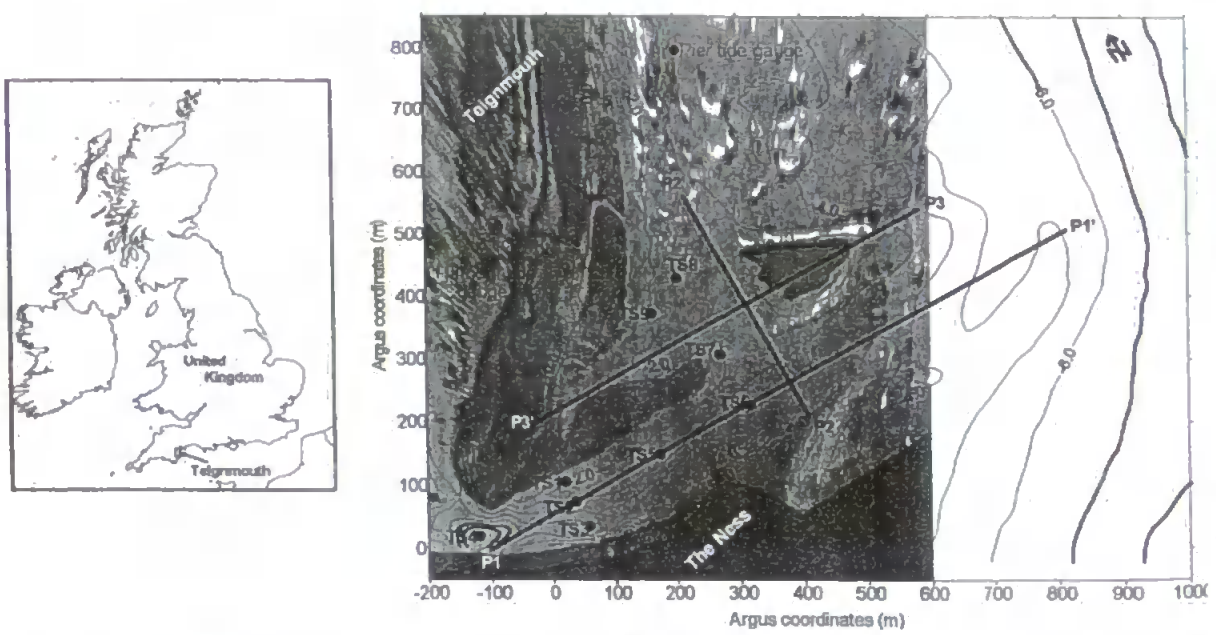

Figure 1. Study area. The nearshore bathymetry is plotted over a rectified Argus image highlighting the positions of Profile 1 (P1 – P1'), Profile 2 (P2 – P2'), Profile 3 (P3 – P3'), extracted time series (TS1 to TS9) and the Pier and Harbour tide gauges.

MIKE21 HD solves the vertically integrated equations of continuity and momentum in two horizontal dimensions. The equations are solved by implicit finite difference techniques with the variables defined on a spatially staggered grid. MIKE21 HD makes use of a Alternating Direction Implicit (ADI) technique to integrate the equations for mass and momentum conservation in the space-time domain. The equation matrices that result for each direction and each individual grid line are resolved by a Double Sweep (DS) algorithm.

MIKE21 Nearshore Spectral Wind-Wave Module (NSW)

MIKE21 NSW is a spectral wind-wave model, which describes the propagation, growth and decay of short period waves in nearshore areas. The model includes the effects of refraction and shoaling due to varying depth, wave generation due to wind and energy dissipation due to bottom friction and wave breaking. The effects of current on these phenomena are included.

MIKE21 NSW is a stationary, directionally decoupled, parametric model. To include the effects of current, the basic equations in the model are derived from the conservation equation for the spectral wave action density. A parameterisation of the conservation equation in the frequency domain is performed introducing the zeroth and the first moment of the wave-action spectrum as dependent variables. The basic equations in MIKE21 NSW are derived from the conservation equation for the spectral wave action density based on the approach proposed by HOLTHUIJSEN *et al.* (1989). The various wind formulations in MIKE21 NSW are discussed and compared in JOHNSON (1998).

MODEL SETUP

The model covers the whole estuary and an area of approximately 3.5 km seaward and 4 km alongshore, resulting in a total grid area of 10 x 4 km (Figure 2). The grid resolution is 10 m in x and y directions, resulting in approximately 180,000 water points. As the MIKE 21 flow model is a finite difference model, the grid area has to be rectangular with the computational points displayed in a square or rectangular grid. The bathymetry used for the coastal region is the result of a survey carried out by HR Wallingford in October 1999. Bathymetry for the estuary was obtained from a 1979 digitised chart.

Boundary conditions applied to the hydrodynamic model include river discharge, water level (offshore boundary) and flux (north and south boundaries). Water level and flux boundaries were obtained from a larger well-validated model (Delft3D – Continental Shelf Model – WALSTRA *et al.*, 2001a). The wave model (NSW) used as offshore data the measured wave data and water level.

Since both modules (HD and NSW) work separately, it is necessary to run the NSW model using measured wave data (offshore boundary) and water level for the specified period. The radiation stresses calculated through the NSW are then used as input in the HD model.

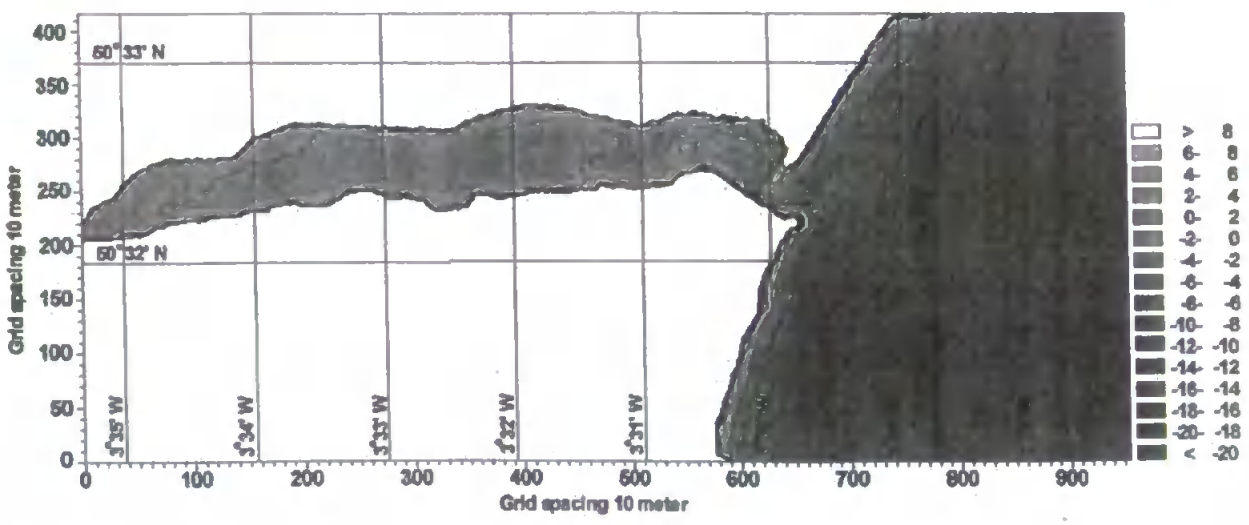

Figure 2. Model grid and bathymetry.

CALIBRATION AND VALIDATION

The MIKE21 model was calibrated and validated against field data obtained during the COAST3D project. In this section a brief explanation of the calibration and validation is given, but a more detailed description is given in SIEGLE *et al.* (in prep.).

There is no standard procedure for model calibration and verification in the modelling literature (CHENG *et al.*, 1991). Typically, calibration or validation is accomplished by qualitative comparison of short time-series of water level or velocity produced by the numerical model with field data for the same location and for the same period of time (CHENG *et al.*, 1993). The COAST3D datasets provide an excellent database for the calibration and validation of coastal area models (SUTHERLAND, 2001; WALSTRA *et al.*, 2001a). These data include accurate bathymetric surveys and a spatially dense array of instruments measuring neap/spring tides and calm/storm conditions.

After the sensitivity tests were carried out with varying eddy viscosity and resistance values, the model was calibrated through comparisons (measured against calculated) of water level and velocity time series for different eddy viscosity and bed resistance values. Two spring tide periods were chosen for the model calibration, including calm conditions (25-29/10/1999) and storm conditions (10-14/11/1999).

Time series of measured data and modelled results were compared and a more objective analysis of the results was also carried out using linear regression analysis and the Relative Mean Absolute Error (RMAE) (WALSTRA *et al.*, 2001b). The best agreement between measured and calculated data was obtained with the use of depth varying resistance coefficients (Chezy numbers) as given in Table 1.

Time series comparison of calculated water level and the measured data for the pier (offshore) and harbour (in the estuary) for both calibration periods, show that the model predicts accurately the water level, with maximum residuals of about 5 cm offshore and 15 cm in the estuary at high water. The RMAE values of 0.009 and 0.016 (pier) and 0.036 and 0.097 (harbour), for each calibration period respectively, indicate an excellent agreement. Figure 3 compares measured and calculated water level time series for the second calibration period, during which the experiments presented in this paper were carried out. As shown in SIEGLE *et al.* (in prep.), velocities are also well predicted by the model, reproducing most of the rapid variations in the measured tidal currents. To validate the model, it was successfully applied at different periods, which present different tide and wave conditions from those of the calibration period.

Table 1. Depth varying Chezy numbers.

Depth (m)	Chezy numbers ($m-s^{-1}$)
H < -3	40
-3 < H < -1	34
-1 < H < 1	32
1 < H	31

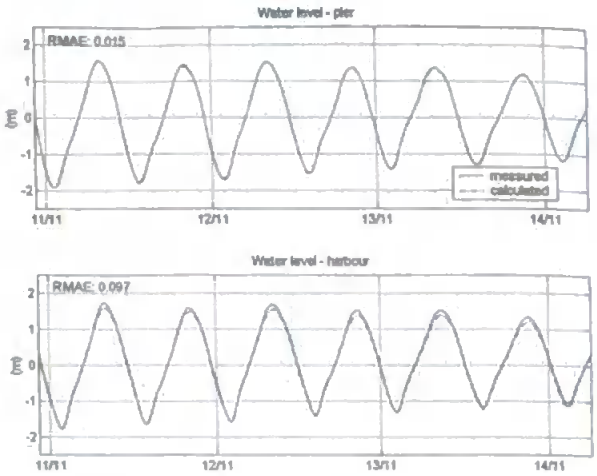

Figure 3. Measured and calculated water level time series for the second calibration period (pier and harbour tide gauge positions).

WATER SURFACE TOPOGRAPHY

Water surface topography is defined as the spatial water level distribution over the area of interest, and is quantified through the analysis of water level deviations in relation to a fixed water level reference point. The reference point used for Teignmouth is the position of the pressure sensor at the Teignmouth pier (Figure 1).

The calculation of the water surface topography from MIKE21 water depths model results involves the following steps: (1) subtraction of the bathymetric data of the water depth grid, resulting in a surface elevation grid file; and (2) the subtraction of the correspondent reference water levels for each time step of interest. Additional steps include the exclusion of dried area data from the emerged sandbars and the extraction of water level residual time series and profile series at points of interest.

Using the calibrated model a series of experiments were conducted aiming to quantify the relative importance of tidal range, wave conditions and river discharge on the water level topography. A sensitivity analysis of the response of the main processes was carried out to define the design of each modelling experiment. Model tests were

focused on the spring tidal phase since maximum variability in water surface topography was observed during this period. It is also during spring tide conditions that the coastline extraction from video images is more important as this permits shoreline detection over a wider area.

Tidal Range

To test the water surface topography distribution in relation to different tidal ranges, the analysis of two runs was carried out, one at neap tide and the other at spring tide conditions. Each test period covers 25 hours (two tidal cycles). During the neap tide period (16/11 – 17/11/1999) the tidal range was 1.6 m and conditions were calm, with significant wave heights (H_{sig}) of about 0.1 m. During the spring tide tests (11/11 – 12/11/1999) the tidal range was approximately 4 m, with H_{sig} varying from 0.7 to 1.4 m. As described below, over the spring tide period, tests with a range of wave conditions were carried out, allowing the analysis the influence of waves to be separated from that of the tidal range.

Wave Conditions

Wave set-up and run-up at the beach are usually included in the techniques to extract morphology from video images (e.g. DAVIDSON *et al.*, 1997; KINGSTON *et al.*, submitted). The aim of this experiment is to quantify the wave effects causing an overall increase in the water level residuals (e.g. in the inlet channels) and also to assess their relative influence across the area. This was carried out during the modelled spring tide period.

Sensitivity tests showed that the most important wave parameter for the water surface topography distribution is Hsig, with the wave period having no significant effect. For this reason, only the Hsig was changed for each run, varying from no waves (0.0 m) to 1.8 m. The period and direction were maintained constant with values of 6.6 s and 115o respectively, as they were the averaged values over the modelled period.

MIKE21 NSW was run for each wave condition using the same parameters as for the calibration period. The parameters governing wave breaking were set as suggested by HOLTHUIJSEN *et al.* (1989): =1.0 (maximum steepness parameter), =0.8 (maximum H/d parameter; H is wave height and d is water depth) and =1.0 (adjustable constant).

River Discharge

Different values of river discharge were also defined for model runs over the spring tide period, evaluating its importance to the water surface topography at the inlet and adjacent coast. As shown before, the Teign river discharge varies significantly during the year (from less than 20 $m^3 s^{-1}$ to 100 $m^3 s^{-1}$). During the modelled spring tide period, the measured river discharge was of about 7 $m^3 s^{-1}$, but for the experiment purpose the discharge was incremented gradually to up to 100 $m^3 s^{-1}$.

RESULTS AND DISCUSSION

Analysis of extracted time series and profile series at different locations around the area of interest, at the positions shown in Figure 1, allows the quantification and assessment of the relative importance of each of the studied processes. Results are described and discussed for each of the processes analysed during the modelling experiments.

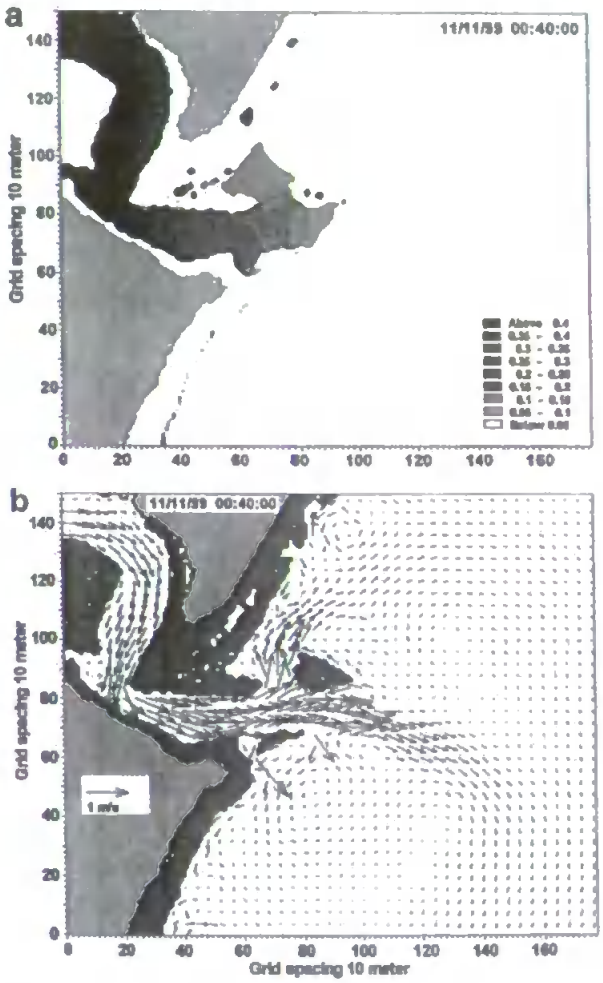

Figure 4. Contour plot of the water surface topography (a) and velocity vector plot (b) at maximum water level residuals (11/11/99 00:40:00).

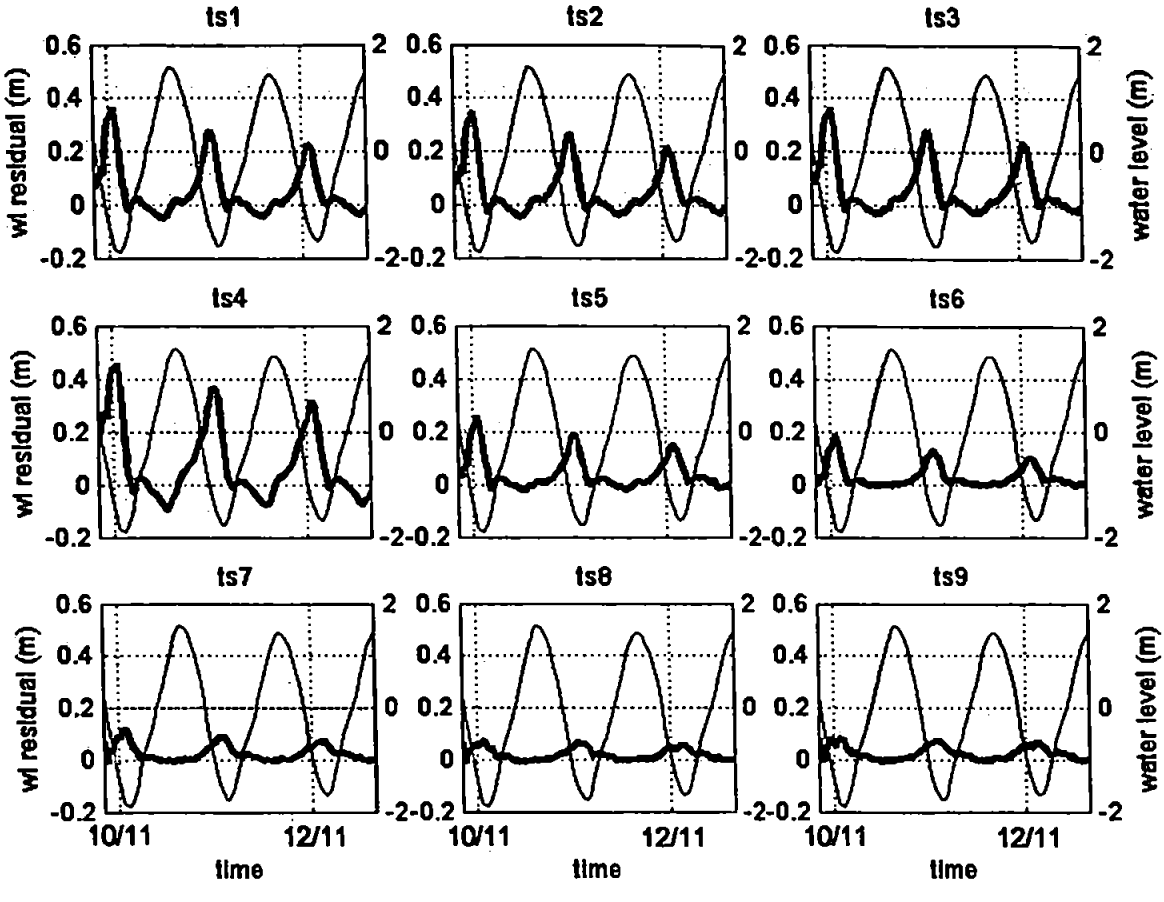

Figure 5. Time series of water level residuals (thick line) and water level (thin line) for each of the extracted locations (TS1 to TS9).

Tidal Range

Water surface topography is directly related to the tidal range, with highest water level residuals during spring tide periods. During the modelled neap tide period, only small changes in water surface topography are registered, with a virtually flat surface around the area. Maximum residual elevations in relation to the pier reference point are less than 5 cm. Conversely, water surface topography varies significantly during spring tide conditions, with maximum and minimum water level residuals in the inlet channel of 0.4 and -0.2 m, respectively. The emerged sandbars at low water spring tide periods play an important role in the funnelling and friction effects of the channel. This is clearly seen in the analysis of a sequence of contour plots of water surface topography over the modelled spring tide period, as shown in Figure 4 for the time of maximum residuals (final stages of ebb tide). During the early stages of the ebb tide, the deeper water column and wider channel reduce these funnelling and friction effects in the channel. This is also seen in time series of water level residuals at different locations (Figure 5). The extracted time series show that maximum residuals are registered at approximately local LW – 1 hour and minimum values at local HW – 1 hour, coinciding with ebb and flood peak currents. Figure 6 shows how the channel current velocities are phase locked with the water level residuals, a response to the pressure gradient forces created by the difference in water level in the estuary and offshore.

The water surface slope between the estuary and the open sea is shown at its maximum gradient in Figure 7a for Profile 1, in the middle of the channel. Figures 7b and 7c

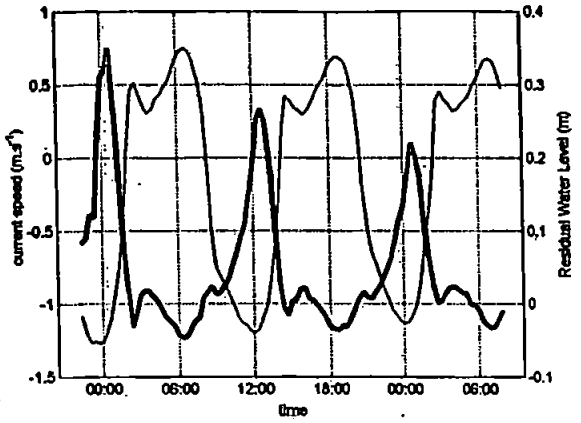

Figure 6. Current speed (thin line) and residual water level (thick line) in the middle of the channel (TS2).

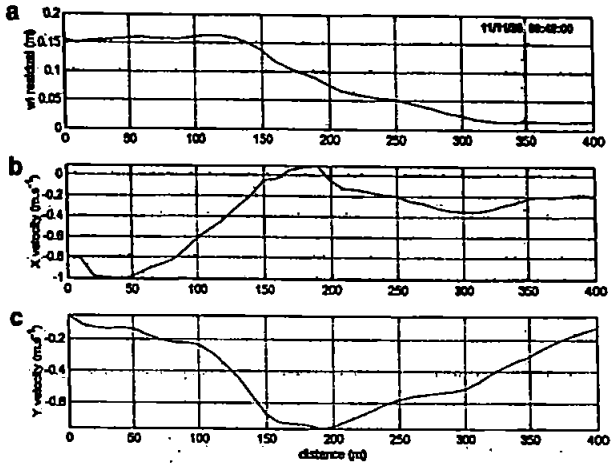

Figure 8. Water slope (a), x-velocity (b) and y-velocity (c) along Profile 2 (P2 = 0 m; P2' = 400 m).

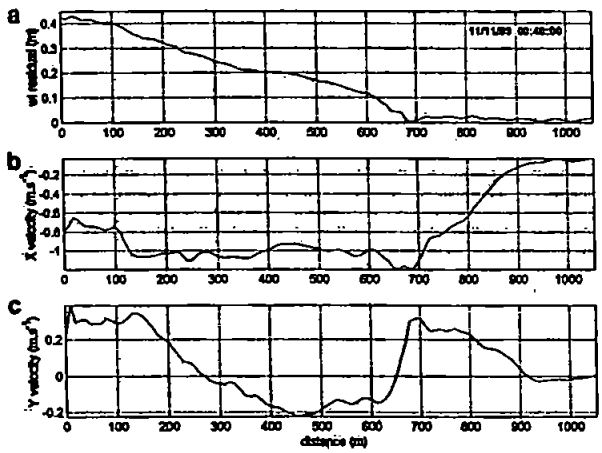

Figure 7. Water slope (a), x-velocity (b) and y-velocity (c) along Profile 1 (P1 = 0 m; P1' = 1050 m).

present the cross and longshore velocities along the same profile, illustrating the relation between them and the surface slope. It shows the dominant cross-shore velocities (x) in the funnelled channel associated with higher water level residuals that generate the slope. When it reaches the end of the channel, the flow spreads out and the slope reaches its end, with values of water level residuals close to zero. This is followed by a decrease in the cross-shore velocity and a slight increase in the longshore velocity as the flow turns to the south as it leaves the channel. Similar behaviour is observed for the longshore slope (Profile 2), from the channel crossing in between the sandbars (Figure 8). Figure 8a shows high residuals inside the channel (up to 140 m from the start of the profile), associated with high cross-shore velocities (Figure 8b). When the secondary flow is channelled northwards through the sandbars, residuals are still significant, with values of about 0.1 m, associated with the high longshore current velocities (Figure 8c). The cross-shore and longshore slopes cycles, from flat surface to the maximum slope and back to flat surface takes of about 5 hours of the ebb tide period.

The interaction between the tidal phase and the sandbar morphology, which defines the velocity field in the channels, has a major influence on the water surface topography distribution across the region. The funnelled flow during ebb tide results in high current velocities and maximum pressure gradient forces between the estuary and the offshore region.

Wave Conditions

The experiments with different modelled wave conditions show their distinct influence across the area of interest. To assess wave influence on the water level residuals, the average values of the extracted time series for each position were used to apply a polynomial regression analysis (Figure 9). The curves fitted present an r squared value higher than 0.99 for all positions. The range in water level residual values shown in Figure 9 also shows the relative increase in wave influence in the region outside the main inlet channel (increasing from TS7, TS8 reaching the maximum influence at TS9, behind the outer Pole sandbar). This region behind

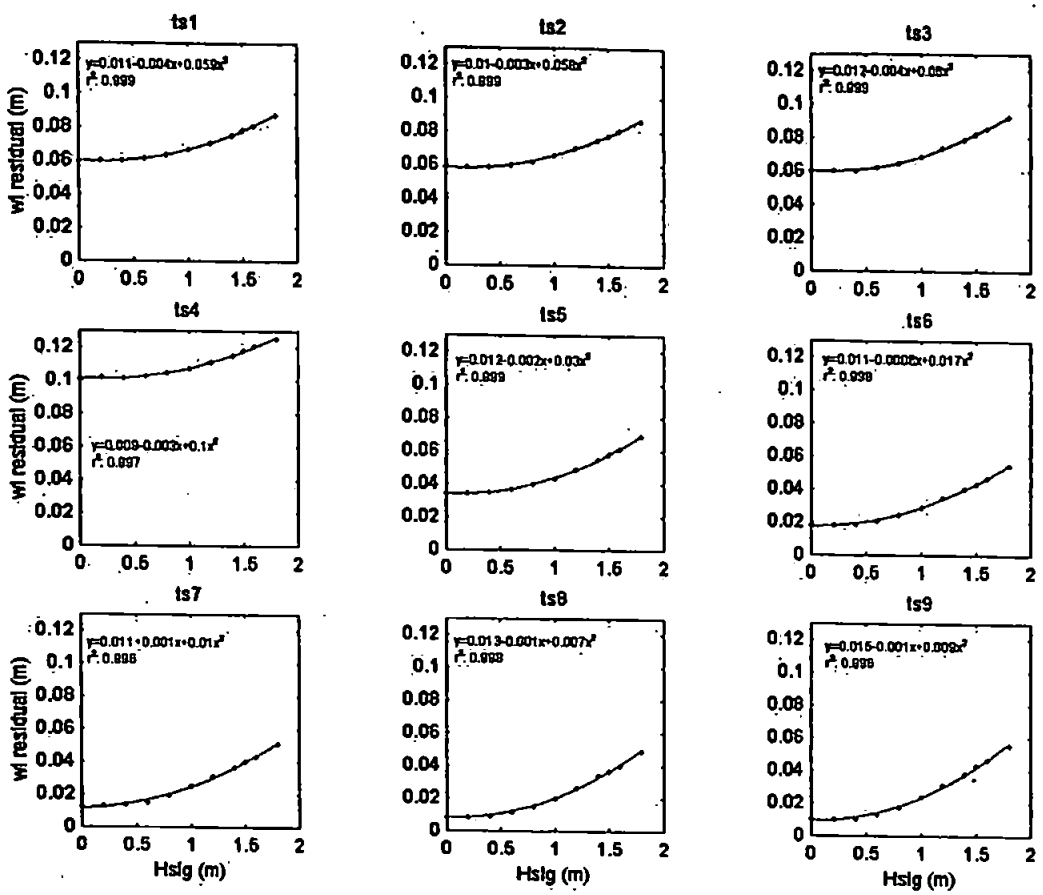

Figure 9. Polynomial regression analysis of the wave induced water level residuals for each of the extracted locations (TS1 to TS9).

the outer Pole sandbar is a region were the waves cause a piling up of the water due to refraction effects around the sandbar. The profile shown in Figure 10 is a cross-shore profile at low tide over the sandbars (Profile 4 in Figure 1). Water level residuals for different wave conditions are plotted showing the significant increase in water residuals mainly behind the outer sandbar. At the outside of the outer sandbar, the waves generate an increase in water level residual after breaking. As only shallow water wave breaking is being considered, the maximum wave height is taken from $H_m = d$ (JOHNSON, 1998).

An increase in wave height also causes an increase in the time of occurrence of the residual, and this also becomes more important when we move to lower tidal range periods. This is illustrated in Figure 11, which is a plot of water level residuals for the extreme experiments (without waves and with H_{sig} of 1.8 m) and the tide elevation.

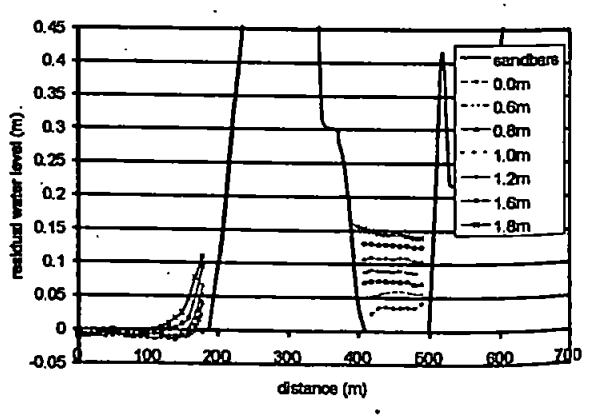

Figure 10. Wave condition effects along the Profile 3 (P3 = 0 m; P3' = 700 m).

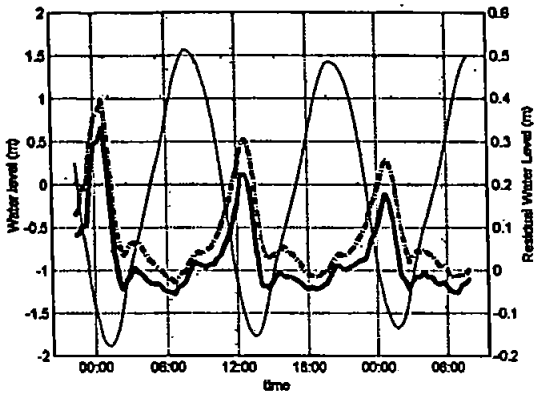

Figure 11. Water levels (thin line) and water level residuals for H_{sig} = 0.0 m (solid thick line) and for H_{sig} = 1.8 m (dashed thick line) in the middle of the channel (TS2).

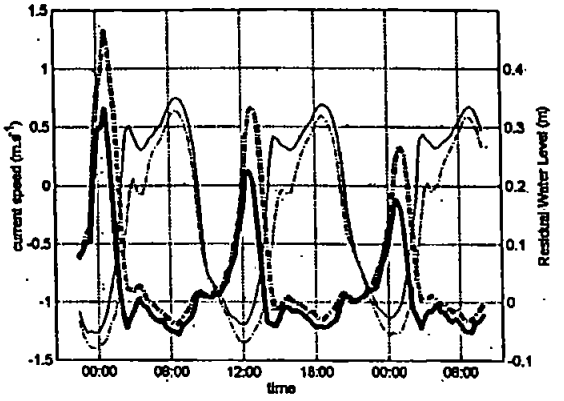

Figure 12. Mid-channel (TS2) current speed (thin lines) and related water level residuals (thick lines) for real condition discharge (solid lines) and for 100 m^3 s^{-1} discharge (dashed lines).

River Discharge

River discharge values varying between the real conditions (of about 7 m^3 s^{-1}) during the modelled period and 100 m^3 s^{-1} caused a maximum increase of about 12 cm coincident with the peak ebb tide currents (Figure 12). Average values over the 25 hour period for high discharge show an increase of about 5 cm compared to low discharge periods. The opposite is verified for the minimum residuals (negative), since the flood currents are reduced due to the residual flow during high discharge periods (Figure 12). This causes the water level residuals during high discharge events to be closer to zero at flood periods, while for low discharge events the residuals become negative in relation to the pier reference point.

The water surface slope gradient in the inlet channel also shows an increase in residual water level during high discharge events. Figure 13 illustrates this for the slope along the Profile 1 for high and low river discharge. The slope gradient is significantly increased at high discharge, but the offshore end of the slope is the same for both conditions, being defined by the channel morphology. The channel and sandbar morphology defines the maximum extend of the water surface deviations across the area of interest. This highlights the importance of the channels and sandbar morphology for the water surface topography variability and distribution. The water surface slopes shown in Figure 13 also show a flattening of the slopes at around 400 m, which is coincident with the secondary channel that guides the flow northwards. This allows part of the flow to spread before it is funnelled again in the final part of the main channel.

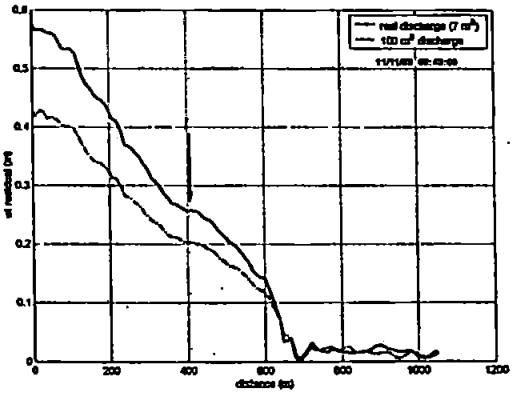

Figure 13. Water slope along Profile 1 for real discharge and for 100 m^3 s^{-1} discharge conditions. The arrow indicates the flattening in the curve at around 400 m distance (P1 = 0 m; P1' = 1050 m).

CONCLUSIONS

A calibrated and validated numerical model (MIKE21 HD, NSW) has been used to model the water surface topography at the complex estuarine inlet system at Teignmouth. The water surface topography at the inlet and adjacent coast presents high spatial and temporal variability, mainly related to the tidal phase. The interaction between tidal phase and sandbar morphology, defines the velocity field in the channels, and drives the water surface topography distribution across the region. Maximum pressure gradient forces between the estuary and the offshore region occur when the flow is funnelled in the channels during ebb tide. The water surface slope presents its maximum gradient at this stage, with its shape directly related to the channel morphology.

The effects of waves increase gradually in the regions outside the main channel, where refraction processes cause water to pile up. River discharge plays an important role in the water surface topography since it is directly related to the velocities in the channel. The higher the river discharges, the higher are the velocities in the channel, and hence the higher are the water level residuals.

This study demonstrates the importance of the water surface topography variations in the coastal region, where a small difference in water level may result in significant deviations of the horizontal shoreline position. As video-imaging techniques to define the coastline rely on water elevation, the knowledge of water surface topography distribution will increase its accuracy.

ACKNOWLEDGEMENTS

The data used in this paper was collected by the partners of the EC COAST3D (MAS3-CT97-0086) project and provided by Dr James Sutherland (HRWallingford). Offshore boundary conditions for the modelled period was kindly provided by Dr Dirk-Jan Walstra (WLIDELFT). The authors are also thankful to the Danish Hydraulic Institute (Dr Pierre Regnier and Dr Hans J. Vested) for the opportunity to use the MIKE21 modelling system in this study through the collaboration in the EC SWAMIEE (FMRX-CT97-0111) project. The Argus video monitoring programme was established by Prof. Rob Holman (Oregon State University). Installation of the Teignmouth Argus system was funded by the ONR NICOP project "Intermediate Scale Coastal Behaviour" (Award No. N00014-97-1-0792). ES is funded by CNPq – Brazil (Ref. No. 200784/98-6).

LITERATURE CITED

AARNINKHOF, S.G.J. and ROELVINK, J.A., 1999. ARGUS based monitoring of intertidal beach morphodynamics. *Proceedings of the Coastal Sediments'99 Conference*. (Long Island, USA, ASCE), pp. 2429-2444.

CHENG, R.T.; BURAU, J.R. and GARTNER, J.W., 1991. Interfacing data analysis and numerical modelling for tidal hydrodynamic phenomena. *In*: PARKER, B.B. (ed.), *Tidal Hydrodynamics*. John Wiley, New York, pp. 201-219.

CHENG, R.T.; CASULLI, V. and GARTNER, J., 1993. Tidal, residual, intertidal mudflat (TRIM) model and its applications to San Francisco Bay, California. *Estuarine, Coastal and Shelf Science*, 36, 235-280.

CRAIG-SMITH, S.J., 1970. *A hydrodynamic analysis of the approaches to Teignmouth*. University of Leicester. Masters thesis.

DAVIDSON, M., HUNTLEY, D.A., HOLMAN, R.A. and GEORGE, K., 1997. The evaluation of large scale (km) intertidal beach morphology on a macrotidal beach using video images. *Proceedings of the Coastal Dynamics'97 Conference* (Plymouth, UK, ASCE), pp. 385-394.

HOLLAND, K.T. and HOLMAN, R.A., 1997. Video estimation of foreshore topography using trinocular stereo. *Journal of Coastal Research*, 13, 81-87.

HOLMAN, R.A., 1994. The ARGUS Program. *Bulletin of the Coastal Imaging Lab*. Oregon State University, Corvallis, OR 97331.

HOLTHUIJSEN, L.H., BOOIJ, N. and HERBERS, T.H.C., 1989. A prediction model for stationary, short-crested waves in shallow water with ambient current. *Coastal Engineering*, 13, 23-54.

JANSSEN, P.C., 1997. *Intertidal beach level estimations from video images*. Delft University of Technology (Delft Hydraulics, Report Z2079), Masters thesis.

JOHNSON, H.K., 1998. On modelling wind-waves in shallow and fetch limited areas using the method of Holthuijsen, Booij and Herbers. *Journal of Coastal Research*, 14(3), 917-932.

KINGSTON, K.S., MALLET, C., PLANT, N.G. and DAVIDSON, M.A. (submitted). Intertidal mapping of morphological features from remotely sensed data. *Journal of Geophysical Research*.

LIPPMANN T.C. and HOLMAN, R.A., 1989. Quantification of sand bar morphology: a video technique based on wave dissipation. *Journal of Geophysical Research*, 94(C1), pp. 99-1011.

MILES, J.R., RUSSELL, P.E. and HUNTLEY, D.A., 1997. Introduction to COAST3D field study site at Teignmouth. *COAST3D Kick-off Workshop Report*. EC MAST Project No. MAS3-CT97-0086.

PLANT, N.G. and HOLMAN, R.A., 1997. Intertidal Beach Profile Estimation using Video Images. *Marine Geology*, 140, 1-24.

ROBINSON, A.H.W., 1975. Cyclical changes in shoreline development at the entrance to Teignmouth Harbour, Devon, England. *In*: HAILS, J. and CARR, A. (eds.). *Nearshore Sediment Dynamics and Sedimentation*. John Wiley, London. pp. 181-198.

SIEGLE, E., HUNTLEY, D.A. and DAVIDSON, M.A. (in preparation). Modelling a complex coastal region – Teignmouth, UK.

SOULSBY, R., 2001. Overview of COAST3D project. COAST3D Final volume of summary papers. *HR Wallingford Report TR 121*.

SUTHERLAND, J., 2001. Synthesis of Teignmouth coastal area modelling. COAST3D Final volume of summary papers. *HR Wallingford Report TR 121*.

WALSTRA, D.J.R., SUTHERLAND, J., HALL, L., BLOGG, H. and VAN ORMONDT, M., 2001a. Verification and comparison of two hydrodynamic area models for an inlet system. *Proceedings of the Coastal Dynamics'01 Conference* (Lund, Sweden, ASCE), pp. 433-442.

WALSTRA, D.J.R., VAN RIJN, L.C., BLOGG, H. and VAN ORMONDT, M., 2001b. Evaluation of a hydrodynamic area model based on the COAST3D data at Teignmouth 1999. COAST3D Final volume of summary papers. *HR Wallingford Report TR 121*.

WARREN, I.R. and BACH, H.K., 1992. MIKE21: a modelling system for estuaries, coastal waters and seas. *Environmental Software*, 7, 229-240.

WHITEHOUSE, R. 2001. Synthesis of Teignmouth process measurements and interpretation. Evaluation of a hydrodynamic area model based on the COAST3D data at Teignmouth 1999. COAST3D Final volume of summary papers. *HR Wallingford Report TR 121*.

WHITEHOUSE, R. and WATERS, C., 2000. COAST3D Teignmouth experiment. An overview of the main experiment October – November 1999. *Volume of abstracts. COAST3D Workshop*, Caen, France.

References

Aarninkhof, S.G.J. 1996. Quantification of bar bathymetry from video observations. *Master thesis*, Delft University of Technology (Delft Hydraulics, Report H2443).

Aarninkhof, S.G.J. and Roelvink, J.A. 1999. ARGUS based monitoring of intertidal beach morphodynamics. *Proceedings of Coastal Sediments '99*, ASCE, Long Island. pp. 2429-2444.

Aarninkhof, S. and Kingston, K. 2002. The Argus runtime environment. Guidelines on installation and use. *WL|Delft Hydraulics*. 29 pp.

Aarninkhof, S.; Ruessink, B.G.; Roelvink, J.A.; De Kruif, A.C. 2003. Quantification of surf-zone bathymetry from video observations of wave breaking. *Proceedings of Coastal Sediments '03*, ASCE, Clearwater Beach, USA. CD-ROM.

Abbott, M.B.; McCowan, A.D; Warren, I.R. 1981. Numerical modelling of free-surface flows that are two-dimensional in plan. In: Fischer, H.B. (Ed.) *Transport Models for Inland and Coastal Waters*. Academic Press, pp 222-283.

Abbott, M.B. and Larsen, J. 1985. Modelling circulations in depth-integrated flows. *Journal of Hydraulic Research*, **23**: 309-326.

Abbott, M.B. and Minns, A.W. 1998. *Computational Hydraulics*. 2nd ed. Ashgate, USA. 557 p.

Ackers, P. and White, W. R. 1973. Sediment Transport: New Approach and Analysis. *Journal of the Hydraulic Division*, ASCE, **99**(11): 2041-2060.

Andersen, O.H.; Hedegaard, I.B.; Deigaard, R.; De Girolamo, P.; Madsen, P. 1988. Model for morphological changes under waves and currents. *Proceedings IAHR Symposium of the Mathematical Modelling of Sediment Transport in the Coastal Zone*, Copenhagen, pp. 310-319.

Andersen, O.H.; Hedegaard, I.B.; Ronberg, J.K.; Deigaard, R.; Madsen, P. 1991. Model for morphological changes in the coastal zone. *IAHR Symposium on Suspended Sediment Transport*, Florence, Italy, pp. 327-338.

Aubrey, D.G. & Speer, P.E. 1983. A study of non-linear tidal propagation in shallow inlet/estuarine systems. Part I: observations. *Estuarine, Coastal and Shelf Science*, **21**: 185-205.

Balouin, Y. and Howa, H. 2002. Sediment transport patterns at the Barra Nova Inlet, South Portugal: a conceptual model. *Geo-Marine Letters*, **21**: 226-235.

Battjes, J.A. and Janssen, J.P.F.M. 1978. Energy loss and set-up due to breaking of random waves. *Proceedings of the 16th International Conference on Coastal Engineering*, Hamburg, Germany, pp. 569-587.

Battjes, J.A. and Stive, M.J.F. 1985. Calibration and verification of a dissipation model for random breaking waves. *Journal of Geophysical Research*, **90**(C5): 9159-9167.

Bijker, E.W. 1967. Some considerations about scales for coastal models with movable bed. Publication No. 50, *Delft Hydraulics Laboratory*, Delft, The Netherlands.

Boothroyd, 1985. Tidal inlets and tidal deltas. In: R.A. Davis (Ed.) *Coastal Sedimentary Environments*. Springer Verlag, New York. pp. 445-532.

Brady, A.J. and Sutherland, J. 2001. COSMOS modelling of COAST3D Egmond main experiment. *HR Wallingford Report TR 115*.

Bruun, P. and Gerritsen, F., 1960. *Stability of Coastal Inlets*. Amsterdam: North Holland. 123 p.

Bruun, P. 1978. *Stability of Coastal Inlets-Theory and Engineering*. Amsterdam, Elsevier. 510 p.

Camenen, B. and Larroudé, P. 2003. Comparison of sediment transport formulae for the coastal environment. *Coastal Engineering*, **48**: 111-132.

Carter, D. and Bray, M. 2003. SCOPAC sediment transport study: Volume 5 Start Point to Portland Bill. *Report to SCOPAC*. University of Portsmouth.

Cayocca F. 2001. Long-term morphological modelling of a tidal inlet: the Arcachon Basin, France. *Coastal Engineering*, **42**: 115-142.

Charfas, C. 1990. The fringe of the ocean – under siege from land. *Science*, **248**: 4952, 163-164.

Cheng, R.T. and Burau, J.R.; Gartner, J.W. 1991. Interfacing data analysis and numerical modeling for tidal hydrodynamic phenomena. In: Parker, B.B. (Ed.) *Tidal Hydrodynamics*, John Wiley & Sons. pp. 201-219.

Cheng, R.T.; Casulli, V.; Gartner, J. 1993. Tidal, residual, intertidal mudflat (TRIM) model and its applications to San Francisco Bay, California. *Estuarine, Coastal and Shelf Science*, **36**: 235-280.

Dalrymple, R.W.; Knight, R.J.; Lambiase, J.J. 1978. Bedforms and their hydraulic stability relationships in a tidal environment, Bay of Fundy, Canada. *Nature*, **275**: 100-104.

Davidson, M.; Huntley, D.A.; Holman, R.A. and George, K. 1997. The evaluation of large scale (km) intertidal beach morphology on a macrotidal beach using video images. *Proceedings of Coastal Dynamics '97*, ASCE, Plymouth, UK. pp. 385-394.

Danish Hydraulic Institute. 2000a. MIKE21 Hydrodynamic Module. *User Guide and Reference Manual.*

Danish Hydraulic Institute. 2000b. MIKE21 Nearshore Spectral Wind-Wave Module. *User Guide and Reference Manual.*

Danish Hydraulic Institute. 2000c. MIKE21 Sand Transport Module. *User Guide and Reference Manual.*

Davies, A.G. and Villaret, C. 2002. Prediction of sand transport rates by waves and currents in the coastal zone. *Continental Shelf Research*, **22**: 2725-2737.

Davies, A.G.; Van Rijn, L.C.; Damgaard, J.S.; Van de Graaff, J.; Ribberink, J.S. 2002. Intercomparison of research and practical sand transport models. *Coastal Engineering*, **46**: 1-23.

Davies, A.G.; Ribberink, J.S.; Temperville, A.; Zyserman, J.A. Comparisons between sediment transport models and observations made in wave and current flows above plane beds. *Coastal Engineering*, **31**: 163-198.

Davis, R.A. 1983. *Depositional systems: a genetic approach to sedimentary geology.* Englewood Cliffs, New Jersey, Prentice Hall. 669 p.

Davis, R.A. 1994. Barrier island systems – a geologic overview. In: R.A. Davis (Ed.) *Geology of Holocene Barrier Island Systems*. pp. 1-46.

De Vriend, H.J. 1987. 2DH mathematical modeling of morphological evolutions in shallow water. *Coastal Engineering*, **11**(1): 1-27.

De Vriend, H.J. 1991. Mathematical modelling and large-scale coastal behaviour, Part 1: physical processes. *Journal of Hydraulic Research*, **29**: 727-740.

De Vriend, H.J. 1994. Two-dimensional horizontal and weakly three-dimensional models of sediment transport due to waves and currents. In: Abbott, M.B. and Price, W.A. (Eds.) *Coastal, Estuarial and Harbour Engineers' Reference Book*, E & FN Spon. pp. 215-238.

De Vriend, H.J. 1996. Mathematical modeling of meso-tidal barrier island coasts. Part I: empirical and semi-empirical models. In: Liu, P.L-F. (Ed.) *Advances in Coastal and Ocean Engineering*, Vol. 2, World Scientific Publishing. pp. 115-149.

De Vriend, H.J. and Ribberink, J.S. 1996. Mathematical modeling of meso-tidal barrier island coasts part II: process-based simulation models. In: Liu, P.L.F. (Ed.) *Advances in Coastal Engineering*, Vol 2, World Scientific Publishing, pp 151-197.

De Vriend, H.J.; Zyserman, J; Nicholson, J.; Roelvink, J.A.; Péchon, P.; Southgate, H.N. 1993 Medium term 2DH coastal area modeling. *Coastal Engineering*, **21**: 193-224.

Deigaard, R.; Fredsøe, J.; Hedegaard, I.B. 1986a. Suspended sediment in the surf zone. *Journal of Waterway, Port, Coastal and Ocean Engineering*, **112**(1): 115-128.

Deigaard, R.; Fredsøe, J.; Hedegaard, I.B. 1986b. Mathematical model for littoral drift. *Journal of Waterway, Port, Coastal and Ocean Engineering*, **112**(3): 351-369.

Down, S.J. 1999. Analysis of surface current velocities using video-imaging techniques at Teignmouth, Devon. *Master thesis*, University of Plymouth, Institute of Marine Studies. 78p.

Dyer, K.R. 1997. *Estuaries: a Physical Introduction*. John Wiley & Sons. 140 p.

Dyke, P.P.G. 2000. *Coastal and Shelf Sea Modelling*. Kluwer Academic Publishers, 272 pp.

Dyke, P.P.G. 1996. *Modelling Marine Processes*. Prentice Hall, 152 pp.

Engelund, F. and Fredsøe, J. 1976 A sediment transport for straight alluvial channels. *Nordic Hydrology*, 7: 296-306.

Engelund, F. and Hansen, E. 1976. A monograph on sediment transport in alluvial channels. *Nordic Hydrology*, 7: 293-296.

Escoffier, F.F. 1940. The stability of tidal inlets. *Shore and Beach*, October, pp. 114-115.

Fenster, M.S. and Dolan, R. 1996. Assessing the impact of tidal inlets on adjacent barrier island shorelines. *Journal of Coastal Research*, **12**: 294-310.

Fenster, M.S. and FitzGerald, D.M. 1996. Morphodynamics, stratigraphy, and sediment transport patterns of the Kennebec River estuary, Maine, USA. *Sedimentary Geology*, **107**: 99-120.

FitzGerald, D.M. and Nummedal, D. 1977. Response characteristics of an ebb-dominated tidal inlet channel. *Journal of Sedimentary Petrology*, **53**: 833-845.

FitzGerald, D.M. 1984. Interactions between the ebb-tidal delta and landward shoreline: Price Inlet, South Carolina. *Journal of Sedimentary Petrology*, **54**(4): 1303-1318.

FitzGerald, D.M. 1982. Sediment bypassing at mixed energy tidal inlets. *Proceedings of 18th Coastal Engineering Conference*, ASCE, Cape Town, South Africa. pp. 14-19.

FitzGerald, D.M. 1984. Interactions between the ebb-tidal delta and landward shoreline: Price Inlet, South Carolina. *Journal of Sedimentary Petrology*, **54**(4): 1303-1318.

FitzGerald, D.M.; Buynevich, I.V.; Fenster, M.S.; McKinlay, P.A. 2000a. Sand dynamics at the mouth of a rock-bound, tide-dominated estuary. *Sedimentary Geology*, **131**: 25-49.

FitzGerald, D.M. 1988. Shoreline erosional-depositional processes associated with tidal inlets. In: Mehta, A.J. (Ed.) *Estuarine Cohesive Sediment Dynamics*. Lecture Notes on Coastal Estuarine Studies. pp. 186-225.

FitzGerald, D.M. 1996. Geomorphic variability and morphologic and sedimentologic controls on tidal inlets. *Journal of Coastal Research*, **SI 23**: 47-71.

FitzGerald, D.M.; Kraus, N.C.; Hands, E.B. 2000b. Natural mechanisms of sediment bypassing at tidal inlets. *US Army Corps of Engineers*, CHETN-IV-30, 10 pp.

Fredsøe, J. 1984. The turbulent boundary layer in combined wave-current motion. *Journal of Hydraulic Engineering*, **100**: 1103-1120.

Frijlink, H. 1952. Discussion des formules de débit solide de Kalinske, Einstein et Meyer-Peter and Müller compte tenue des mesures récentes de transport dans les rivières néerlandaises. *2nd Journal Hydraulique, Société Hydraulique de France*, pp. 98-103.

Golden Software, 1995. SURFER for Windows. *Manual*. Golden, Colorado. Golden Software Inc.

Goldsmith, V.; Byrne, R.J.; Sallenger, A.H.; Drucker, D.M. 1975. The influence of waves on the origin and development of the offset coastal inlets of the southern Delmarva peninsula, Virginia. In: Cronin, L.E. (Ed.) *Estuarine Research*. Academic Press, 2, 183-200.

Goodwin, P. 1996. Predicting the stability of tidal inlets for wetland and estuary management. *Journal of Coastal Research*, **SI 23**: 83-101.

Hayes, M.O. (ed.) 1969. Coastal Environments: NE Massachusetts and New Hampshire. *Guidebook, Fieldtriep for Eastern Section of SEPM*. 462 p.

Hayes, M.O. 1975. Morphology of sand accumulations in estuaries: an introduction to the symposium. In: L.E. Cronin (Ed.) *Estuarine Research*. Vol. 2. Academic Press, New York, N.Y. pp. 3-22.

Hayes, M.O. 1979. Barrier island morphology as a function of tidal and wave regime. In: Leatherman, S.P. (Ed.) *Barrier Islands*. Academic Press, New York. pp. 1-28.

Hayes, M.O. 1980. General morphology and sediment patterns in tidal inlets. *Sedimentary Geology*, **26**: 139-156.

Hicks, D.M. and Hume, T.M. 1996. Morphology and size of ebb tidal deltas at natural inlets on open-sea and pocket-bay coasts, North Island, New Zealand. *Journal of Coastal Research*, **12**(1): 47-63.

Hoekstra, P. and Bell, P.; Van Santen, P.; Roode, N.; Levoy, F.; Whitehouse, R. 2001. Hydrodynamics, intertidal bedforms and sediment transport at the mouth of Teign estuary (UK). *COAST3D, Final Volume of Summary Papers, HR Wallingford Report TR 121.*

Holland, K.T. 1998. Beach cusp formation and spacings at Duck, USA. *Continental Shelf Research*, **18**: 1081-1098.

Holland, K.T. and Holman, R. 1997. Video estimation of foreshore topography using trinocular stereo. *Journal of Coastal Research*, **13**: 81-87.

Holland, K.T.; Holman, R; Lippmann, T; Stanley, J.; Plant, N. 1997. Practical use of video imagery in nearshore oceanographic field studies. *Journal of Oceanic Engineering*, **22**: 81-92.

Holman, R.A.; Lippmann, T.C.; O'Neill, P.V. and Hathaway, K. 1991. Video estimation of subaerial beach profiles. *Marine Geology*, **97**: 225-231.

Holman, R.A.; Sallenger Jr., A.H.; Lipmann, T.C. & Haines, J.W. 1993. The application of video image processing to the study of nearshore processes. *Oceanography*, **6**(3): 78-85.

Holman, R.A. 1994. The ARGUS Program. *Bulletin of the Coastal Imaging Lab.* Oregon State University, Corvallis, OR 97331.

Holthuijsen, L.H.; Booij, N.; Herbers, T.H.C. 1989. A prediction model for stationary, short-crested waves in shallow water with ambient current. *Coastal Engineering*, **13**: 23-54.

Horiuti, K. 1987. Comparison of conservative and rotational forms in large eddy simulation of turbulent channel flow. *Journal of Computational Physics*, **71**: 343-370.

Hume, T.M. and Herdendorf, C.E. 1988. A geomorphic classification of estuaries and its application to coastal resources management – a New Zealand example. *Ocean and Shoreline Management*, **2**: 249-274.

Hume, T.M. and Herdendorf, C.E. 1992. Factors controlling tidal inlet characteristics on low drift coasts. *Journal of Coastal Research*, **8**(2), 355-375.

Huntley, D.A.; Leeks, G.J.L.; Walling, D.E. 2001. From rivers to coastal seas: the background and context of the land-ocean interaction study. In: Huntley, D.A.; Leeks,

G.J.L.; Walling, D.E. (Eds.) *Land-Ocean Interaction: measuring and modelling fluxes from river basins to coastal seas*. IWA Publishing, London. pp 1-7.

Janssen, P.C. 1997. Intertidal beach level estimations from video images. *Master thesis*, Delft University of Technology (Delft Hydraulics, Report Z2079).

Jarrett, J.T., 1976. Tidal prism-inlet area relationships. *GITI Report No. 3, U.S. Army Corps of Engineers*, Waterways Experiment Station, Vicksburg, Mississipi, 54p.

Johnson, H.K. 1998. On modelling wind-waves in shallow and fetch limited areas using the method of Holthuijsen, Booij and Herbers. *Journal of Coastal Research*, **14**(3): 917-932.

Kana, T.W.; Hayter, E.J.; Work, P.A. 1999. Mesoscale sediment transport at Southeastern US tidal inlets: Conceptual model applicable to mixed energy setting. *Journal of Coastal Research*, **15**: 303-314.

Kingston, K.S.; Mallet, C.; Plant, N.G.; Davidson, M.A. (*in preparation*). Intertidal mapping of morphological features from remotely sensed data.

Komar, P.D. 1996. Tidal-inlet processes and morphology related to the transport of sediments. *Journal of Coastal Research*. **SI 23**: 23-45.

Latteux, B. 1980. Harbour design including sedimentological problems using mainly numerical techniques. *Proceedings of 17th International Conference on Coastal Engineering*, Sydney, Australia, pp. 2213-2229.

LeConte, L.J. 1905. Discussion of "Notes on the improvement of river and harbor outlets in the United States" (D.A. Watt). *Transcripts of the ASCE*, Vol. LV, December, 306-308.

Leendertse, J.J. 1967. Aspects of a computational model for long water wave propagation. *Rand. Corp., RH-5299-RR*, Santa Monica, California.

Leonard, A. 1974. Energy cascades in large-eddy simulations of turbulent fluid flows. *Advances in Geophysics*, **18**: 237-247.

Lilly, D.K. 1966. On the application of the eddy viscosity concept in the inertial subrange of turbulence. *NCAR Manuscript No. 123*. National Centre for Atmospheric Research, Boulder, Colorado.

Lippmann T.C. and Holman, R.A. 1989. Quantification of sand bar morphology: a video technique based on wave dissipation. *Journal of Geophysical Research*, **94**(C1), pp. 99-1011.

Lippmann, T.C. and Holman, R.A. 1991. Phase speed and angle of breaking waves measured with video techniques. *Proceedings of Coastal Sediments '91*, ASCE. pp.542-556.

Livezey, R.E.; Masutani, M.; Ming, J. 1996. SST-forced seasonal simulation and prediction skill versions of the NCEP/MRF model. *Bulletin of the American Meteorological Society*, 77(3): 507-517.

Lyne, V.D., Butman, B. and Grant, W.D. 1990. Sediment movement along the U.S. east coast continental shelf- I. Estimates of bottom stress using the Grant-Madsen model and near-bottom wave and current measurements. *Continental Shelf Research*, **10**(5): 397-428.

Madsen, P.A.; Rugbjerg, M.; Warren, I.R. 1988. Subgrid modelling in depth integrated flows. *Coastal Engineering Conference*, Malaga, Spain. Vol. 1, pp505-511.

Mariño-Tapia, I.J. 2003. Coastal transport processes on natural beaches and their relation to sandbar migration patterns. *Unpublished PhD Thesis*. University of Plymouth. 312 pp.

Masselink, G. and Short, A.D. 1993. The influence of tide range on beach morphodynamics: a conceptual model. *Journal of Coastal Research*, **9**: 785-800.

Mehta, A.J. 1996. A perspective on process related research needs for sandy inlets. *Journal of Coastal Research*, **SI 26**: 3-21.

Meyer-Peter, E. and Müller, R. 1948. Formulas for bed-load transport. *Proceedings of 2nd IAHR Congress*, Stockholm, Sweden.

Miles, J.R., Russell, P.E. and Huntley, D.A. 1997. Introduction to COAST3D field study site at Teignmouth. *COAST3D Kick-off Workshop Report*. EC MAST Project No. MAS3-CT97-0086.

Morris, B.D.; Davidson, M.A.; Huntley, D.A. 2001. Measurements of the response of a coastal inlet using video monitoring techniques. *Marine Geology*, **175**: 251-272.

Morris, B.D.; Davidson, M.A.; Huntley, D.A. (*in press*). Estimates of the seasonal morphological evolution of the Barra Nova inlet using video techniques. *Continental Shelf Research*.

Moslow, T.F. and Heron, S.D. 1994. The outer banks of North Carolina. In: R.A. Davis (Ed.) *Geology of Holocene Barrier Island Systems*. pp. 46-75.

Murphy, A.H. and Epstein, E.S. 1989. Skill scores and correlation coefficients in model verification. *Monthly Weather Review*, **117**: 572-581.

Nicholson, J.; Broker, I.; Roelvink, J.A.; Price, D.; Tanguy, J.M.; Moreno, L. 1997. Intercomparison of coastal area morphodynamic models. *Coastal Engineering*, **31**: 97-123.

Nielsen, P. 1979. Some basic concepts of wave sediment transport. *Series Paper 20.* Institute of Hydrodynamic and Hydraulic Engineering, Technical University of Denmark.

Nunney, R.S. 1980. A study of sediment dynamics in a shallow estuary, River Teign, Devonshire. *Unpublished PhD Thesis*. University of Exeter. 364 p.

O'Brien, M.P., 1931. Estuary tidal prisms related to entrance areas. *Civil Engineering*, **1**: 738-739.

O'Brien, M.P., 1969. Equilibrium flow areas of inlets on sandy coasts. *Journal of Waterways, Harbors and Coastal Engineering Division*, (ASCE 95-WWI): 43-52.

O'Connor, B.A.; Famos, A.M. and Cathers, B. 1981. Simulation of coastal sediment movements by computer models. 2nd Int. Conf. of Eng. Software, Imperial College, London, March 1981, Paper VI/6, Ed. R.A.Adey, (Computataional Mechanics, S'ton), 554-568.

O'Connor, B.A. and Nicholson, J. 1992. An estuarine and coastal sediment transport model. In: Prandle, D. (Ed.) *Dynamics and Exchanges in Estuaries and the Coastal Zone*. Springer Verlag, New York. pp. 507-526.

O'Connor, B.A.; Williams, J.J.; Arens, B.; Davidson, M.A.; Dias, J.M.A.; Howa, H.; Sarmento, A. and Voulgaris, G. 1998. The INDIA Project. In: Barthel, K.G.; Barth, H.; Bohle-Carbonell, M.; Fragakis, C.; Lipiatou, E.; Martin, P.; Ollier, G. and Weydert, M. (Eds.) *3rd Marine Science and Technology Conference (European Commission, Brussels)*, 601-609.

Oertel, G. F. 1972. Sediment transport on estuary entrance shoals and the formation of swash platforms. *Journal of Sedimentary Petrology*, **42**(4): 857-863.

Oertel, G.F. 1975. Ebb tidal deltas of Georgia estuaries. In: L.E. Cronin (Ed.) *Estuarine Research*, Vol. 2. Academic Press, New York. pp. 267-276.

Oertel, G.F. 1977. Geomorphic cycles in ebb tidal deltas and related patterns of shore erosion and accretion. *Journal of Sedimentary Petrology*, **47**(3): 1121-1131.

Oertel, G.F. 1988. Processes of sediment exchange between tidal inlets, ebb deltas and barrier islands. In: D.G. Aubrey and L. Weishar (Eds.) *Hydrodynamics and Sediment Dynamics of Tidal Inlets*. Lecture Notes on Coastal Estuarine Studies. pp. 279-318.

Pan, S.; O'Connor, B.A.; Bell, P. and Williams, J.J. 2001. Interactive numerical modelling of the hydrodynamics of combined waves and tides. *Proceedings of Coastal Dynamics '01*, ASCE, Lund, Sweden. pp. 162-171.

Pan, S.; Nicholson, J.; O'Connor, B. 2001. 2DH modelling of the Teignmouth site. *COAST3D, Final Volume of Summary Papers, HR Wallingford Report TR 121.*

Péchon, P.; Rivero, F.; Johnson, H.; Chesher, T.; O'Connor, B.; Tanguy, J.-M.; Karambas, T.; Mory, M.; Hamm, L. 1997. Intercomparison of wave-driven current models. *Coastal Engineering*, **31**: 199-215.

Pickrill, R.A. 1986. Sediment pathways and transport rates through a tide-dominated entrance, Rangaunu Harbour, New Zealand. *Sedimentology*, **33**: 887-898.

Plant, N.G. and Holman, R.A. 1997. Intertidal Beach Profile Estimation using Video Images. *Marine Geology*, **140**: 1-24.

Pritchard, M. 2000. Dynamics of a small tidal estuarine plume. *Unpublished PhD Thesis.* University of Plymouth. 176 pp.

Pritchard, M. and Huntley, D.A. 2002. Instability and mixing in a small estuarine plume front. *Estuarine, Coastal and Shelf Science*, **55**: 275-285.

Ranasinghe, R., Symonds, G. and Holman, R.A. 1999. Quantitative characterisation of rip dynamics via video imaging. *Proceedings of Coastal Sediments '99*, ASCE, Long Island, USA. pp. 987-1002.

Raudkivi, A.J. 1988. The roughness height under waves. *Journal of Hydraulic Research*, **26**(5): 165-178.

Reddering, J.S.V. 1983. An inlet sequence produced by migration of a small microtidal inlet against longshore drift: the Keurbooms Inlet, South Africa. *Sedimentology*, **30**: 201-218.

Reniers, A.; Symonds, G.; Thornton, E. 2001. Modelling of rip currents during rdex. *Proceedings of Coastal Dynamics '01*, ASCE, Lund, Sweden. pp. 493-499.

Robinson, A.H.W. 1975. Cyclical changes in shoreline development at the entrance to Teignmouth Harbour, Devon, England. In: Hails, J. and Carr, A. (Eds.) *Nearshore Sediment Dynamics and Sedimentation*, John Wiley, London. pp. 181-198.

Rodi, W. 1980. Turbulence models and their application in hydraulics – a state of the art review. *Special IAHR Publication.*

Roelvink, J.A. and Van Banning, G.K.F.M. 1994. Design and development of DELFT3D and application to coastal morphodynamics. *Proceedings of Hydroinformatics '94.*

Sha, L.P. 1989. Cyclic morphological changes of the ebb-tidal delta, Texel Inlet, The Netherlands. *Geologie en Mijnbow*, **68**: 35-48.

Sierra, J.P.; Sanchez-Arcilla; Mösso, C. 2001. Teignmouth modelling using LIMOS model. *COAST3D, Final Volume of Summary Papers, HR Wallingford Report TR 121.*

Siegle, E; Huntley, D.A.; Davidson, M.A. 2002. Modelling water surface topography at a complex inlet system – Teignmouth, UK. *Journal of Coastal Research*, **SI 36**: 675-685.

Siegle, E.; Huntley, D.A.; Davidson, M.A. 2003. Sediment transport patterns and morphodynamics at a complex inlet system. *Proceedings of Coastal Sediments'03*, ASCE, Clearwater Beach, USA. CD-ROM.

Siegle, E.; Huntley, D.A.; Davidson, M.A. (*in press*). Physical controls on the dynamics of inlet sandbar systems. *Ocean Dynamics*.

Simmons, H.B. 1955. Some effects of upland discharge on estuarine hydraulics. *Proceedings of the American Society of Civil Engineers*, **81**: 301-312.

Slingerland, R. 1983. Systematic monthly morphologic variation of Assawoman Inlet: nature and causes. *Earth Surface Processes and Landforms*, **8**, 161-169.

Smagorinsky, J. 1963. General circulation experiment with the primitive equations. *Monthly Weather Review*, **91**(3): 99-164.

Smith, S.D. and Banke, E.G. 1975. Variation of the sea surface drag coefficient with wind speed. *Quarterly Journal of the Royal Meteorological Society*, **101**: 665-673.

Smith, J.B. and FitzGerald, D.M. 1994. Sediment transport patterns at the Essex River inlet ebb-tidal delta, Massachusetts, U.S.A. *Journal of Coastal Research*, **10**(3): 752-774.

Soulsby, R. 1998. Coastal sediment transport: the COAST3D project. *Proceedings of the 26th International Conference on Coastal Engineering*, ASCE, Copenhagen, Denmark. pp. 2548-2558.

Soulsby, R. 2001. Sediment transport and morphodynamics on complex coastlines – the COAST3D project. *Proceedings of Coastal Dynamics'01*, ASCE, Lund, Sweden. pp 92-101.

Spratt, T. 1856. An investigation of the movements of Teignmouth bar. John Weale, London.

Stevenson, T. 1886. *The Design and Construction of Harbours: a Treatise on Maritime Engineering*. 3rd ed., A & C Black, Edinburgh, UK.

Stockdon, H.F. and Holman, R.A. 2000. Estimation of wave phase speed and nearshore bathymetry from video imagery. *Journal of Geophysical Research*, **105**(C9): 22,015–22,033.

Stumpf, R.P. and Goldschmidt, P.M. 1992. Remote sensing of suspended sediment discharge into the western Gulf of Maine during the April 1987 100-year flood. *Journal of Coastal Research*, **8**: 218-225.

Sutherland, J. and Soulsby, R. 2003. The use of model performance statistics in modelling coastal morphodynamics. *Proceedings of Coastal Sediments'03*, ASCE, Clearwater Beach, USA. CD-ROM.

Sutherland, J.; Hall, L.J.; Chesher, T.J. 2001. Evaluation of the coastal area model PISCES at Teignmouth (UK). *HR Wallingford Report TR 125.*

Swart, D.H., 1974. A schematization of onshore-offshore transport. *Proceedings of the 19th International Conference on Coastal Engineering*, ASCE, pp. 884-900.

Symonds, G.; Holman, R.A.; Bruno, B. 1997. Rip Currents. *Proceedings of Coastal Dynamics'97*, Plymouth, UK. pp. 584-593.

Van de Kreeke, J. 1992. Stability of tidal inlets; Escoffier's Analysis. *Shore and Beach*, January. pp. 9-12.

Van de Kreecke, J. 1996. Morphological changes on a decadal time scale in tidal inlets: modeling approaches. *Journal of Coastal Research*, **SI 23**: 73-81.

Van Enckevort, I.M.J. and Ruessink, B.G. 2003. Video observations of nearshore bar behaviour. Part 1: alongshore uniform variability. *Continental Shelf Research*, **23**: 501-512.

Van Enckevort, I.M.J. and Ruessink, B.G. 2003. Video observations of nearshore bar behaviour. Part 2: alongshore non-uniform variability. *Continental Shelf Research*, **23**: 513-532.

Van Lancker, V. Lanckneus, J. Morkerke, G. 2001. Sedimentological and morphological development of the nearshore area of Teignmouth (UK). *COAST3D, Final Volume of Summary Papers, HR Wallingford Report TR 121.*

Van Leeuwen, S.M. and De Swart, H.E. 2002. Intermediate modelling of tidal inlet systems: spatial asymmetries in flow and mean sediment transport. *Continental Shelf Research*, **22**: 1795-1810.

Van Noort, J.C. 1997. Rip currents morphodynamic simulations. *Master thesis*, Delft University of Technology (Delft Hydraulics, Report Z2308).

Van Rijn, L.C.; Grasmeijer, B.T.; Ruessink, B.G. 2000. Measurement errors of instruments for velocity, wave height, sand concentration and bed levels in field conditions. University of Utrecht/Delft Hydraulics Report.

Van Rijn, L.C.; Ruessink, B.G.; Mulder, J.P.M. 2002. *COAST3D-Egmond, the behaviour of straight sandy coast on the time scale of storms and seasons*. Aqua Publications, Amsterdam.

Van Rijn, L.C.; Walstra, D.J.R.; Grasmeijer, B.; Sutherland, J.; Pan, S.; Sierra, J.P. 2003. The predictability of cross-shore bed evolution of sandy beaches at the time scale of storms and seasons using process-based profile models. *Coastal Engineering*, **47**: 295-327.

Vincent, C.E. and Downing, A. 1994. Variability of suspended sand concentrations, transport and eddy diffusivity under non-breaking waves on the shoreface. *Continental Shelf Research*, **14**(2-3): 223-250.

Walstra, D.J.R.; Sutherland, J.; Hall, L.; Blogg, H. and Van Ormondt, M., 2001. Verification and comparison of two hydrodynamic area models for an inlet system. *Proceedings of Coastal Dynamics'01*, ASCE, Lund, Sweden. pp. 433-442.

Walton, T.L. and Adams, W.D. 1976. Capacity of inlet outers bars to store sand. *Proceedings of the 15th Conference on Coastal and Ocean Engineering*, ASCE. pp. 1919-1937.

Wang, J.D. 1990. Numerical modelling of bay circulation. *The Sea, Ocean Engineering Science*, 9, Part B, Chapter 32, pp. 1033-1067.

Wang, Z.B.; Louters, T.; De Vriend, H.J. 1995. Morphodynamic modelling for a tidal inlet in the Wadden Sea. *Marine Geology*, **126**: 289-300.

Warren, I.R. and Bach, H.K. 1992. MIKE21: a modelling system for estuaries, coastal waters and seas. *Environmental Software*, **7**: 229-240.

Whitehouse, R.J.S. and Sutherland, J. 2001. COAST3D data report – 3D experiment, Teignmouth, UK. *HR Wallingford Report TR 119*.

Williams, J.J.; Arens, S.A.; Aubrey, D.; Bell, P.; Bizarro, A.; Collins, M.; Davidson, M.; Dias, J.; Ferreira, O.; Heron, M.; Howa, H; Hughes, Huntley, D.A.; Jones, M.T.; O'Connor, B.A.; Pan, S.; Sarmento, A.; Seabra-Santos, F.; Shayler, S.; Smith, J.; Voulgaris, G. 1999. Inlet Dynamics Initiative Algarve (INDIA). *Proceedings of Coastal Sediments'99*, ASCE, Long Island, USA. pp. 612-627.

Williams, J.J.; O'Connor, B.A.; Arens, S.A.; Abadie, S.; Bell, P.; Balouin, Y.; Van Boxel, J.H.; Do Carmo, A.J.; Davidson, M.; Ferreira, O.; Heron, M.; Howa, H; Hughes, Z;

Kaczmarek, L.M.; Kim, H.; Morris, B.; Nicholson, J.; Pan, S.; Salles, P.; Silva, A.; Smith, J.; Soares, C; Vila-Concejo, A. 2003. Tidal Inlet function: field evidence and numerical simulation in the INDIA project. *Journal of Coastal Research*, **19**(1): 189-211.

Zyserman, J.A. and Fredsøe, J. 1992. Inclusion of the effect of graded sediment in a deterministic sediment transport model. *MAST G6M-Coastal Morphodynamics Final Workshop*, Abstracts-in-depth. Pisa, Italy.

Zyserman, J.A. and Fredsøe, J. 1994. Data analysis of bed concentration of suspended sediment. *Journal of Hydraulic Engineering*, **120**(9): 1021-1042.